The Changes of Hailuogou Glacier in the Southeastern Tibetan Plateau and the Impacts on Glacier Dynamics from the Mechanical Ablation

By

Shuyang Xu (MSc, BSc)

Supervised by

Dr. Ping Fu	**University of Nottingham Ningbo China**
Dr. Meili Feng	**University of Nottingham Ningbo China**
Prof. Stuart Marsh	**University of Nottingham**
Prof. Duncan Quincey	**University of Leeds**

University of Nottingham
UK | CHINA | MALAYSIA

A thesis submitted in partial fulfilment of the requirements of the University of Nottingham Ningbo China, for the award of Doctor of Philosophy

September 2022

To my family and friends

Declaration

I hereby declare that the work presented in this thesis has not been submitted for any other degree or professional qualification, and that it is the result of my own independent work.

Shuyang Xu

Full Name Goes Here (Candidate)

16/02/2023

Date

Abstract

Glaciers in the Tibetan Plateau are melting at an unprecedented rate in the context of global warming. As the critical resources of fresh water, the recession and continuous negative mass balance of glaciers have induced local, regional, or even global issues (e.g., water shortages, glacial lake outbursts, mudslides, and sea level rise).

Hailuogou (HLG) Glacier, a typical partly debris-covered temperate valley glacier in the southeastern margin of the Tibetan Plateau, has been experiencing rapid receding in recent two decades. The terminus of HLG Glacier has been becoming highly crevassed and fractured, which can be described as the glacier losing mass through frontal mechanical ablation induced by the intensive interaction between glacier ice and water (e.g., collapsing and calving). The frontal mechanical ablations partly control the dynamics of the glacier terminus and even might have negative impacts on the entire glacier, for which the quantification of these is critical for improving the understanding of future projections of HLG Glacier.

This thesis presents three major components: **1)** the outcomes of nine field trips to HLG Glacier terminus/tongue, including aerial images, ground control points from Real-time kinematic positioning (RTK) and field surveying. Based on the datasets captured from field trips, orthophoto mosaics and digital surface models are generated by using Uncrewed Aerial Vehicle (UAV) images and the algorithm of Structure from Motion with Multiple View Stereo (SfM-MVS). Then, quantitively investigation on mechanical ablations at the glacier terminus was conducted through geomorphological mapping, Digital Eelevation Model (DEM) of Difference (DoD), and digital image correlation (DIC) to derive the landform changes in the glacier terminus area, the ice volume changes of glacier terminus and the glacier surface displacements, respectively. **2)** This thesis also provides four comprehensive time-sequenced landform maps for the entire/partly HLG Glacier tongue from 2018 to 2021 showing the detailed evolution of glacier changes as the ice recedes, including geomorphological, hydrological, and glaciological features. **3)** Photogrammetrically satellite-based stereopsis (ASTER-based stereophotogrammetry) and daily updated high-resolution images (PlanetScope imagery) are used to derive the multiple-year DEMs and glacier extents from 2002 to 2021, respectively. Thus, the ice volume changes and corresponding mass balance changes are then estimated, quantitively illustrating the dynamic evolution s of HLG Glacier for the recent two

decades. Combined with the rough estimation of ice volume change attributed to the mechanical ablation, the contribution of mechanical ablation to the overall mass balance change is then calculated.

The main findings are that **1)** the dynamics of the glacier have changed by interpreting the mapped features from 2018 to 2021. The glacier is in the process of rapid recession, and even possible disintegration. **2)** By analysing the UAV-derived datasets between 2017 to 2020, the HLG Glacier experienced a severe recession as evident by the reduction of the terminal area, the retreat of the terminus position, and reduce of ice volume at the glacier terminus. The margin of the glacier terminus retreated - 132.12 m and in the area affected by the ice collapse events retreated – 236.42 m. The overall ice loss is - $184.61 \pm 10.32 \times 10^4$ m^3, within which the volume change induced by the ice collapse events comprises roughly 28%. **3)** Comparisons between multitemporal DEMs derived from ASTER-based stereophotogrammetry indicate that the mass balance of the entire HLG Glacier is - 12.60 ± 0.89 metre water equivalent (m w.e.) with 19 years from 2002 to 2021 and the annual mean ice mass change is - 0.66 ± 0.05 m w.e.. The annual average is 1.5 times higher than the period of 1968 to 2000 (i.e., 32 years). HLG Glacier has undergone negative mass balance for several decades and the mass loss has been accelerating in the most recent 20 years. **4)** The contribution to the mass balance change of the entire glacier that is attributed to frontal ice collapse is limited (i.e., ranges from 0.48% to 1.12% from 2017 to 2021). However, the mechanical ablation (e.g., frontal ice collapse and subglacial/englacial conduit's roof collapse) has changed the glacier dynamics and the way of losing ice mass to some extent.

The processes of thinning-retreating with extensive mechanical ablation (i.e., frontal ice collapsing-ablation) in HLG Glacier terminus are important to improve the understanding of this form of ice loss from mechanical ablating margins at valley glaciers. Investigations into this with UAVs, optical satellite images, stereophotogrammetry, and alternatively supportive meteorological data provide insights into the glacier changes and impacts of frontal mechanical ablation events via different scales. The results of this thesis not only contribute to the recent changes of HLG Glacier and its projected dynamics, but also the mechanical ablation of the valley glacier and the forecasting of changes in regional glacierized areas.

List of Publications

The following peer-reviewed journal articles have either been published/reviewed or are under the preparation as the result of the work undertaken as part of this Ph.D. thesis.

1. **Xu, S**., Fu, P*., Quincey, D., Feng, M., Marsh, S., & Liu, Q. (2022). UAV-based geomorphological evolution of the Terminus Area of the Hailuogou Glacier, Southeastern Tibetan Plateau between 2017 and 2020. Geomorphology, 108293. https://doi.org/10.1016/j.geomorph.2022.108293
2. **Xu, S**., Fu, P*., Quincey, D., Feng, M., Marsh, S., & Jia, T. Recent (2018-2021) glaciological, hydrological and geomorphological landscape changes of Hailuogou Glacier tongue, southeastern Tibetan Plateau. Journal of Maps. DOI: 10.1080/17445647.2022.214702g
3. Glacier area change and mass balance changes in Mt. Gongga region from 2000 to 2022 (in preparation).

The following peer-reviewed journal articles have either been reviewed or are under preparation, but not as part of this Ph.D. thesis.

1. Feng, M., Zhu, Y., Ren, J., & **Xu, S.** (2022). Water quality response to hydropeaking regulation of the Three Gorges Dam and Gezhouba Dam, China. River research and applications. (Under review)

Conferences:

1. **Xu, S.** and Fu, P., "Short-term Glacial Dynamics Detection of a Maritime Glacier in Southeastern Tibetan Plateau using Cost-effective UAV and Rapid Photogrammetry Techniques", 2021. EGU General Assembly 2021. Online. doi:10.5194/egusphere-egu21-12007.
2. **Xu, S.**, Fu, P., Quincey, D., Feng, M., Marsh, S., Liu, Q., and Jia, T.: The Changes of Hailuogou Glacier in the Southeastern Tibetan Plateau and the Impacts on Glacier Dynamics from the Mechanical Ablation, EGU General Assembly 2023, Vienna, Austria, 24–28 Apr 2023, EGU23-2555, https://doi.org/10.5194/egusphere-egu23-2555, 202
3. **Xu, S.** and Fu, P., "Ice thickness changes and ice volume changes of Hailuogou Glacier, Southeastern Tibetan Plateau for recent 20 years", 2019. Annual Conference of Geographical Society of China (Eastern China), Ningbo.

Acknowledgements

The University of Nottingham Ningbo China has been with me for the last few years. I am filled with gratitude that the University and the people here have allowed me to manifest my dreams. I would like to thank all the people that helped me during my Ph.D. studies.

First and foremost, I would like to thank the supervision team formed by Dr. Ping Fu, Dr. Meili Feng, Prof. Stuart Marsh (UNUK), and Prof. Duncan Quincey (LEEDS) for their invaluable advice and constant encouragement throughout the Ph.D. journey. They provided me with continuous help when drafting the proposal, sharpening the research topic, writing the journal manuscript, and preparing the Ph.D. thesis. Without their guidance, the achieved results would not have been possible.

My deepest gratitude goes to my lead supervisor, Dr. Ping Fu. The fact I must admit that I am not a perfect Ph.D. student, making trouble, self-doubting, and confusion about research throughout the whole process. With careful and patient guidance from her, I start to push through the rough times. Especially, I would like to thank her for bringing me back to the University from the brink of giving up my study, encouraging me to face the challenges of research, and teaching to how to become a responsible person. Research and life are both marathons that require persistence and endurance. Both the recognition and unwillingness of my supervisors to give up gave me the confidence and courage to face the challenges ahead. So, I want to thank my supervisors again for guiding me in enjoying moments with optimism.

Special thank you to Dr. Faith Chan, who gave me the work opportunity as a research assistant at the School of Geographical Science, UNNC, then introduced me to the valuable Ph.D. position, and cared for me whether in life or research. Dr. Nicholas Hamm, who has served as an internal assessor for the past years, deserves my sincere gratitude for his invaluable and objective assessment of my research works and constructive suggestions for improving the quality of research works.

I would also like to extend my sincere thanks to all my friends at the University of Nottingham Ningbo China, for the wonderful time spent together, Mr. Tian Jia, Dr. Jiadi Yin, Ms. Rui Zhao, Dr. Bo Li, Mrs. Renee Gu, Dr. Yuyao Xu, Ms. Sitong Liu. And the thanks also go to everyone who has offered help during the field trips. Thanks to the examiners, Prof Yong Nie (IMHE, CAS) and Dr Stephen Grebby (NGI, UNUK), for taking time out of their busy schedules to conduct the PhD viva for me and provide valuable help to improve the quality of the thesis.

Last, I cannot express how thankful I am to my family for their endless and unconditional love. I would not have come this far without their constant encouragement and trust. My greatest thanks go to my wife Mary Xianghan Peng, who has stood by me through all my travails, my absences, my fits of pique and impatience. She gave me support and help, discussed ideas, and prevented several wrong turns. She also supported the family during much of my graduate studies.

Table of contents

List of figures

List of tables

List of abbreviation

Abbreviation	Definition
a.s.l.	above sea level
ALOS	The Advanced Land Observing Satellite
ASP	Ames Stereo Pipeline
DEM/DSM	Digital elevation model/digital surface model
DIC	Digital Image Correlation
DJI	Dajiang Innovation Ltd.
DoD	DEM of Difference
FFT	Fast Fourier Transformation
FCC	False color composite
GCP	Ground Control Point
GLONASS	Global Navigation Satellite System in Russian
GNSS	Global Navigation Satellite System
GPS	Global Positioning System
GRACE	Gravity Recovery and Climate Experiment
HLG	Hailuogou
Landsat -MSS, -TM. -ETM, OLI	Multispectral Scanner System (MSS), Thematic Mapper, Enhanced Thematic Mapper, Operational Land Imager
Mt.	Mountain
MVS	Multiple View Stereo
NDSI	normalized difference snow index
NDVI	normalized difference vegetation index
NDWI	normalized difference water index
PPM	parts-per-million
RGB	Red-green-blue
RTK	Real-time kinematic
SfM	Structure from Motion
SE TP	Southeastern Tibetan Plateau
Terra ASTER L1A	Terra Advanced Spaceborne Thermal Emission and Reflection Radiometer (ASTER) Level 1A
TIR	Thermal infrared
TP	Tibetan Plateau
UAV	Uncrewed Aerial Vehicle

Chapter 1: Introduction

1.1 Background

Glaciers are the sensitive indicator of climate change and the vital storage of freshwater supply for the majority of the population in the world (Yao et al., 2012, 2007). As the most glaciated region excluding the polar regions, massive glaciers have developed in the Tibetan Plateau and its surroundings with an area of about 116,180 km^2 (Zhang et al., 2012).

Under the context of global climate change and the consequently sustained ice mass loss in high mountain regions, the glacier recession in large parts of the High Mountain Asia region has been observed prevalently over near half-century (King et al., 2019; Liu et al., 2020; Oerlemans et al., 2009; Wang et al., 2014a). According to the International Panel on Climate Change Sixth Assessment Report (IPCC AR6, 2019), the glaciers have lost ice mass more in the last decade from 2010-2020 than in any other decades. Within the context of continuous climatic warming, the glaciers will lose mass consistently. The main way of ice mass loss from glaciers is melting, which is highly linked with recent temperature changes (Cao et al., 2014; Ding et al., 2006; Wu et al., 2020; Yao et al., 2007). Massive glacier shrinkage with an accelerated rate in the Tibetan Plateau (apart from the region of Karakoram) has been indicated by the current estimation of glacier mass balance (Brun et al., 2017; Nie et al., 2021; Yao et al., 2012). The comparison between the first (2000) and second (2015) Glacier Inventory of China reveals that the glacier areas reduced about 17.2% (Zhang et al., 2021). The estimated mass balance change of the glaciated area is approximately -16.3 ± 3.5 Gt yr^{-1} between the decade from 2006 to 2016 as derived from satellite stereo imagery (Brun et al., 2017; Hugonnet et al., 2021).

Most studies on glacier changes in the Tibetan Plateau associate recent glacier ice mass loss mainly with rising temperature (Cao et al., 2014; Ding et al., 2006; Wu et al., 2020; Yao et al., 2007). However, apart from temperature and precipitation-dependent factors, the mechanical ablation events of glaciers amplify the ice mass loss and glacier retreat such as through ice frontal calving and collapsing (King et al., 2019, 2018). Mechanical ablation can be described as the process by which ice fractures from the host glacier, most commonly as a consequence of ice-marginal water-glacier interactions (Falatkova et al., 2019; Haresign, 2004; Sakai, 2012; Sakai and Fujita, 2010)

Mechanical ablation as an efficient way of ice mass loss is caused by structural instability mainly due to water-ice/glacier interactions at the ice margin or the rapid dynamics of the subglacial channels. Mechanical ablation introduces mechanical destabilization into the glacier system via various forms, such as ice calving, ice collapsing, and ice flaking, as a non-linear response to recent climate change (Carrivick and Tweed, 2013). The glacier mechanical ablation events accompanied by water-ice/glacier interactions (i.e., the occurrence of glacial lake/ponding at the glacier terminus) are an important element for contributing to the total ice mass loss budget in the Himalayan region. It is evident that having water bodies existing in the glacier terminus will accelerate the ice mass loss (Falatkova et al., 2019; Liu et al., 2020, 2016; Nie et al., 2017; Sakai, 2012; Sutherland et al., 2020). At present, knowledge of the mechanical ablation events along with water-glacier interaction in their glacier tongues and their impacts on the dynamics of their host glaciers remains relatively limited. Thus, it is imperative that we explore the mechanical ablation pattern of glaciers as well as the water-glacier interactions.

Usually, it is a shared understanding that mechanical ablation events (e.g. ice calving or ice collapsing) happen in marine-terminating, tidewater glaciers, and lake-terminating glaciers as a sensitive response to climate change (Rignot, 2006). Likewise, many mountain glaciers distributed in the Tibetan Plateau exhibited similar phenomena in recent years. For mountain glaciers, mechanical ablation events like the ice calving/collapsing events often occur in lake-terminating glaciers, such as Longbasaba Glacier in the central Himalayas and Tarkading Glacier in the Nepal Himalaya (i.e., Tsho Rolpa Glacial Lake in the frontal area of the glacier) (Sakai et al., 2009; Sakai, 2012).

Generally speaking, glaciers with proglacial lakes or numbers of englacial/subglacial conduits will be saturated by water in the basal of the lower part of the glacier tongue, so that the disintegration of ice floor increases the water depth and results in bottom calving or front collapsing (Liu et al., 2020; Sakai, 2012). Recent works on mechanical ablation events with water-ice/glacier interaction usually focus on subjects in terms of the proglacial lakes, supraglacial ponds/lakes, lake-terminating glaciers, etc. (Colonia et al., 2017; Falatkova et al., 2019; Fujita et al., 2008; King et al., 2019, 2018; Liu et al., 2020, 2016; Sakai et al., 2009; Sakai, 2012). The recent climatic warming in the Tibetan Plateau has promoted the glacial lake formation and enlarged the glacial lake expansion, and dramatic changing impact on the glacier retreating. However, some rapid retreating glaciers accompanied by strong water-glacier interactions in the glacier terminus - but having no proglacial lakes existed (i.e. to some extent, land-terminating glaciers) - in the southeastern Tibetan Plateau occurred with the same or similar processes of mechanical ablation, especially through ice calving and collapsing, etc. (Liu et al., 2020). In other words, the mechanical ablation events for this kind of mountain glacier have not been recorded and reported properly, which is a notable process of ice transport and ice loss contribution besides other common ablation processes.

As a typical example, Hailuogou (HLG) Glacier, a temperate mountain glacier located in the eastern slope of Mt. Gongga, southeastern edge of the Tibetan Plateau (Figure 1.1), has been a rapidly retreating glacier with an annual retreat of ca. 25 m from 2004 to 2006 and 12 m decreasing in thickness in the glacier tongue from 1993 to 2004. (Li et al., 2010; Xu and Yi, 2017; Zhang et al., 2011). HLG Glacier experienced strong processes of thinning-retreating with extensive frontal ice collapsing-ablation as shown in Figure 1.2 (Xu et al., 2022).

Several subglacial/englacial streams flow through the glacier tongue (Li et al., 2010; Liu et al., 2010). The outlet of the englacial/subglacial water channels will form an ice cave in the glacier terminus and then vanish to ice chuck, seracs and clefts through ice disintegration, calving and collapsing as well as the falling down of englacial conduits' roof after a period of time (Li et al., 2010). The periodic occurrences of the frontal ice cave and the shortening of the occurring cycle are evidence of intensive ablation of the HLG Glacier. In most cases, the arising of ice cave formed in the HLG Glacier terminus in accompanied by a high discharge river originating beneath it. For this reason, this strong water-ice/glacier interaction process with a tendency for accelerating retreating in HLG Glacier, compared with lake-terminating glaciers, forms one of the similar preconditions to have ice calving or massive ice collapsing events. Several occurrences of ice calving and collapsing were observed during the field trips from 2017 to 2020. It was observed that some small proglacial ponds of HLG Glacier were exposed after the frontal ice collapse happened during the field trip of 2020, where part of the glacier terminus was slightly immersed in the proglacial pond. Despite the HLG basin has sufficient precipitation all year round and a fraction of the water supply permeated from valley cliffs, the main source of water of HLG basin is from ice/snow-water transformation in the condition of climatic warming according to relevant statistics (Li et al., 2010). In this connection, the mechanical ablation processes acted upon ice calving or collapsing, as a considerable component in the transformation of ice/snow-water which deeply influences the glacier mass balance, and need to be concerned and studied.

The regional climate of southeastern Tibetan Plateau is dominated by southwest (India and Bengal monsoons) and southeast Asian monsoons during the summer (wet season) and by the westerly circulation during the winter (dry season) (Li et al., 2010; Zhang et al., 2010). There are number of glaciers under similar impacts from monsoons in the southeastern and southern Tibetan Plateau, even to a part of the inner Tibetan Plateau (i.e., some transition zones from monsoonal temperate glaciers to continental glaciers). Further, glaciers with similar natural/geographical/topographical/geomorphic features such as HLG Glacier are documented over the massif region in the Tibetan Plateau such as Hengduan, Nyainqentanglha, Gangdise Mountains, central and eastern Himalayas most likely.

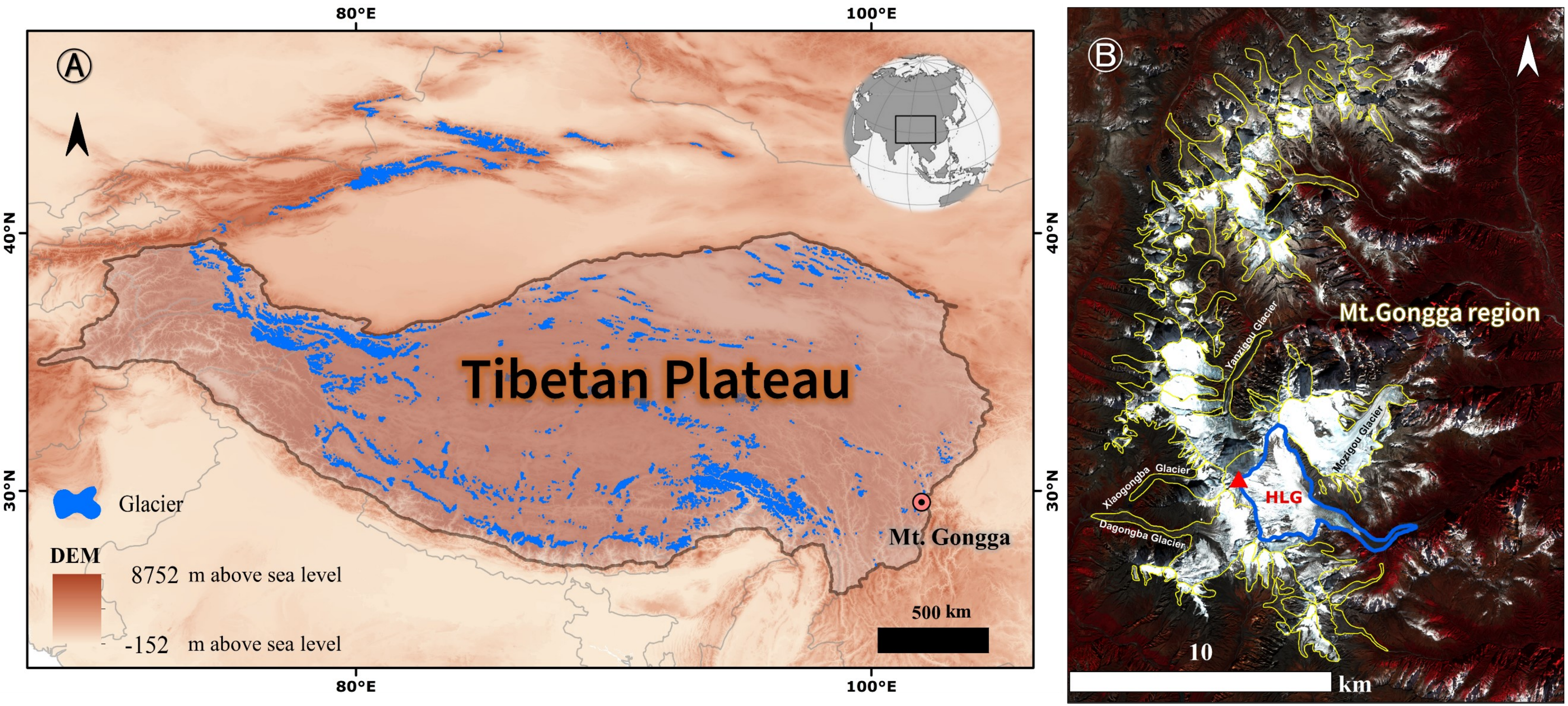

Figure 1.1 A diagram showing the extent and location of the Tibetan Plateau (Zhang et al., 2019) and the glaciers developed in the region of Mt. Gongga. (A) An illustration of the rough extent of the Tibetan Plateau and the location of the Mt. Gongga. The glacier outline is from the Second Glacier Inventory of China version 1 (Liu et al., 2014). The terrain background was extracted from GTOPO30 (~ 1 km resolution) (USGS, 1997). (B) Glaciers of the Gongga Mountain range are highlighted in yellow, and the extent of the HLG Glacier is outlined in blue. The background image is a false-color composite of Sentinel 2A of 10^th^ November 2020.

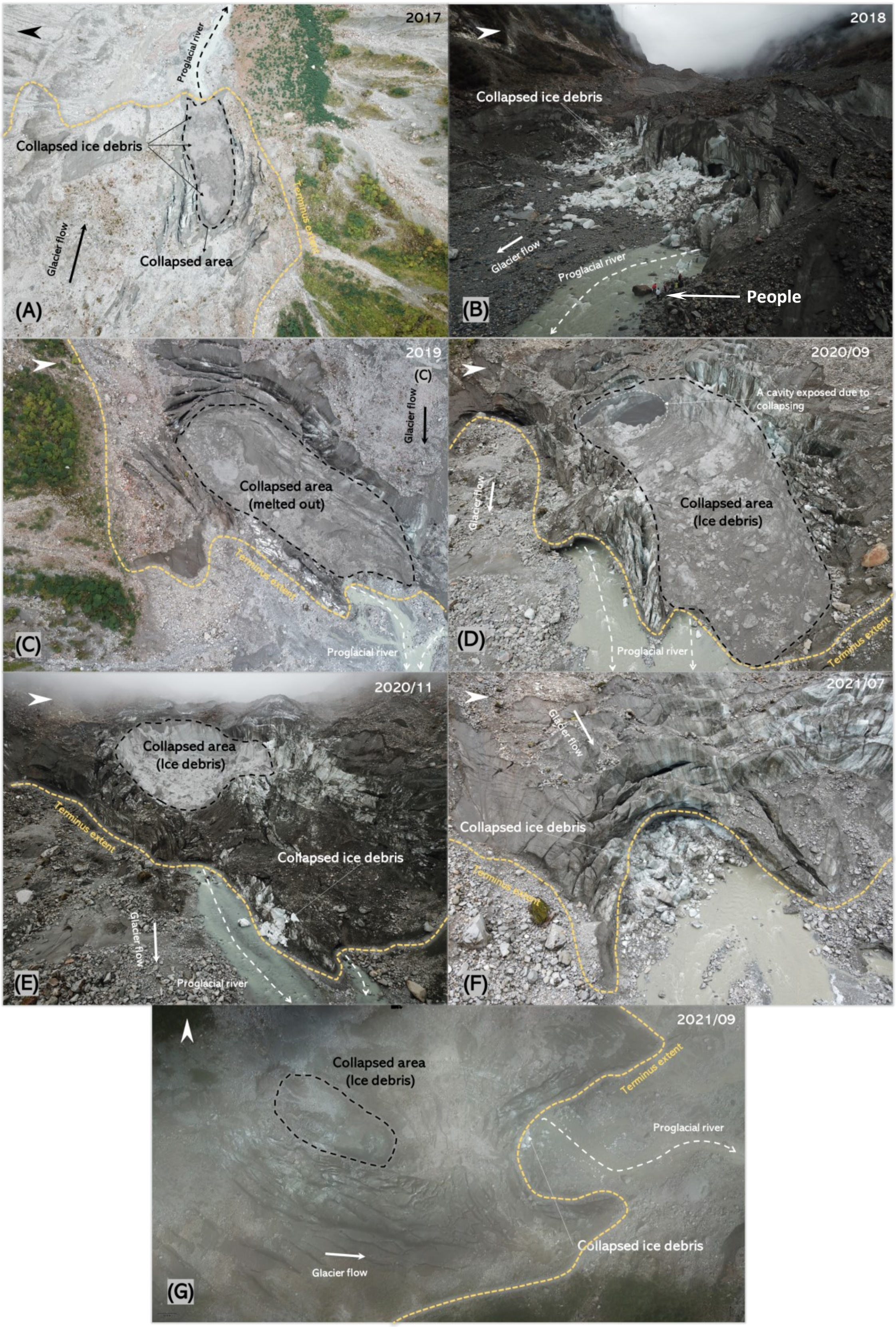

Figure 1.2 Traces of collapsing events at HLG Glacier terminus from drone images captured during field trips from 2017 to 2021.

1.2 Aim and objectives

The primary aim of this study is to improve the understanding of mechanical ablation that occurred at the HLG Glacier terminus. This is for contributing the knowledge about how mechanical ablation (e.g., ice collapse) affects the glacier mass balance changes and its impacts on the glacier dynamics of HLG Glacier, southeastern Tibetan Plateau.

There are many land-terminating glaciers that are undergoing strong processes of water-ice/glacier interactions in their terminus and losing ice mass mechanically. Under sustained regional warming, those glaciers may continue to retreat dramatically with similar mechanical ablation processes (e.g., ice calving, ice collapsing, etc.) caused by water-ice/glacier interactions. Furthermore, those mechanical ablation processes will impact the future dynamics of glaciers significantly. Hereby, I summarized the following objectives:

1. to characterize the evolution of the surface features of HLG Glacier tongue for indicating the changing ice dynamics as well as likely future patterns in ice loss.
2. to investigate the processes of mechanical ablation of the HLG Glacier terminus by using aerial images captured from Uncrewed Aerial Vehicles (UAV) from 2017 to 2020.
3. to reconstruct the time-sequenced mass balance changes of HLG Glacier to estimate the contributions of mechanical ablation that occurred in the HLG glacier terminus to the ice mass loss and the total ice mass balance for its host glaciers.

Novelty: This is the first study to quantitatively estimate the ice mass loss from the mechanical ablation (i.e., frontal ice collapse) in HLG Glacier, a mountain glacier in the southeastern Tibetan Plateau, and its contribution to the mass balance change. The estimation of mechanical ablation for the HLG Glacier enhances the understanding of the glacier recession in the southeastern Tibetan Plateau under the climate change.

1.3 Thesis structure

This thesis investigates the mechanical ablation (i.e., frontal ice collapses) of mountain glaciers and its contribution to glacier dynamics by illustrating three aspects: to present the recent changes in landform features of HLG Glacier tongue, to quantify the mechanical ablation of HLG Glacier terminus, and to reconstruct the sequence of glacier mass balance changes over the observation period.

To achieve this, **Chapter 2** provides a succinct literature review to present the reader with the key themes of glacier mass balance, the mechanical ablation processes, the glacio-hydrological components that are highly related to mechanical ablation, and the mainstream of current glacier observation technologies. The study area (i.e., the Tibetan Plateau and the HLG Glacier) and surrounding landscapes are discussed in **Chapter 3**, including the past glaciations within the HLG Glacier valley, the previous research on the contemporary HLG Glacier, the surface morphological changes, and a brief introduction about the hydrological system of HLG Glacier and past efforts at the research of the HLG Glacier mass balance changes. **Chapter 4** presents the datasets and methods used in this thesis to characterize the spatiotemporal changes of the HLG Glacier tongue and terminus, and to reconstruct the mass balance. This is followed by **Chapter 5**, in which the detailed mapping results are provided by using high-resolution UAV-derived orthophoto mosaics based on the pre-defined mapping criteria to illustrate the interannual changes of landform features of the HLG Glacier tongue. **Chapter 6** applies the drone-captured images and videos to quantify the spatiotemporal change of the glacier terminus to further understand the magnitude of the mechanical ablation events (ice collapse events) that occurred at the glacier terminus and discuss its impact on the glacier dynamics. In **Chapter 7**, stereo images extracted from ASTER L1A images are used to produce the time sequences of digital elevation models based on the satellite-based stereophotogrammetry, and then the subsequent glacier mass changes are derived from differencing of time series of DEMs. Frontal ice collapse events and their contribution to the overall mass balance changes are identified and roughly estimated, respectively. **Chapter 8** is about the discussions, in which synthesis is provided to incorporate the main results and findings from the above chapters to describe the changes of HLG Glacier since our first observations, enhancing the understanding of the frontal mechanical ablation at the glacier terminus and the recent response of the glacier in the near future. **Chapter 9** concludes the thesis and the main aims, and objectives are revisited. The future direction is identified based on the foundation of above analysis and findings.

Chapter 2: Literature review

2.1 Introduction

This chapter seeks to provide a review of research on the glacier dynamics associated with the mechanical ablation processes (e.g., ice collapse and ice calve), its mechanism, and the potential inducing causes, as well as the current observation technologies.

Mechanical ablation at the glacier snout not only modifies the morphology of the glacier terminus even to the lower part of the glacier tongue (i.e., due to the propagation of ice crevasses), but also induces non-linear ice losses and subsequent glacier mass balance changes in response to climate change. Therefore, firstly, we need to determine the components of glacier mass balance so as to be more beneficial to us to understand the glacier mass balance change due to the effects of mechanical ablations, and its importance in the overall mass balance.

Secondly, on the basis of understanding the mass balance of the glacier, the mechanical ablation process was reviewed, including the key reasons for the occurrence of mechanical ablation (formation of ice crevasses, propagation of ice crevasses, and ice disintegrating to collapsing), the driving factors leading to the glacier mechanical ablation, and the mechanism of mechanical ablation.

Thirdly, many studies have shown that the formation and development of proglacial lakes are closely related to the occurrence of mechanical ablation at the glacier terminus. In other words, the existence and persistence of proglacial water bodies exacerbate glacier ice loss. The ablation pattern of glacier snout, the related evolution of glaciers, and the resulting mass balance changes have in common with water-terminating glaciers. Therefore, it is necessary to review the formation, evolution, effects, and life cycle of proglacial lakes to help the exploration of the mechanical ablation of the HLG Glacier. At the same time, the development of the supraglacial lake at the lower part of the ablation zone of the glacier is one of the factors affecting mechanical ablation. On the one hand, the occurrence and evolution of the supraglacial lake are one of the pre-conditions for the formation of the proglacial waterbody. On the other hand, the supraglacial lakes are closely linked with supraglacial runoff, ice cliffs, ice crevasses, and englacial conduits, therefore, a brief understanding of supraglacial lakes is also necessary, especially the role of supraglacial lakes on mechanical ablation. Moreover, the subglacial and englacial hydrological evolution can affect the meltwater runoff at the glacier terminal and then affect the hydrological process of the glacier river. The expansion of the subglacial channel network and the spatial distribution and morphology of the englacial conduits will impact the structure and stability of the ice at the glacier snout. Therefore, subglacial channels and englacial conduits need to be introduced. Combined with proglacial lakes and supraglacial lakes, the basic hydrological system within the glacier is formed.

Finally, multiple techniques of earth observation that are used to monitor the glacier were reviewed. The recent innovation in observation sensors and processing technologies has brought new applications for glacier-related studies, not only remotely sensed techniques, but also in-suit toolkits (Taylor et al., 2021).

2.2 Glacier mass balance

2.2.1 Overall

Glacier mass balance (or glacier mass budget) is known as the summation of the input and output of all forms of water, snow, ice, and melting components occurring in a glacier system that governs the behavior and dynamics of glaciers. Mass balance is the variations in changes of a glacier over a period of time (Cogley et al., 2011)

A glacier can be divided into two parts conceptually, the *accumulation* part (i.e., accumulation exceeds ablation) and the *ablation* part (i.e., ablation exceeds accumulation), where the position that mass gain (i.e., accumulation) and mass loss (ablation) are equivalents is termed as the equilibrium line altitude (ELA). In the scenario of climate warming, the ELA will be climbing, altering the glacier terminus to retreat subsequently (Figure 2.1). Successive years of fresh snow were progressively compacted and layered to lead to the reduction of the air in the ice pores, and then form the glacier ice (i.e., accumulation). In the meantime, the ablation removes glacier mass in various ways from the glacier system once the glacier ice is formed (Figure 2.2).

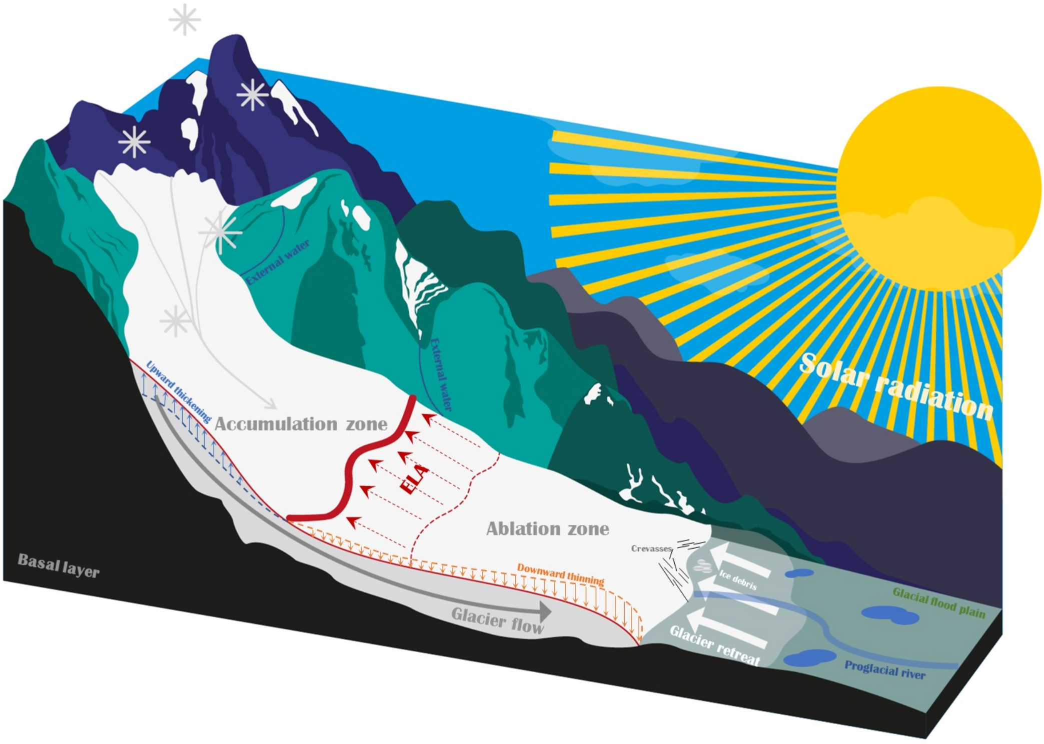

Figure 2.1 Conceptual illustration of the mass balance of a valley glacier within a particular scenario of climate warming (Modification based on the map from OGGM-EDU; https://edu.oggm.org/en/latest/glacier_basics.html/).

The mass balance is the key factor to evaluate glacier health (Zhang et al., 2012). The variation of the mass balance is the underlying influencer for changes in the glacier morphology, regional fresh-water supply, and even the contributions to the sea levels (Zhang et al., 2018). It is well-acknowledged that sustaining warming is the major force of the recently negative glacier mass balance (Liu et al., 2021). In the past half-century, the majority of mountain glaciers have been shrinking, inducing a series of abrupt variations in regional water cycling, geo-hazards, and bio-environment crisis (Yang et al., 2013). Based on the 2nd Chinese Glacier Inventory (CGI), the glacier area in western China has decreased compared to the situation in the 1970s, with a decrease 18% (Guo et al., 2015; Liu et al., 2021; Wei et al., 2014).

The primary representative of the mass balance changes of glaciers is the glacier surface elevation changes. About 440 glaciers across the world have been monitored for mass balance by the approaches of direct field measurement according to the available data in the World Glacier Monitoring Service (WGMS; Rabatel et al., 2017). Among these 440 glaciers listed in the WGMS, only 40 glaciers have been monitored uninterruptedly for more than 40 years. Limited sample datasets restricted the study of the mass balance changes varied with time and the understanding of the underlying connections between the climatic forces and the glacier dynamics. the second place is the remoteness and logistic supply for conducting fieldwork in those glaciated regions. Therefore, there is an urgent need for the acquisition of mass balance changes regionally and individually from other approaches besides direct field measurements. For the last half-century, many studies have shown the advanced strength of satellite-based methods for tracing glacier characteristics (Barella et al., 2020; Berthier and Toutin, 2008; Fahnestock et al., 2016; Gaddam et al., 2021; Li et al., 1998; Paul et al., 2016; Shiramizu et al., 2017; Suzuki et al., 2007; Wei et al., 2014). With the increase of the stereo-sensors aborded in satellites and the space-based photogrammetric techniques, the glacier surface topography has been allowed to be mapped repeatedly, and further to generate the geodetic mass balance in return (Berthier et al., 2007; Garg et al., 2022; Rabatel et al., 2017; Wu et al., 2018).

2.2.2 Ablation to mass balance changes

The glacier ablation process that removes the ice mass from the glacier through various forms (Figure 2.2) such as evaporation, melting, wind-derived ablation, sublimation, calving, and associated glacial runoff (Benn and Evans, 2013). The glacier mass balance can be influenced greatly by altering the means of ablation and its magnitude (i.e., increasing and decreasing ablation). For instance, reducing ablation may occur at debris-covered glaciers with relative thick supraglacial debris-mantle on the glacier surface as the mantled surface has a lower albedo compared with clean ice, isolating the glacier ice from solar radiation (Etienne Berthier et al., 2007; Fujita et al., 2000; Gardelle et al., 2013). Enhancing ablation may occur through mechanical ice loss processes such as frontal ice avalanching or ice calving, which deeply results in great deficits in ice mass budget and affects the subsequent glacier dynamics within the context of varying climates (Benn and Åström, 2018; Chauché et al., 2014; Diolaiuti et al., 2004; Rea and Evans, 2007). These two kinds of ablation processes (reducing/enhancing ablation) can affect the glacier dynamics in isolation or can occur in parallel as a combination to generate a circumstance of strong water-ice/glacier interaction for glacier development, such as HLG glacier (i.e., supraglacial debris cover, and ice mass loss related to terminus ice calving and collapsing) (Figure 2.2).

Within the context of global warming, the glaciological mass balance of High Mountain Asia (HMA) is situated in the negative balance (Yang et al., 2013; Yao et al., 2007), and their glacial dynamics are greatly influenced by the forms of ablation as well as their magnitudes. For example, glacier ablation of mountain glaciers might be amplified via mechanical ice loss processes, such as frontal ice collapsing and ice calving, induced by the seasonal enhanced water-ice interactions.

Thus, more and more frequent mechanical ablation occurring in the glacier terminus is influencing the pattern of mass balance changes for the whole glacier recently. In other words, the mechanical ablation may account for more proportions in the mass balance changes for the entire glacier with the warming. On the one hand, the mechanical ablation of glaciers can modify the geomorphological landscape for the glacier terminus part. On the other hand, as an amplified factor for glacier ablation, it induces a non-linear rate of ice loss and forces the glacier dynamics to decouple from the drivers of climate changes (Carrivick et al., 2013; Carrivick and Tweed, 2013).

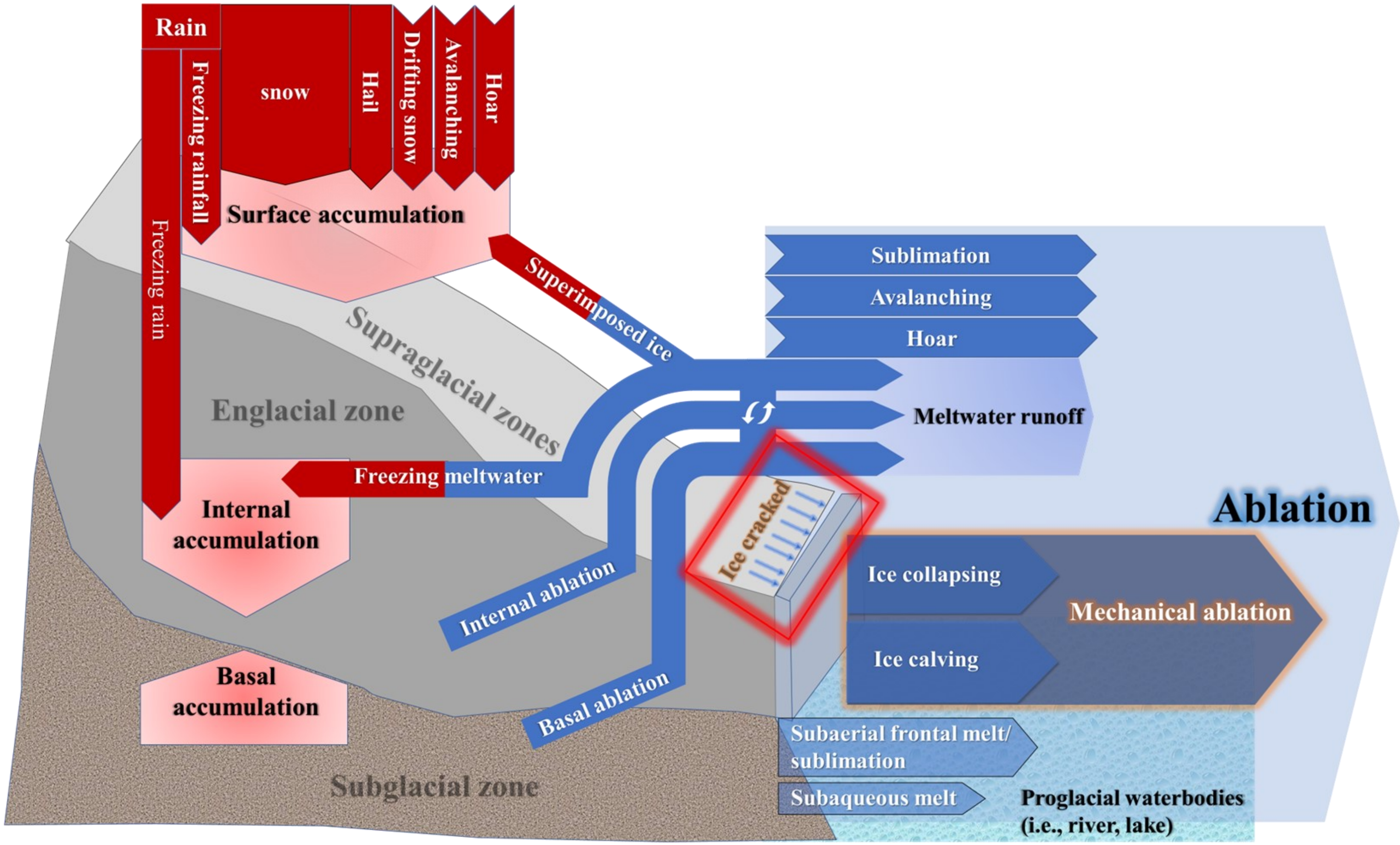

Figure 2.2 Conceptual illustration of the mass balance of a glacier system. Plenty of means of glacier ablation remove the ice mass from the host glacier (modified from Cogley et al (2011)). Glaciers lose ice mass through mechanical ways at the glacier terminus, e.g., collapse or calve.

2.2.3 The effects of debris mantles on mass balance changes

Compared with clean ice or snow, the debris mantle has a unique thermal effect on its covered objects and leads to a different ablation process for the covered glacier ice (Sakai and Fujita, 2010; Zhang et al., 2018; Zhang et al., 2011). Presently, the comprehensive effects of the debris mantle of glacier surface on glacier ablation are still in controversial. In general, the debris mantle on the glacier surface may accelerate the glacier ablation process (i.e., the ablation of the debris-covered glacier is great than the ablation of a clean ice glacier), when the mantle thickness is smaller than a typical threshold of the thickness (~20 to 30mm). On the contrary, the thermal resistance effect from the debris mantle may restrain the glacier ablation with the thickening of the debris mantle (Nakawo and Young, 1982; Östrem, 1959; Zhang et al., 2018).

The wide distribution of debris mantle on maritime glaciers indicates the maritime glacier has strong glacial erosion and transportation. Furthermore, the extent and thickness of debris covers on the glacier ablation zone may alter the process of surface thermal transmission, thereby influencing the ablation, mass balance, and melting runoffs. Meanwhile, heterogeneity of glacier ablation in the debris-covered zone might form more complicated structures in the glacier system and facilitate the glacier ablation process, for example, ice crevasses, ice cliffs, supraglacial lake/ponds, englacial/subglacial conduits (Benn et al., 2012; Benn and Lehmkuhl, 2000; Zhang et al., 2011). Debris-covered glacier is a common type of glacier distributed widely over the Tibetan Plateau and its surroundings. As indicated by the 2nd CGI, 1,723 debris-covered glaciers exist in China with a total area of 12,974.7 km^2 and these debris-mantle occupy around 11.5 % of the total area of these glaciers (Liu et al., 2015, 2014; Zhang et al., 2018). Debris-covered glaciers are mainly distributed in Tien Shan, Himalaya, eastern Pamirs, Nyainqentanglha, Karakoram, and Kunlun Mountain regions, of which the debris-covered glaciers in Tien Shan region have the largest quantity and distributed area (Zhang et al., 2018).

2.3 Mechanical ablation process

Apart from the common ablation processes that remove ice mass from the glacier system, the mechanical ablation processes are enhancing ablation processes such as ice avalanches, ice collapsing and ice calving. As a disturbance to glacier mass balance, their occurrences result in significant deficits in the total ice budget (Benn and Åström, 2018). There are four types of calving events categorized by the surrounding setting, ranging from tidewater, freshwater (lacustrine) ice-shelves and ground-landing (also known as dry calving) (Benn and Åström, 2018; Benn and Evans, 2013; Diolaiuti et al., 2004; Dykes, 2013). At the glacier terminus occurs the calving event, although one calving margin might be governed by one typical calving mechanism, all types of calving events possibly be found at all glacier terminuses. For instance, tidewater- and lacustrine glaciers may have multiple types of calving events happening in their termini such as dry calving from the steep slope, frontal calving by the decomposition of ice cliffs/crevasse, and subaqueous calving by water thermos-erosion, etc., (Benn et al., 2007; Benn and Åström, 2018; Benn and Evans, 2013; Sakai, 2012). The dry calving (or can be described as the appearance of ice avalanching in the glacier terminus) is referred to as a form of ice loss where ice block falls on the ground into the low altitude of glacier or melting in-situ, constraining within the local stress concentrations. The dry calving not only particular occurs at dry-land terminating glaciers, but also might be found in other types of glaciers if they have a steep inclination in the terminus (e.g. hanging glaciers) (Benn and Åström, 2018; Dykes, 2013). It is noted that the melting rate of ice sections is more rapid when they fall on the ground rather than in the water. Dry calving events are commonly found around the Arctic glaciers, but the exact mechanism that controls them is still not clear. Studies related to dry calving are limited and still in the theoretical stage due to its lower significance to glacier ablation compared to iceberg calving events and melting processes. For a typical example, a study investigated the serac formation processes and concomitant local stress-derived dry calving events (Pralong and Funk, 2005). However, apparently, the mechanism that governed the occurrence of dry calving events is not only dominated by the local stress concentrations, but they have also been influenced by other internal and external factors, and their proportion is increasing in the glacier ablation processes. Considering the proglacial status of the HLG Glacier and its mechanical ablation pattern around the glacier terminus, other than ice collapse events from water involved and dry calving events, ice calving of the HLG Glacier is in the middle state among them.

2.3.1 Ice disintegrating to collapsing and calving

Theoretically, ice calving events are the consequences of a series of propagations of ice fractures (e.g., disintegrations and crevassing of ice) in response to the local compositive forces and stresses. The ice fractures as the underlying factors of the initiation of ice calving are key to the position, cycle, rate, and magnitude of ice calving (Benn et al., 2007). Various processes within the ice fractures provide a line or patch of weakness where the ice calving is developing and occurring. A glacier is a typical example in plastic rheology as a non-Newtonian medium, which means the glacier has both characteristics of toughness and brittleness under external and internal applied stresses (Nye, 1951). In the case of ice fractures, plastic deformation can be transformed from brittle fragmentation when the fracture strength of glacier ice is surpassed by an arrangement of compositive stress applied to the part of the ice body (tensile or compressive) (Benn and Evans, 2013; Nye, 1951).

There are three types of conceptual modes for the development of ice cracks to ice crevasses identified by Benn et al. (2007) as shown in Figure 2.3. For all three modes, the precondition is particular stress applied to the existing ice cracks with a particular direction so that the ice fractures will occur once the stress threshold is exceeded. In mode A, ice block is pulled apart by tensile force to form ice fractures, which may lead to ice crevasses or other fragmentations. Mode B indicates an ice crack that develops along the shearing directions and two ice sections are mutual sliding. Mode C mirrors a representation of ice fractures caused by tearing stress. In reality, glacier ice fractures might appear as the combination of two or all three modes with varying proportions simultaneously.

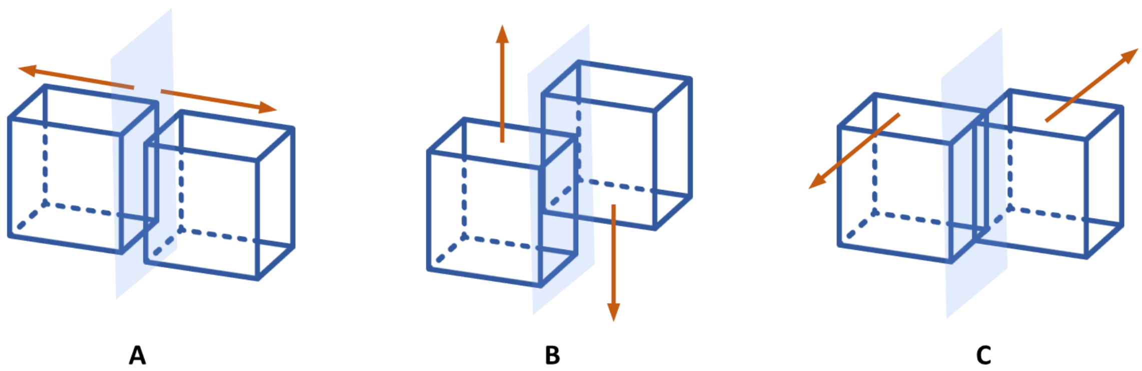

Figure 2.3 Conceptual diagram of three ice fracturing modes, modified from Benn et al (2007). A: ice fracturing under tensile force; B: ice fracturing under shearing stress; C: ice fracturing under tearing stress.

With the growth of ice fracturing and their propagation to the ice body, the depth of crevasses is considered to be a significant factor in controlling the collapsing/calving margin. In other words, the depth of crevasses determined the size or magnitude of the ice calving to some extent as the ice crevasses will continuous deepening in some circumstances until the ice crevasses penetrate the ice body to the glacier bed or isolate ice sections for calving (Colgan et al., 2016). From a perspective of stress analysis, the tensile force from the stretching of ice and compressive force from the weight of the ice body is matched, which limits the ice crevasses going deeper (as shown in Figure 2.4) (Benn et al., 2007; Dykes, 2013). Thereby, Ney (1957) derived a theoretical depth function based on given conditions aimed at crevasse growth under mode A (i.e., tensile stress). However, the crevasse depth model of Nye (1957) is effective only under perfect conditions, in other words, it cannot fit the actual case. For example, in reality, the existence of water may influence the ice crevasses depth to a great extent such as water retention within the ice crevasses or englacial conduits existing (Figure 2.4). Driven by cryostatic pressure, the ice crevasses will propagate to deeper ice bodies if sufficient water supplies through to the glacier bed and establish connections to the subglacial channels. Therefore, Benn et al. (2007) established a new formula based on the Nye (1957)'s model to calculate the depth of ice crevasse (d) considering the presence of water as follows:

$$\mathbf{d} = \frac{2}{\rho_I g}\left[\left(\frac{\dot{\varepsilon}}{A}\right)^{\frac{1}{n}} + (\rho_W g d_w)\right] \qquad (1)$$

Where $\mathbf{d}$ is the depth of crevasse, g is the gravity, $\dot{\varepsilon}$ is the tensile stress, ρ_I is the ice density, **A** and **n** are the flow law parameters, ρ_W and d_w are the water density and depth within the ice crevasses, respectively.

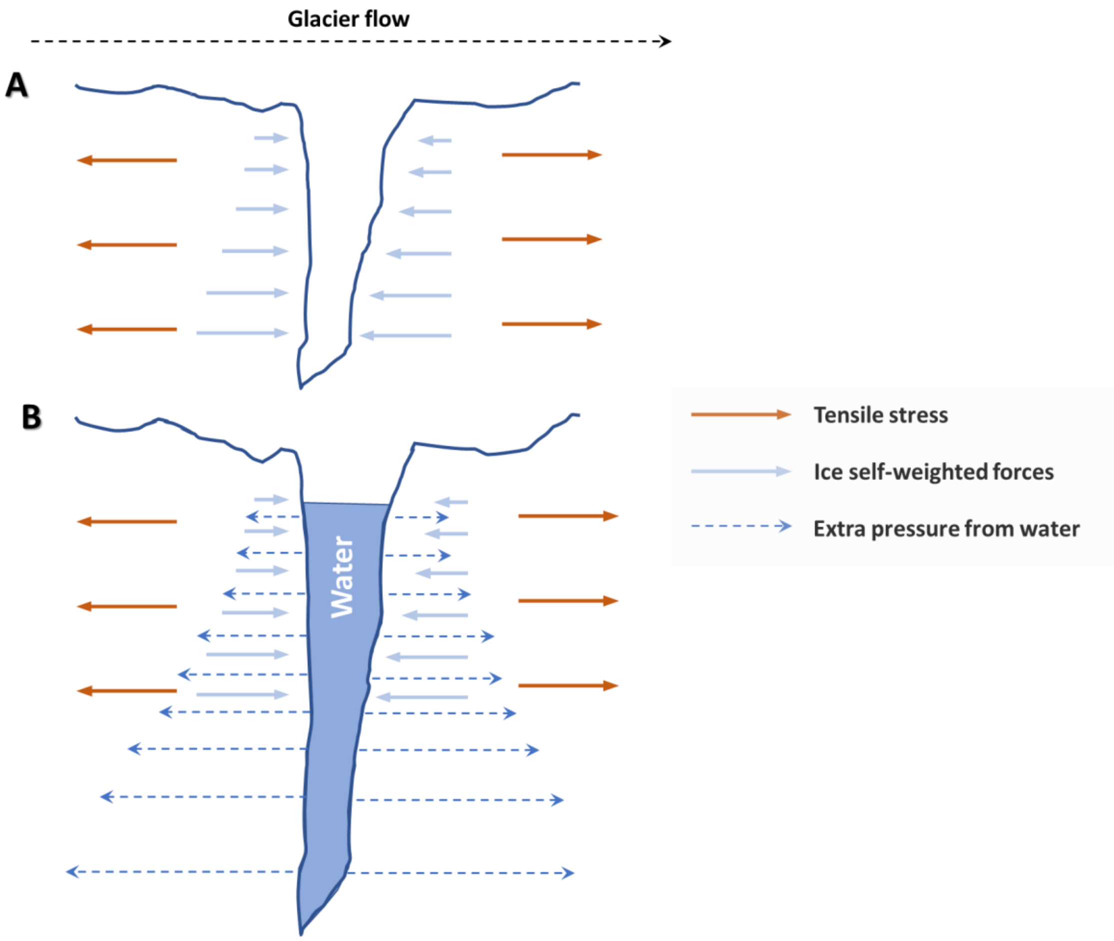

Figure 2.4 Conceptual diagram representing force condition of ice crevasses development and its propagation. A shows an ideal case that the ice crevasses are under the combination of tensile stress and compressive force by the weight of the ice body. B shows an approximate reality case of ice crevasses growth considering water retention in it. (modified from Benn and Evans (2013)).

Additionally, the orientation of ice crevasses is another factor that influences the glacier surface form and geomorphology, especially for ice crevasses near the glacier terminus which shape the geometry of the glacier terminus and ice calving margin (Benn et al., 2007; Dykes, 2013). For mountain glaciers, local tensile and shear stress caused by lateral drag, ice flow and the own weight of the glacier can result in various representations of ice crevasses in a single glacier. In order to facilitate the understanding of the orientation of ice crevasse, the following diagrams show the conceptual representations of ice crevasses patterns under different force conditions. There are three common patterns initially identified by Nye (1957) and enriched by Benn and Evens (2013): chevron-shaped crevasses (i.e., V-shaped), transversal crevasses, and splaying-shaped crevasses (see Figure 2.5) (Benn and Evans, 2013; Nye, 1951). Figure 2.5 – A represents the chevron-shaped ice crevasses formed by lateral drag and shearing forces during the glacier flow, referring to a real case from blue boxes in Figure 2.6. With the extension of the glacier ice flow, transversal-shaped ice crevasses that are slightly curved commonly occur under the combined forces of ice flow and lateral shearing as shown in Figure 2.5 – B, referring by real cases heightened with blue boxes in Figure 2.6 (i.e., the upper part of glacier arches and zone that near the glacier terminus, respectively). Compressive glacier flow might cause lateral shearing stress and longitudinal shearing stress and may bring splaying crevasses, consequently: see Figure 2.5 – C for a conceptual representation and blue trapezoid in Figure 2.6 (zone below the icefall; ice supply falls into a narrow valley and flow to lower altitude) for a real case example.

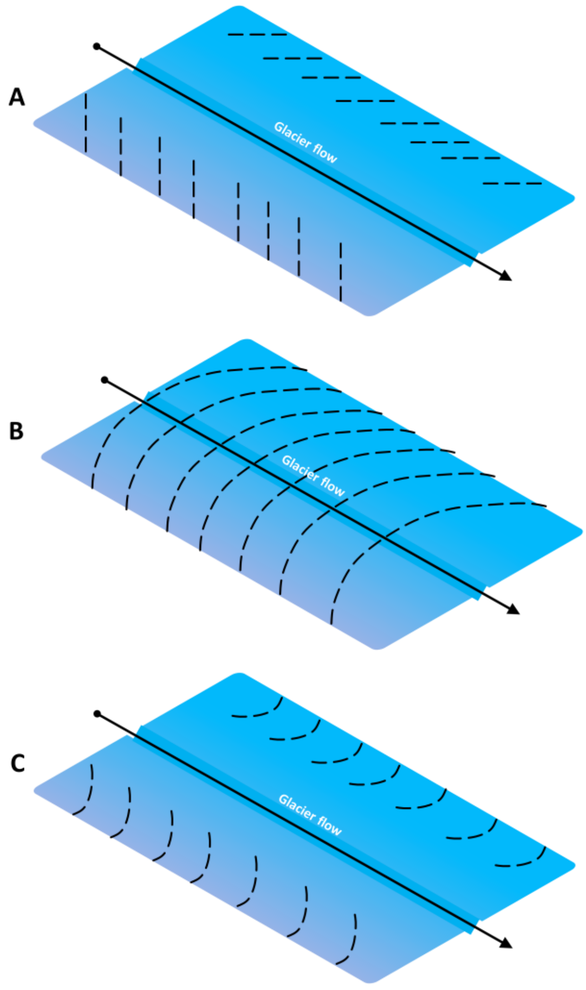

Figure 2.5 Conceptual diagrams showing three typical patterns of ice crevasses orientation found in mountain glaciers. A is chevron crevasses caused by lateral drag and shearing force. B is transversal-shaped crevasses with curved slightly along the glacier flow. C is splaying crevasses developed by compressive forces from glacier flow (modified from Benn and Evans (2013)).

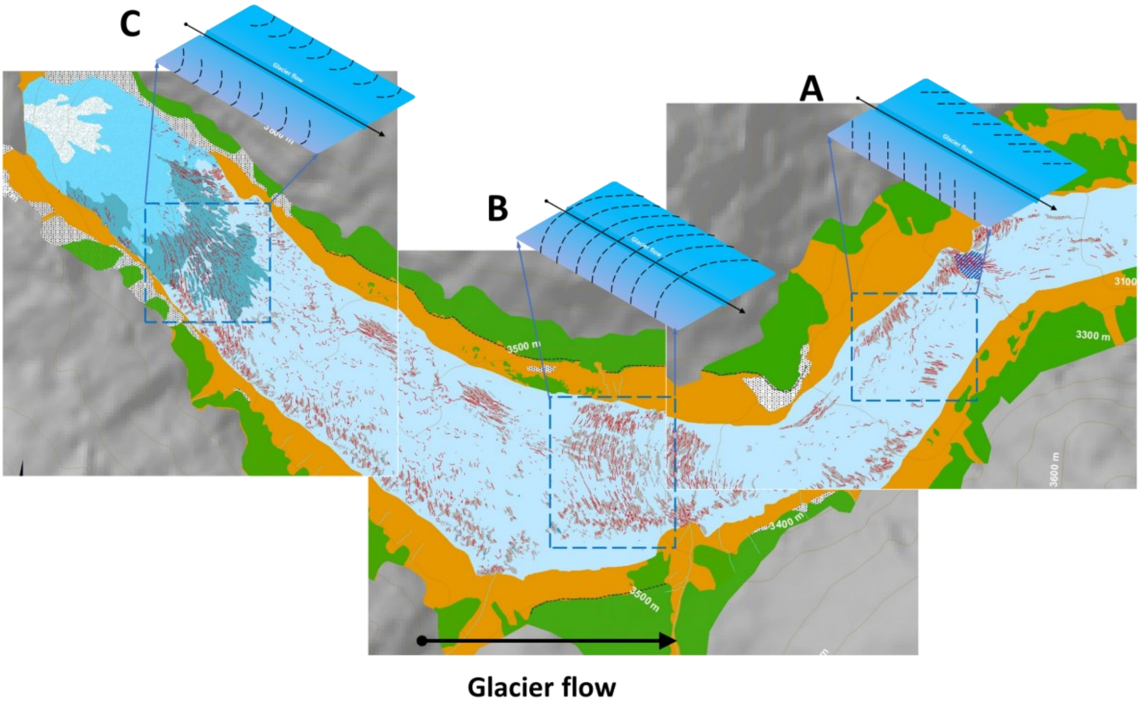

Figure 2.6 Mapping results (i.e., maps sources: Xu et al.(2022b)) representing the real cases of ice crevasses in HLG Glacier. A: A chevron-pattern crevasses in the lower part of the HLG Glacier tongue. B is transversal-shaped crevasses in the middle section of HLG Glacier tongue. C is splaying crevasses distributed the areas lower the glacier icefall.

2.3.2 The driver of the mechanical ablation process

Collapse/calving occurs when the ice stresses at the margin exceed the tensile strength of the ice. There are four kinds of calving mechanisms in glaciers identified by numerous of studies (e.g., Benn and Åström, 2018; Benn et al., 2007; Haresign, 2004). These four calving mechanisms can be briefly described as following (Figure 2.7): A) over-steepening in the subaerial part of ice cliffs induces the ice calving, sometimes dry calving; B) instabilities of the ice cliffs caused by thermo-erosion of waterline; C) tubular ice calving at pre-existed weak waterline driven by buoyancy; D) subaqueous calving in the glacier front. These four mechanisms can be reduced principally to two points: the first one is the changes in ice dynamics resulting from force imbalance and relatively high surface velocity gradients at the glacier terminus, which contributes to the formation of ice crevasses, providing the initial weakness line for ice calving (A and B). The second one is calving events induced by waterline melting and subaqueous melting. And these melting-derived calving accompanied by buoyancy deriving forces may further exploit the weakness line (Benn et al., 2007).

In terms of the nature of ice calving and its complexity, the hierarchy of ice calving should be taken into consideration. According to the above-mentioned mechanisms, there are two control orders named by Benn et al (2007), the first order to control the ice calving is changes in ice dynamics, for instance, the longitudinal/lateral strain rate from high surface velocity gradients and force imbalance at supportless ice cliffs. These kinds of ice dynamics change (i.e., strain rates and forces imbalances) control the formation and propagation of surface ice crevasses and provide the lines of weakness, which results in the calving events. The second order is the thermo-erosional notch, which is superimposed on the ice dynamics changes. Likewise, the buoyancy-driven calving can be considered as a second-order of calving mechanism as it is superimposed on the basis of glacier thickness and the position of the grounding line.

Besides, Haresign (2004) has proposed a continuum to link calving mechanisms with ice velocity, that is, each mechanism has importance varied with ice velocity. According to Haresign's theory (2004), the over-steepening by ice flow and undercutting by water line dominate the ice calving when the ice velocity is slow, whereas the longitudinal stretching and the buoyancy are the primary dominance at high ice velocity as the terminal force imbalance and the waterline undercutting can be neglected due to their low marginal impact at high ice velocity.

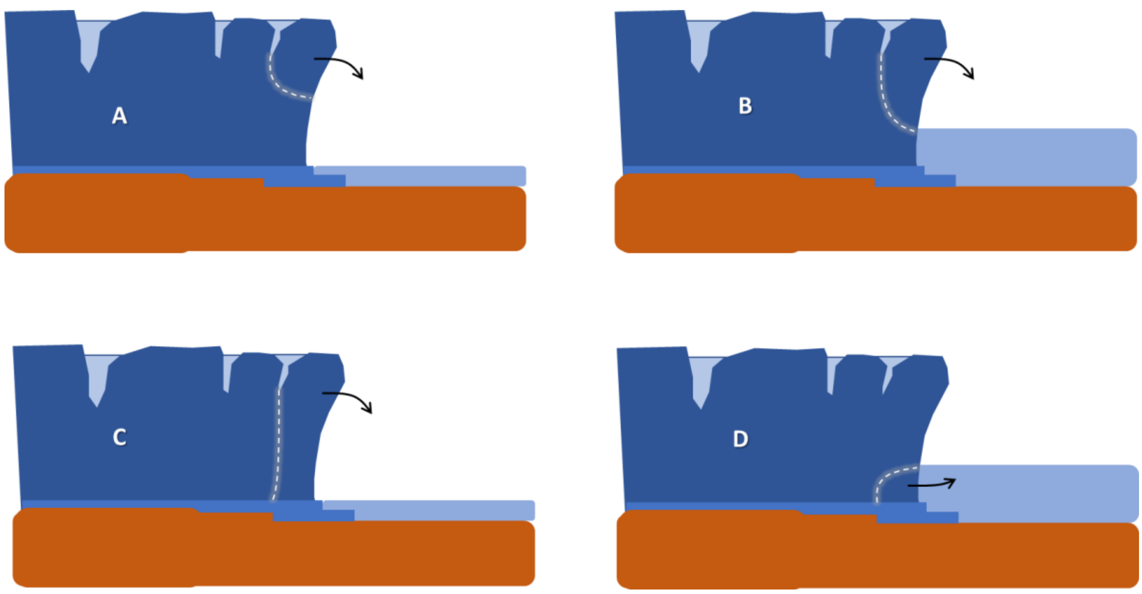

Figure 2.7 Conceptual illustration of ice calving mechanisms (modification from Dykes (2013)). A) over-steepening in the subaerial part of ice cliffs induces the ice calving, sometimes dry calving; B) instabilities of the ice cliffs caused by thermo-erosion of waterline; C) tubular ice calving at pre-existed weak waterline driven by buoyancy; D) subaqueous calving in the glacier front.

2.3.3 Mechanism of mechanical ablation

Calving law and quantifying ice calving has been a hot research issue as an over-arching calving law is a basis of calving models to accurately describe and predict ice calving (Benn et al., 2007; Dykes, 2013). Generally, these calving laws and calving models mainly serve for water-terminating glaciers due to some parameters involved with buoyant-derived factors and waterline undercutting factors. However, it is hard to unify the consensus in the influence factors, processes and underlying deriving forces of ice calving due to the risk and difficulties of measuring the dynamics of ice calving.

One basic calving law is to calculate the calving rate, known as the ice loss volume per unit of timer per unit of area (Benn and Evans, 2013), which can be described as the differences (u_c) between ice velocity and terminal position changes for a certain time as shown in the Equation(2) (Vieli et al., 2001).

$$\boldsymbol{u_c = u_i - \frac{\Delta L}{\Delta t}} \qquad (2)$$

where $\mathbf{u_i}$ is the averaged ice velocity, **L** is the glacier length and **t** is the time. In the calculation of calving rate, the surface melting is excluded in the equation as the impact of surface melting is negligible compared with ice loss from calving. However the ice loss from surface melting needs to be taken as an independent factor into account as the surface melting counts a large proportion of overall ice loss, especially for glacier with low ice velocity. Therefore, the calving rate can be represented as a relation of mass flux per unit of width (Benn et al., 2007; Motyka et al., 2003) as shown in Equation(3).

$$\boldsymbol{Q_C + Q_M = Q_{in} - Q_{out}} \qquad (3)$$

where $\mathbf{Q_c}$ is ice calving flux, $\mathbf{Q_m}$ is melting flux, $\mathbf{Q_{in}}$ is ice flux into the terminus, and $\mathbf{Q_{out}}$ is the rate of change of the terminus. The equation can be reformatted into Equation (4):

$$\boldsymbol{Q_C = Q_{in} - \frac{\Delta L}{\Delta t}} \qquad (4)$$

where the $\frac{\Delta L}{\Delta t}$ is the rate of volume change at the terminus. In this equation **Qc** includes calving and subaqueous melting at the glacier terminus.

Ice calving is considered as the slave to the glacier dynamics when calving events increase as result from changes of glacier dynamics (e.g., glacier thinning, glacier ice acceleration). In contrast, when ice calving contributes to glacier flow acceleration and glacier thinning, the calving is seen as the master to glacier dynamics. These interactions or distinctions between taking the increasing ice calving as the master or the slave bring uncertainties between the interactions of calving and ice dynamics (Motyka et al., 2003). As a result of uncertainties, several models and laws have been developed to understand the ice calving and glacier dynamics. Basically, there are two approaches to solve the equation (2): one is the changes of calving rate and the ice velocity can control the glacier retreat, another is terminus position is controlled by the geometry of glacier terminus ice cliffs and the calving rate varies with the changes of ice velocity and terminus position. The first one is based on the empirical calving function and the second one concentrates on the terminus position changes and glacier dynamics to predict the calving rates (Benn et al., 2007; van der Veen, 2002; Vieli et al., 2001). Additionally, process-based models are the third approach, with a focus on the physical principles, for instance, the fracture mechanics and stress distribution at the terminus.

2.4 Hydrological system of glaciers

2.4.1 Proglacial and supraglacial channels

Many studies have documented the supraglacial and proglacial pond/lake formation, their development, and their effects on the dynamics of their host glaciers. Many studies concentrated on the debris-covered glacier in the Himalayan region (e.g., Falatkova et al., 2019; Fujita et al., 2008; King et al., 2019; Liu et al., 2020; Nie et al., 2017; Sakai, 2012). Most of these studies revealed that the development and the dynamics of glacial pond/lakes, either supraglacial or proglacial pond/lake, have significant impacts on glacier mass loss for most parts of the Himalaya. As a typical example by King et al. (2019), a statistical analysis of regional mass balance study for Himalayan glaciers indicates that, although the retreat rate has been enhanced without exception in the context of climatic warming, the pond/lake-terminating glacier retreated dramatically with an average retreating rate of 15.9 $\pm$ 1.1 meter annata^{-1} (m a^{-1}) compared with the land-terminating glacier (7.1 $\pm$ 1.1 m a^{-1}) over the period from 1974 to 2000. Likewise, a similar decreasing pattern has appeared in the length comparison for glacier centrelines.

Hence, the formation and development of glacial pond/lakes exacerbate the mass loss of glaciers, suggesting more broadly that the interaction of water-ice/glacier in the glacier terminus have great impact on the glacier dynamics, and associated mechanical ablation processes may bring about disturbances to the glacier mass balance such as dry calving and ice collapsing. Longer term, the formation of strong water-ice/glacier interaction at glacier terminus margins has further decoupled these glaciers from climatic variation, with a transition from primarily melting – dominated ablation processes to ice calving dominated – ablation processes appearing to weaken the weightiness of subsequent climatic inputs (Carrivick and Tweed, 2013; Dykes, 2013; Sutherland et al., 2020).

Plenty of studies have documented the delineation the glacial ponds and lakes and analysed their spatial-temporal changes in area and volume. Nie et al. (2017) investigated the spatially explicit changes of glacial lakes by delineating 534 proglacial lakes and 173 supraglacial lakes as well as 2705 unconnected glacier-fed lakes in 2015 out of 4950 glacier lakes over the entire region of Himalaya. Liu et al. (2020) compared the retreating rate, thinning rate, and surface velocity distribution of a lake-terminating glacier with counterparts nearby land-terminating glacier located in the transition zone from monsoonal temperate glaciers to continental glaciers (i.e., the southeastern Tibetan Plateau to the inner Tibetan Plateau) by using Landsat series images. They confirmed that the impacts of the proglacial lake on the ice flow dynamics will enhance the lake-ice/glacier interactions and subsequent glacier retreating processes. Specifically, the formation and expansion of proglacial lakes will impact the rate of glacier retreating. The expansion of glacial lakes indicates that the glacier ice calving from subaqueous ice melting is controlled by wind-driven water currents (Sakai et al., 2009).

Lake-terminating glaciers are typically referred to mountain glaciers, whose glacier dynamics (thinning/accelerating/retreating) are impacted greatly by characteristics of proglacial ponds/lakes (Liu et al., 2016). Sakai and Fujita (2010) identified the formation conditions of glacial lakes development and expansions by two easily calculable parameters, that is the inclination of the glacier surface and the Difference between the Glacier surface and lateral Moraine (DGM). The DGM describes glacier surface lowering by calculating the difference between the glacier surface and lateral moraine. They concluded that, basically, all glaciers with large supraglacial lakes have the values of DGM exceeding 60m and the slope gradient is less than 2.0°. That is to say, the low inclination refers to relatively small ice flux for the lower part of the glacier and the high DGM value indicates the proximity of glacier and water level in glacier ice, of which the former one produces the glacier shrinkage and the later one brings supraglacial lakes. According to their study, the glacial lakes form with a strong relation to the glacier surface lowering and the glacial lakes exacerbate the disintegration of the glacier terminus and the lowering rate of glacier surface in turn. A comprehensive review of glacial lakes of the Himalayan region by Sakai (2012) describes the processes of formation and expansion of glacial lakes, which start from several small pondings distributed over the glacier terminus, then ice coalescing accompanied by terminus ice disintegration to form together one proglacial lake and rapid expanding of lakes through calving or other forms of ice collapsing eventually.

A series of studies summarized that glaciers with relative thinner debris mantle and high rates of ablation tend to develop glacial lakes (Quincey et al., 2007; Reynolds, 2000; Sakai, 2012; Suzuki et al., 2007). Quincey et al. (2007) used Synthetic Aperture Rada (SAR) data (i.e., ER2-1 and ERS-2), SPOT-5 HRS optical imagery and high-resolution historical aerial photography as the study dataset to illustrate glacier velocity field and to calculate the glacier surface gradients and to derive Digital Elevation Models (DEMs). Reynolds (2000) proposed a relationship scheme that demonstrates the connection between glacier surface gradient and supraglacial lake development. They stated that the surface gradient is less than 2° where supraglacial ponds/lakes may tend to be formed.

Numerical modeling for the development of glacial lakes provides a projection insight into the sustaining influences of glacial lakes' life cycle on the host glacier dynamics. Sutherland et al (2020) implemented a numerical model called BISICLES to test the impacts of a lake on glacier recession within two simulating scenarios (i.e., land-terminating glacier and lake-terminating glacier). The result from the BISICLES simulation showed that a glacial lake has a significant impact on the geometry (grounding line position, ice margin shape, and ice thickness distribution), ice flow, and rate of glacier retreating during the transition period of land-terminating to lake-terminating under similar climatic control.

Watson et al. (2017) summarized previous research related to ice cliffs and supraglacial ponds mainly from three aspects, that is, modelling involving ice cliffs and ponds dynamics, ice cliffs observation, and ice cliffs energy balance. In accordance with three aspects, **1)** they emphasized that quantifying the ice cliffs and the supraglacial pond is critical for modeling the projected glacier behavior, as these particular ablation processes are not integrated into most available numerical models (Soncini et al., 2016). **2)** although direct observing the ice cliffs behavior is not feasible possibly, it is self-evident that it is important to ablation processes, for instance, using differencing multi-temporal DEMs to demonstrate ice cliffs ablation as well as estimating its contribution to the glacier surface lowering, reveal a fact that the ice cliffs cover a relative small area but have a considerable contribution to the surface lowering; 3) few south-facing ice cliffs are observed while north-facing ice cliffs persist across the debris-covered area of glaciers, which may explain this occurrence is that the relatively high solar radiation absorption value for south-facing ice cliffs so that causing rapid decaying and burial.

The spatial distribution of ice cliffs and supraglacial ponds/lakes exhibit a high spatial correlation. Lowering the glacier surface is the predominant response to the glacier mass loss for debris-covered glaciers, instead of terminus retreating (Watson et al., 2017). Watson et al. (2017) analyzed the spatiotemporal distribution and geometrical characteristics of ice cliffs for 14 debris-covered glaciers in the region of Everest. Results show that although most of the debris-covered zone of these studied glaciers have ice cliffs, there are no distinct relationship between ice cliffs distribution and the host glacier velocity field, which indicates that the ice cliffs may not appear to form on those stagnating glacier terminals where supraglacial ponds disintegrate. However, they indicated a high coherence in spatial distribution between ice cliffs and supraglacial ponds, i.e., 77% of supraglacial ponds had adjacent ice cliffs and nearly 50% of ice cliffs had adjacent ponds for all study glaciers. A fact based on the results is that regardless of the glacier flow direction, the north-facing ice cliffs can persist prior whilst the south-facing ice cliffs may be rapidly declining and vanishing as south-facing may absorb much more solar energy. In order to assess the ice cliffs dynamics, the ice cliffs density is introduced here. They conclude that the ice cliff density has a positive correlation with glacier surface lowering.

An automated detection tool developed by Herreid and Pellicciotti (2017) uses surface slope from DEMs to map ice cliff geometry and then to generate the ice cliff probability maps. This novel approach requires three types of input data, namely glacier outlines (i.e., to identify the glacier extent), multispectral satellite imagery (i.e., to map the debris-covered area) and DEMs (i.e., to identify the ice cliff location and area). For the best practice, DEMs should have a fine spatial resolution and precision for resolving the size and shape of ice cliffs, with the input DEM derived from photogrammetric images usually meeting the requirements.

2.4.2 Subglacial and englacial channels

The hydrological system in glaciers plays a critical role in the interaction between surfaces (i.e., supraglacial ponds or streams), interiors (i.e., englacial conduits), bases (i.e., subglacial channels), snouts (i.e., subglacial channel outlets) and proglacial waterbodies of glaciers (Shreve, 1985) as shown in Figure 2.8. Maritime glaciers (also known as temperature glacier) are widely distributed over the southeastern Tibetan Plateau, Hengduan Mountain region, and the middle east section of Nyainqentanglha region (Liu and Liu, 2012). One of the typical characteristics of a maritime glacier is the active drainage system through the glacier. The maritime glacier is at the melting point most of the time of the year. Surface meltwater runoff and rainfall can flow along englacial conduits through moulins or surface ice crevasses to reach the glacier bed, joining with subglacial meltwater to form subglacial channels. These subglacial channels may flow through the glacier body and flow out from the glacier terminus (subglacial channel outlet) in laminar, linear, or reticular formations. Another case is that these waters may be stored in the glacier or in the subglacial area to form englacial and subglacial lakes. These supraglacial, englacial and subglacial hydrographic nets form the glacier drainage system (Fountain and Walder, 1998).

The evolution of englacial and subglacial hydrology not only affects the meltwater discharge and melting water runoff as well as the hydrological process of glacier river outflow at the glacier terminus, but also influences the glacier movements (basal sliding, surging, or ice body uplifting) (e.g., Iken, 1981; Iken and Truffe, 1997; Iken et al., 1983) and glacier erosion (e.g., Beaney and Shaw, 2011; Glasser et al., 2004) through a subglacial hydraulic process. HLG Glacier is the earliest study area for maritime glacier drainage systems in China (Liu and Zhang, 2017). Huang et al. (1996) investigated the englacial water level from borehole observation by hot water drilling in the ablation zone of HLG Glacier. Their results verified that the HLG Glacier is a temperate glacier, and that the interior of the ablation zone is filled with water, indicating the coexisting of ice and water. The main subglacial channel and englacial conduits expanded and situated in the pressure flow during the ablation season. The basal sliding was dominant (~83% during the observation period) in the total glacier movements (Huang et al., 1996). Lu and Zhong (1996) analysed the records of 1994 from hydrometric station near the HLG glacier terminus and abrupt fluctuations of water level in subglacial channel were found, suggesting subglacial drainage system near the glacier terminus may had been blocked and busted frequently. The reason for this phenomenon may link to ice crevasses evolution. Subglacial channels of the glacier tongue of HLG Glacier have distinct seasonal variations (i.e., seasonal expansion and contract happened in summer and the end/beginning of ablation period, respectively) according to repeating dye tracer tests and simulations of advection-dispersion model (ADM) (Liu and Liu, 2012). Combined with hydrological analysis of glacier terminus runoffs and their hydraulic process, the condition of formation and main process of seasonal changes of these subglacial channels were revealed (Liu et al., 2018; Liu and Liu, 2010). Additionally, the spatial structure of subglacial channels of HLG Glacier is not complicated due to the morphology of narrow strips for HLG Glacier ablation zone, specifically, the main subglacial channel flows along the centreline of glacier tongue generally and few tributaries exist (Liu and Liu, 2010; Liu and Zhang, 2017). It is evident by reporting from several related works (e.g., Benn et al., 2017; Benn and Evans, 2013; Dykes, 2013; Gulley and Benn, 2007; Miles et al., 2017, 2020) that the formation and development of glacial drainage system in debris-covered glacier differs from a glacier with clean-ice. As suggested by the results of these works, the supraglacial pond may become successively saturated to deeper layers to form an unstable drainage pathway, connecting supraglacial, subglacial and englacial networks if sustaining englacial conduit collapsing.

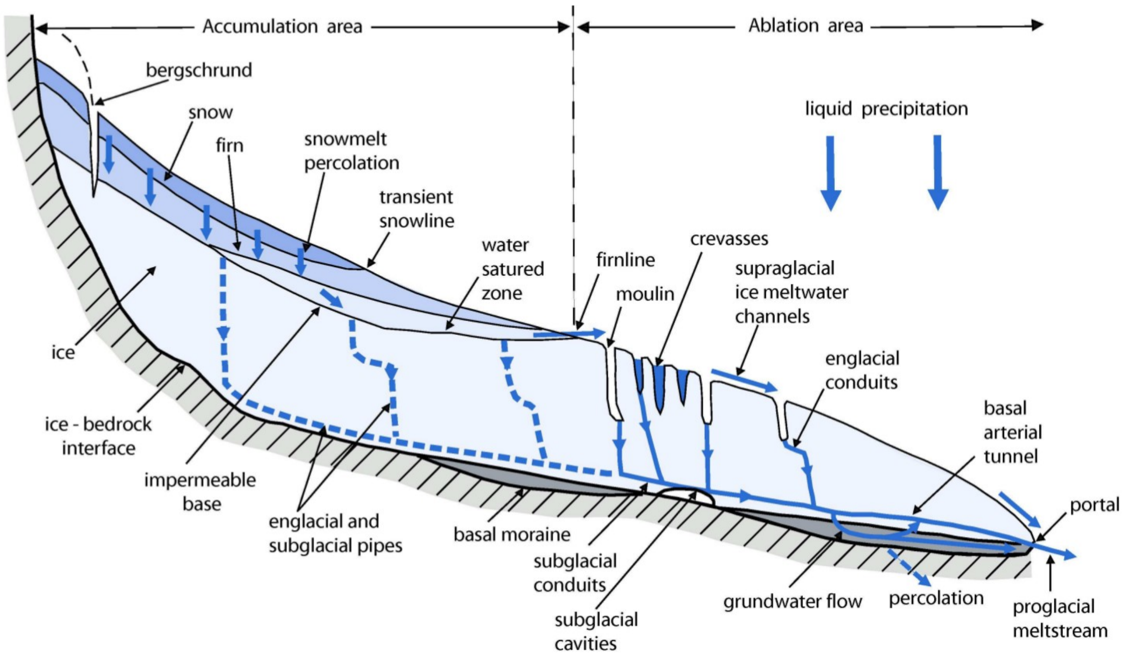

Figure 2.8 A conceptual figure shows water pathways through the glacier (Werder, 2016; Shreve, 1985)

2.5 Applications of remotely sensed datasets for glaciology

Glaciological studies originated about 200 years ago when early mountaineers and explorers started glacier exploration by their activities in the Alpine region, and during their expeditions a large number of glacier landscapes and associated topography were recorded. Around 1827, Franz Josef Hugi first measured glacier flows in reality. He established an observation station in the neighbourhood of a boulder on the medial moraine of the Unteraargletscher Glacier in Switzerland. He used the visual alignment with fixed geographical setting to measure the physical displacements of the boulder. The results showed that the boulder had moved more than a kilometre in nearly a decade (Clarke, 1987).

After that, glaciological studies were gradually evolving towards quantitative studies. Hot-water drilling was firstly used for determining the ice thickness distribution and then seismic equipment was used to detect the basal and internal environment. Gravimeter and radar were also used to investigate the glacier flow dynamics. Repeated stick measurements provide a relatively reliable and accurate way to monitor the glacier flow and ice thickness changes (Paterson, 1977). Several sticks were inserted into the glacier ice, and their locations and lengths were recorded periodically to estimate the glacier velocity and ice surface elevation changes. Some people also unitized the weather and precipitation datasets recorded from observation stations to estimate the glacier changes. Therefore, before the boom of remote sensing, the area of glacier-related investigations is limited and restricted as the logistics of field trip is labour-consuming and dangerous. In other words, with the advantages of remote sensing, especially the satellite remotely sensed data, it is enabled to investigate the glaciology from the scale of a single-glacier to regional/global scale (Rivera and Bown., 2013).

2.5.1 Optical satellites

The increasing availability of appropriate spatial and temporal resolution, global coverage, and the accessibility of open remote-sensing data, will allow a faster, more automated, and improved-quality monitoring of changes in glacier characteristics at multiple scales (Quincey et al., 2005; Racoviteanu et al., 2008). Before the era of satellite-based Earth Observation, field survey measurement and air-borne images dominate the investigation of regional glacier changes. However, the highly financial cost and labour-consuming in the logistic of investigation still hindered the development of glaciology. With the development of the space-borne sensors in 1970s, various satellites with middle resolution (10 to 30 m) have been applicated for glacier-related studies, including Landsat sensors (e.g., MSS, TM, ETM, and OLI), Terra ASTER, IRS, Sentinel-2, ALOS, and SPOT (Barella et al., 2020; Berthier and Toutin, 2008; Fahnestock et al., 2016; Gaddam et al., 2021; Li et al., 1998; Paul et al., 2016; Shiramizu et al., 2017; Suzuki et al., 2007; Wei et al., 2014). Satellites with meter-/submeter-level resolution have comparable performance in the investigation of basin level to a single glacier (e.g, supraglacial lake/river, ice cliffs, moulins, etc.), such as Quickbrid, Gaofen, Ziyuan, IKONOS, GeoEye, and Planet Scope (Altena and Kääb, 2017; Ghuffar, 2018; Kääb et al., 2019). The declassified spy satellites provide an alternative to retracing the historical changes of glaciers, for example, the CORONA (i.e., 1960 to 1972).

Optical sensors monitor the Earth's surface by solar radiation reflected at the visible and near-infrared electromagnetic spectrum (0.35 - 2.5 μm) bands, but also capture the radiation emitted by features in the thermal infrared band (8 - 14 μm), which are recorded by the sensors as brightness temperatures. These sensors are capable of acquiring data in multispectral mode at a medium spatial resolution of 10 m to 90 m (Winsvold et al., 2016; Racoviteanu et al., 2008). They also have relatively large mapping ranges (e.g., 185 km for Lansdat, and 60 km for ASTER) and relatively short revisit intervals (e.g.,16 days for ASTER) in terms of glacier change time scales, making them useful for regional glacier mapping. The thermal band of Landsat ETM+ (10.4-12.5 µm, pixel size of 60 m) and the multispectral thermal band of ASTER (8.125 - 11.65 µm, pixel size of 90 m) have demonstrated potentials in distinguishing glacier debris cover from clean ice (Bolch and Kamp, 2005; Liao et al., 2020; Wang et al., 2020). In addition, ASTER, SPOT5, IRS-1C and CORONA KH-4, KH 4A and KH 4B have the ability to acquire stereo images from which elevation data can be extracted for 3D monitoring of the glacier surface (Florinsky et al., 2018; Hirano et al., 2003; Shean et al., 2016; Wu et al., 2020). Presently, ASTER is probably still the most applicable sensor for tracking of glacier parameters, including mass balance applications. Strengths against other sensors for glaciological applications may include: (1) 15m spatial resolution of ASTER for VNIR is sufficient for conducting regional-scale geological studies; (2) high spectral resolution then enables to perform multispectral image classification (3) photogrammetrically stereo images (3N and 3B). The main limitation of VNIR satellites is the restriction to clouds and shadows during the daytime, which is difficult to acquire data under these circumstances.

2.5.2 Synthetic aperture radar

Although the optical imagery has been widely used for the different applications of glacier observations (e.g., mapping the changes of glacial geometry; Kääb et al., 2016), but their performances in the mountain and high-altitude areas are largely restricted by the cloud covers or polar night. As the active sensor of Earth Observation, synthetic aperture radar (SAR) can penetrate the cloud, and it is insensitive to the weather conditions. The combination of optical and SAR sensors should be of significant in the investigation of glacier-related studies (Du et al., 2020; Krieger et al., 2007; Liu et al., 2019).

Synthetic Aperture Radar Interferometry (InSAR) is another approach for elevation change detections that have been widely used in the deformation, ice velocity and geodetic measurements since the 1990s (Zhu et al., 2021), for example, ERS-1/2, JERS-1, ALOS/PALSAR and Sentinel-1, Ziyan series, etc. In recent, the space-borne bistatic InSAR shows advantages in the detection of the surface deformations, such as the

TerraSAR-X and TanDEM-X from DLC of Germany (Krieger et al., 2007; Strozzi et al., 2002).

With the improvements of InSAR and associated image processing algorithms, more complicated and detailed glacier characteristics can be recorded or derived, such as time-sequenced glacier surface elevation variation, spatial distribution of glacier surface velocity field, ice cliff density, supraglacial ponds identification, distinguishing debris-covered glacial area, ice thickness change and ice volume detection (Andreassen et al., 2015; Benn et al., 2012; Berthier et al., 2016; Farinotti et al., 2009; Herreid and Pellicciotti, 2018; Sun et al., 2017; Zhang et al., 2011). Not only mapping the glacier extent and the glacier terminus position, but also providing various characteristics as mentioned above in the glacier mapping, this multi-parametric approach has significance on assessing the comprehensive glacier healthy.

2.5.3 Uncrewed Aerial Vehicle

UAV, also known as the unmanned aerial system (UAS), remotely piloted aerial system (PRAS), or drone, is considered a platform that carries customized sensors onboard (Bhardwaj et al., 2016; Śledź et al., 2021; Xu et al., 2022). Recently, multiple sensors have been mounted on the UAVs to execute missions of various purposes, including RGB cameras, high-spectral cameras, thermal infrared cameras, and lasering radar (e.g, Bash et al., 2018; Magnússon et al., 2016; Patel et al., 2019). The initiation of UAVs was military-purposed back in Cold War and this tool was firstly used for scientific aims in about the 1990s. Many previous studies have proved the high effectiveness of data acquisition from UAVs (Pajares, 2015), including the flexibility in the temporal resolution and very fine spatial resolution. Therefore, surveying by UAVs is more efficient and economical for the case of relatively smaller study areas, providing an alternative for high-resolution satellite images.

For the last decades, the innovation of UAVs and the development of Structure-from-Motion (SfM) improve the capability of land surveying and geomorphological mapping, which further satisfies the growing requirement of monitoring for the rapid dynamics of glacial and glacier-related landscapes within the recent global climate changes (Bash et al., 2018; Chudley et al., 2019; Di Rita et al., 2020; Fu et al., 2021; Rossini et al., 2018; Smith et al., 2016; Taylor et al., 2021; Westoby et al., 2012; Xu et al., 2022; Yang et al., 2020; Zhong et al., 2021).

2.5.3.1 Types of UAVs and onboard sensors

Although there is a long history of applying remotely sensed data into the field of Glaciology, drones with fixed-wings dominated the UAV-based glaciological investigations until Dajiang Innovation (DJI; https://www.dji.com/) first introduced the Phantom series, multiple-rotor drones, to the market in 2013 and then the DJI Phantom 2 was firstly used for field investigations about 2014 (Evans et al., 2016; Ewertowski et al., 2016). Subsequently, many studies started to utilize DJI series drones and the portion of DJI in geoscience increased from that time, which attributes to the advanced performance in the logistics (i.e., small size and ease to carry) and the well-trade-off between the cost and relatively high capability of image acquisition. Currently, there are two series of drones that are widely used in the geoscience-related fields, Sensefly (e.g., eBee) and DJI (e.g., Phantom and Mavic) (Rossini et al., 2018).

With the growth of drone performances, new generations of drones carry multiple built-in sensors (e.g., RGB, thermal infrared, LiDAR), which enable the capture the acquisition of various datasets. Also, it allows the sensors of drones to be replaceable to adjust to the targeted environment quickly. The most advanced aspect of drone-based mapping is very high-resolution orthophoto mosaics and DEMs (i.e., 0.01 to ~1 m ground sampling distance), thereby obtaining results with finer resolution but low financial costs compared with other airborne and satellite images. These advantages are able to provide small-scale of surface morphology and evolution of some minor land features (e.g., moulins, periodic supraglacial streams, fluted moraines, and crevasses traces).

2.5.3.2 Mapping by UAVs

Mapping the landform features in detail is the main UAV-based application for glacier-related studies, including the mapping of geomorphic, glacial, and glaciological features (Bhardwaj et al., 2016). Combined with the generated orthophoto mosaics, DEMs, and field validation datasets, detailed mapping can be yielded, usually focusing on the glacier tongue, proglacial zone, glacial forelands, preglacial lands, paraglacial regions and deglaciated region or paleo-glacierized areas (Chandler et al., 2020, 2018, 2016; Chudley et al., 2019; Rossini et al., 2018; Xu et al., 2022; Zhong et al., 2021).

UAV-derived datasets can also integrate with other remotely sensed datasets to illustrate the detailed analysis for a specific feature and its evolution under more extensive geographical content. For example, the geomorphological evolution of the forelands of a valley glacier usually occurs around a small patch of land, which is a consequence between a highly dynamic glacier ablation zone and proglacial/preglacial zone. This can be inferred from a combination of a less detailed satellite-based mapping result for an entire glacier ablation zone (or lower patch of glacier tongue) and a finer UAV-based mapping result for the proglacial zone and preglacial zone (Evans et al., 2016), such as focusing on the evolution of braided proglacial river, proglacial morphology due to deglaciation, changes of proglacial ponds. The UAV combined with the SfM workflow can improve the details of change detection to a further extent (i.e., volumetric and 2D geometric). The cumulative data over the years from the time-series orthophoto and the time-series DEM, and subtracting the date before, and after yields the 2D evolution and DEM of difference, respectively (Di Rita et al., 2020; Xue et al., 2018).

Chapter 3: Study area

3.1 Introduction

HLG Glacier is the longest-temperature glacier located in the southeastern margin of the Tibetan Plateau (Figure 3.1). The dynamics and status of the glacier in this region have been widely concerned since the 1930s (Heim, 1936). In this chapter, the Tibetan Plateau and the Mt. Gongga region are introduced to provide information about the physical setting and the characteristics and present state of the glaciers developed through the regions. The specific emphasis across this chapter is highlighted at the evolution of the HLG Glacier located at the east slope of Mt. Gongga, including the past glaciations that occurred within the HLG valley and the accelerated shrinking process of the contemporary HLG Glacier. Besides, an in-depth introduction on the surface morphological changes and the mass balance changes of the HLG Glacier are provided from previous studies. As the liquid water and thermal regime is highly associated with the mechanical ablations, the hydrological system of the HLG Glacier is illustrated to draw an overview of the connection between the mechanical ablation-induced water-ice interactions and the glacier dynamics.

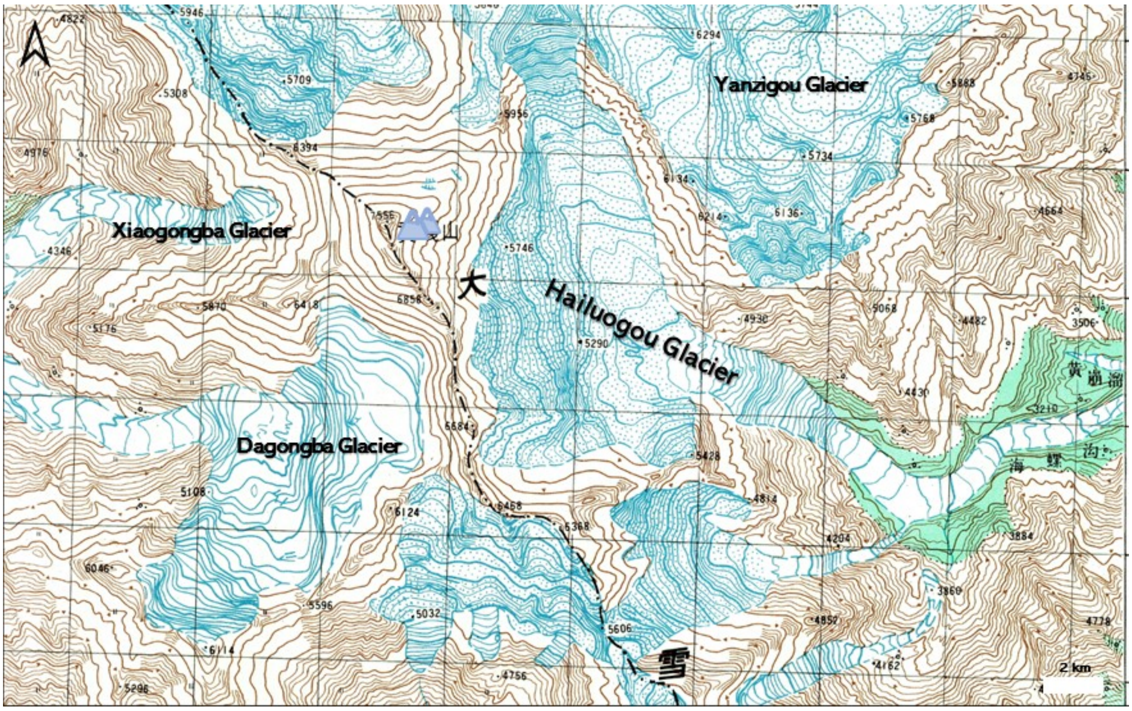

Figure 3.1 Topographic map of the HLG Glacier. The topographical map was mapped by the Surveying and Mapping Bureau of General Staff Headquarters of the People's Liberation Army in 1971. The topographic map is provided by the Institute of Mountain Hazards and Environment, Chinese Academic Science

3.2 Tibetan Plateau and Mt. Gongga region

The Tibetan Plateau (Figure 1.1 a) is the largest and highest plateau all over the world, with an average elevation of 4500 m above sea level (m a.s.l.) (Chen et al., 2006; Clark, 2011; Fu et al., 2005; Phan et al., 2012). It is also known as "the roof of the world" or "Third Polar" (Liu and Chen, 2000; Yao et al., 2012; Yao and Greenwood, 2009). The Tibetan Plateau is the youngest plateau in the world and was formed by the continental collision, or orogeny, between Indo-Australian Plate and the Eurasian Plate about 50 million years ago (Harrison et al., 1992). Apart from the polar regions, the Tibetan Plateau and surrounding high mountain areas have the largest number of glaciers with a total glacial area of ca. 100,000 km^2 (Yao et al., 2012), which are the headwater of many large rivers and hence affect millions of people in that regions (Ding et al., 2006; Lindholm and Heyman, 2016; Yao et al., 2012; Zhao et al., 2014). Present climate patterns over the Tibetan Plateau are dominated by the Indian monsoon in the summertime and the westerlies in the winter (Yao et al., 2012). Glaciers on the Tibetan Plateau can be divided into two classes: continental glaciers and maritime glaciers according to their dominating climate and their ice temperature (Fujita et al., 2000). Continental glaciers mainly occur in central to northwestern regions and maritime glaciers concentrate in the southeastern regions (Fujita et al., 2000; Shi et al., 1999).

The majority of glaciers on the Tibetan Plateau have been retreating since the early 20th century with an increasing tendency due to climatic warming (Ding et al., 2006; Li et al., 2008; Yao et al., 2007). The largest glacial retreat in the Tibetan Plateau occurs at the southeastern margins, while the least retreat occurs in the central of the Tibetan Plateau since the 1980s (Pu et al., 2004; Yao et al., 2012). Glaciers in the southeastern Tibetan Plateau (mostly is temperate glaciers) have been reported to have experienced intensive retreating and shrinking. For example, HLG Glacier in the Hengduan Mountains has been reported have experienced a continuous and intensive retreat since 1930 with a fluctuant rate (Pu et al., 2004).

Multiple glaciations have occurred during the Quaternary in the Tibetan Plateau and covered one-quarter of the plateau during the maximum glaciation (Li et al., 1991; Owen et al., 2005; Shi et al., 2006). Therefore, glaciological and paleo-glaciological research about glacier volume/changes on the Tibetan Plateau is of significance (Ma et al., 2010; Xu et al., 2013; Zhang et al., 2013). A number of studies have investigated the Quaternary glaciations in the southeastern Tibetan Plateau and found evidence of the oldest glaciation back to more than 200 ka years ago (Fu, 2013; Mei et al., 2013; Owen et al., 2005; Zhang et al., 2015; Zheng and Ma, 1994; Zhu et al., 2013). Four glacial stages (the Last Glacial Maximum, early to middle Holocene, the Neoglacial, and the Little Ice Age) in the HLG valley have been identified and the younger two stages have been confirmed with aid of cosmogonic radionuclide (Owen et al., 2005; Zheng and Ma, 1994).

Mt. Gongga (i.e. Minya Konga) is located on the southeastern edge of the Tibetan Plateau (29.6° N, 101.9° E), which is the highest mountain in the eastern of Tibetan Plateau and region of the Hengduan Mountain with a summit of 7556 m a.s.l. (Figure 1.1) (Li et al., 2010; Zhang et al., 2010; Liu et al., 2010; Sun et al., 2018; Yu, 2018; Wang et al., 2013). Mt. Gongga lies in the interactive zone between the Tibetan Plateau and the Sichuan Basin with a full diversity of various features including glaciers, vegetation, geology, biology, and climate (Li et al., 2010; Zhang, 2012). Mt. Gongga region is one of the east-end glacial zones in China (Li et al., 2010). According to the Glacier Inventory of China, 74 glaciers developed around the region of Mt. Gongga (Liu and Zhang, 2017; Pu, 1994). Most glaciers within Mt. Gongga are categorized as monsoonal temperate glaciers, in which glaciers in the HLG catchment (area of 80.5 km^2) (Figure 1.1) are the typical representatives of them (Li et al., 2010; Liu and Zhang, 2017).

3.3 Hailuogou Glacier

3.3.1 Site overview

HLG Glacier is the longest temperate glacier located on the eastern slope of Mt. Gongga (29.6° N, 101.9° E), which is the highest mountain on the southeastern margin of the Tibetan Plateau as shown in Figure 3.3 (Li et al., 2010). Mt. Gongga (i.e. Minya Konga) has the highest summit reaching 7556 m a.s.l. and the region surrounding Mt. Gongga is one of the most extensively glaciated regions in the southeastern Tibetan Plateau (Zhang et al., 2012, 2010). 74 glaciers developed in the region of Mt. Gongga (Liu and Zhang, 2017), but only five of them exceed 10 km in length (Li et al., 2010). The temperate glaciers in this region are considered as a glacier with a high mass turnover and a high ice flow velocity due to high ablation and high accumulation simultaneously in summer (Aizen and Aizen, 1994; Liu et al., 2018; Su and Shi, 2000).

The climate of HLG catchment is characterized by southwest (India and Bengal monsoons) and southeast monsoons, which dominate during the summer (wet season), and by the westerly circulation, which dominates during the winter (dry season) (Li et al., 2010; Zhang et al., 2010).

Within the HLG catchment, there are seven contemporary glaciers with total areal coverage of 36.44 km^2 (Zhang et al., 2012; Xu and Yi, 2017). HLG Glacier is the largest glacier in the HLG catchment with a length of about 13 km, 25 km^2 in area, and covering an altitude range of 2901 – 7556 m a.s.l. (Li et al., 2010; Zhang et al., 2010; Liu et al., 2010; Sun et al., 2018; Wang et al., 2013). Below the ice fall, the ablation area is about 2 km^2 and most of the glacier tongue is covered by supraglacial debris due to processes of frost weathering and rock avalanches (Zhang et al., 2012, 2011). The Equilibrium Line Altitude (ELA) of HLG Glacier was about 5,273 m a.s.l. in 2009 and the ELA for most glaciers in this region ranges from 4,200 to 5,200 m a.s.l. (Li et al., 2010; Zhang et al., 2018). The thickness of supraglacial debris increases progressively from the icefall down to the terminus, where it has been measured at 0.6 m according to Zhang et al. (2010).

Due to rapid ablation being experienced across the glacier tongue, coupled with a reduction in ice flux from the up-glacier accumulation zone, the icefall has thinned and narrowed, and bedrock has become increasingly exposed since the appearance of the first glacier-hole at the icefall in 1993 (Li et al., 2010). The bottom of the icefall (i.e., the upper section of the glacier tongue) has a gradient of ~10° and is partly covered by an fan-shaped structure formed by ice avalanching from the icefall (Zhong et al., 2022). The part below the icefall is about 5 km in length and 300-500 m in width, and is overlain by supraglacial debris (i.e., the thickness of debris-covers varies from several millimeters below the icefall to more than 1 m at the glacier terminus area) due to the processes of frost weathering and rock avalanches (Zhang et al., 2011, 2012). Glacier flow gradually transitions from southeast-orientated to northeast-orientated, forming a glacier arch with intense crevassing in the middle part of the glacier tongue. Several seasonal streams flow from higher cliffs into the hydrological system of the glacier, draining out from the subglacial channel outlet in the highly crevassed terminus (Figure 3.2).

Previous works have addressed the rapid changes in the HLG Glacier, in terms of changes in the surface geomorphology, glaciological landscapes, glacier mass balance and the glacial hydrological system (Heim, 1936; Lu and Gao, 1992; Huang et al., 1996; Liu et al., 2010; Liu and Liu, 2010; Zhang et al., 2012). Accelerated warming since the 1980s has exerted profound effects on glacier dynamics. Recent studies have demonstrated that the HLG Glacier underwent severe recessions, particularly in terms of ice collapse events at the glacier terminus (Xu et al., 2022; Zhong et al., 2022).

Figure 3.2 A: The icefall with elevation differences of ~1080 m (image date: July 2021). Areas marked with red boxes are the exposed bedrocks due to the intense ablations. B: The viewing in the middle section of the glacier (~3250 m a.s.l.). The glacier surface is covered by debris-mantle and intensively crevassed (image date: July 2021). C: The scene from the old viewing platform (~ 3180 m a.s.l.). The glacier surface is highly debris-covered. Several long ice cliffs were exposed, and a highly crevassed lateral margin induced by external stream can be seen (image date: July 2021). D: The highly crevassed glacier terminus with frontal ice collapsing, and the proglacial river flows from the subglacial channel outlet (image date: July 2021). Blue arrows indicate the external streams flow into the glacier lateral margin from higher elevation (e.g., fed by tributary small glaciers).

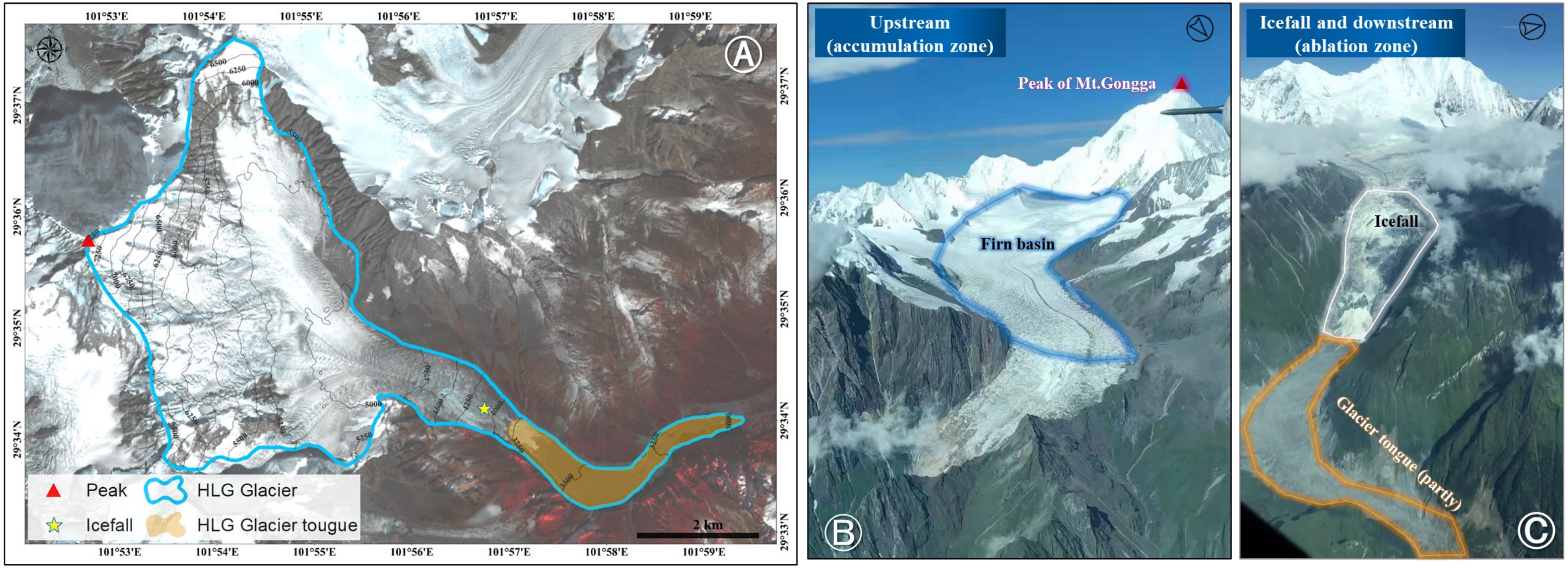

Figure 3.3 The illustration shows the HLG Glacier and its upper and lower part. (a): indicates the extent of the entire HLG Glacier and the glacier tongue. The background image is the false color composite of Sentinel 2A of 10th November 2020 (https://sentinel.esa.int/web/sentinel/missions/sentinel-2). The HLG Glacier outline and the distribution of glaciers in the Tibetan Plateau are from the Second Glacier Inventory of China version 1 (Liu et al., 2014). (b) and (c) are captured by high-performance UAV at the elevation of more than 6000 m a.s.l (Photo credit: Qiao Liu from CAS).

3.3.2 Glaciations in the Hailuogou valley

Glaciers across the Mt. Gongga are categorized as the monsoonal maritime glacier and they are also characterized by rapid ice flow, high ice temperature, and strong capability of surface erosion, thus plenty of paleo glacial records have been formed by multiple glaciations in response to the fluctuation of climate during the glacial-interglacial epochs of Quaternary. A number of studies have investigated the Quaternary glaciations in Mt. Gongga (Figure 3.4), southeastern Tibetan Plateau and found evidence of the oldest glaciation back to more than 200 ka years ago (Fu, 2013; Mei et al., 2013; Owen et al., 2005; Zhang et al., 2015; Zheng and Ma, 1994; Zhu et al., 2013).

The glacial relics on the western slope are more completely preserved in the Gongba valley where the Dagongba and Xiaogongba Glaciers are located, and there are several sets of terminal moraines and corresponding lateral moraines in the valley. According to the degree of weathering of the moraine, deposition of landform location can also be clearly divided into 5 sets of moraines (Figure 3.5).

Basically, there are five sets of relatively well-documented moraines in the HLG valley reported by previous studies (Yu, 2018; Zhang, 2012). Moraines are distinguished from the terminus of contemporary glaciers to the Moxi Platform, called by local names such as Gongga I and II, Laoguanjingtai, Guanjingtai and HLG (Wang et al., 2013; Xu and Yi, 2017b; Zheng and Ma, 1994). By radiocarbon dating of those sets of moraines, four glacial stages are recognized by Zheng and Ma (1994), including Last Glacial Maximum, early to middle Holocene, Neoglacial and Little Ice Age. According to Owen et al. (2005), the timing of Neoglacial and Little Ice are conformed to Zheng and Ma (1994) by cosmogonic radionuclide samples testing.

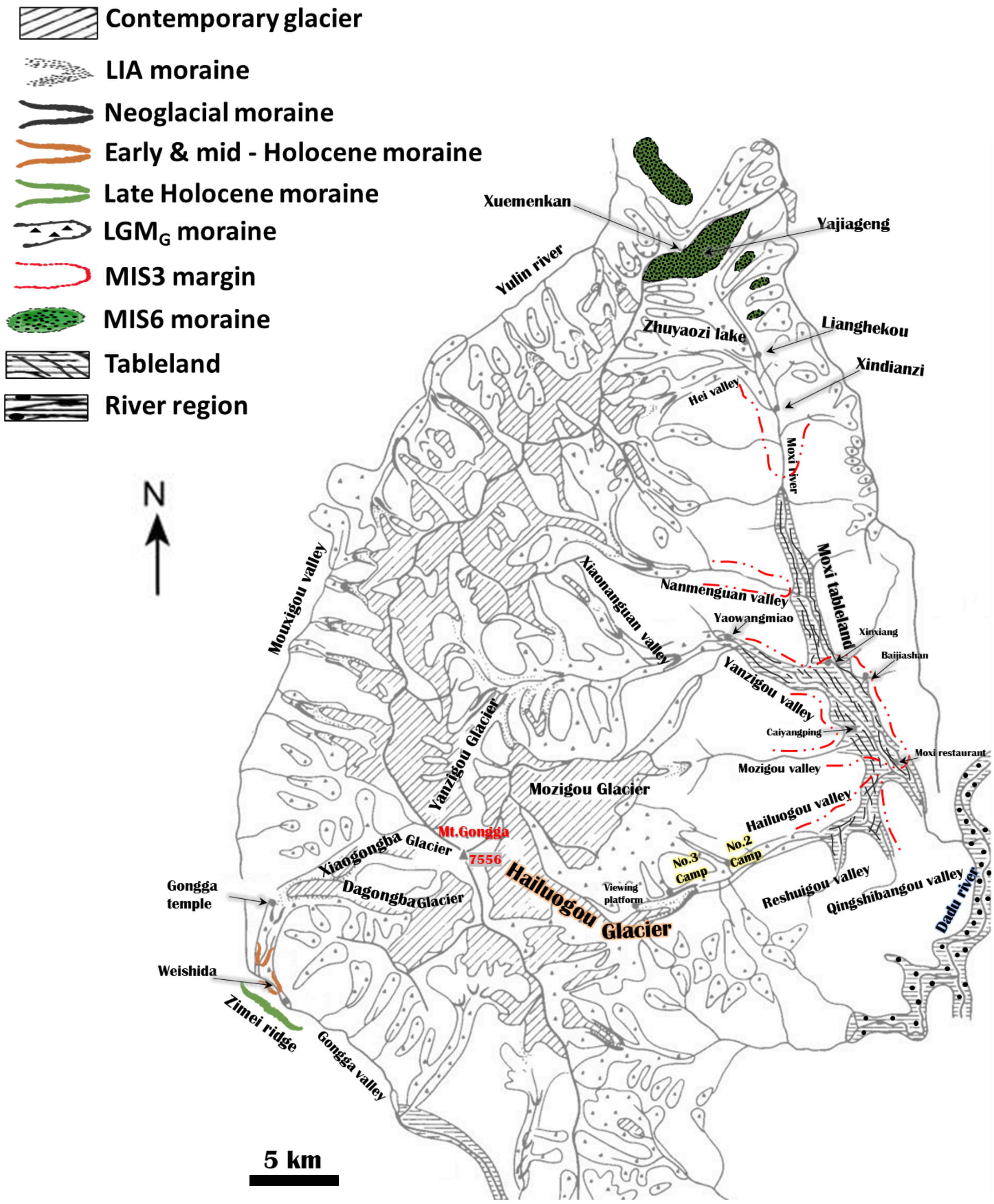

Figure 3.4 The spatial distribution of moraines from Neoglaciation in the Mt. Gongga region, modoified form Zheng and Ma (1994).

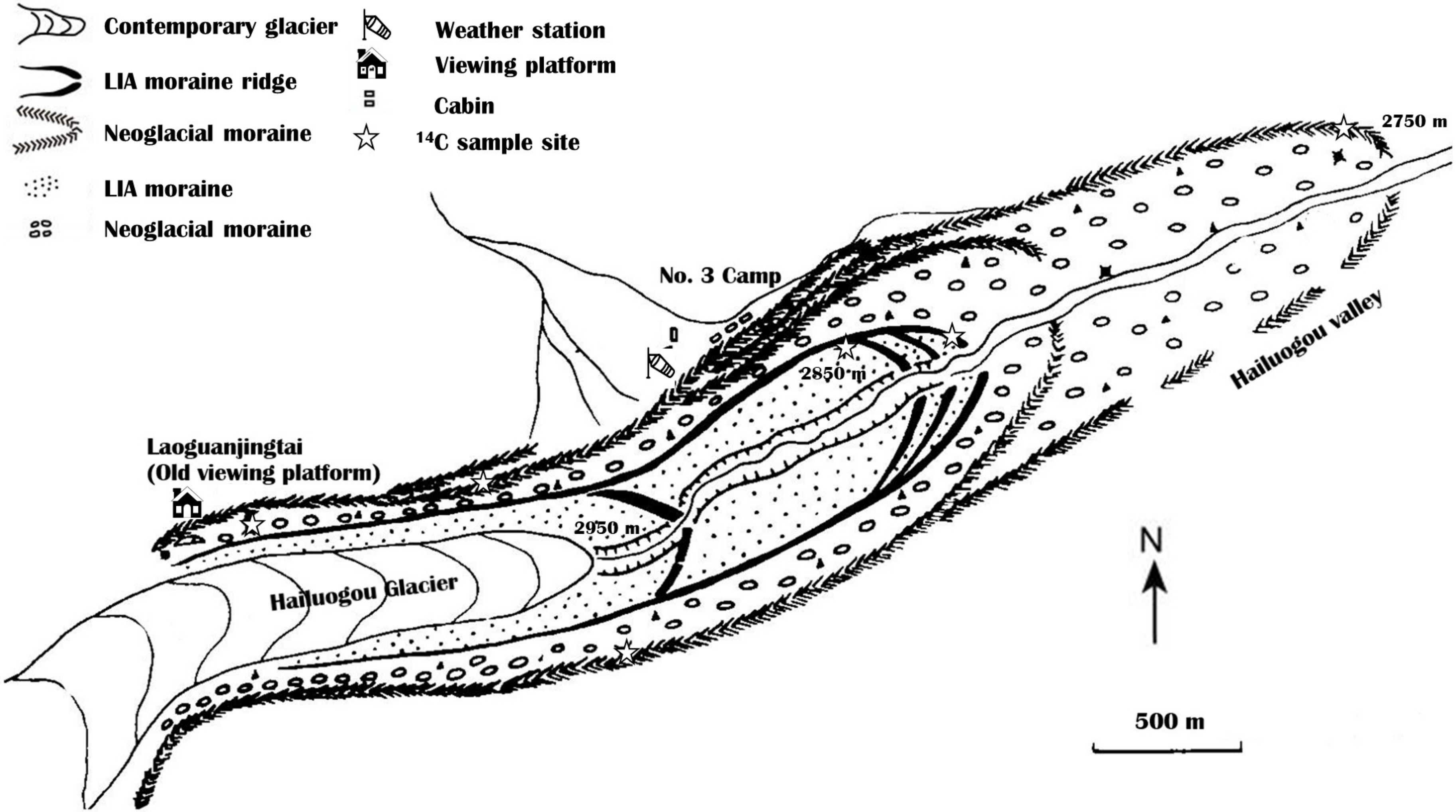

Figure 3.5 The spatial distribution of five sets of moraines from Neoglaciation in the HLG valley, modoified form Zheng and Ma (1994).

3.3.3 Pervious research on the contemporary Hailuogou Glacier

The tendency of glacier retreating is increasing in the maritime glacier distributed area of the western glaciation region of China with the climatic warming effects. As a typical maritime glacier in the Mt.Gongga region, the glacier terminus has retreated about 2 km since the 1930s (Liu and Zhang, 2017). HLG Glacier retreated ~1.15km from 1966 to 2010 with an annual retreat rate of 25 ~ 30 m/a (Zhang et al., 2015). According to the recent data of glacier surface elevation changes from 1989 to 2008, the thickness of HLG Glacier tongue is thinned with an average of 33.9±11.2 m, which equals to 26% thickness of 1990 (~130m) (Liu and Zhang, 2017). Based on the repeated stick surveying, the overall velocity was decreasing and the average velocity decreased by about 31% in the ablation zone from 1981 to 2008 (Zhang et al., 2015; Zhang et al., 2010). With the observations by remotely sensed datasets, the total glaciated area in the HLG Glacier basin reduced to 228.5 km^2 from 257.7 km^2 from 1966 to 2009, decreasing by about 29.2km^2, which far exceeds the inner and western Tibetan Plateau (Pan et al., 2012). There is a location-varying difference of area between the eastern and western slopes in the region of Mt. Gongga with a decreasing ratio of 9.8 and 14.6% respectively, showing an obvious mass loss in the western slope (Zhang et al., 2015). Based on the repeated surface elevation investigations by differential Global Positioning System (dGPS) for the most of ablation zones of HLG Glacier, Yanzigou Glacier and Dagongba Glacier, the annual average thinning rate is 0.90 ± 0.45 m/a, 1.12 ± 0.45m/a and 1.06±0.45m/a, respectively (Zhang et al., 2016).

Several research studies have investigated the changes in HLG Glacier in terms of using glacier mapping from topographical maps and remotely sensed data (Li et al., 2009; Liu et al., 2010; Zhang et al., 2015). Zhang et al., (2015) used two topographical maps (1966 and 1989) and a Landsat image (path 131, row39, 2nd Jan 1989; 8th Aug 2010) to delineate the glacier terminal and to identify the glacier area changes. They estimated the surface elevation changes and glacier volume changes by comparing with two DEMs from contour maps and a generated DEM from the RTK survey (as shown in Table 3.1). Liu et al., (2010) used the same topographical maps (Dec 1966 and Nov 1989), post-processed RTK data (2008), and a set of satellite images (i.e., Landsat MSS (1975 Oct 4)/TM (1994 Sept 5) and Terra ASTER (2007 Dec 15)) to delineate the glacier terminus and glacier extent and then calculate the glacier surface changes. Results of

Liu et al., (2010) indicated that the area shrinkage is 0.92 km^2 from 1966 (25.65) to 2007 (24.73), the terminus retreated 295 ± 60, 252 ± 45, 181 ± 23 m for 1966 - 1975, 1975 - 1994 and 1994 – 2007, respectively.

Table 3.1 HLG Glacier changes from 1966 to 2010 (adapted from Zhang et al., 2015)

Characteristics of Changes	1966-1989	1989-2010	Total
Terminus retreat (m)	743	410	1153
Area changes (km^2)	0.30	0.50	0.80
Elevation changes (m)	15.10 ± 22.80	24.11 ± 11.03	39.21 ± 20.03
Volume changes ($10^{-3}km^{-3}$)	-		- 1.71

3.3.4 Surface morphological changes within the Hailuogou Glacier valley

The morphology in the HLG Glacier surface has experienced remarkable changes since the first observation by the explorers. Several studies have recorded the morphological changes on the HLG Glacier surface (Heim, 1936; Li et al., 2010; Lu and Gao, 1992; Mei et al., 2013; Zhang et al., 2011).

According to the observation at the beginning of the 21st century, there has been a significant change in the glacier surface, specifically for the zone from the icefall to the glacier terminus. Firstly, the thickness of the glacier tongue was decreased by about 12 m between 1993 to 2004, probably due to the intensive ablation since regional warming after the 1980s (Li et al., 2010). Secondly, several holes were clearly observed in the icefall in 2006, and one in 1993, three in 2000, and more than four in 2004 reported by the locals, reconfirming the lifting of the Equilibrium Line Altitude (ELA) and the enhancing of the ablation rate. These holes had transferred to a large area crack between upper icefall and lower icefall and this crack was gradually expanded so that the icefall is almost disconnected based on our observation from 2017 to 2022 (Figure 3.6). The reason for the formation and expansion of these holes lies in the consequence of the lifting of ELA. With the rising of ELA, the ablation duration may be prolonged than before, and the ablation rate was partly enhanced. Therefore, massive ice would avalanche from upstream and form holes, especially during summertime (Li et al., 2010). Thirdly, there was a long and giant ice cliff existing in the lower part of the glacier tongue with a length of about 300 m in 2006. This large ice cliff still existed around 2018/19 based on our field observations (see Appendix Maps 1-2). According to Li et al. (2010)’s interpretation, this ice cliff, as well as its surrounding ice crevasses, is caused by high surface ablation and a large amount of runoff from englacial meltwater. The HLG Glacier has a well-developed hydrological network for its englacial and subglacial zones (Liu et al., 2010; Lu and Zhong, 1996). Many glacier arches were observed in the middle part of the glacier tongue before 1980, but these glacier arches disappeared gradually and transformed into ice crevasses.

Figure 3.6 Time-sequenced changes of the icefall from 2017 to 2022.

3.3.5 Hydrological system

HLG Glacier has a longitudinally steady subglacial channel network in the lower ablation region with a relatively high hydraulic efficiency (Liu et al., 2018). The subglacial drainage system of temperate glaciers transforms into a fast drainage system around the beginning of the ablation season and continues the high drainage capacity until the end of the ablation season (Fountain and Walder, 1998; Hooke, 1989; Liu and Liu, 2010; Walder, 2010). As for HLG Glacier, within the period from May to November, nearly all water from rain and melting enters the glacier via the crevasses and flows within the seasonal efficient drainage networks. In this situation, large amounts of water will flow through the englacial and subglacial drainage networks until it drains into the proglacial rivers (Liu and Liu, 2010).

3.3.6 Mass balance changes of Hailuogou Glacier

The southeastern Tibetan Plateau is the main distribution area of maritime glaciers (e.g., HLG Glacier), of which, the ablation zone of most of the maritime glaciers are covered by debris mantles, bringing about a more complicated response to climate changes (Zhang et al., 2016, 2012). Several research studies have made efforts on the modeling of mass balance for HLG Glacier. Based on a short-term observation of meteorological data and glacier ablation, a net mass balance of HLG Glacier from 1989 to 1990 (i.e., - 0.12 m) was calculated from an empirical equation by Aizen and Aizen (1994). Xie et al., (2001) estimated the mass balance of HLG Glacier from 1988 to 1997 based on the two methods: the method of Zero Equilibrium Line and maximum entropy principle, and a relatively consistent result were given from two methods, indicating the average mass balance was - 470 mm in 10 years. As mentioned in Chapter 2.2, a time series dataset of mass balance from 1952 to 2009 for the HLG Glacier basin has been developed by Zhang et al., (2018) and the reliability and the accuracy of the model used in their study have been validated by other researches (Zhang et al., 2015; Zhang et al., 2016, 2012). According to Zhang et al. (2018), an energy-mass balance model in catchment-scale was built based on energy balance and heat transfer to form a time series of maritime glacier mass changes. This surface energy-mass balance model not only takes into account the conversion of snow to ice and the refreezing of melting water, but also couples with the glacier ablation process under the debris covers and the glacier area changes. The results indicate that the state of mass balance of HLG basin from 1959 to 2009 is in an overall mass loss with an average mass balance of -0.42 m, especially for the period of 2001 to 2009, when the mass loss was accelerating with an average mass balance of - 0.79 m (i.e., 2.3 times for the mass balance of 1959 to 2000 approximately) (Liu and Zhang, 2017; Zhang et al., 2018; Zhang et al., 2012).

Apparently, mechanical ablation processes occurring at the glacier terminus are difficult to detect and predict. As mentioned in the section of Introduction, it cannot be neglected that the mechanical ablation of a glacier, as an efficient way for ice loss apart from the factors related to change of temperature and precipitation, has a deep influence on glacier mass balance and future glacier dynamics. However, most of the previous studies on glacier mass balance and glacier changes in HLG Glacier are based on multi-year data to estimate the overall mass balance changes or average mass balance changes, in which the short-term impacts of glacier mechanical ablation are not considered in the mass balance changes (i.e., not be quantified specifically) in these works. Moreover, there is still a lack of understanding of the impacts of the mechanical ablation process of the HLG Glacier on future glacier behavior. In the context of the accelerated retreating of HLG Glacier, the mechanical ablation process and needs to be quantified precisely, to quantitatively evaluate its effects on mass balance changes and ongoing glacier development.

3.4 Conclusion to this chapter

This chapter has introduced the Tibetan Plateau and Mt. Gongga briefly and then provides a review of HLG Glacier, the southeastern margin of the Tibetan Plateau, including a site overview, glaciations that occurred within the HLG Glacier valley, and studies on the contemporary HLG Glacier. It also reviewed the surface morphological changes in the valley to build the fundamental knowledge of various glacier features for the subsequent mapping work. The glaciohydrology system of HLG Glacier and its variations are also discussed from supraglacial to subglacial and proglacial zone as the HLG Glacier is a temperate glacier and it has a well-developed hydrological system so it can provide insight into the triggering reason of mechanical ablation and other-hydrofracturing events.

Chapter 4: Datasets and methods

4.1 Introduction

Fieldworks and multiple-sourced geospatial datasets are combined to conduct the study to improve the understanding of mechanical ablation that occurred at the HLG Glacier terminus. Several pieces of equipment and source datasets used in the study are discussed in this chapter. Equipment includes two types of UAVs, real-time kinematic (RTK) and an external RTK plugin adopted by a UAV.

The main dataset is aerial images captured by UAVs. Multi-temporal orthophoto mosaics and digital surface models are generated from UAV images. Planet scope images are also used to delineate the monthly glacier extents. ASTER L1A images are used to perform satellite-based photogrammetry to derive the time-sequenced DEMs.

The methods used in this study can be divided into two categories according to the used datasets: **1)** methods related to UAV-captured images, included Structure from Motion with Multiple View Stereo (SfM-MVS), Geomorphic mapping, Digital Image Correlation with Fast Fourier Transformation (DIC-FFT), DEM of Difference (DoD); **2)** methods related to optical satellite images, included visual interpretation from spectral waveband combinations and feature delineations, and satellite-based photogrammetry (NASA AMES Stereo Pipeline)

A summary of datasets and methods used in the study is listed in Table 4.1.

Table 4.1 Brief summary of datasets and methods in this thesis

Equipment	Datasets	Methods	Possible outputs
UAV	Aerial images and videos	Structure from Motion with Multiple View Stereo	Orthophoto mosaics and digital surface models
		Geomorphic Mapping	Mapping of features in the glacier valley
		Digital Image Correlation- Fast Fourier Transformation (DIC-FFT)	Glacier surface velocity field: surface displacements and their vectors
		Differencing of DEM	Ice height changes and the corresponding volumetric variations
GNSS-RTK	Ground control points (post-processing)	-	Co-georeferencing
RTK plugin adopted by UAV	-	-	1) Improve accuracy of location obtained by the UAV onboarded GNSS system 2) Tie points
Satellite	Planet scope images	Band combinations Visual digitization	1) Monthly glacier extents 2) Ice collapse events at the glacier terminus
	ASTER L1A images	NASA AMES Pipeline	Time-sequenced DEMs

4.2 Datasets

The date of each field trip was listed in Table 4.2. The Planet image and ASTER L1A images used for this study were listed in Table 7.1 and S 3.

4.2.1 Field trips

From 2017 to 2021, totally 9 field trips were conducted to HLG Glacier, most of which fell within ablation months (June to November). Drone sorties and field observations were conducted around the HLG Glacier valley. Owing to the flying capacity of the UAV and the unsteady weather conditions, the area covered, and the flight altitude of mapping varied between campaigns.

Table 4.2 Date of each field trip

No.	Date (YYYY/MM/DD)	Drone
1	2017/10/17	Mavic Pro
2	2017/12/04	Mavic Pro
3	2018/06/30	Mavic Pro
4	2018/10/28	Mavic Pro
5	2019/10/03	Mavic Pro
6	2020/09/05	Mavic Pro
7	2020/09/10	Mavic Pro
8	2020/11/05	Mavic Pro
9	2021/07/18	Mavic 2 Pro advanced

4.2.2 Uncrewed Aerial Vehicle

a) UAV Platform

Two drones were used in the field investigations (Figure 4.1). DJI Mavic Pro UAV (i.e., 12.71 megapixels for the camera sensor), and DJI Mavic Pro 2 Enterprise Advanced UAV (i.e., 48 megapixels for the camera sensor).

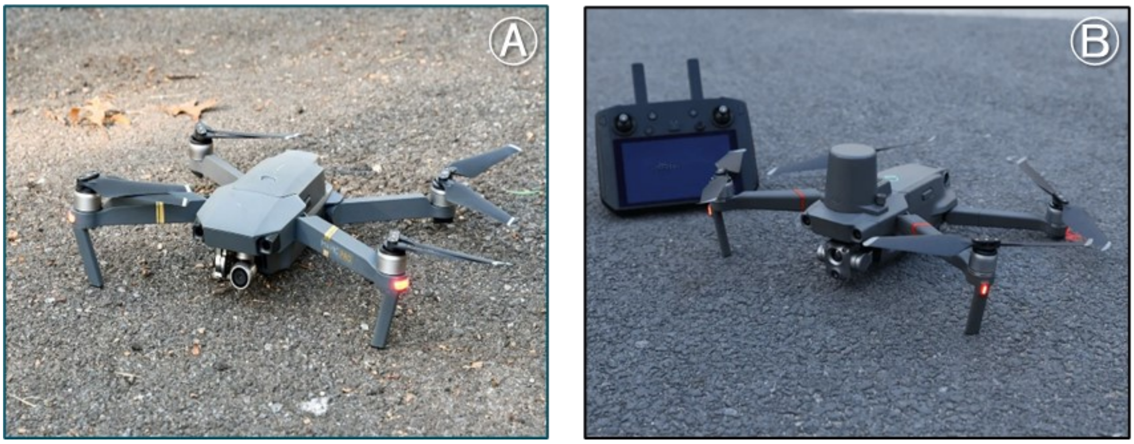

Figure 4.1 UAVs used in the field trips. (a) is the DJI Mavic Pro; (b) is the DJI Mavic Pro 2 Enterprise Advanced and the external RTK plugin.

Firstly, a consumer-grade quadcopter, DJI Mavic Pro, was used for implementing image collection during the eight field trips from 2017 to 2020, for its high-performance in high mountain regions, as well as being compact size, having good handling ability, and relatively low cost for conducting high-resolution landform investigations (Hendrickx et al., 2019; Stucky de Quay et al., 2019). The onboard RGB camera is a 12.71-megapixel sensor with the ability to capture JPEG format or RAW images in the visible light range. The onboard camera is an FC220 with a focal length of 4.73 mm.

Secondly, aerial images were also captured by employing a UAV of DJI Mavic Pro 2 Enterprise Advanced in the last field trip of 2021 (Hill et al., 2020; Tămaș et al., 2022; Xu et al., 2022). Two cameras were equipped on the UAV, the RGB camera and thermal camera, and worked synchronously to capture the visual image and thermal infrared (TIR) image. The RGB camera has 48 megapixels with a focal length of 24 mm and the ability to capture an image with a field of viewing of 84 degrees. The thermal camera has an Integrated Radiometric Thermal sensor (i.e., Uncooled Vox microbolometer) with a focal length of 38 mm.

Coordinates of aerial images were obtained by an integrated GNSS system of GPS and GLONASS with meter-level for both DJI drones and then written into the header file of the images. Additionally, with the aid of an external plugin of Real Time Kinematic (RTK) positioning, it improves the accuracy of the collected coordinates based on network RTK and enables the geolocation of UAV images being captured with a mean quality of 1 cm + 1 ppm horizontally and 1.5 cm + 1 ppm vertically.

b) Drone implementation and aerial image capturing

We used Pix4D-Capture to plan flight missions in detail and execute missions automatically. The flight parameters can be set up in advances such as camera posture, overlapping parameters, and drone speed. Each UAV survey has a total of 60 km in length of flight path and 1.5 hours in flight duration to cover the entire glacier tongue approximately. However, it is not suitable to conduct a fully automatic flight mission for the entire ablation zone of the HLG Glacier due to its high relief and frequently unstable weather conditions. We, therefore, flew manually for parts of the ablation zone to ensure sufficient image overlap and quantity. Specifically, firstly we adopted the terrain-following flight mission strategy for the UAV mapping as the elevation of the HLG Glacier tongue is ranging from ~2900 to 3500 m a.s.l. In other words, the mapping area was covered separately with four gridded flight paths with variable flying heights to maintain relatively constant ground resolutions. The onboard camera of the UAV was pre-set with a nadir viewing angle to obtain orthophotos with a longitudinal and side overlapping of 70% and 80%, respectively. The drone was not able to capture images beyond the icefall (yellow star in Figure 3.3) given its altitude, so the mapping area covers from icefall to the glacier terminus and part of the periglacial forest (as shown in Figure 5.2).

4.2.3 Ground control points and tie points

a) Ground control points

We collected six sets of Ground control points (GCPs; Figure 4.2) during the field trip in 2018. These GCPs are distributed around the proglacial zone of the HLG Glacier since the glacier surface is highly unstable and points are often difficult to locate in aerial imagery. We aimed to identify features from artificial and stable constructions, such as road junctions, using two GNSS geodetic receivers simultaneously (i.e., one was set as the master station and the other is the rover). The master station was installed on the rooftop of a hotel in the HLG Glacier Park to acquire the long-time observation needed for a static referencing point. The rover measurement was conducted by occupying the GCPs for at least 2 mins during periods of comprehensive satellite coverage, and the resulting coordinates were post-processed to export the GCPs.

Multiple-temporal datasets captured from UAV need to be overlapped to derive the changes of the HLG Glacier, so that the positioning information of the UAV datasets require corrected and optimized. The reason for it is the geolocations of the UAV-images obtained by the on-boarded GNSS equipment (e.g., GPS) has limited georeferenced accuracy (i.e., meter-level). Thus, the coordinates of GCPs are input into the structure-from-motion workflow during the bundle adjustment. In other words, georeferencing with GCPs makes multitemporal UAV datasets registering to a same benchmark so that the changes derived from them is reliable and accurate.

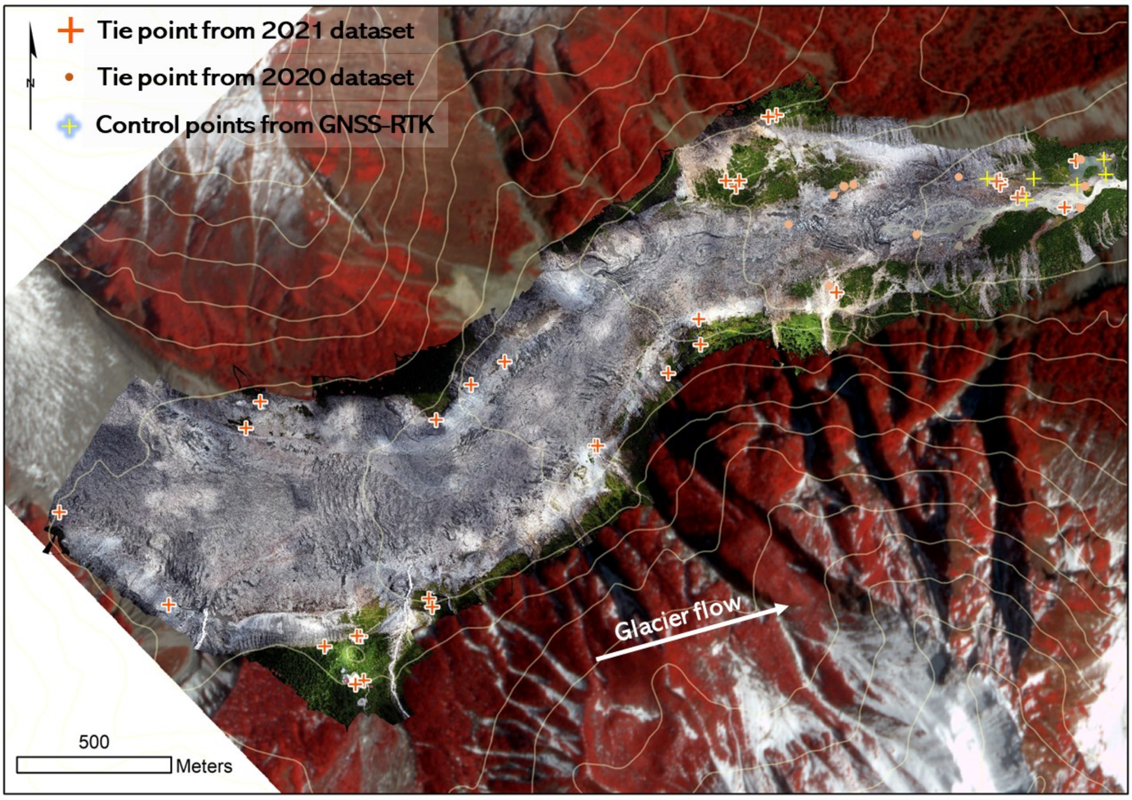

Figure 4.2 Ground control points and two sets of tied points used in the thesis. The false color background is the Planetscope image of May 15th, 2018. The HLG Glacier tongue was shown by the high-resolution orthophoto mosaic of July 2021.

b) Tie points

Limited by the scale and the rugged surface of the glacier tongue, it is impractical to set ground control points during UAV missions. The primary embedded GNSS sensors of the UAV enable meter-level accuracy in location. For the most recent (2021) survey, we benefited from an external Real-Time kinematic (RTK) plug-in adapted by DJI Mavic Pro 2 Enterprise, which supports Network RTK and therefore high accuracy photogrammetric mapping (i.e., centimeter-level) without the need for external ground control points (GCPs). The RTK plug-in enables the coordinates with a mean quality of 1 cm + 1 ppm (RMS) (Zhong et al., 2022) horizontally and 1.5 cm + 1 ppm vertically. Accordingly, we considered the most recent dataset (2021) as the benchmark and extracted locations of points that are easily identifiable and stable surface features from it as the locations of tie-points to refine the geo-registering and georeferencing of the other three maps (i.e., datasets of 2018, 2019 and 2020 for ***Chapter 5***) (Figure 4.2). In ***Chapter 6***, only the DJI Mavic Pro was used for this part (i.e, without external RTK plugin). Therefore, the dataset of November 2020 was georeferenced by using external GCPS and then several tie points for the HLG Glacier snout were also extracted from it, and consequently the remaining datasets were registered to the georeferenced dataset.

4.2.4 Optical remotely sensed satellite image

Two kinds of optical satellite datasets were used in the thesis, that is, Planet scope images and ASTER Level 1A images (ASTER L1A Reconstructed Unprocessed Instrument Data V003). Planet scope images (https://www.planet.com/explorer/) are used to delineate the monthly glacier extent from 2016 to 2022 and detect ice collapse events at the glacier terminus. ASTER L1A (https://search.earthdata.nasa.gov/search/) are applied on the satellite-based photogrammetry (i.e., NASA Ames Stereo pipeline) to derive the time-sequenced DEMs.

4.2.4.1 PlanetScope images

Planet CubeSat constellation (or nanosatellites), also known as the Planet scope imagery, has roughly 150 cube satellites on the two near-polar orbits (i.e., inclining ~ 8° and ~ 98° with an altitude of about 475 km), capturing multispectral images of the ground features of Earth surface at local morning (Altena and Kääb, 2017; Ghuffar, 2018; Kääb et al., 2019). Each Planet satellite can be described as a sensor of cube units (i.e., 10 ×10×30 cm), consisting of a telescope and CCD area array camera. Each CCD area array camera has roughly 29 mega-pixels (i.e., 6600 × 4400 pixels) and acquires Red-Green-Blue (RGB) and Near-infrared (NIR) data bands synchronously in 12-bit radiometric resolution (Kääb et al., 2019). Currently, most of the PlanetScope images were captured at an altitude of approximately 500km orbit with a spatial resolution of about 3.7 m (then resampled to 3 m) and the size of the field of view is about 25-30 km × 8-10 km per scene. The constellation keeps itself updated by continuously new satellites entering its orbits.

4.2.4.2 ASTER Level 1A images

The satellite Advanced Space Thermal Emissions and Reflection Radiometer (ASTER) is carried by Terra Satellite as part of the Earth Observing System of NASA in the December of 1998 (Bhattacharya et al., 2021; Zhang et al., 2018). The ASTER sensor can obtain data for multiple spectral imageries ranging from optical to thermal infrared and its coverage area ranges between 82°N and 82°S (Table 4.3). The ability for extracting DTM from ASTER imagery comes from the stereo image recorded in band 3 of the ASTER sensor (Zhu et al., 2021), which has along-track stereoscopic capabilities (Bhattacharya et al., 2021). Two sub-bands in VNIR, i.e., a nadir and a backward, form an along-track stereo image pair with a base-height (B/H) ratio of ~ 0.6, which is suitable for producing ideal DEMs using a semi-automatic workflow (Figure 4.3; Hirano et al., 2003). Figure 4.3 indicates the principle of the DEM generation from different viewing positions (Kääb , 2008, 2007). Steps for generating DEMs from ASTER bands 3N and 3B are discussed in **Chapter 4.3.6**.

Table 4.3 Information of ASTER spectral bands

Band	Wavelength (µm)	Spatial Resolution (m)	Usages
1	0.52 - 0.60	15 m	Visible and Near-Infrared
2	0.63 - 0.69	15 m	Visible and Near-Infrared
3N	0.78 - 0.86	15 m	Visible and Near-Infrared
3B	0.78 - 0.86	15 m	Visible and Near-Infrared
4	1.600 - 1.700	30 m	Shortwave Infrared
5	2.145 - 2.185	30 m	Shortwave Infrared
6	2.185 - 2.225	30 m	Shortwave Infrared
7	2.235 - 2.285	30 m	Shortwave Infrared
8	2.295 - 2.365	30 m	Shortwave Infrared
9	2.360 - 2.430	30 m	Shortwave Infrared
10	8.125 - 8.475	90 m	Thermal Infrared
11	8.475 - 8.825	90 m	Thermal Infrared
12	8.925 - 9.275	90 m	Thermal Infrared
13	10.25 - 10.95	90 m	Thermal Infrared
14	10.95 - 11.65	90 m	Thermal Infrared

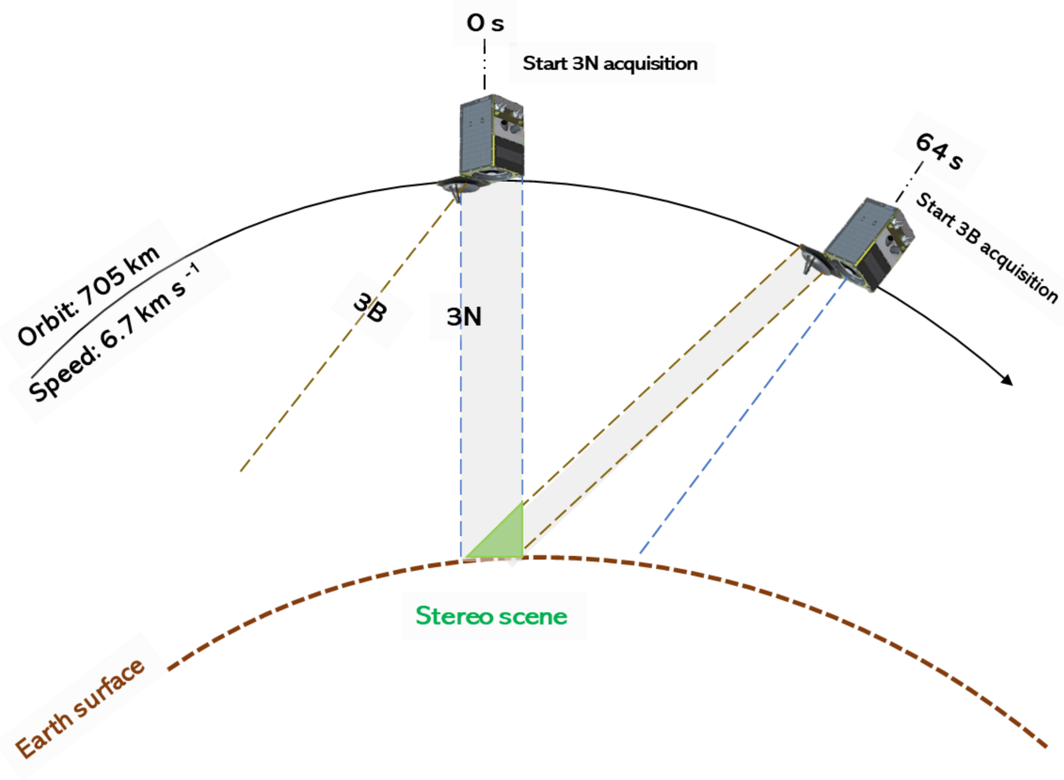

Figure 4.3 ASTER stereo geometry and timing of the nadir-band 3N and the back-looking sensor 3B

4.2.5 Meteorological data

4.2.5.1 Meteorological data from the Chinese Ecosystem Research Network

Alpine Ecosystem Observation and Experiment Station of Gongga Mountain, Chinese Academic of Sciences (CAS), is part of Chinese Ecosystem Research Network (http://www.cern.ac.cn/0index/index.asp). We applied for and collected a comprehensive meteorological dataset of the Mt. Gongga region from the website of Chinese Scientific Data (http://www.csdata.org/p/411/#referencebib7/).

Two meteorological stations, named HLG station and Moxi station (Figure 4.4), were established by the Institute of Mountain Hazards and Environment, Chinese Aacademy of Science, in 1987. The HLG station is located at the altitude about 3000 m a.s.l. and the Moxi station is about 1600 m a.s.l. These two stations were fully functional since 1988 (HLG station) and 1992 (Moxi station), respectively (Wu et al., 2013). They automatically collected meteorological data every hour and stored data in-suit memory cards.

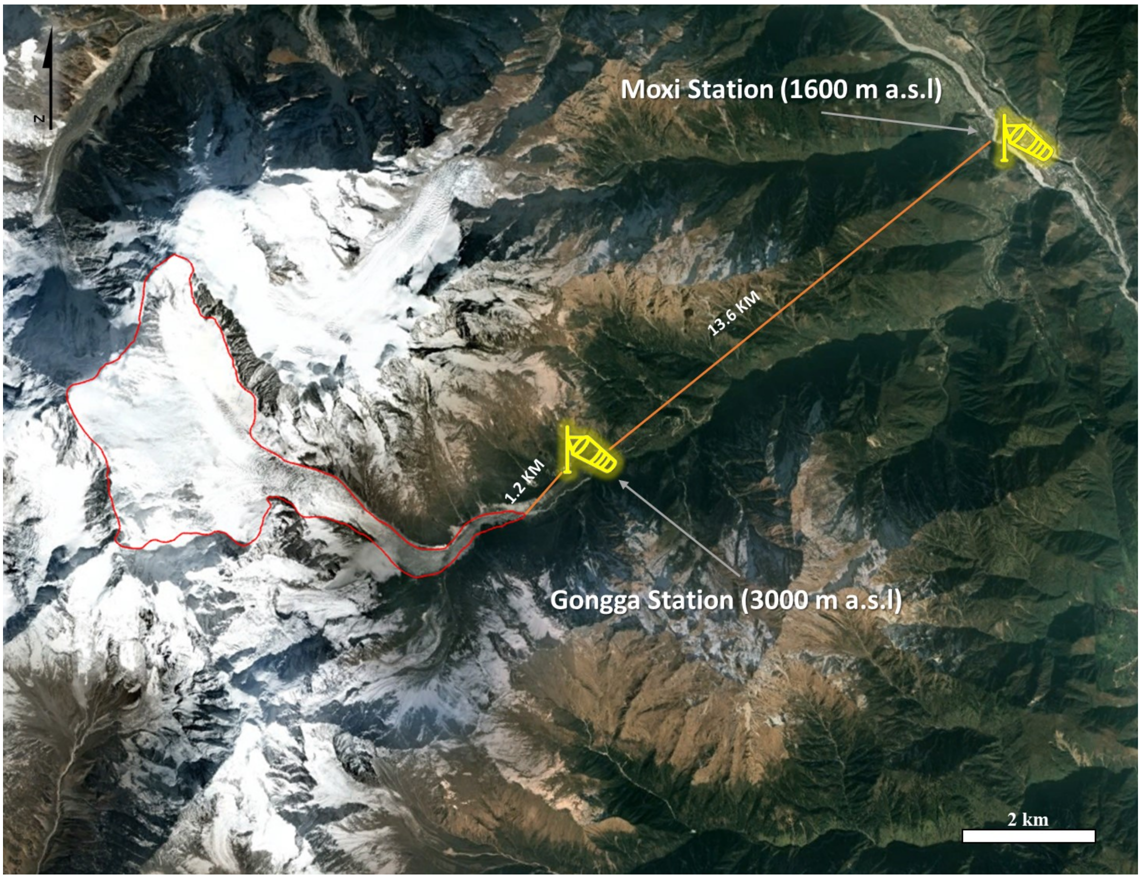

Figure 4.4 The locations of Gongga and Moxi station and their distance to the HLG Glacier terminus

This meteorological data of the Mt. Gongga region mainly corresponds to the eastern slope of Mt. Gongga. There are a total of 19 recorded parameters from 1998 to 2018: air pressure, water vapor pressure, sea level pressure, air temperature, dew point temperature, relative humidity, precipitation, wind speed, 10-minute average wind speed, 2-minute average wind speed, hourly maximum wind speed, surface temperature, 5 cm soil temperature, 10 cm soil temperature, 15 cm soil temperature, 20 cm soil temperature, 40 cm soil temperature, 60 cm soil temperature, 100 cm soil temperature.

The data of temperature and precipitation was extracted as these two factor are highly linked with glacier changes (i.e., ablation and accumulation):

1) Temperature: The air temperature was observed with the HMP45D temperature sensor.
2) Precipitation was observed with an RG13H rain gauge and calculated every minute.

We have pre-processed the extracted data and listed them in Table 4.4 to Table 4.7, and highlighted the Max, Min, and second Max values with yellow, blue, and green, respectively.

Table 4.4 Temperature data (° C) from Gongga (HLG) station - 3000 m a.s.l.

	JAN	FEB	MAR	APR	MAY	JUN	JUL	AUG	SEP	OCT	NOV	DEC
1998	-	-2.3	0	7	9.36	10.8	13.4	11.9	9.5	6	2.2	-3.8
1999	-5	-2.3	0.6	5.6	6.9	10.5	11.5	11.4	10.6	5.2	1.2	-4.2
2000	-5	-4.8	-1.5	2.9	7.9	10.4	12.4	11	9	6.2	-0.3	-3.1
2001	-4.6	-3.5	0.1	3.9	6.7	10	13.2	11.2	9.8	6.3	0.5	-3.8
2002	-4.4	-1.8	0.6	-	7	11.5	12.1	11.2	8.5	5.2	0.8	-2.8
2003	-4.2	-1.4	-0.1	5.3	7.4	9.3	12.5	12.6	9.8	4.8	1.2	-3.7
2004	-5.2	-3.2	1.2	5.2	6.9	9.2	11.6	12	9.3	3.9	0.6	-2.4
2005	-4.2	-2.5	0.4	4.2	8.6	-	-	11.7	10.9	-	1.5	-3.8
2006	-	-	-	5.2	8.3	10.8	14.4	13.7	10	6.9	1.7	-3.2
2007	-5.6	-0.6	1.2	4	9.3	10.8	12.9	13.1	9.5	6.3	1.4	-2.4
2008	-5.8	-6.2	1.4	5.7	8.9	11.1	12.8	11.3	11	6.9	0.7	-1.9
2009	-4	0.5		5.6	7.8	10.3	13	12.7	11.9	5.9	0.2	-2.8
2010	-2	-1	1.9	4.8	8.9	9.8	13.8	13.2	10.7	5.8	1.1	-2.6
2011	-7.7	-0.7	-2	4.7	8.8	11.4	12.6	13	10	5.4	2.2	-
2012	-6.6	-3.9	0.2	4.2	8.9	9.9	13	13.2	9.3	5.5	1	-3.2
2013	-4.5	-0.3	3	5	8.3	12.7	-	-	9.6	-	1.5	-4.5
2014	-3.3	-2.7	0.7	6.1	7.8	10.4	13	11.6	11.2	6.9	0.8	-3.9
2015	-2.8	-1.3	2.6	5.4	9.1	11.6	-	-	9.5	6.8	-	-3.6
2016	-5	-3.8	1.6	5.2	9.4	12	13.6	14	9.4	7.4	1.9	-1.4
2017	-3.2	-1.8	-0.5	4.7	7.9	10.1	-	-	-	6.7	1.3	-2.7
2018	-4.7	-3.7	2.4	5.8	8.7	10.8	13.5	13.1	-	-	0.5	-3.7
MAX	-2	0.5	3	7	9.4	12.7	14.4	14	11.9	7.4	2.2	-1.4
MIN	-7.7	-6.2	-2	2.9	6.7	9.2	11.5	11	8.5	3.9	-0.3	-4.5
AVG	-4.39	-2.49	0.77	5.29	8.64	11.23	13.70	13.05	10.53	6.36	1.16	-3.34

Table 4.5 Temperature data (° C) from Gongga (Moxi) Station - 1600 m a.s.l.

	JAN	FEB	MAR	APR	MAY	JUN	JUL	AUG	SEP	OCT	NOV	DEC
1998	3.4	6.8	9.1	16.2	17.4	18.4	20.5	19.4	17.4	13.7	10.7	6.1
1999	3.9	7	9.7	14.7	14.9	18.8	19.5	18.5	18.5	13.3	9.7	4.5
2000	3.6	4.1	8.7	12.8	16.5	18.7	20.8	19	16.6	14.3	7.5	5
2001	4.1	5.8	10	13.4	15.4	18.2	21.5	19	17.6	14.2	9.2	4.5
2002	4.5	7.7	10.3	15.3	16.4	19.4	20	19.4	16.7	13.6	9.3	4.9
2003	4.7	8.1	9.9	14.8	16.1	17.3	20.4	20.6	17.5	12.4	9.1	4.5
2004	3.9	6.3	10.5	14.6	15.5	16.8	19.5	19.9	16.9	11.9	9.1	6.1
2005	3.4	5.3	8.8	13.4	16.8	18.7	20.6	18.9	18.4	12.5	9.1	4
2006	4.4	6.4	9.7	14.5	16.8	18.6	22.2	21.9	17.7	14.8	10	5.1
2007	3.4	8.6	10.9	13.1	17.6	18.7	20.4	20.8	17.4	13.5	9.7	5.6
2008	1.9	2.9	10.5	14.8	16.9	19	20.7	18.4	18.5	14.8	8.6	5.3
2009	3.9	9.5	10.7	13.5	16.2	18.5	20.6	20.4	19.3	13.7	8.2	5.2
2010	5.6	7.9	10.4	12.6	17	17.5	21.2	20.6	18.2	13.6	9.4	5.5
2011	0.9	7.6	6.9	14.2	16.7	19.4	20.3	21	17.6	13.6	10.9	
2012	2.4	4.2	9.3	13.9	17.6	17.7	20.4		16.8	13.6	9.5	5
2013	4.5	8.5	12.6	13.8	16.5	20.5	21.5	22.1	17.3	13.3	9.9	4.4
2014	5.1	6.5	10.4	15.3	16.5	18.5	20.7	19.2	18.5	15	9.1	4.6
2015	5.9	7.6	12.6	14.8	18	19.4	19.8	19.6	17.3	15.2	11.8	5.4
2016	4	5.6	11.4	14.3	17.9	20.3	21.2	22	17.1	15.5	9.7	6.8
2017	6.4	6.9	9.1	14.1	16.6	18.3	21.3	21.4	18.4	14.2	10.3	5.7
2018	4.5	5.6	12.1	14.6	17	19	21.2	21			8.5	5.3
MAX	6.4	9.5	12.6	16.2	18	20.5	22.2	22.1	19.3	15.5	11.8	6.8
MIN	0.9	2.9	6.9	12.6	14.9	16.8	19.5	18.4	16.6	11.9	7.5	4
AVG	4.0	6.6	10.17	14.22	16.68	18.65	20.68	20.16	17.69	13.83	9.49	5.17

Table 4.6 Precipitation data (mm) from Gongga (HLG) station - 3000 m a.s.l.

	JAN	FEB	MAR	APR	MAY	JUN	JUL	AUG	SEP	OCT	NOV	DEC
1998		0	58.8	117.1	251.3	335.6	359.9	282.9	206.5	165.4	94.6	31.1
1999	22.7	29.8	55.5	166.2	315.3	331.8	337	348.3	240.5	170.1	80.8	19.6
2000	21.8	43.4	81.4	205.3	235.8	278	171.3	309.9	264	117.8	61.4	19
2001	38.5	30.7	78.7	194.8	198.9	348	214.4	438.5	264.8	138.2	69.2	29.2
2002	0	23.5	105.9		211.7	314.3	265.8	266.5	184.3	180.6	84.5	8.2
2003	17	11.9	40.3	175.7	242.9	367.6	341.8	311.8	213.5	153.8	34.5	21.7
2004	17.8	57	131.1	166.5	289.1	310.6	281.5	300.4	265.6	173	87.8	24.8
2005	19.3	39.5	102.9	183.6	303.6	333.8	336.5	339.2	203.8	196.2	45.1	12.1
2006	4.6	15.8	36.6	146	262	224.8	204.8	223.8	247.6	189.8	88.8	35.2
2007	37.2	71	36	181.8	252.4	284.6	293.2	281.6	248.8	110	41.4	18.2
2008	14.4	70	142.6	180.2	323.2	209	234.2	301	176	185.2	48	12.6
2009	25.2	12	45.4	171.4	236	144.8	212	277.4	159.4	132.8	50.8	53.4
2010	10	22	108.2	177.8	233.2	323.6	359.2	281.8	202.6	174.8	81	36.6
2011	24.2	23.6	51.2	151.8	157	253.2	295.6	115.2	157.6	103.6	53	17.4
2012	20.8	23	98.2	164	186.2	323.8	359	280.8	240.4	151	26.2	16.2
2013	17.8	11.2	82	168.6	251	197.6	148.6		286.2	168.4	52.2	36.4
2014	33.4	23.8	77	102.4	197.8	318.2	303	348.2	237.2	129	54.2	26.6
2015	26.4	19.2	54.4	178.2	172.6	312.6	166.6	72.8	232.4	117	16.8	37.8
2016	27.8	58.4	101	246.2	155.6	311.4	309	190	292	93	28.8	31.8
2017	14.2	30.2	107.8	224.2	270	302.4	189.6	300	191.2	152.6	55	22
2018	17.2	36	153.2	176	237	373.6	318.4	236.6	143	104.8	50.6	25.2
MAX	38.5	71	153.2	246.2	323.2	373.6	359.9	438.5	292	196.2	94.6	53.4
MIN	0	0	36	102.4	155.6	144.8	148.6	72.8	143	93	16.8	8.2
AVG	20.51	31.05	83.25	173.89	237.27	295.20	271.50	275.34	221.78	147.96	57.37	25.48

Table 4.7 Precipitation data (mm) from Gongga (Moxi) station – 1600 m a.s.l.

	JAN	FEB	MAR	APR	MAY	JUN	JUL	AUG	SEP	OCT	NOV	DEC
1998	2.3	3.4	12.8	83.1	133.3	133.1	271.8	196.1	105.7	71.8	23.3	1.7
1999	2.9	4	9.7	70.1	126.8	194.2	190.3	180.2	216	126.2	21	2.3
2000	2.4	6.3	15	74.3	144.9	154.2	96.9	137.8	164.4	4.3	11.6	1.9
2001	2.4	10.2	30.7	120.2	82.4	190.6	105.8	280.5	140	52.5	22	0.2
2002	16.5	1.8	45.8	33	93.7	184.9	195	170.2	124.8	110.7	19.7	2
2003	2	0	26.8	73.8	108.7	199.9	206.5	242	132.4	62.8	13.8	8.3
2004	3.7	12.1	45.5	65.9	110.2	227.1	226.8	204.8	161.2	59.4	35.4	0.9
2005	3	13.8	36.1	63	170.5	199.8	242.1	230.8	113	77.9	18.2	2.1
2006	0	0.8	25.6	49.4	156.4	109.6	212.6	124	6.4	0	2.4	4.4
2007	7.4	25.4	2.4	91.2	133.6	170.6	195.6	291.4	107.2	89.6	25.2	3.8
2008	1.2	17.2	58	115.4	161	111.2	116.2	262.8	135.8	81.6	6.4	1.2
2009	7.8	0.6	29.2	101.8	108.2	108.6	195.2	193.6	125.6	32	8.2	14
2010	0.6	1.6	41.8	56	105	140.6	291	204.8	137.6	67	7.4	7
2011	5.2	2.4	33.6	50.2	143.8	151.8	243.2	43.2	129.8	48.4	52.8	
2012	1.4	1.4	59.8	64	97.4	124.8	219.2	74.4	82.6	38.4	0.4	1.4
2013	1.6	0	55.6	100	109	217.2	324.4	58.8	134.6	68.4	0.6	8.4
2014	7	2.8	20.4	3.6	5.6	115.2	187	225.8	77	2.2	0	13
2015	1.6	0.6	23.2	51.2	72	199	149.6	161.2	88.2	58.6	5	6
2016	1.4	16.6	35.2	107.8	82.4	187.2	295	158	193.8	45	13.8	7.6
2017	0	8.8	28	108.8	125.6	171.2	166.6	335	104.6	60.6	7.6	1.4
2018	2.4	17.6	77	124.6	97.4	279	279.4	106.4			9.6	2.4
MAX	16.5	25.4	77	124.6	170.5	279	324.4	335	216	126.2	52.8	14
MIN	0	0	2.4	3.6	5.6	108.6	96.9	43.2	6.4	0	0	0.2
AVG	3.47	7.02	33.91	76.54	112.76	169.99	210.01	184.85	124.04	57.87	14.50	4.50

4.2.5.2 Interpretation from previous meteorological datasets

The average annual temperature at the HLG station has climbed from 3.9°C to 4.2°C over the past two decades. There were two phases of temperature increases. The first phase terminated in 1998, with the annual mean temperature peaking at its highest value in the last 20 years, and then declined sharply to its lowest value in 2000. The second phase of the warming started in 2001. The most significant warming occurred in the first decade of the 21st century as recorded. In general, the average annual temperature at HLG station is high whereas the precipitation is low, suggesting an opposite pattern of temperature and precipitation changes in the last two decades (Figure 4.5).

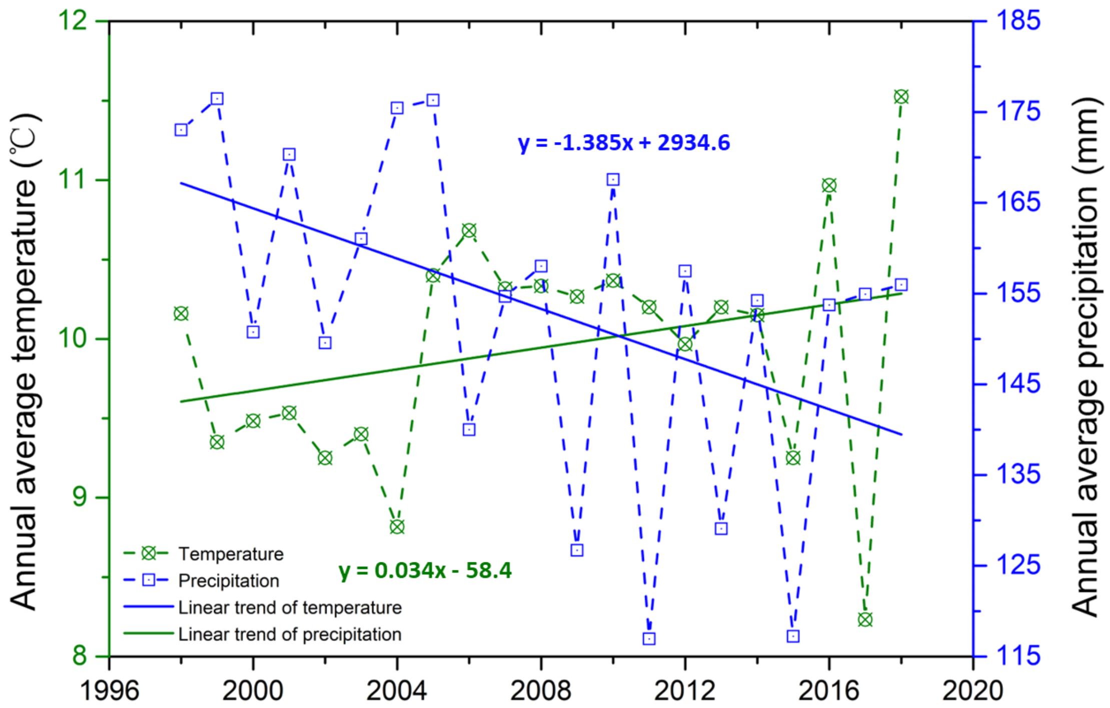

Figure 4.5 The variations of average temperature and annual average precipitation, based on datasets from HLG station (3000 m a.s.l.). Green indicates the terperature changes and blue indicates the precipitation changes.

4.3 Methods

4.3.1 Structure from Motion and Multiple View Stereo

Structure from Motion with Multi-View Stereo (SfM-MVS) was applied to produce multi-temporal Digital Surface Models (DSMs) and orthophoto mosaics in Agisoft Metashape Professional version 1.5.3 (AgiSoft LLC). In addition, some images were extracted by screenshots with a constant time interval from the aerial videos. These extracted images were integrated with the still aerial images to form an input dataset for the 3D surface reconstruction. Agisoft Metashape Professional is now a well-established and widely used 3D reconstruction software in landform investigations (Bash et al., 2018; Rossini et al., 2018; Rusnák et al., 2018; Verhoeven, 2011).

Firstly, UAV-captured images need to be pre-checked to ensure image quality and sufficient multi-viewing overlapping before running the reconstruction workflow. The alignment of photos will be then implemented by the algorithm of feature recognition based on the method of Scale Invariant Feature Transformation (SIFT) (Lowe, 2004; Rossini et al., 2018). Specifically, UAV images can be aligned through SIFT algorithm by detecting and matching high-contrasted or unique surface features automatically (e.g., ice cliff edge, margins of ice crevasses, giant stones, and boundary of artificial constructions). Subsequently, with the algorithm of interactive bundle adjustment, the 3D geometry of the landform and the refined camera position is reconstructed from a multi-viewing sequence of 2D images and then the sparse point cloud is derived (Rossini et al., 2018). High accuracy in image aligning was set for matching more recognized feature points and increasing corresponding image point pairs. The highly accurate geodetic field measurement techniques are used to obtain Ground Control Points (GCPs) in many UAV-based glacial studies such as dGPS and RTK (Chandler et al., 2018; Rossini et al., 2018). The built-in integrated GNSS system of the drone is able to write location and orientation information into the head file of captured aerial images. This written-in GNSS information from the onboard navigation instrument enables the camera positions and the 3D sparse cloud to be autonomously georeferenced with meter-level precision. The GCPs are then imported to be manually marked on the corresponding images so that the camera positions and the geometry of the 3D sparse point cloud could be refined and improved, respectively. Subsequently, the sparse point cloud was to be enriched by a multi-viewing stereo image matching algorithm, evolving into the dense point cloud (Hendrickx et al., 2019; Rossini et al., 2018). Based on the generated dense point clouds, DSMs and ortho-images can be converted through interpolation methods. Combined with the GCPs from dGNSS or RTK-GNSS, the generated DSMs and ortho-images yield coordinate information of submeter-level resolution and centimeter-scale error value (Chandler et al., 2018; Ewertowski et al., 2019; Rossini et al., 2018).

We followed a standard SfM-MVS processing workflow by using Agisoft Metashape pro, as described in many previous studies (Immerzeel et al., 2014; Rossini et al., 2018; Ryan et al., 2015; Smith et al., 2016). A complete workflow of the 3D scene reconstruction for the case of the HLG Glacier is shown in Figure 4.6.

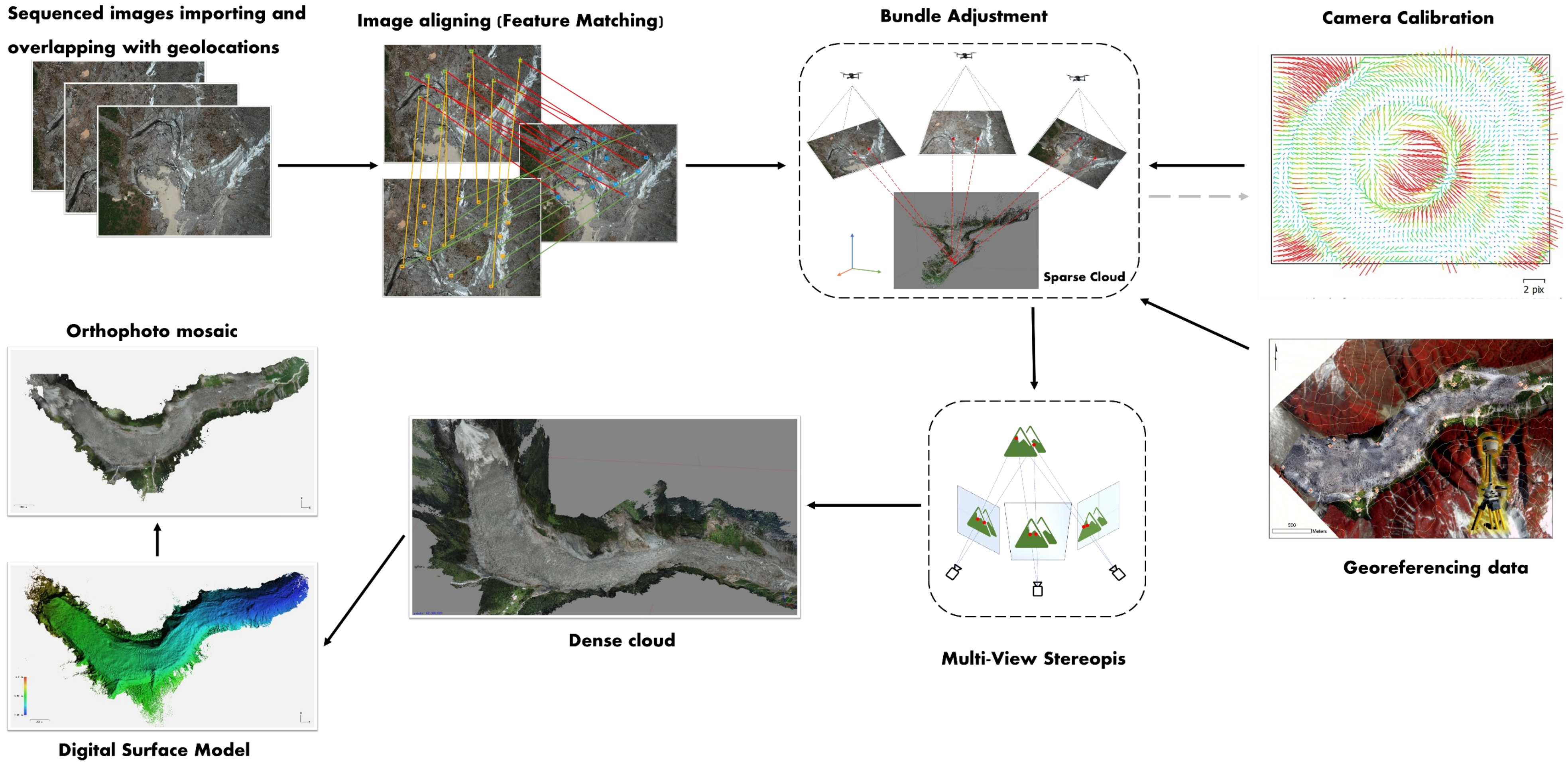

Figure 4.6 The principle of Structure from Motion with Multi-View Stereo in the reconstruction of HLG Glacier surface.

4.3.2 Mapping of landform features

The primary datasets for the mapping were the orthophoto mosaics derived from UAV datasets (see Table 5.1 and Table 6.1 for the details of UAV-derived datasets). Their sub-decimetre spatial resolution provided an unprecedented view of the evolving glacier geomorphology, and the opportunity to characterize landform features in exceptional detail (Chandler et al., 2018; Fu et al., 2013). The georeferenced orthophoto mosaics were imported to ArcGIS to digitize glacial geomorphic features by visual interpretation, such as glacier terminus extent, calved or collapsed area, ice cliffs, ice crevasses, marginal fresh ice, proglacial river/ponds, periglacial vegetation, supraglacial ponds, and lateral landslides. To ensure the precise interpretation of the features, the three-dimensional scene of the dense point clouds and DSMs were consulted in cases of ambiguity, such as where the boundary between marginal ice cliffs and the valley walls was unclear, or where the orientation of ice cliffs was vertically variable. The use of multiple viewing perspectives in this way is important because three-dimensional viewing can provide information on the structure and morphology of the features, which is not always immediately apparent from the two-dimensional perspective.

Identification and mapping of the landform feature depend on the premise that the landform features have distinctive traits that can be used to extract and categorize them (Chandler et al., 2018; Fu et al., 2013; Schneider et al., 2021). A variety of factors affect how the criteria of feature identification and extraction are defined, including the mapping extent, means of data acquisition, the methodology of mapping, the evolution pattern, and the life cycle of targeted landform features, as well as the aims illustrated by the final map productions. Many of glacier-related features can be classified based on variable interpretation and mapping criteria and many studies have illustrated their mapping strategies, for example, the mountain glacier glaciomorphological features classifications (Figure 4.7) by Shi et al (2011).

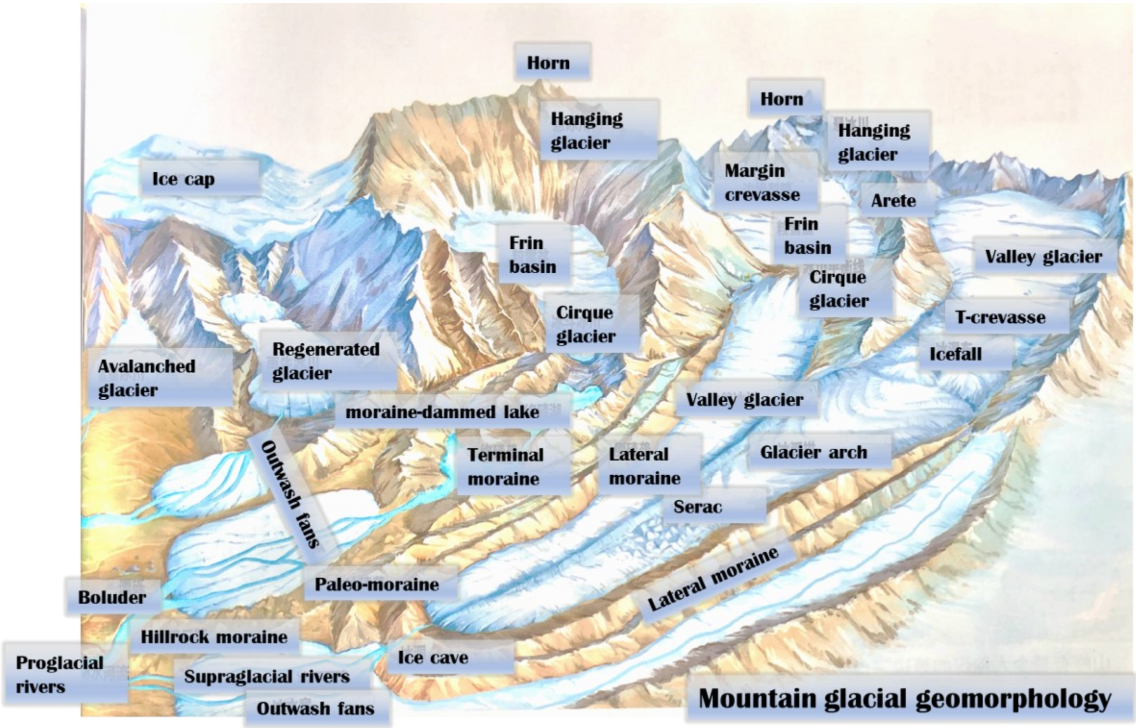

Figure 4.7 Geomorpholoical feature classification of mountain glaciers (modified from Shi et al (2011))

From the DSMs and orthophoto mosaics, the primary geomorphological features were visually interpreted and manually mapped, for example, ice crevasses, ice cliffs, trim-line, faults, supraglacial ponds, proglacial rivers, etc. To ensure the precise interpretation of the features, the 3D scene of the corresponding dense point cloud and DSM were consulted in cases of ambiguity, such as where the boundary between marginal ice cliffs and the valley walls was unclear, or where the orientation of ice cliffs was vertically variable. The use of multiple viewing perspectives in this way is important because 3D viewing can provide information on the structure and morphology of the features, which is not always immediately apparent from the two-dimensional perspective.

4.3.3 Glacier velocity field derived from Digital image correlation – Fast Fourier Transformation (DIC-FFT)

We also derived glacier flow fields from each pair of orthophotos (resampled to 0.25 m/pixel) because previous work has shown that the surface displacement can be strongly linked with frontal processes – in particular for the glacier frontal ice collapses (Che et al., 2020). The method based on DIC, also known as feature tracking, is frequently used to identify the movement of common features between subsequent images (Bickel et al., 2018; Heid and Kääb, 2012; Strozzi et al., 2002). Here we used an open-sourced DIC algorithm based on Fast Fourier Transform (DCI-FFT) (Bickel et al., 2018; Guizar-Sicairos et al., 2008). We employed a Wallis filter to mitigate the negative effect of unsteady lighting conditions in the glacier valley – based on a locally-adaptive contrast enhancement and filtered the outputs to remove noise and improve the aesthetics of the results (Figure 4.8).

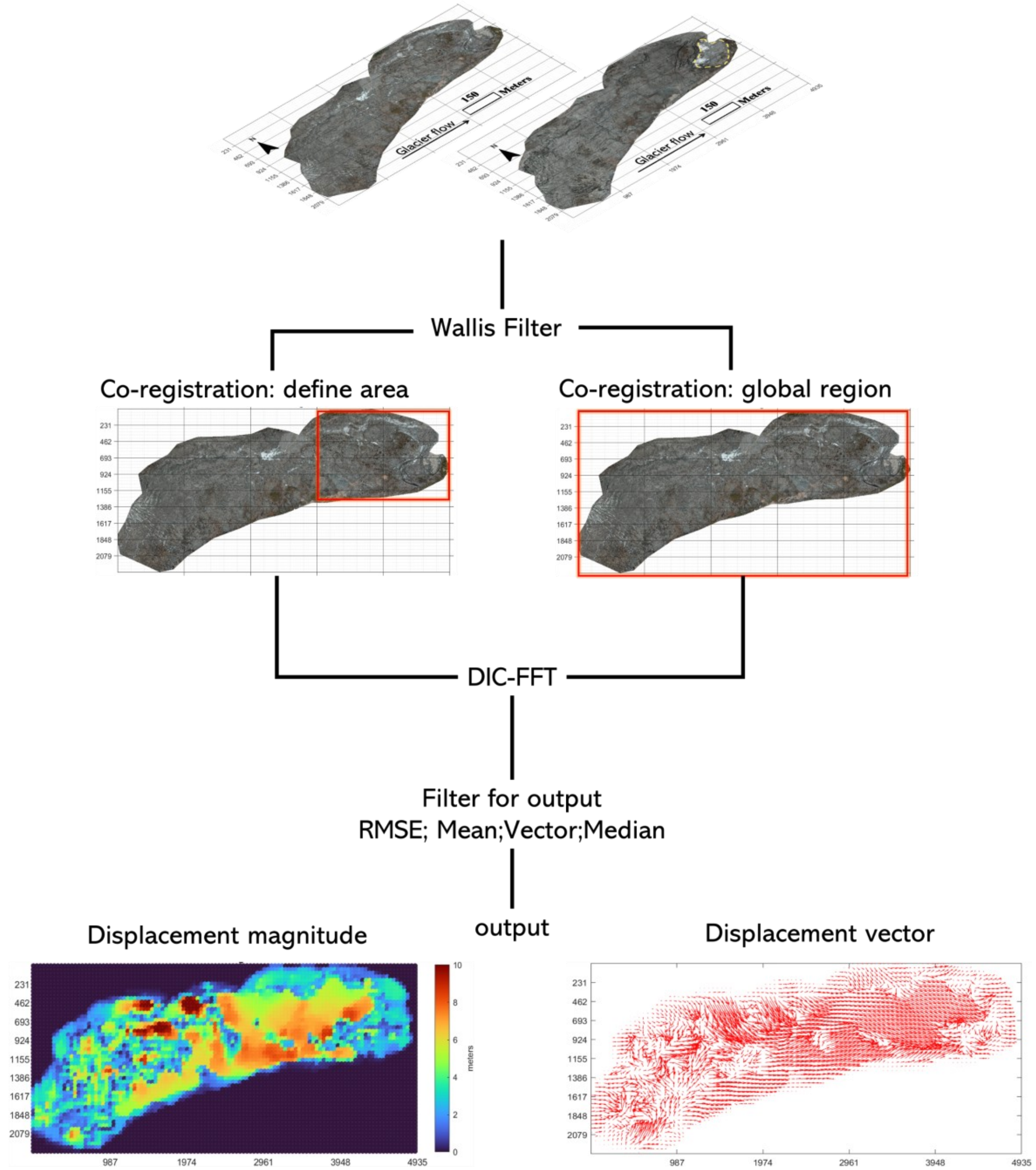

Figure 4.8 The workflow of DIC-FFT.

4.3.4 DEM of Difference (DoD)

Quantifying the surface elevation changes, and their corresponding volume changes is critical for evaluating the landform development. DoD Figure 4.9) represent a possible approach to tracking landform changes (Wheaton et al., 2009). We used the open-source software ***Geomorphic Change Detection*** (James et al., 2012; Wheaton et al., 2009) to compute the ice height changes and the corresponding volumetric variations. The eight DSMs were re-sampled to 0.5 m/pixel, as a compromise between maximizing information retention and computational efficiency. Seven DoDs were computed from these DSMs, to characterize surface changes between each of the field campaigns. We used the Minimum Level of Detection (MinLoD) as a threshold for distinguishing real surface variation from the noise (Fuller et al 2003). A conservative MinLoD of 0.5 m was identified based on the previously published rates of surface elevation change over subsequent ablation seasons.

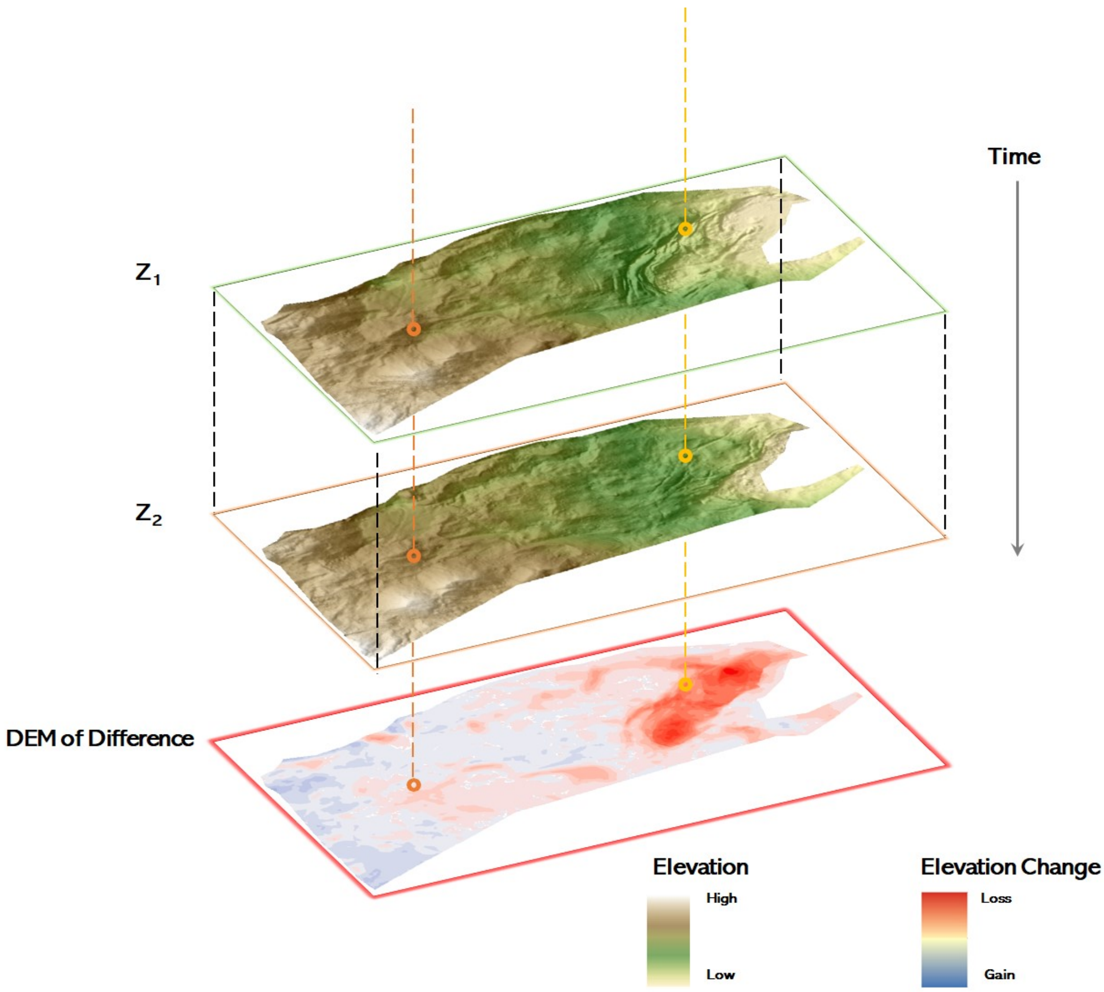

Figure 4.9 The principle of the methon of DoD.

4.3.5 Glacier extent extraction

Glacier extent extracted from glacier mapping using multispectral and multi-temporal satellite images is a well-established approach for monitoring glacier changes, and providing general information about a specific glacier or regional glaciers. The core objective of mapping glaciers is to present the morphology of glaciers with precision and credibility. This general information about glaciers is the major input parameter for most of the glaciological and related hydrological modeling, e.g., glacier extent, glacier area, glacier length, etc. Moreover, the reliability of this general information has significant in other disciplines, such as glacial hazard assessment, hydro-resources management, and regional climatic variation (Bolch and Kamp, 2005; Kaushik et al., 2019; Paul et al., 2016; Vasuki et al., 2014).

Satellite images provide more possibilities for observing glacier characteristics with rapidness, high effectiveness, and better visualization, which mitigates the difficulties that using ground-based approaches. Numerous studies have reported studies in relation to glacier characteristics at various time scales and spatial scales (Bolch and Kamp, 2005; Fahnestock et al., 2016; Li et al., 1998; Paul, 2000; Paul et al., 2016). Specifically, glacier extent and glacier terminus position are the widely-used and highlighted features for assessing the health status of glaciers (Cao et al., 2014; Urbanski, 2018).

With the improvements in observation technologies, e.g. satellite imagery resolution, iterations of Synthetic Aperture Radar Interferometry (SAR), the performance of pan-tilt systems and electro-mechanical system of drones and associated image processing algorithms, more complicated and detailed glacier characteristics can be recorded or derived, these include time-sequenced glacier surface elevation variation, spatial distribution of glacier surface velocity field, ice cliff density, supraglacial ponds identification, distinguishing debris-covered glacial area, ice thickness change and ice volume detection (Andreassen et al., 2015; Benn et al., 2012; Berthier et al., 2016; Farinotti et al., 2009; Herreid and Pellicciotti, 2018; Sun et al., 2017; Zhang et al., 2011). Not only mapping the glacier extent and the glacier terminus position but also providing various characteristics mentioned above in the glacier mapping, this multi-parametric approach has significance in assessing the comprehensive glacier health.

Hence, there are mainly two approaches involving glacier mapping from remote sensing data, which refers to manual and automated image processing. The manual image processing for glacier mapping initially starts from delineation with standard False Color Composites (FCC) of Landsat MSS, which is time-consuming and low-efficiency handwork. Manual processing may bring errors and biases to the mapping results due to the differences in subjective indexes in identifying and recognizing surface characteristics of glaciers, mainly relying on the expertise and experiences of the image interpreter. For another, the characteristics of the image scene are the additional factor that influences the accuracy of mapping, for instance, the cloud coverage, seasonal snow coverage, and hill shadow. Therefore, the manual image processing for differentiating the glacier area and non-glaciated area can be referred to as an integration of a standard layer stack of spectral bands with aid of image enhancement and terrain parameters. In order to determine the glacier terminus and glacier extent with reliable accuracy, some geomorphological features (e.g., ice cliffs at the terminus, proglacial waterbodies, and outlet of subglacial conduits) are needed to be identified for assisting purposes. So, choosing images from major ablation season months (e.g., May to October) and less cloud coverage (less than 10%) might be the best strategy. In conclusion, although manual images processing for glacier mapping is still regarded as labor-intensive work, it is used widely in glaciation studies when the typical high grade of mapping accuracy is demanded.

Automated image processing for glacier mapping provides glaciologists with fast and reliable approaches. For instance, the multi-band/single ratio method (e.g., the normalized index of snow or vegetation) might be the most effective and well-established way for glacier mapping, which has been reported as rapid and robust with high reproducibility. For clean ice, it can be easily differentiated by relying on the differences in reflectivity between visible/NIR and SWIR. Moreover, under the various surrounding settings, the Normalized Difference Snow Index can be used to distinguish the slight debris-covered ice from clean ice aided with slight changes to the band ration threshold. Furthermore, it is still challengeable for debris-coved glaciers (e.g., HLG Glacier or other glaciers in the southeastern Tibetan Plateau) to map their glacier extent, glacier terminus, or other detailed surface characteristics due to the annoying in distinguishing the supraglacial debris from periglacial debris and lateral debris. Therefore, it might be impossible to complete debris-covered glaciers by satellite image alone so that it may be figured out by using add-in approaches such as unsupervised/supervised classification, combined with other datasets (e.g., thermal data, vegetation data), object-oriented image analysis, etc.

In this study, visual interpretation and manual mapping are the primary methods in the glacier extent extraction. For the extraction of HLG Glacier outlines, it is challenging for distinguish the exact glacier surface from the lateral and frontal margins as the HLG Glacier is a partly debris-covered glacier, especially for the relatively thick debris-covered glacier snout. The primary of dataset for the glacier extent extraction was collected from PlanetScope image with a spatial resolution of 3 m. Although PlanetScope images have high spatial resolution and temporal resolution, it is not reasonable to visual interpret the glacier outlines. Therefore, a reliable delineation of the outline of the HLG Glacier requires additional consultancies. There are five aspects can be used to assist the extraction of HLG Glacier outlines (see Section 7.3 for details), that is, 1) Observations from field trips; 2) UAV mapping results; 3) False color composite (FCC): FCC images can provide distinguished texture and pattern of vegetation from other surface features. here, near infrared, red and green bands were used to generate the FCC images; 4) Normalized Difference Water Index (NDWI); 5) The spatial distribution of the lateral ice crevasses.

4.3.6 Satellite-based stereo-photogrammetry: NASA Ames Stereo Pipeline

4.3.6.1 Satellite-based stereophotogrammetry

When two or more images for the same area are captured from a different angle of view successively, the geometric information for the mapping area can be extracted based on the principle of a stereoscope, just as scenes are acquired by naked eyes and 3-dimensional information are reconstructed in the brain.

Satellite-based stereo-photogrammetry is based on the same principle, while using a stereo-pair of satellite images (i.e., pairs of images focusing on the same area from different viewing angles) (Beyer et al., 2018; Shean et al., 2016). As shown in Figure 4.10, in an ideal model, two points are marked with A and B, indicating a higher elevation location and a lower elevation location, respectively. In the right image, a and b indicate the locations for each point (i.e., A and B) recorded on the principle of the camera sensors. In the left image, a’ and b’ mark the location of each point (i.e., A and B) recorded on that image with the satellite flying from T1 to T2. Due to the sensor has moved, a and a’ are different spots on the image, and again b and b’ are different. From the perspective of measurements, the distance between a and a’ is greater than that between b and b'; and the reason for that is A is closer to the satellite than B. Therefore, these distances illustrate the information of geometry about the satellite to each point and the altitude of each point also called the parallax. However, in the real world, deriving the geolocations of A and B, or the elevation model of the entire surface needs more and rigorous external restricts, for example, the accurate relative positioning of two images (i.e., locating enough identifiable surface features), the position and orientation of the satellite when capturing two images (i.e., locations in the space provided by the onboarded GNSS instrument), and the internal structure of the camera sensor (i.e., details of the camera provided by the equipment manufactures).

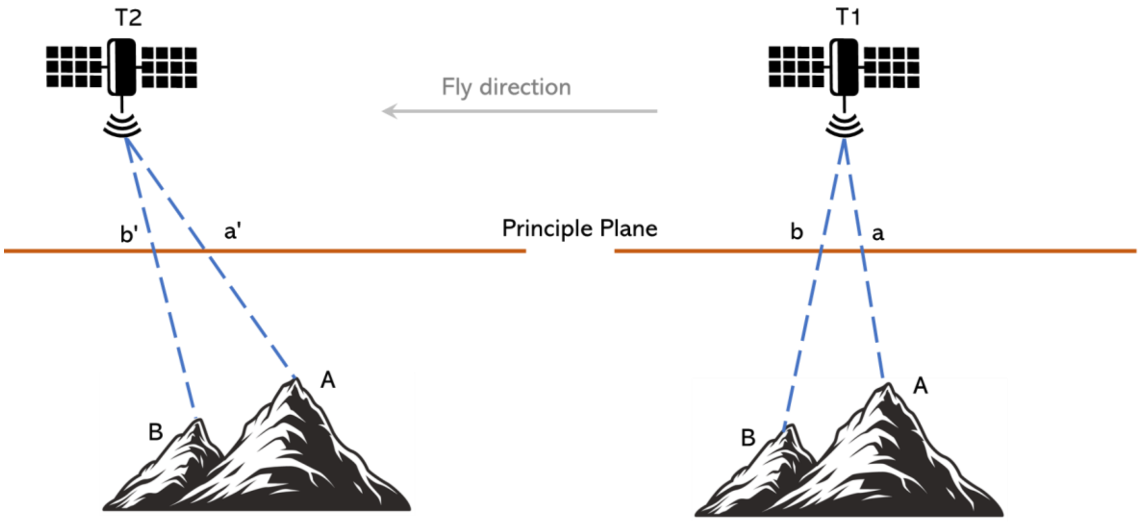

Figure 4.10 An illustration of changes in pairs of stereo images between two positions.

4.3.6.2 NASA AMES Stereo Pipeline (NASA ASP)

NASA AMES Stereo Pipeline (ASP; version 3.1.0) is a set of open-sourced, automated toolkits for the derivation of 3D geometric information from satellite optical images (or other sourced visual images) by stereophotogrammetry (https://github.com/NeoGeographyToolkit/StereoPipeline/). NASA ASP contains a series of functions, aiming to help operate and process terrain information and conduct mapping missions, such as reprojections, geo-registration, extraction of camera postures and adjustment, format transformation, and data exporting and visualizing (Shean et al., 2016). Currently, NASA ASP is able to process most of the Earth-orbiting imagery datasets.

Reconstructing the terrain from images based on ASP stereophotogrammetry can be described as the following steps (Figure 4.11; Shean et al., 2016).

1) ***Inputs:*** the inputs for the reconstructing process are two images focusing on the same area from different points of view. Here, two images refer to the ASTER_L1A 3N and ASTER_L1A 3B. These two sub-bands can be extracted from ASTER_L1A data by the function of *aster2asp* directly.
2) ***Pre-processing:*** raw data delivered from the sensor is complicated so that it might be unsuitable to import directly to the ASP for the next stereo processing: for example, the issues related to sensing instrument (i.e., read-out noise, flat fielding), issues related to the position of the camera sensor in the space and issues related to the mapped complicated landscapes in the sensed frames. Most of them need an approximate camera model or even a rigorous camera model to remove these internal artifacts. Fortunately, most instruments have detailed information about the camera model, also known as the camera intrinsic parameters. These parameters should be applied to correct and refine the data before conducting the stereophotogrammetry. In this case, the rigorous camera model and the camera extrinsic parameters (i.e., camera position and camera pose) of ASTER L1A images have been written in the metadata file and can be extracted by the function aster2asp (i.e., ASTER L1A 3N/3B. xml).
3) ***Image aligning:*** considering the computational efficiency in conducting the stereo algorithm, it is necessary to perform alignment for images to narrow down the calculation of searching corresponding points between two images that are used in the stereo pipeline. In the default setting, the ASP uses the affined epipolar-based method, which applied the affine transformation to both left and right images. Moreover, the more advanced approach is reprojecting the left and right images onto a DEM of the coarse resolution, which enhances the similarity between the left image and right image and improves the correlations. Here, we use the NASA DEM to perform the alignment by applying the function of *mapproject.*
4) ***Stereophotoprammetric processing:*** this is the core part of the ASP. This is a set of algorithms for computing corresponding relations between the left image

and the right images. The image correspondence in ASP is called disparity maps. The algorithms are initially conducted with down-sampled input images. Next, they will be split into several blocks for pyramidal processing and the stereo results will be refined based on that.

5) ***Subpixel refinement:*** generally, once the disparity maps have been produced, the corresponding relations of pixel to pixel between left and right images have been confirmed. Following the triangulations can be performed to reconstruct the stereo-geometry. However, the quality of results from the triangulation cannot be guaranteed at this stage, therefore the correspondence needs to be subpixel level refinement to further improve the quality of stereophotogrammetry. In the latest version of ASP, there are 12 modes of subpixel refinement. The commonly used and rapid method of subpixel refinement is based on parabola-fitting, but this method cannot solve the pixel-locking issue. The parabola-fitting method is mainly used for the purpose of quick DTM generation. The reliable approach is the method based on the Bayes expectation-maximization (EM) weighted affine-adaptive window correlator. The Bayes EM can produce high-quality stereo-matched pairs with a very low level of noise. The Bayes EM subpixel refinement can be executed by the function of *subpixel (2)*.
6) ***Triangulation and DEM:*** after the completion of the rigorous correlations for both images, then the results will be converted to the 3D coordinates in the real world, which is exported as the format of point clouds. These point clouds can be converted into DEM by using the function of *point2dem.*

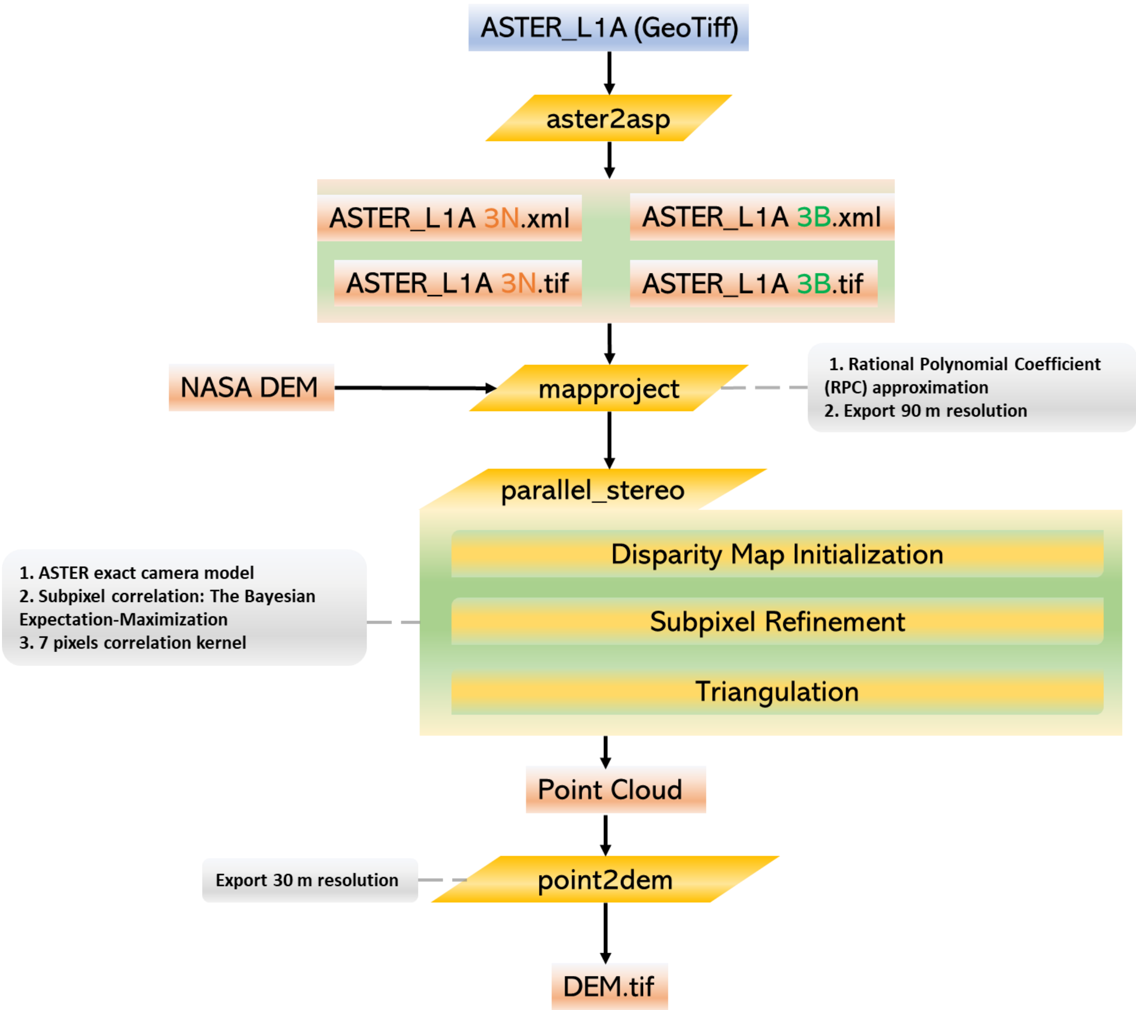

Figure 4.11 The workflow NASA AMES Stereo Pipeline.

4.3.7 Conversion from geodetic elevation changes to glacier mass changes

Geodetic measurements provide insight into the integrated changes in large regions and limited accessible glaciers, including surface elevation changes and volumetric changes. However, it only provides the volume changes through repeated surface geodetic surveying, which needs to be further converted to mass changes based on a predefined ice density (Huss, 2013). The study based on a simplified glacier model with ideal climate forcing and long-term mass balance data have revealed that the density of ice used for converting mass change to calculate the glacier budget is not a constant factor in most cases, and the conversion factor is usually smaller than the real ice density (Cogley, 2009; Huss, 2013; Magnússon et al., 2016). Many geodetic mass balance-related studies also indicate that the ice density assumption of 850 ± 60 kg m^{-3} is a suitable value for most conditions (Berthier et al., 2007; Brun et al., 2017; Hugonnet et al., 2021; Kumar et al., 2020; Magnússon et al., 2016; Maurer et al., 2019;

Taylor et al., 2022; Wang et al., 2014; Zhang et al., 2018). However, it needs to be noticed that the assumed value (i.e., 850 $\pm$ 60 kg m^{-3}) might be varied from 0 to 2000 kg m^{-3} for cases where the geodetic surveying interval is relatively small or a gradient of mass changes. Therefore, the geodetic mass balance changes can be calculated based on the following Equation (5) (Huss, 2013; Brun et al., 2017):

$$\boldsymbol{B_N} = \frac{\boldsymbol{\rho}}{\boldsymbol{S_g}} \sum_{\boldsymbol{i=1}}^{\boldsymbol{N}} \Delta \boldsymbol{h_i s_i} \qquad (5)$$

where $\boldsymbol{B_N}$ is the glacier mass balance; ρ is the assumed ice and snow density; $\boldsymbol{S_g}$ is the glacier ice surface area; $\boldsymbol{N}$ is the pixel quantity of DEM of the glacier; $\Delta\boldsymbol{h_i}$ is the differences calculated from DoD between two DEMs; and $\boldsymbol{s_i}$ is the cell size of a single pixel and it equals the spatial resolution of the ASTER-derived DEMs (i.e., 30 m).

Chapter 5: Mapping of Hailuogou Glacier tongue

5.1 Introduction

Mountain glaciers all over the world have been receding at an unprecedented rate during the last decade (2010-2020) interpreted by the satellite and in-situ observations (Zemp et al., 2015), and they will continue to lose mass for further decades with predicted climate warming (IPCC, 2022). Many studies associated with mountain glacier changes have reported a substantial shrinkage of the glaciers in the southeastern Tibetan Plateau since the 1980s (Li et al., 2010; Liu et al., 2010). The sustained ice loss of glaciers in southeastern Tibetan Plateau has a clear impact on regional water supply and eco-environmental systems (Jouberton et al., 2022; Yang et al., 2013).

Persistently accelerated glacier mass loss may induce rapid changes in glacier dynamics, such that stresses and strain within the glaciers are redistributed in response to the mass perturbations, which then further alters the glacier structure (Azzoni et al., 2017). Rapid evolution in glacier dynamics forms a series of distinctive features on the glacier surface, and in the proglacial zones (e.g., crevasses, ice cliffs, proglacial rivers and vegetations). The analysis of the formation and development of these features can provide insights for improving the short- and long-term projection of glacier evolution in the context of global climate change (Benn et al., 2017).

HLG Glacier is a rapidly retreating temperate valley glacier in southeastern Tibetan Plateau with a disintegrating terminus. Several studies have investigated the recent changes of HLG Glacier from the perspective of changes in the glacier geometry, glacier ice temperature, mass balance and glacial hydrology (Li et al., 2010; Liao et al., 2020; Liu et al., 2010; Zhang et al., 2010, 2011; Zhong et al., 2022). However, there are few detailed studies that characterize the evolution of the surface features. In this study, we provide detailed mapping results for the HLG Glacier tongue using UAV photogrammetry. The aims are to 1) map the glaciological, hydrological and geomorphological features of the lower part of the HLG Glacier valley (i.e., lower part of the glacier tongue, proglacial/paraglacial zones) through the high-resolution ortho-mosaics derived from UAV images collected in 2018, 2019, 2020 and 2021; and 2) discuss the spatiotemporal evolutions of the HLG Glacier from 2018 to 2021 based on the changes in particular features (e.g., ice crevasses and ice cliffs).

5.2 Digital surface models (DSMs) and orthophoto mosaics

5.2.1 RAW data and SfM-MVS processing

Four field trips to HLG Glacier were conducted during the ablation seasons from 2018 to 2021 (Table 5.1). The first three surveys (June 2018, October 2019 and September 2020) used a DJI Mavic Pro (12.71 megapixels for the camera sensor), and the fourth survey (July 2021) used a DJI Mavic Pro 2 Enterprise Advanced (48 megapixels for the camera sensor).

Table 5.1 Spatial resolution for DSMs and orthophoto mosaic, and Z error and total RMS errors in alignment for each dataset

No.	Date (YYYY/DD/MM)	Photo aligned	DSM (m/px)	Orthophoto mosaic (m/px)	Z error (m)	Total errors (m)
1	2018/06/30	2358/2358	0.36	0.09	0.63	0.81
2	2019/10/03	2755/2757	0.35	0.09	0.39	0.90
3	2020/09/05	2290/2298	0.07	0.04	0.42	0.94
4	2021/07/18	1216/1217	0.18	0.05	Benchmark	Benchmark

Flight missions differed with launch sites and flying heights as the surface elevation of the glacier tongue ranged from 2920 m a.s.l. (i.e., the glacier terminus of 2021) to 3900 m a.s.l. (i.e., the bottom of the glacier icefall) with consistent ground sample resolution. The glacier tongue was mapped separately with four gridded blocks and the UAV was launched from three sites as shown in Figure 5.2. The onboard camera was maintained in a nadir viewing angle for ortho-photogrammetric mapping with a lateral overlap and longitudinal overlap of 70% and 80%, respectively. The flight missions were pre-programmed and conducted in automatic mode. Each UAV survey has a total length of 60 km flight path, taking around 1.5 hours in flight duration to cover the entire glacier tongue in each case. The mapping area was divided into four gridded flight paths and covered separately with variable flying elevation in order to keep constant ground sample resolutions. Specifically, the glacier tongue was divided into four elevation bands for UAV mapping and further analysis of feature changes: < 3100 m a.s.l. (Sector 1), 3100 – 3300 m a.s.l. (Sector 2), 3300 - 3500 m a.s.l. (Sector 3), > 3500 m a.s.l. (Sector 4) (Figure 5.2). Nearly 8900 images were acquired in the four flight missions. Additional images captured by manual operation were needed depending on the unsteady weather and lighting conditions in the glacier valley.

Multitemporal ortho-mosaics and digital surface models (DSMs) were produced based on SfM-MVS in Agisoft Metashape Pro v1.5.3 (Agisoft LLC, 2020). We followed the SfM-MVS workflow (Figure 5.1) as described by other studies in detail (Bash et al., 2018; Chudley et al., 2019; Mallalieu et al., 2017; Rossini et al., 2018; Smith et al., 2016). Tie-points were extracted from the 2021 dataset for co-registration with the earlier three datasets (i.e., all root mean square errors < 0.94 m; refers to Table 5.1). All orthophoto mosaics were then resampled to 0.1 m/pixel for subsequent visual interpretation and analysis.

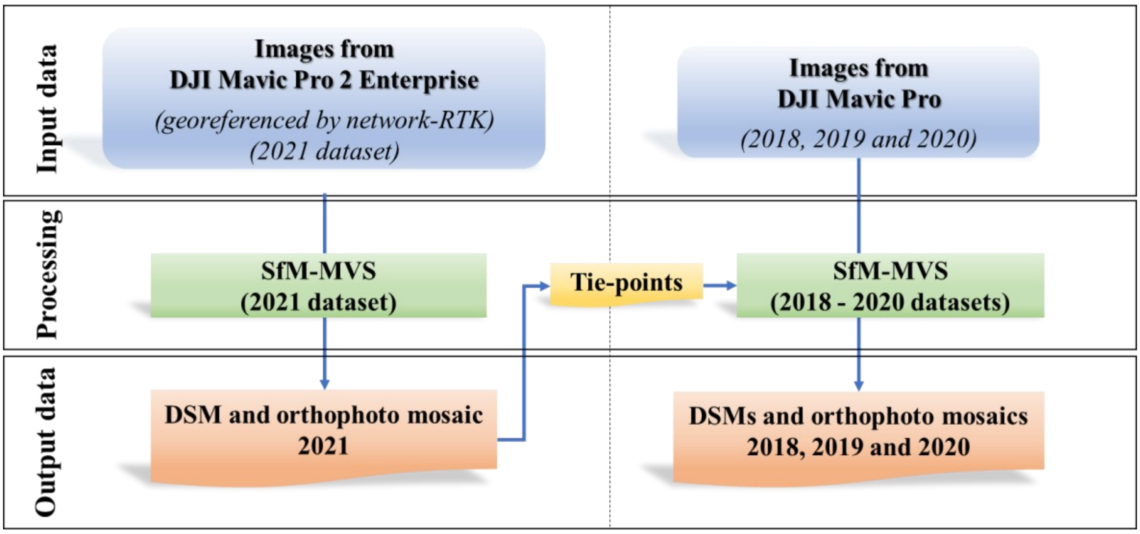

Figure 5.1 Workflow of UAV image processing was applied to datasets of 2018, 2019, 2020 and 2021 to derive the DSMs and orthophoto mosaics. Tie-points were extracted from the datasets of 2021 and then used for co-registering with 2018, 2019 and 2020 datasets.

5.2.2 Co-alignment of datasets

For the most recent (2021) survey, we benefited from an external real-time kinematic plug-in, and therefore achieving high accuracy photogrammetric mapping without external ground control points from GNSS equipment. The real-time kinematic plug-in records the coordinates with a mean root mean square error of 1 cm + 1 ppm (i.e., 1 ppm means the error has a 1 mm increase for every 1 km of movement from the drone) horizontally and 1.5 cm + 1 ppm vertically (Zhong et al., 2022). Accordingly, we considered the most recent dataset as the benchmark and extracted 33 points that are easily identifiable and stable surface features from it as the tie points (Figure 5.1).

5.3 Criteria of feature identification and mapping

The evolution and spatial distribution of features in the glacier valley result from the varying controls on glacier motion, glacier hydrology, erosion, deposition, surrounding topography and ice thermal regime. Representative features need to be predefined to characterize the changes in the glacier valley. To achieve this, I classified the features into four categories: (i) Glaciological features related to structural deformation of glacier ice and surface motion; (ii) hydrological features associated with the transport of meltwater and external water; (iii) geomorphological features in relation to effects of past glaciations; (iv) other landforms in the valley (Figure 5.3).

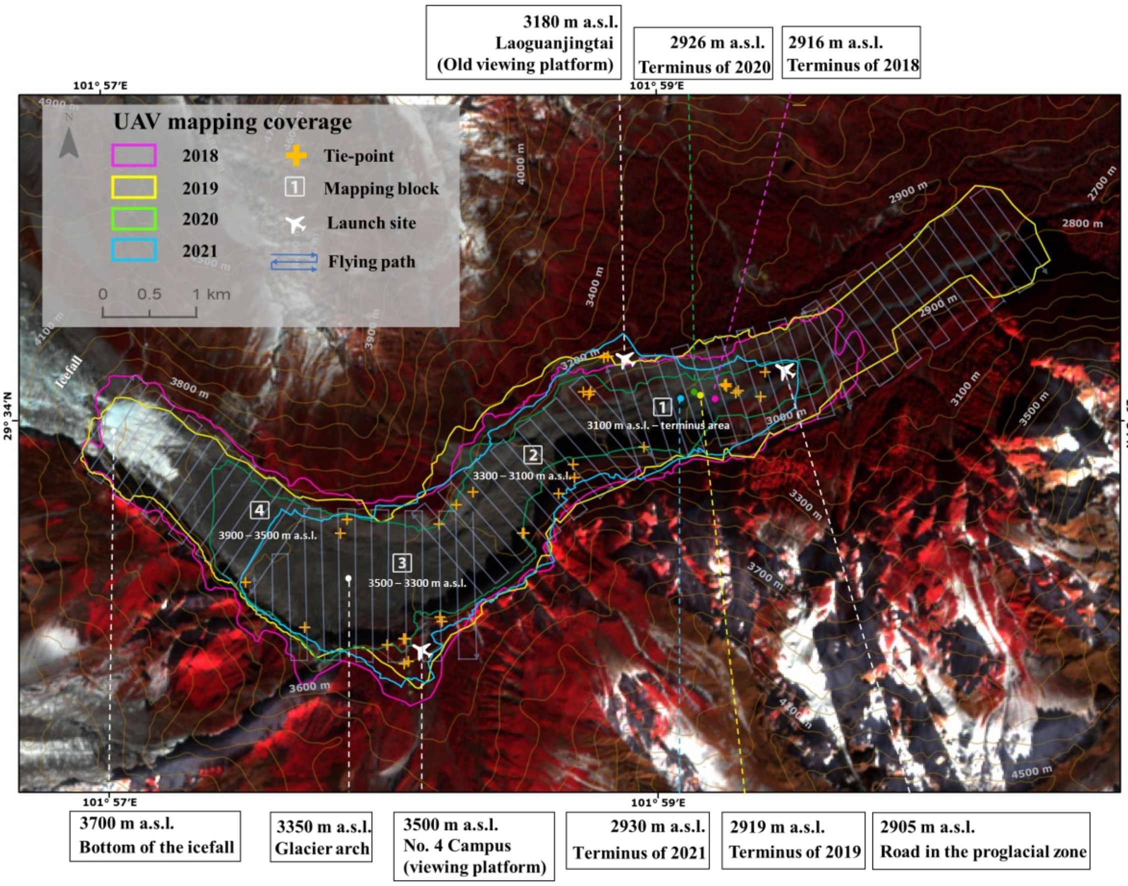

Figure 5.2 The spatial coverage of four UAV mapping areas and their elevation ranges, the distribution of the tie-points, the flight pathways, and the locations of three launch sites.

5.3.1 Glaciological features

a) Crevasse

Crevasses are open cracks in the glacier ice formed by changing stress as the glacier flows (Colgan et al., 2016; Jennings et al., 2016). The spatial distribution of crevasses provides information on the adjustment of stress and strain within the glacier

(Goodsell et al., 2005; Jones et al., 2018). Once the stress exceeds the critical threshold (i.e., the strength of ice body), the ice fractures to form ice crevasses with different widths, lengths, and orientations, marking significant evidence of glacier changes (Benn and Evans, 2013; Vaughan, 1993).

Crevasses dominate the HLG Glacier tongue. Crevasse lengths range from less than a meter to more than 130 m, and the widths are consistently less than 10 m. We identified them by the generally curved dark cracks and mapped as polylines. Although crevasses have different widths and depths, we only mapped them along their long axes (Figure 5.3A). Their morphology changes along with the glacier longitude profile. For instance, crevasses in the upper section of the glacier tongue appear as relatively long and splaying, aligned with low spatial density. The uppermost crevasses were orientated parallel with the direction of glacier flow. Conversely, in the middle section of the glacier tongue, the orientation of the crevasses was transverse to the direction of the glacier flow. In the lateral margin of the glacier, the crevassed surface may be formed by rotational strain within the ice along the edges. The morphology of ice crevassing is affected by the existence of water to some extent (Sakai et al., 2009), particularly for the regions of the inlets of streams from the higher elevation of the valley walls. The ice here becomes more fractured, resulting in more crevassed areas surrounding the inlets.

b) Ice cliffs

Ice cliffs are commonly described as (sub-) vertical ice walls, usually found around the margins of supraglacial ponds (Watson et al., 2017). For debris-covered glaciers, ice cliffs may be formed in two processes (Kirkbride, 1993; Kirkbride and Warren, 1999; Sakai et al., 2002), specifically, the first process is resulted from the sliding of supraglacial debris due to a steepening slope; the second is associated with surface depressions caused by roof collapse of a subglacial or englacial channel.

Here, we delineate ice cliffs as exposed ice faces with either clean ice or dirty ice (i.e., slightly thin debris on the surface) (Watson et al., 2017) (Figure 5.3B). Ice cliffs are apparent and the majority of them are observed as linear banded, crescent-shaped, and half arch-shaped bare glacier ice surrounded by relatively thin debris mantle. There are two patterns of ice cliffs on the HLG Glacier tongue by the philosophy of ice cliff formation (Sakai et al., 2002). A large amount of linear banded and crescent-shaped ice cliffs was identified on the lower section of the glacier tongue. The ice cliffs in this region might be formed by the exposure of the subglacial channels or voids due to the intensified glacier surface lowering (Li et al., 2010). The remaining ice cliffs were distributed across the upper section and lateral sides of the glacier tongue; most of them were exposed by debris sliding as a consequence of a steepening surface or ice crevassing.

c) Inter-crevassed blocks

Inter-crevassed blocks (Figure 5.3C) refer to a cluster of highly fractured ice bodies where seracs develop between crevasses (Jennings and Hambrey, 2021). The inter-crevassed blocks of the HLG Glacier are found at the north lateral margin (i.e., 3250 m a.s.l.). Here, there is a lateral stream flowing from the higher elevation into the lateral margin of the HLG Glacier. The continuous effect of external water on the glacier ice gradually erodes the surface. The inter-crevassed blocks on HLG Glacier were most likely formed by spatially variable glacier dynamics as well as the effects of frequent and persistent water activity.

d) Features associated with icefall

The icefall (i.e., 3650-4980 m a.s.l.) transports the ice mass down-valley, controlled by the rapid extrusion of ice flow and disorganized ice crevassing (Zhang et al., 2010). In the zone between the base of ice fall and the upper part of the middle section of the glacier tongue, which is also the transition zone of extending and compressional ice flow, there are particular features mainly associated with avalanches of the icefall, namely fresh ice, an ice fan and thinly debris-covered ice (Su et al., 1996) (Figure 5.3D).

These three features show a clear spatial pattern (see example in Figure 5D). Specifically, the uppermost portion is fresh ice, most of which is composed of ice chunks with a long axis of 1-2 m. Fresh ice can be identified by its white color, and the avalanche trace can be roughly identified consequently. Exterior to the fresh ice is a fan structure formed by successive avalanches (and subsequent melting) of ice. This fan-shaped structure is distributed in a tongue-like pattern, with a length of ~1000 m and a width that traverses the entire glacier. It is primarily composed of the varied size of firn and ice, with a mixture of ice and rock, yielding them gray and yellow-white in color. Below the fan-shaped structure is the ice surface with a thin debris cover, which can be considered as the transition zone between clean ice and the debris-covered surface.

5.3.2 Hydrological features

a) Supraglacial pond

Supraglacial ponds (Figure 5.4A) plays an important role in the hydrological system of the glacier (Reynolds, 2000). Supraglacial ponds generally form in natural depressions and are fed by meltwater from the glacier surface drainage system or local melting (Watson et al., 2016; Yang and Liu, 2016). Ablation is highly spatially variable according to the varied thickness of the debris mantle. This difference in ablation between debris-covered ice and debris-free ice often creates an undulating topography with natural pits in which meltwater can collect (Lardeux et al., 2016). After the formation of supraglacial ponds, the meltwater stored by these ponds promote ablation to facilitate the edges becoming steeper, such that the debris cover thins, and ablation is further enhanced in a mechanism of positive feedback (Miles et al., 2017). Some supraglacial ponds might drain out following hydrofracture (Liu et al., 2018). Their life cycle is short due to the rapid thinning of the glacier tongue and frequent collapse of subglacial channels, so their existence may not persist between sequential surveys. The supraglacial ponds mainly distributed in the lower patch of the glacier tongue (i.e., areas lower than 3500 m a.s.l.), with some outward ice cliffs and some lateral crevasses.

b) Stream

The HLG Glacier has a well-developed hydrological system in its lower ablation region (Liu and Liu, 2010). External waters from higher elevations flow into the drainage system within the glacier and discharge through the subglacial channel outlet along with the meltwater, forming the proglacial river. The majority of streams (Figure 5.4B) on the study site were defined as the streamflow at the lateral side of the glacier valley from the higher elevation and some of them were additionally fed by the nearby small glaciers.

c) Proglacial waterbody

Proglacial waterbodies of the HLG Glacier (Figure 5.4C) include the proglacial river and proglacial ponds. The proglacial river is not only the main force eroding the proglacial zone and periglacial zone, but also the sources of sediments. The proglacial zone is shaped by the evolution of the proglacial river, which forms highly active braided stream networks (Jones et al., 2018). Proglacial ponds usually occur near the south and north side of the proglacial river. They are commonly seen as single water features or a series of circular intersecting ponds.

5.3.3 Geomorphological features

a) Lateral moraine

Moraine is the accumulation of till material that is laid down by glaciers or ice shelves (Benn and Evans, 2013). Glacial till refers to all loose sediments produced, transported, and deposited by the glacier. Glacial till is ubiquitous across the glacier system, and it includes every size of glacial sediment, from silt-sized glacial flour to large boulders. They mound to form a ridge of unsorted sediments called the end moraine, and the farthest end moraine is the terminal moraine for a glaciation. Lateral moraines (Figure 5.5A) refer to ridge-shaped marginal features commonly found along the lateral sides of the glacier valley (Fu et al., 2012). For HLG Glacier, the lateral moraine is distinctive, but it also needs to be carefully cross-compared with the orthophotos and DSMs to identify the glacier margin. The terminal moraine is absent, so, this area is therefore mapped as proglacial till.

b) Glacial polished rock wall

Polished rock walls (Figure 5.5B) are referred to as the glacial eroded lateral cliffs in the glacier valley. Polished rock walls in the HLG Glacier valley can be found on both lateral cliffs. On these walls, various glacial erosion trails can be identified, such as striae, grooves and fissures. Over the study period, the polished rock walls were mapped with varying-sized polygons due to the vegetation cover on the walls.

c) Trimline

The trimline (Figure 5.5C) is an almost horizontal linear landform feature usually found along the sidewalls of a glacial valley. It marks the higher elevation of the erosion by the former glaciation and serves as an indicator of the thickness of the previous glacier

(Li and Fu, 2019). During previous glaciations, the glacier advanced downstream and removed the vegetation on the surface by erosion. With the glacier retreating and the surface lowering, a series of distinct edges on the hillsides can be identified to separate the well-vegetated terrain from the poorly vegetated region (i.e., glacier-eroded area). Based on the sharp contrast of the color and textures on the slope, the trimlines in the HLG Glacier valley are particularly clear. Some parts of the trim-line were interrupted by lateral landslides due to the unsteady paraglacial slope.

5.3.4 Other features

Three other features in the glacier valley were also mapped, categorized simply as artificial lake, road, and vegetation. The HLG Glacier and its surrounding regions have been developed for tourism since 1987. There are even some constructions that can be identified near to the glacier terminus. In this study, we mapped the artificial lake and the impervious road. The colonization of vegetation expands rapidly in the HLG Glacier valley with distance downstream (Zhong et al., 2021). Patches of Abies fabri forests can be found on both sides of the glacier valley along the LIA accumulated lateral moraine. The regional climate of the HLG Glacier valley is characterized by warm and moist conditions, such that vegetation with shallow roots, such as mosses and shrubs, can soon occupy any newly exposed areas in the proglacial zones, lateral moraine, and some stagnant surfaces near the glacier lateral margin.

		Landforms	Example	Description	Interpretation	References
Glaciological landforms	A	Crevasses		Curved-shaped open dark cracks on the glacier surface. This is a ubiquitous feature across the glacier surface. Four main types on the Hailuogou Glacier: splaying crevasse, en-echelon crevasse, transverse crevasse and longitudinal crevasse (Jennings and Hambery, 2021).	The representative of the brittleness in the glacier dynamics and it is formed from the internal stress exceeding the ice strength. The pattern of crevasses varies depending on the internal force field. Mapped as polylines.	Colgan et al., (2016) Jennings et al., (2016) Jennings and Hambrey, (2021) Jones et al., (2018) Goodsell et al., (2005) Benn and Evans, (2013)
	B	Ice cliffs		Zonal bare (or thin debris-covered) glacier ice with crescent-shaped, semicircular-shaped, circular-shaped, half arch-shaped or linear banded structures.	Ice cliffs create spots with higher ablation rate than the surrounding debris-covered ice surface. They are usually formed by the depression of the ice surface induced by conduit's roof reduction, or the surface being exposed due to the deep slope and the glacier dynamics. Mapped as polygons	Watson et al., (2017) Sakai et al., (2002) Kirkbride and Warren, (1999) Kirkbride et al., (1993) Kneib et al., (2021)
	C	Inter-crevasse blocks		A patch of highly crevassed glacier surface, mainly affected by the external water supply from lateral higher elevation. The crevasses are centered at the inlet of the external runoff and organized in a radial pattern. The closer to the margin of the glacier, the more the ice is fragmented.	This set of crevasses is formed by the impacts of perennial runoff (fed by tributary glaciers within the valley). As a combined result of intense ablation and the external water, a highly and radially crevassed surface can be developed in the lower and middle parts of the tongues (i.e., thinned ice body). Mapped as polygons.	Jennings and Hambrey, (2021)
	D	Features associated with icefall	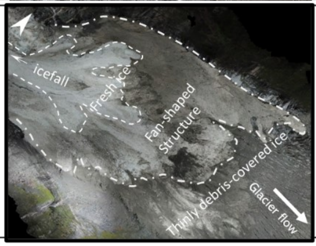	Fresh ice can be identified by pure white color and the avalanche traced can be consequently derived. The exterior fan-shaped structure is induced by ice avalanches and melting. The thinly-debris covered ice surface is below the fan structure. The color is progressive transition from pure white to gray-black.	The three fan-shaped features associated with ice debris avalanched from icefall show a progressive transition from icefall bottom to upper part of the ice tongue. Mapped as polygons	Su et al., (1996) Zhang et al., (2010)

Figure 5.3 Visual identification of glaciological features in the HLG Glacier valley.

		Landforms	Example	Description	Interpretation	References
Hydrological landforms	A	Supraglacial pond		Milky-coloured features, often approaching a circular shape, and surrounded by glacier surface debris	The major component of water storage on the glacier surface generally formed at depression area fed by the meltwater from the glacier surface drainage system or local melting. Mapped as polygons	Watson et al., (2016) Yang and Liu, (2016) Lardeux et al., (2021) Miles et al., (2017)
	B	Stream	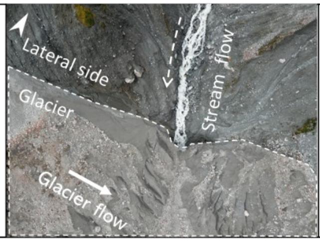	The alternative surface surface streams from the melting of upstream ice and higher elevation. The stream flows into the glacier from an inlet at the glacier lateral margins.	Perennial runoff (i.e., fey by small hanging glaciers in the HLG basin) and non-perennial runoff (irregular periodic runoff flowing from the conifer forest at the top of the valley cliff) coexisted in the valley. Mapped as polylines	Liu and Liu, (2010)
	C	Proglacial waterbody		Proglacial pond and proglacial river. Proglacial rivers are usually muddy with a milky or earthy color as they contain substantial volumes of glacial sediments. Proglacial ponds are relatively small and approaching a circular shape. The colors are clear and earthy-colored, probably due to their different formation mechanisms.	HLG Glacier has a perennial proglacial river discharging water from its hydrological system and it carries glacial deposits from the glacier erosion. Some clear proglacial pond may be kettles as the melted out of the isolated dead ice blocks. Some earthy-colored pond may be left by the variation of braided river.	Jones et al., (2018)

Figure 5.4 Visual identification of hydrological features in the HLG Glacier valley.

		Landforms	Example	Description	Interpretation	References
Geomorphological landforms	A	Lateral moraine	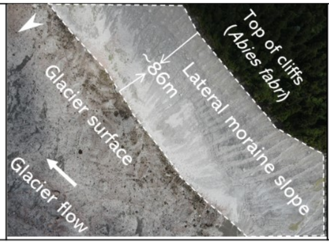	Lateral moraine of HLG Glacier is distinctive from its terminal moraine as some of them are well preserved. Ridge-shaped marginal features, commonly found along the glacier sides and consist of debris from the slope failure or the accumulation of paleoglacier surface.	The forest of *Abies fabri* can be found at the top of both of the lateral moraines, which is stable since Little Ice Age (Zhong et al., 2022). The height of lateral moraines to the present glacier surface ranges from ~80 to 160 m. A cableway connects the lateral moraines on it north and south sides. Mapped as polygons	Zhong et al., (2022) Benn and Evans, (2013) Fu et al, (2012)
	B	Glacial polished rock wall	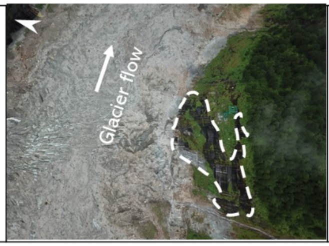	Faceted features, often found at the lateral side of the valley wall, with grooves and scratches of varying depth on the surface. Some of them are partly covered with vegetation.	The basin walls were progressively polished by the erosion of the glacier, and they left scrapes as traces of former glacier in eroding the walls, a trail of the dynamics of the paleo-glaciers. Mapped as polygons.	Darnault et al., (2012) Owen et al., (2008)
	C	Trimline	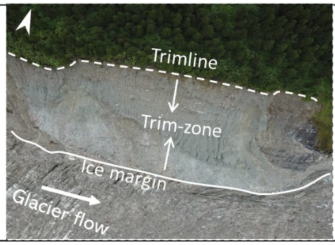	Linear feature along the sidewalls of the valley. A series of edges delineating the well-vegetated from poorly vegetated regions.	Denotes a former maximum extent of the glacier. Mapped as polylines.	Li and Fu, (2019)
Other	D	Artificial lake, roads, and vegetations	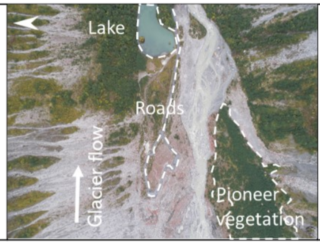	An artificial lake and roads located in the proglacial area. And pioneer vegetations occupied the proglacial zone and both of lateral sides of valley walls (i.e., herbaceous species). Abies fabri forests are steadily occupied the ridge sides of lateral moraines since LIA	Mapped as polygons	Zhong et al., (2022)

Figure 5.5 Visual identification of geomorphological features and others in the HLG Glacier valley.

5.4 Mapping results

5.4.1 Overall

The spatiotemporal changes of the mapped features were compared year by year. It should be noted that the two most recent maps (2020 and 2021) have limited data for Sector 4 (i.e., 3576 and 3521m a.s.l. for their upmost elevation, respectively). Therefore, only three Sectors (1-3) were used for the 2021 datasets, and elevations ranging from 3500 to 3576 m a.s.l. were taken as the extent of Sector 4 for the 2020 dataset. To illustrate ice crevasse orientation and ice cliff aspect, the eight cardinal and intercardinal points of the compass were used (Figure 5.6 and Table 5.2). Areal and surface elevation data for the four sectors of the glacier are illustrated in Figure 5.7A and Figure 5.7B, respectively. The statistical analysis for crevasses, and ice cliffs, is summarized in Figure 5.6, Figure 5.7C, and Figure 5.7D. Changes in supraglacial pond characteristics are listed in Table 5.3.

HLG Glacier has been in rapid recession during the observation period, as demonstrated by the areal decline of the lower part of the glacier tongue (Figure 5.7A). A decrease in surface elevation has been observed along the glacier center flowline (Figure 5.7B). Figure 5.7B demonstrates clearly that the glacier terminus retreated more than 300 m and the elevation of the terminus climbed from 2916 to 2930 m a.s.l. over the observation period.

Across the glacier tongue, ice crevasses and ice cliffs were the dominant glaciological features within each elevation section. At least four types of ice crevasse can be found over the glacier tongue, including chevron crevasses (e.g., the upper part of Sector 4), en-echelon crevasses (e.g., lateral zone of the lower part of Sector 4, and upper part of Sector 3), transverse crevasses (e.g., middle of Sector 3) and longitudinal crevasses (e.g., along the glacier flowline). The majority of crevasses were spatially clustered at several zones, such as at the bottom of the icefall, the middle section of the glacier tongue, the glacier terminus, and the lateral margin in particular. A few areas particularly impacted by the inlet of the lateral stream were also identified as being highly crevassed. However, the morphological pattern of crevasses is spatially heterogeneous along the glacier flow. While in some areas the crevasses were spatially clustered, they differed in their morphology longitudinally, determined largely by the direction of glacier flow.

Following here we describe the interannual change for the major glaciological and hydrological features.

5.4.2 Interannual change for the major features

Three major features, e.g., ice crevasses, ice cliffs and supraglacial ponds, were tracked to illustrate the glacier dynamics during the observation period. The crevasse density (km/km^2) and ice cliff density (%) are used to demonstrate the spatial distribution of crevasse and ice cliffs, respectively. Although the HLG Glacier experienced rapid recession from 2018 to 2021, some features, e.g., lateral moraines, trimline and glacial polished rocks in geomorphological features have not changed much so they were not included in the interannual analysis. The minimum mapping unit (MMU) for the ice crevasse, supraglacial pond, and ice cliffs is 0.5 m, 0.5 m^2 (50 pixels), and 1 m^2 (100 pixels), respectively.

5.4.2.1 2018 surface features

On the 2018 map (see Appendix map 1), ice crevasses mainly present a NE-SW orientation for Sectors1 and 2, while those in Sectors 3 and 4 are orientated NW-SE instead (refer to Table 5.2). Sector 4 has the highest crevasse density (i.e., 41.27 km/km^2), which was about twice as high as Sectors 2 and 3, and five-times higher than Sector 1 (see Figure 5.7C).

The density of ice cliffs reaches 17.74% in Sector 3, whereas ice cliff density in lower sectors do not exceed 13% (see Figure 5.7D and Table 5.4). NW and N are the dominant aspects for Sectors 1 and 2 (i.e., 36.96% and 27.21%; Figure 5.6 and Table 5.4), respectively, while W and SW are dominant in Sectors 3 and 4 respectively, with neither less than 23%. For the whole mapped region, NW and W are dominant in determining ice cliff orientation, adding up to more than 43% of the total.

5.4.2.2 2019 surface features

Crevasse directions exhibited in 2019 were largely consistent with those mapped in 2018. However, the total length of the crevasses declined by more than 10 km during the intervening period (Table 5.5). Crevasse density in 2019 reached the highest value in Sector 4, similar to that evident in 2018 (21.98 km/km^2) (Figure 5.7C). The overall density of crevasses for the entire glacier tongue during 2019 was lower by about 5 km/km^2 compared to the previous year (Table 5.5). The density of cliffs this year retained a similar pattern as to the 2018 map (Figure 5.7D), that is, Sector 3 had a maximum density of around 16%, followed by Sectors 2, 1, and 4 (all in excess of 7%).

For ice cliff aspect, the primary orientation was NW- and W-facing, with a range from 20 to 26% of all cliffs in these categories for Sectors 1 to 3 (Figure 5.6 and Table 5.4). However, SE-facing cliffs occupied about 26% of the total for Sector 4, exceeding all other orientations. As per the 2018 map, the dominant orientation overall was NW and W, occupying around 20% of all cases (Table 5.4).

5.4.2.3 2020 surface features

Here, elevations from the glacier terminus up to 3576 m a.s.l. were considered within Sector 4. The crevasse orientations of Sectors 1 to 3 are dominated by both NW-SE and NE-SE, and Sector 4 is also occupied primarily by NW-SE orientated crevasses (Table 5.2). Although the mapped region is less extensive than in 2019, the total length of mapped crevasses is about 35 km, more than 4 km longer than in 2019 (Table 5.5). Crevasse densities are largely consistent, ranging from 24.53 to 28.69 km/km^2 (Figure 5.7C). In contrast to the two previous maps, the highest density occurs in Sector 1, where the crevasses are concentrated at the glacier terminus and produce large ice cliffs.

According to Figure 5.6, cliff aspects of Sectors 1 to 3 are dominated by SW, N, and W-faced cliffs with about a ratio of 22%, while the minimum aspects are SE, E, and NE with a ratio of less than 6.53%. For Sector 4, the primary direction is similar to 2019 maps, that is SE. As a whole, the dominant orientation of 2020 is W (i.e., 20.65 %) and NW (17.06 %), whereas the fewest cliffs face NE and E.

5.4.2.4 2021 surface features

As there are no data for Sector 4 in 2021, we concentrate here on Sectors 1 to 3. The primary direction of ice crevasses is consistent with the 2020 map (Table 5.2). The total length of crevasses is 16.74 km, which is around 12 km, 7 km, and 10 km less than in 2020, 2019, and 2018, respectively (Table 5.4). The crevasse density of Sector 1 is high (38.59 km per square kilometer), which is comparable only to the value calculated for Sector 4 of 2018 (see Figure 5.7C). This illustrates the highly crevassed glacier surface near the glacier terminus. Further, the density of ice cliffs in Sector 1 is noticeably higher than in other sections, at around 24% (Figure 5.7D). The first and second primary directions for the ice cliffs are a combination of N and NW or NW and W. The cliffs with SE, E, and NE orientation are least common within the three sectors.

Table 5.2 The dominated orientation of ice crevasses for each elevation section

	2018	**2019**	**2020**	**2021**
1	NE-SW	NE-SW	NW-SE/NE-SW	NW-SE
2	NE-SW	NE-SW	NW-SE/NE-SW	NW-SE/NE-SW
3	NW-SE	NW-SE	NW-SE/NE-SW	NW-SE/NE-SW
4	NW-SE	NW-SE	NW-SE	-

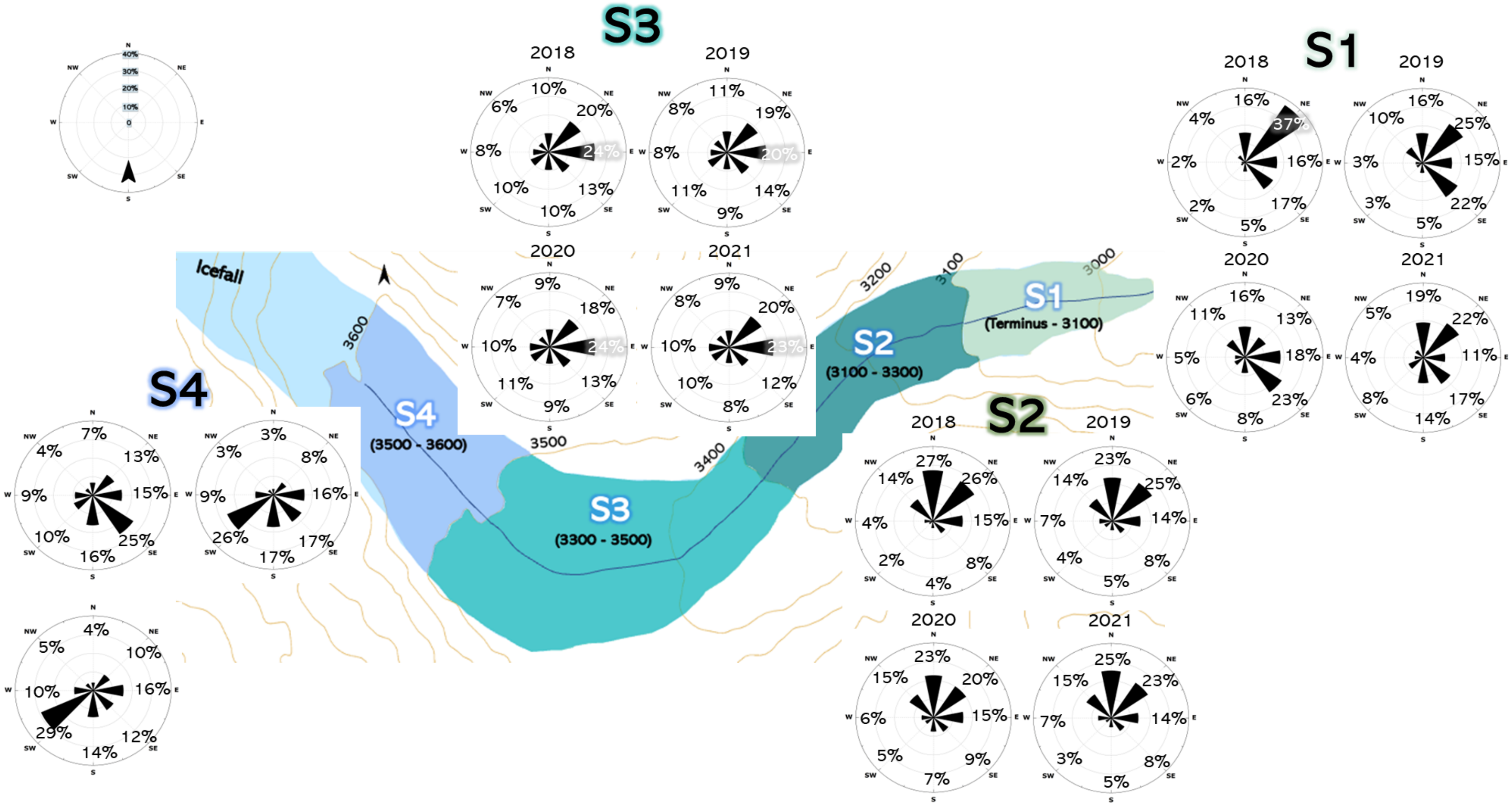

Figure 5.6 The ratio of each aspect (eight directions) of the ice cliffs in each elevation sector (unit: m a.s.l.).

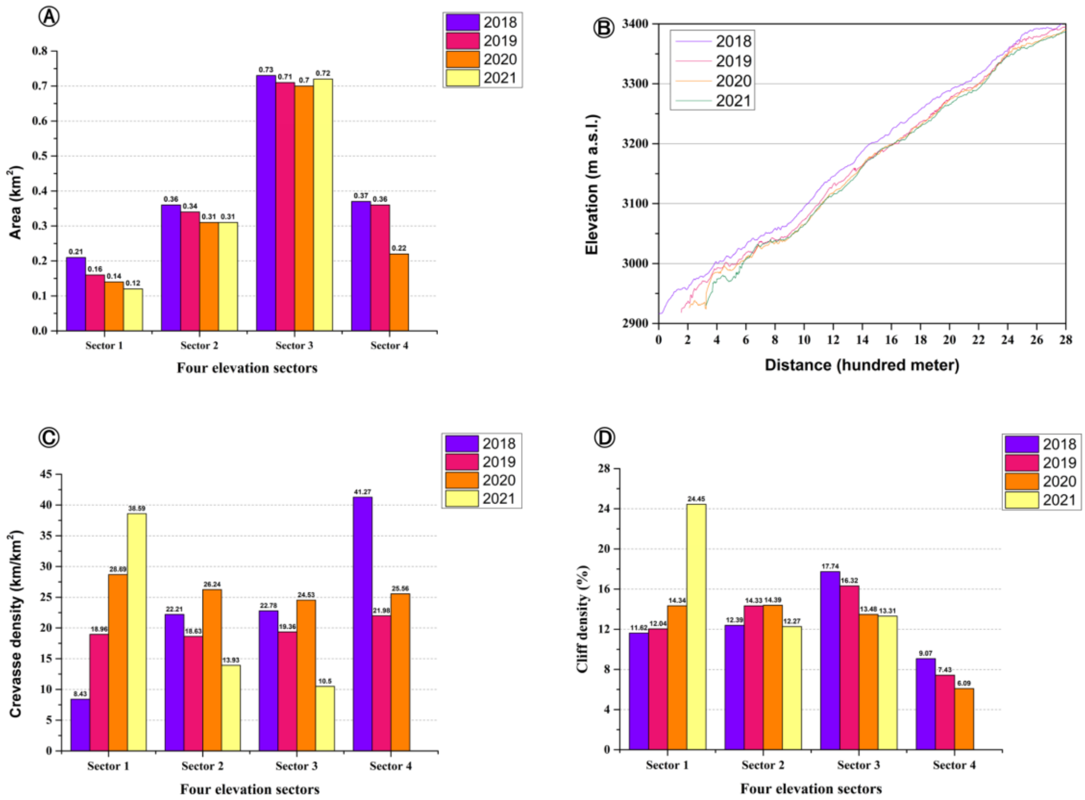

Figure 5.7 A: Annual area changes for each elevation sectors. B: Ice surface elevation along the glacier center flow line. C: Crevasse densities for four elevation sectors. D: Ice cliff densities for four elevation sectors.

Table 5.3 Summary of supraglacial pond for four elevation sectors

	June 2018		**October 2019**		**September 2020**		**July 2021**	
	Quantity	Area (m^2)	Quantity	Area (m^2)	Quantity	Area (m^2)	Quantity	Area (m^2)
1	11	735.49	5	239.22	3	67.42	1	6.02
2	19	453.23	9	111.49	23	118.47	20	463.24
3	50	804.18	52	1094.45	70	479.14	47	594.23
4	19	188.72	51	462.65	42	172.11	-	-
Total	99	2181.62	117	1697.81	138	837.14	68	1063.49

Note: The minimum mapping unit (MMU) for the supraglacial pond is 0.5 m^2 (50 pixels).

Table 5.4 The aspects of ice cliffs

	Max		2nd Max		Min	
2018	**Aspect**	**Ratio**	**Aspect**	**Ratio**	**Aspect**	**Ratio**
1	NW	36.96%	SW	17.28%	E	1.73%
2	N	27.21%	NW	25.75%	SE	2.10%
3	W	23.85%	NW	19.83%	NE	5.92%
4	SW	25.01%	S	16.06%	NE	4.40%
2019	**Aspect**	**Ratio**	**Aspect**	**Ratio**	**Aspect**	**Ratio**
1	NW	25.11%	N	16.04%	SE	3.19%
2	NW	24.56%	N	23.29%	SE	4.34%
3	W	20.21%	NW	19.01%	NE	7.82%
4	SE	25.90%	SW	17.34%	N	3.12%
2020	**Aspect**	**Ratio**	**Aspect**	**Ratio**	**Aspect**	**Ratio**
1	SW	22.57%	W	18.23%	E	4.91%
2	N	22.61%	NW	20.07%	SE	4.61%
3	W	23.50%	NW	17.93%	NE	6.53%
4	SE	29.12%	W	15.52%	N	4.21%
2021	**Aspect**	**Ratio**	**Aspect**	**Ratio**	**Aspect**	**Ratio**
1	NW	22.08%	N	18.82%	E	4.33%
2	N	25.36%	NW	22.66%	SE	3.05%
3	W	22.93%	NW	20.08%	NE	3.05%

Note: 1, 2, 3 and 4 refer to the elevation range of terminus-3100, 3100-3300, 3300-3500 and >3500 m a.s.l., respectively

Table 5.5 Total length of crevasses and total area of ice cliffs for four elevation sectors, and their densities for each sector

	2018				2019				2020				2021			
	Crevasses		Ice cliffs		Crevasses		Ice cliffs		Crevasses		Ice cliffs		Crevasses		Ice cliffs	
	Total length (km)	Density (km/km^2)	Total area (km^2)	Density	Total length (km)	Density (km/km^2)	Total area (km^2)	Density	Total length (km)	Density (km/km^2)	Total area (km^2)	Density	Total length (km)	Density (km/km^2)	Total area (km^2)	Density
1	1.77	8.43	0.02	11.62%	3.13	18.96	0.02	12.43%	3.91	28.69	0.02	14%	4.78	38.59	0.03	24%
2	7.98	22.21	0.04	12.39%	6.27	18.63	0.05	14.28%	8.01	26.24	0.04	14%	4.38	13.93	0.04	12%
3	16.54	22.78	0.13	17.74%	13.75	19.36	0.11	16.32%	17.24	24.53	0.09	13%	7.58	10.50	0.09	13%
4	15.08	41.27	0.03	9.07%	7.89	21.98	0.03	7.45%	5.68	25.56	0.01	6%	-	-	-	-
Total	41.28	24.85	0.24	14.45%	31.04	19.76	0.21	13.37%	34.84	25.49	0.16	11.71%	16.74	14.43	0.16	13.79%

5.4.1 Uncertainty analysis

5.4.1.1 Uncertainty from UAV-derived datasets

Acquiring high-quality aerial images in highly rugged mountainous regions (e.g., HLG Glacier valley, southeastern Tibetan Plateau) by UAV is challenging. The highly variable microclimate within the HLG Glacier valley may induce rapid changes in regional weather, such as mist/fog and clouds, which further causes uneven lighting and unexpected shadows during conducting UAV surveys (Xu et al., 2022). However, visual checking of the sparse and dense point cloud shows that the images with severe shadows were not aligned and were not further processed, and therefore the impacts on the DSM and orthophotos are minimal.

The rigorous ground control points obtained from external GNSS equipment are necessary for conventional photogrammetry (Gindraux et al., 2017). The quality of the absolute georeferencing of the generated DSMs and orthophotos relies on the number of ground control points and their spatial distributions across the study area (Villanueva and Blanco, 2019). However, it is impractical to collect the coordinates of ground control points on the highly crevassed surface of the HLG Glacier. Therefore, our approach is utilizing the orthophoto of July 2021 as the benchmark (i.e., georeferenced by network-RTK) and then co-align the remaining three surveys to this benchmark with 33 tie-points extracted from the 2021 orthophoto (Forlani et al., 2018). Based on that, four DSMs with a spatial resolution of no more than 0.36 m/pixel and orthophotos with a spatial resolution of no more than 0.09 m/pixel (resampled to 0.1 m/pixel afterwards) were produced from the SfM-MVS workflow (refer to Table 5.1). The final root mean square errors from co-aligning with the benchmark dataset are all less than 0.94 m. Although some minor errors might occur in relation to the setting of tie-points for each dataset (2018, 2019, and 2020), their impacts are assumed minimal.

5.4.1.2 Uncertainty from mapping results

Due to the fact that all mapping works were done manually, it is not possible to calculate the range of uncertainty, therefore, we mainly focus on the sources of uncertainty in the mapping work. The arguments are mainly from two aspects: 1) the changes in the density of ice crevasses, and 2) the statistics of the area of each glacier sector (i.e., the delineation of glacier margins).

It can be referred from the Main maps A and B that there is a clear reduction in crevasse density, which can also be interpreted by comparing the orthophoto between 2018 and 2019 (Figure 5.8). As stated in the mapping criteria, we mapped the long axis of the crevasses with polylines, which means we only mapped the length of the crevasses, but the width is ignored. However, the width of crevasses in 2018-Sector 4 is much less than that in 2019-Sector 4. In the context of continued glacier ablation, although the ice crevasse density decreased significantly in 2019 (when counting crevasses length only), the reason for the decrease may be attributed to the fact that the width of ice crevasses is gradually becoming larger. In other words, many long and slender ice crevasses are integrated into massive crevasses with wider widths due to deepening and intense ablation.

The reliability of calculating the change in glacier area can be interpreted as the reliability of outlining glacier margins. It is difficult to distinguish the lateral margin of the glacier, even with very careful cross-referencing of orthophotos, DSM, and 3D point clouds, for instance, the middle part of the HLG Glacier tongue (i.e., Sector 3) is covered by thick debris cover, especially for the lateral margins (Figure 5.9) (Zhang et al., 2019). Therefore, it may bring slight errors when outlining the glacier lateral edge of Sector 3. For Sectors 1, 2 and 3, lateral crevasses or some vegetation can indicate the possible lateral glacier margins so that the extent for these three sectors is relatively confident.

Figure 5.8 A comparison of orthophotos between 2018-Sector 4 and 2019-Sector 4

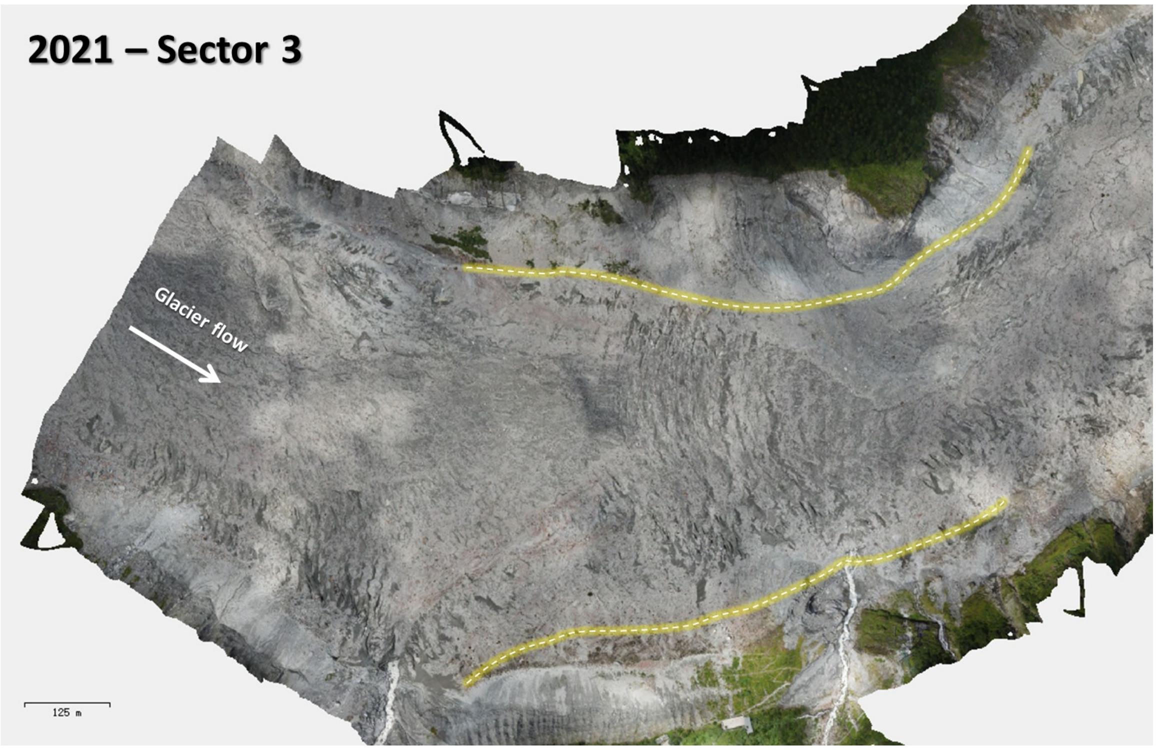

Figure 5.9 Sector 3 of 2021 orthophotos and the yellow dashed lines indicate the lateral margin of the glacier

5.5 Conclusion to this chapter

We mapped a variety of features for the HLG Glacier tongue based on clearly defined mapping criteria. The key features included glaciological, glacial geomorphological and hydrological features. Based on the mapping results and analyses, we assessed the evolution of the HLG Glacier tongue during 2018-2021. We interpret these features to illustrate that the dynamics of the glacier has changed, and the glacier is in rapid recession, and even possible disintegration. The disconnection between the glacier tongue and the accumulation zone has set the lower part of the glacier on a course to becoming stagnant, and ultimately existing only as a block of dead ice. Therefore, it can be hypothesized that the glacier will only recede more rapidly over the next decades, with the exact rate being determined largely by the magnitude-frequency of future terminus ice collapse events.

Chapter 6: Mechanical ablation of Hailuogou Glacier terminus and its contribution to glacier ice mass loss

6.1 Introduction

HLG Glacier has been reported to be receding rapidly in a number of studies, which commonly associate the retreat with warming (Ding et al., 2006; Pan et al., 2012; Wu et al., 2020; Yang et al., 2016). However, apart from processes of ice loss related directly to changes in temperature (i.e., mass loss due to melt), the mechanical ablation of glaciers can also play an important role in contributing to ice mass changes (Benn and Åström, 2018). Mechanical ablation can be described as the process by which ice fractures from the host glacier, most commonly as a consequence of ice-marginal water-glacier interactions (Falatkova et al., 2019; Haresign, 2004; Sakai, 2012; Sakai and Fujita, 2010). The understanding of mechanical ablation and its contribution to overall ice loss has been hindered because it is difficult to track mechanical ablation by commonly-available satellite-based remote sensing datasets, owning to their small-scale but unpredictable natures. Fortunately, the use of imagery acquired by UAV can be acquired with much greater frequency, at lower altitudes, to capture these fine-scale changes. SfM-MVS photogrammetry has been well developed in connection with the UAV technology to reconstruct the three-dimensional glacier surface through time (Bash et al., 2018a; Chandler et al., 2018; Rossini et al., 2018).

It is generally agreed that mechanical ablation can amplify ice loss when compared to glaciers without such processes, leading to glacier (e.g., no lake-terminating glaciers) behavior that is partly decoupled from climatic drivers (Carrivick and Tweed, 2013). Recently, efforts to characterize and quantify the mechanical ablation for mountain glaciers have been carried out on lake-terminating glaciers and their proglacial lakes (Ashraf et al., 2014; Carrivick and Tweed, 2013; Haresign, 2004; King et al., 2018, 2019; Liu et al., 2020; Sakai, 2012; Sakai et al., 2009). However, similar rates of mechanical ablation may also be observed for some land-terminating monsoonal temperate glaciers in the southeastern Tibetan Plateau, such as HLG Glacier, which exhibits ~13° of surface gradient in the lower glacier tongue (Zhong et al., 2021). They have been observed in the field predominantly as collapse events, probably influenced by the ablation induced by the intensive water-glacier interactions along the subglacial channels, around the subglacial outlet (i.e., the intersection between the proglacial river and the glacier terminus), and within the subglacial conduits around the glacier terminus (i.e., the conduit's roof).

Ice collapsing and calving events take place rapidly, meaning their frequency and magnitude can be difficult to ascertain (Haresign, 2004). Though current satellite-based remote sensing technologies have provided multiple options for glacier change monitoring, using optical sensors (e.g., Landsat, ASTER and Sentinel-2), microwave sensors (e.g., Sentinel-1, ALOS) and gravity sensors (e.g., GRACE), (Berthier and Toutin, 2008; Bishop et al., 2007; Chen et al., 2018; Kääb et al., 2016; Li et al., 2008; Strozzi et al., 2002), it is difficult to quantify fine-scale changes using these coarse resolution data sources. Although field investigations can be challenging (e.g., high lateral relief, complex terrain, poor signal transmission, unsteady weather, etc.), several previous studies have been successful in glacier monitoring using low-cost consumer-grade UAVs (Immerzeel et al., 2014; Fugazza et al., 2018; Rossini et al., 2018; Yang et al., 2020; Karimi et al., 2021; Fu et al., 2021). For example, to track the modification of glacial geomorphological features over short timespans (Fugazza et al., 2018), to characterize the sub-annual and annual formation of ice-marginal landforms (Rossini et al., 2018), and to quantify glacier volume changes and the dominant melting processes (Di Rita et al., 2020).

Land-terminating mountain glaciers in the southeastern Tibetan Plateau, such as HLG Glacier, are undergoing remarkable recessions in recent decades (Li et al., 2010, 2009; Liu et al., 2010; Lu and Gao, 1992; Zhang et al., 2011). In this study, we aimed to quantify the extent to which this enhanced recession could be attributed to seasonally enhanced ice-marginal water-glacier interactions (i.e., during summer period), and a consequent increase in mechanical ablation activity. With the employment of UAV-captured imagery over the HLG Glacier from October 2017 to November 2020, and 3D surface reconstruction technology, we sought to achieve the following objectives:

1. to characterize the morphological evolution of the glacier terminus due to mechanical ablation (i.e., collapse activity) using fine spatial resolution images from UAV, and;

2. to quantify volumetric ice loss across the terminus area owing to mechanical ablation as opposed to other ablation processes (i.e., melt and sublimation).

6.2 Workflow for assessing mechanical ablation of Hailuogou Glacier terminus based on UAV datasets

A workflow as shown in Figure 6.1 illustrates the details for processing UAV and derived datasets. The primary dataset here is aerial images captured by DJI Mavic Pro during the field trips from 2017 to 2020. Still images and images that extracted from aerial videos were input to SFM-MVS workflow (i.e., Agisoft Metashape Professional Version 1.5.3) to generate datasets of dense point clouds. Based on that, the Digital Surface Models (DSMs) and orthophoto mosaics can be produced subsequently (Output1). Orthophoto mosaics were used on geomorphological mapping manually through visual interpretation (i.e., ArcMap) and DIC-FFT processing to obtain multi-temporal mapped features and surface displacement fields, respectively. The generated DSMs were then processed by the Geomorphic Change Detection (GCD) to obtain the ice surface height changes and corresponding ice volume changes.

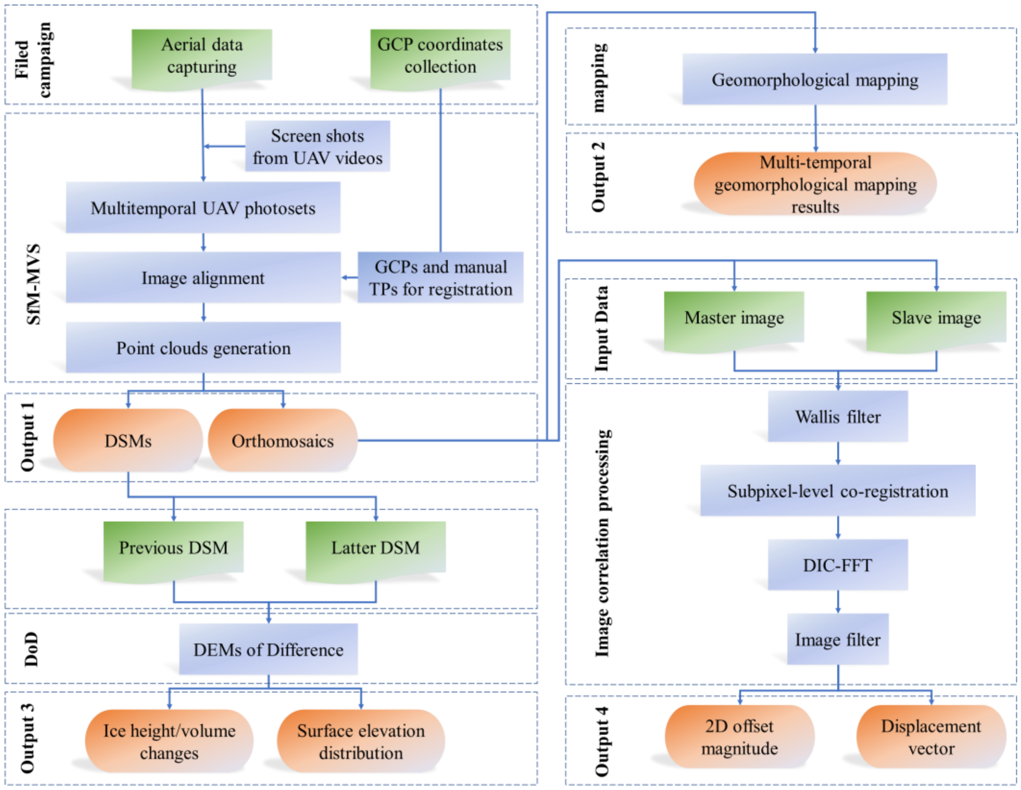

Figure 6.1 The workflow of the quantification of the mechanical ablation events at the glacier terminus. It includes four outputs: 1) the generation of DSMs and orthomosaics from SfM-MVS workflow; 2) multi-temporal geomorphological mapping results; 3) DoD; 4) and surface displacements from the digital image correlations.

6.3 Mapping of Hailuogou Glacier terminus from 2017 to 2020

6.3.1 Georeferencing and co-aligning between UAV-derived datasets

The accuracy of the DSMs generated by SfM-MVS is predominantly influenced by the quality of the captured images. It is particularly challenging to obtain high-quality images by UAV in the rugged high mountain environment, as the rapidly changing regional weather (e.g., mist or cloud) in the HLG Glacier valley causes different lighting conditions and temporally variable shadows. Nevertheless, visual assessment of the resulting point clouds, and the very uniform signal of stability in the off-ice areas, suggests that where shadowing was severe and/or variable, those images were not successfully matched (and therefore had minimal impact on the DSMs or orthophotos).

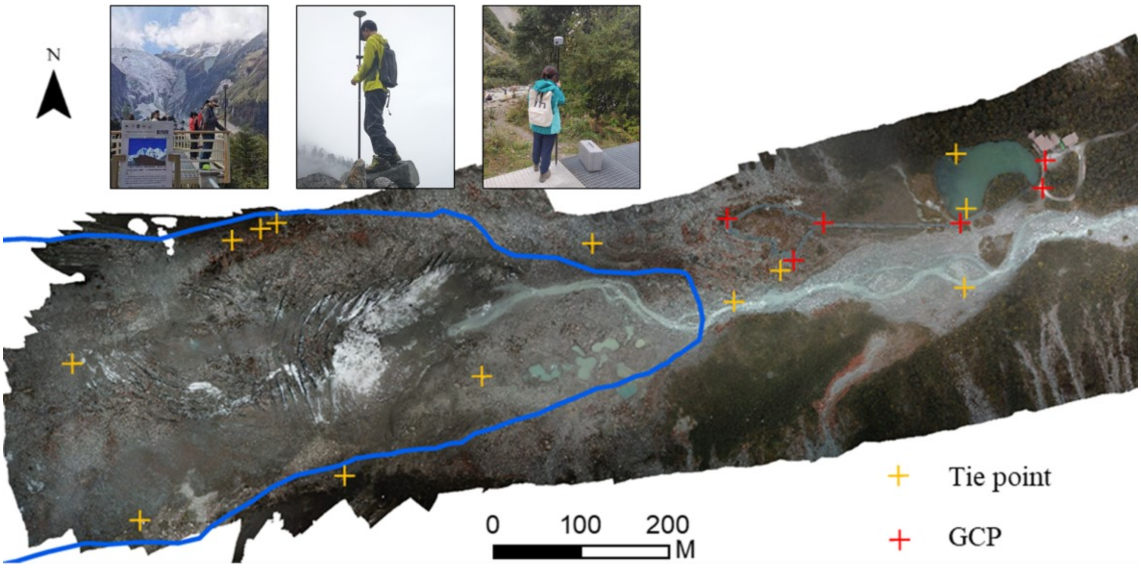

Figure 6.2 Spatial distribution of the GCPs and the tie points. The background orthophoto mosaic is generated from the dataset of November 5th 2020. The blue polygon indicates the HLG Glacier terminus extent (2009) extracted from the Second Glacier Inventory of China (Liu et al., 2014).

The absolute georeferencing of the DSMs and the orthophotos depends primarily on the quantity and quality of the GCPs and their spatial distribution. We were limited to just six GCPs distributed around the proglacial zone, which somewhat limited the positional accuracy of the products generated from UAV images (Figure 6.2). However, our strategy of georeferencing only one of these point clouds, and then co-registering the remainder of our data to this 'master' cloud, minimizes the impact of this limitation. Indeed, given that our confidence in the internal (relative) accuracy of the point clouds is high, the resulting DoDs generated between datasets can be considered similarly robust. There may be some minor error associated with the manual placement of tie-points between each pair of clouds, but it is probably negligible given the high number and careful choice of tie-point locations that we used.

Therefore, eight DSMs and orthophoto images were successfully derived from the overlapping UAV imagery (Table 6.1). The number of points in each cloud varied from ~ 150,000 to ~ 60,000,000 according to their covered area, and then the point clouds were able to produce DSMs with the spatial resolution no more than 0.36 m/px and orthophotos with a spatial resolution of <0.1 m/px. Georeferencing errors were generally of the order of 0.35 m. All DSMs and orthophotos were resampled to 0.5 m/px and 0.25 m/px respectively for multitemporal DSM comparisons and surface displacement analysis, respectively.

Table 6.1 General Information about products generated from SfM-MVS workflow

No.	**Date** (y/m/d)	**Numbers of photo**	**DSM** (m/px)	**Ortho-images** (m/px)	**Z error** (m)	**Total errors** (m)
1	2017/10/17	2463	0.09	0.02	0.08	0.15
2	2017/12/04	1284	0.16	0.04	0.11	0.21
3	2018/06/30	1066	0.27	0.07	0.15	0.25
4	2018/10/28	4850	0.31	0.08	0.17	0.31
5	2019/10/03	3013	0.35	0.09	0.09	0.19
6	2020/09/05	898	0.07	0.04	0.21	0.36
7	2020/09/10	282	0.11	0.05	0.19	0.33
8	2020/11/05	315	0.18	0.05	0.20	0.34

6.3.2 Glacial features in the glacier terminus area

The overall impression of the tongue of HLG Glacier is shown in Figure 6.3. The surface of HLG Glacier is covered with a thick debris mantle, below the icefall. Lateral valley relief presents steep cliffs that are the source of debris falling either directly onto the glacier surface, and transported towards the terminus, or buried in the accumulation area beneath snow cover, and carried englacially for meltout in the ablation area (Zhang et al., 2010). Both lateral sides of the HLG Glacier valley are covered with vegetation such as shrubs and trees etc., and several small streams fed by smaller glaciers in the HLG Glacier valley possibly (Figure 6.3 f and g) flow down from higher elevation to link with the supraglacial river networks or subglacial drainage systems as an external supply of the freshwater to the glacier hydrological system. Meltwater runoff and external water supply transfer into the glacier hydrological system by various means such as supraglacial, englacial and subglacial drainage networks. These runoffs combine towards the terminus to form the proglacial river (Figure 6.3 b).

Clean ice is evident within certain areas of the otherwise thickly debris-covered tongue; one is around the glacier terminus (Figure 6.3 c), and the other is around the icefall (Figure 6.3 i). Around the terminus numerous ice crevasses and ice fractures are evident, especially for the upper part of the frontal collapsed area (Figure 6.3 d), providing the structural weaknesses that eventually become points of failure in calving events. Large ice crevasses and ice fractures are also evident in the glacier arches (i.e., in the elevation zone ranging from 3850 to 3480 m a.s.l.; Figure 6.3 g) and lower part of the icefall (i.e., around 3900 m a.s.l.; Figure 6.3 i). The presence of these large ice crevasses is somewhat different in size and orientation from those around the glacier terminus, indicating their formation might be related to fast flow through the icefall. Below the ice fall, most of crevasses are longer than that in the glacier terminus region, with lengths of about 100 m, while the length of majority of crevasses in the glacier terminus are less than 50 m.

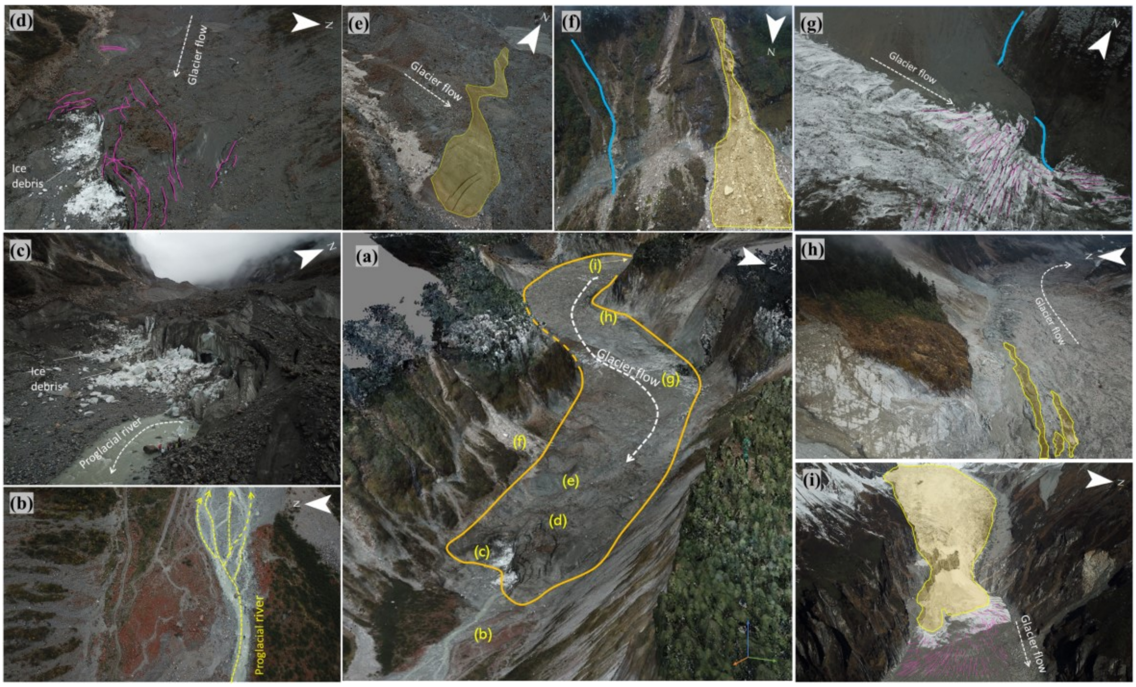

Figure 6.3 An example of the three-dimensional representation of HLG Glacier with an oblique viewing angle and other photos demonstrating glacial features (dataset of 3rd October 2018). The center image (a) is the oblique view of the dense point cloud of most of the glacier tongue (from the icefall to the periglacial forests) produced by the SfM-MVS workflow. The surrounding images are as follows: (b) shows the proglacial river and periglacial zone; (c) shows the calved ice margin, frontal ice cliffs and the subglacial outlet; (d) shows ice crevasses concentrated around the glacier terminus and calved margin; (e) shows a series of ice cliffs on the glacier surface; (f) shows a lateral landslide in the glacier valley and a seasonal stream; (g) shows an inlet of a lateral stream and ice crevasses centered around the inlet; (h) shows a series of lateral marginal ice cliffs distributed near the glacier arches (3850 to 3480 m a.s.l); (i) shows the lower part of the icefall with an extensive falling and collapsing fresh ice mass.

6.3.3 Changes of mapped features and statistical analysis

Over the period of observation, the terminus area of the glacier evolved very rapidly (Figure 6.4). In particular, the subglacial channel outlet (i.e., the frontal ice cave) changed its position several times, which subsequently led to multiple variations of the path of the main HLG Glacier proglacial rivers. This fluctuation impacted heavily on the glacier terminus position. In order to highlight the effects of collapse events on the glacier retreat, we compared the forward-most (hereon the glacier frontal terminus) and the backward-most (hereon the glacier collapsed terminus) points of the glacier terminus. We generated the centerline of HLG Glacier by using the Open Global Glacier Model (OGGM) (Maussion et al., 2019), and used this to define these positions. The area not affected by the subglacial channel (and therefore collapse/calving processes) retreated approximately 132.1 m from 2017 to 2020 (i.e., the distance highlighted by yellow dash lines in Figure 6.4), in contrast to the area to the more dynamic south side of the glacier, which retreated by more than 236.4 m over the same period (i.e., highlighted by blue dash lines in Figure 6.4). The fastest recession for the terminus of HLG Glacier affected (glacier collapsed terminus) or non-affected (i.e., glacier frontal terminus) by the ice collapsing events occurred between 2018-10-28 and 2019-10-03. It is notable that both glacier margins (i.e., glacier frontal terminus and glacier collapsed terminus) have suffered substantial terminus retreating due to ice collapsing events over a relatively short time span (i.e., approximately 2 months) as shown in Figure 6.5 c.

Table 6.2 shows the quantitative analysis of the variation of the HLG glacier terminus. The total areal ice loss between the first and last field campaigns was 51,465 m^2. The fastest reduction in area was during the campaign of June 30th 2018 to October 28th 2018 (i.e., 120 days intervals; 15,812 m^2) and the campaign of October 3rd 2019 to September 5th 2020 (i.e., roughly annual intervals; 16,553 m^2). The recession was evidently highest during the glacier ablation seasons and has generally been increasing in rate through time. The capture of two frontal ice collapsing events, one of which was substantial, confirms the importance of the frontal ice collapsing event as an ablation mechanism for this glacier (i.e., Table 6.2g). This ice collapsing event caused approximately 7,234 m^2 in areal recession over a short interval.

Comparing the surface profiles extracted from UAV-derived datasets with the profile extracted from SRTM (2000) reveals that snout of HLG Glacier underwent an overall lowering of approximately 50 m over the nearly two-decade period. The area within 400 m of the terminus is the main zone for terminus retreat and ice collapsing (Figure 6.5a). As revealed by the surface profiles in Figure 6.5b, terminus retreated successively with varying degrees of lowering. However, in the lower part, approximately 350 m along the center flowline, three surface profiles for 2020-09-05, 2020-09-10 and 2020-11-05 are particular notable. This pattern might be induced by the rapid propagation of ice crevasses from the glacier collapsed terminus towards the upper part of the glacier snout. With the enhanced water-glacier interactions beneath the glacier bodies or above the englacial/subglacial channels, it is feasible that the deep crevassing may be intensified due to the thermal erosion, producing an unexpected ice surface lowering or the roof lowering of subglacial/englacial channels even for some distance from the terminus area. The primary cause for this event is probably the basal melting and positive feedbacks associated with the collapse events, and the impact on strain rates which will have weakened the surrounding ice and along the subglacial channel and outlet.

The near-vertical lines occurring between 2020-09-05 to 2020-11-05 are clear visible in Figure 6.5c, d and e, and they indicate the impact that ice collapse events can have on glacier recession rates. Although the ice collapsing events have a moderate effect on the daily average areal reduction (i.e., Figure 6.6a), its influence on the daily average ice volume changes is obvious (i.e., Figure 6.6b).

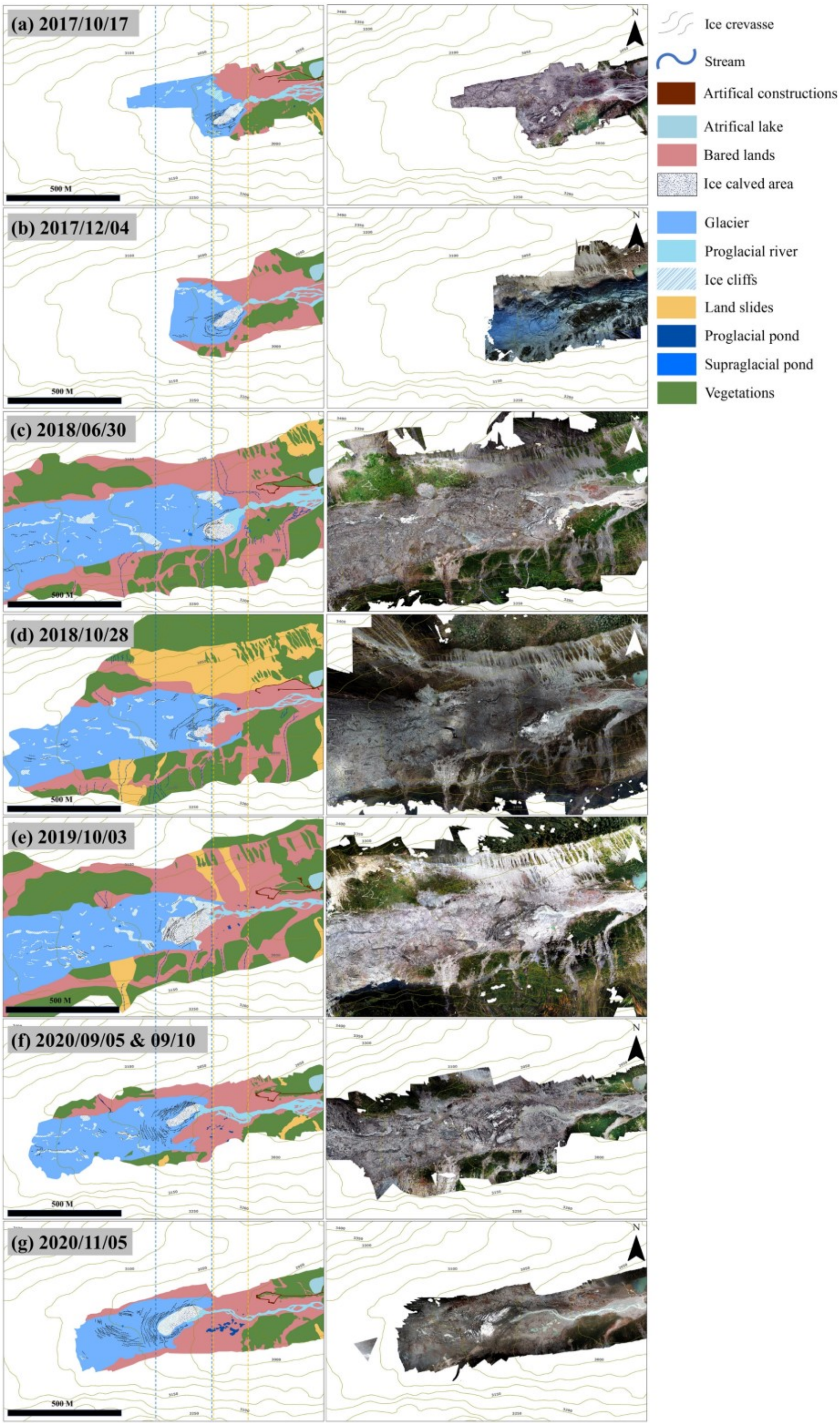

Figure 6.4 Results of geomorphic mapping based on the orthophoto mosaic. Top to bottom (a to g) indicated the glacier terminus changes and the changes of surrounding glacial landscapes from October 2017 to November 2020. Left column and right column are the mapped illustration and orthophoto mosaic, respectively. We used one figure to show 2020/09/05 and 2020/09/10 as their interval is too short to identify geomorphic changes. Although the area mapped in the seven maps are different, they provide sufficient coverage of the glacier terminus to show the evolution surrounding it. The blue and yellow dash lines represented extreme changes of the glacier collapsed terminus and glacier frontal terminus between 2017/10/17 to 2020/11/05, respectively.

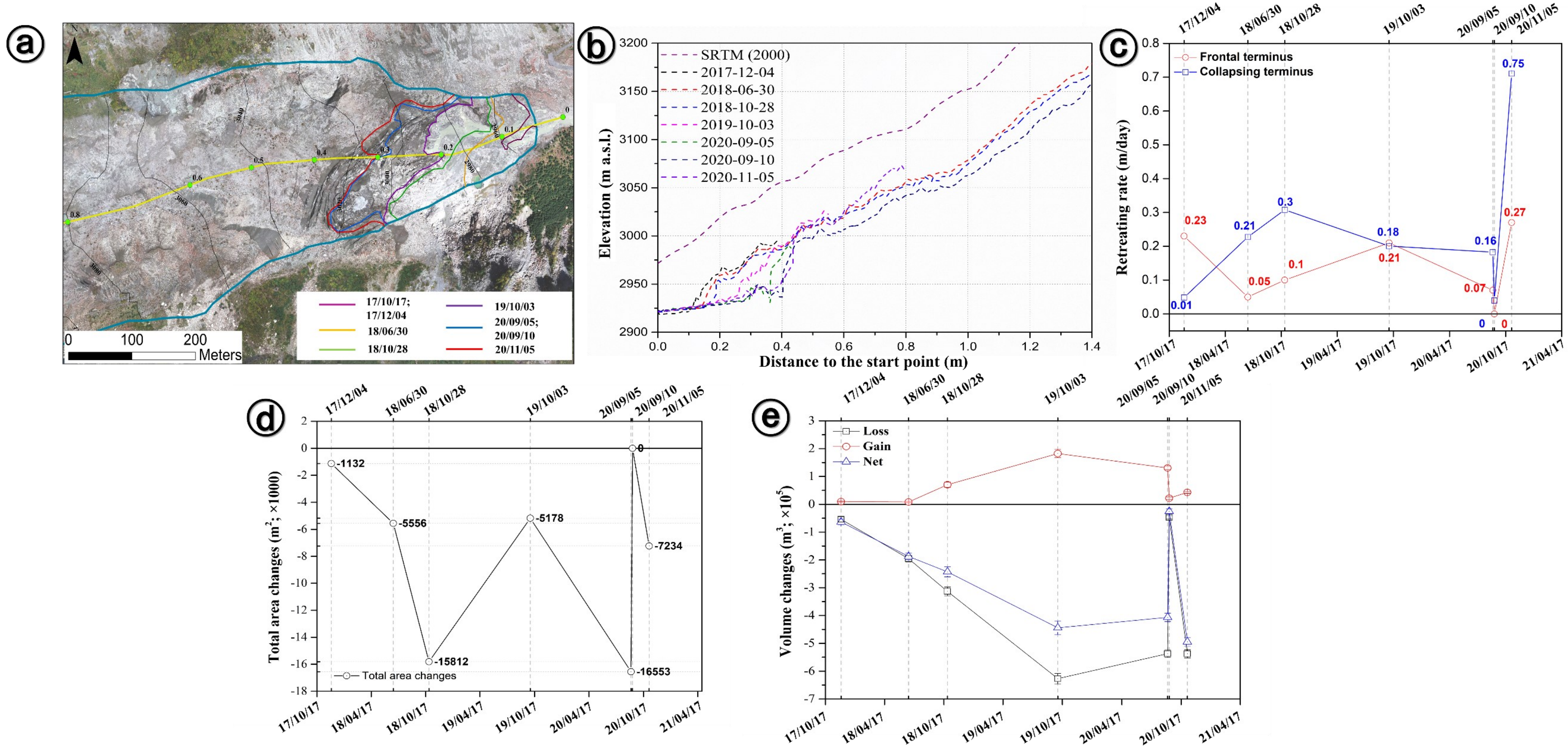

Figure 6.5 Longitude profiles for the HLG Glacier terminus (a and b) and statistical analysis about the HLG Glacier terminus evolution (c-e). (a) shows the spatial distribution of the center flowline of the HLG Glacier and terminus line of HLG Glacier from 2017-10-17 to 2020-11-05. The HLG Glacier extent (2009) was extracted from the Second Glacier Inventory of China and the background orthophoto mosaic is from the 2019-10-03 dataset. (b) shows the profile along the center flowline of HLG Glacier. Profile of SRTM is listed as additional information for reference. (c) shows the retreat distances for the glacier frontal terminus and glacier collapsed terminus. (d) shows the terminal area changes due to the glacier retreat. (e) volumetric changes due to glacier terminus evolutions.

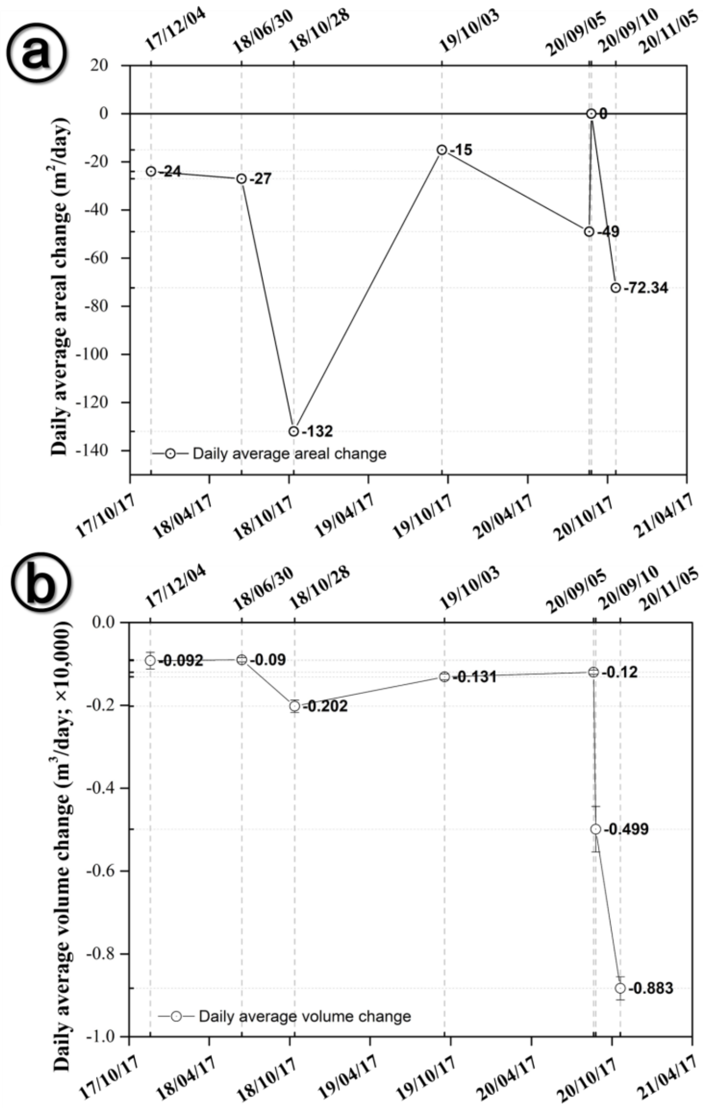

Figure 6.6 Statistical analysis about the HLG Glacier terminus daily evolution (a) daily average areal changes. (b) daily average volume changes.

6.4 Surface elevation changes and ice volume changes

Multi-temporal DSMs were differenced to quantitatively measure the changes of HLG Glacier during the period of observation (Figure 6.5). The greatest surface elevation changes (of roughly -40 m over a 56-day period) occurred in the lattermost pair of DSMs (Figure 6.6b), which included a confirmed large ice calving event. Several other periods (Figure 6.5 c, d, and e) showed surface lowering in excess of 30 m, which we also interpret to portray collapse or calving events. As the ice thickness is known to range between 30 to 40 m around the terminus area of the glacier, it indicates that either calving can propagate all the way to the glacier bed, or in the case of collapse events, that the subglacial chamber formed by the outlet channel is large.

More broadly, the terminus of HLG Glacier presented dramatic surface lowering and ice mass loss during 2017 to 2020, with an overall ice loss volume of 184.61 ± 10.32 × 10^4 m^3. The detailed ice volume changes and the histogram of the surface elevation change is shown in Figure 6.7. The statistics are summarized in Table 6.2. Table 6.2 d and Table 6.2 e present similar interannual magnitudes of total ice volume changes, that is - 44.41 ± 2.41 × 10^4 m^3 and - 40.74 ± 1.62 × 10^4 m^3. However, the total ice volume changes over the lattermost period have the maximum volumetric loss (- 49.51 ± 1.58 × 10^4 m^3) revealing that a single calving event can exceed the interannual ablation from non-mechanical processes. We note here though that our DoDs cannot account for any ice emergence, meaning that ablation may be underestimated.

From the aspect of the daily average of ice volume loss, ice loss due to the small ice collapsing event (i.e., Table 6.2 f) is - 0.50 ± 0.16 × 10^4 m^3, roughly four times the daily losses recorded in the interannual pairs (i.e., Table 6.2 d and e). Ice volume lost during the large ice collapsing event (Table 6.2 g) was about 1.7 times that of the small ice collapsing event (Table 6.2 f).

Table 6.2 The statistical analysis of the HLG Glacier terminus changes

No.	Model pair (YY/MM/DD)	Interval (days)	Frontal/collapsed terminus retreats (m)	Total area changes m^2 ($\times 10^2$)	Average areal change m^2/day	Ice height changes (max/min/mean)	Total volume change m^3 ($\times 10^4$)	Average volume change m^3/day ($\times 10^4$)	Seasons
a	17/10/17-17/12/04	48	1.11/0.33	- 11.32	- 23.58	5.10/- 11.36/- 1.10	- 4.42 ± 0.98	- 0.09 ± 0.02	End of the ablation season
b	17/12/04-18/06/30	208	10.36/44.56	- 55.56	- 26.71	4.86/- 16.84/- 2.57	- 18.71 ± 1.13	- 0.09 ± 0.01	Roughly whole accumulation season
c	18/06/30-18/10/28	120	11.85/36.46	-158.12	- 131.77	9.08/- 31.20/- 2.01	- 24.30 ± 1.82	- 0.20 ± 0.02	Major ablation season
d	18/10/28-19/10/03	340	71.63/60.36	- 51.78	- 15.23	12.81/- 38.31/-2.36	- 44.41 ± 2.41	- 0.13 ± 0.01	Annual
e	19/10/03-20/09/05	338	22.12/52.85	- 165.53	- 48.98	13.60/- 35.88/-4.01	- 40.74 ± 1.62	- 0.12 ± 0.01	Annual
f	20/09/05-20/09/10	5	15.24/42.16	≈ 0	≈ 0	8.82/- 30.34/- 0.33	- 2.52 ± 0.78	- 0.50 ± 0.16	Several days in ablation season
g	20/09/10-20/11/05	56	15.26/42.12	- 72.34	- 129.18	9.47/- 41.83/- 5.32	- 49.51 ± 1.58	- 0.88 ± 0.03	Major ablation season
Total	17/10/17-20/11/05	1115	132.51/236.43	- 514.65	- 46.16		~ 184.61 ± 10.32	~ 0.17 ± 0.01	

Note: f: a small ice collapse event; g: a large ice collapse event.

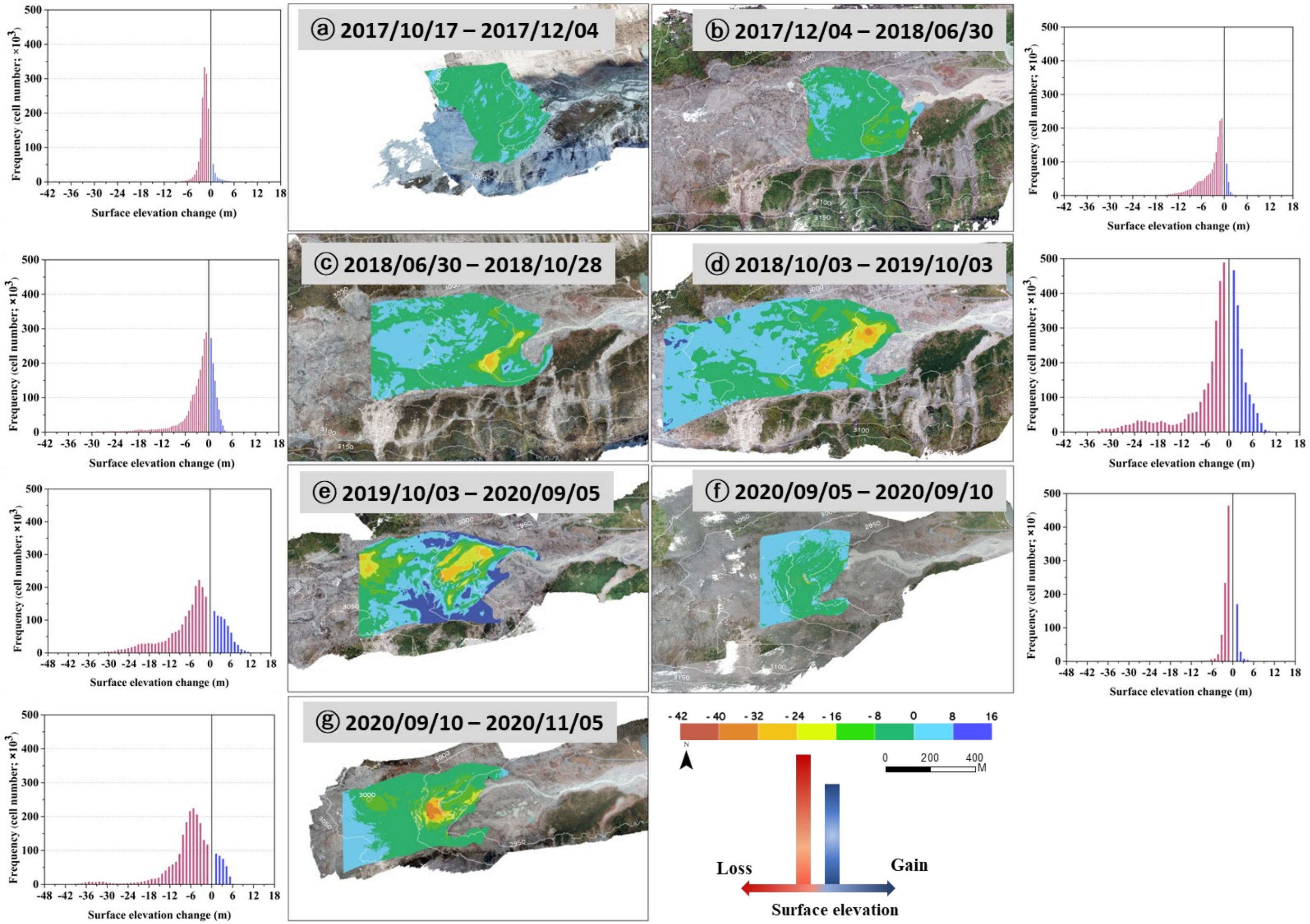

Figure 6.7 Ice height changes and the distribution of glacier surface elevation changes from October 2017 to November 2020 (a to g). The background image is the latter orthophoto image from each pair and the contour line is derived from the DSM of the latter for each DoD. The insert histograms show the surface elevation changes for each compared pair.

6.5 Surface displacements at the glacier snout

The UAV surveys for datasets of 2017-10-17 and 2017-12-04 only covered the frontal margin of the glacier terminus, so that the area of these two datasets were too small to produce valid surface displacement, we used the five datasets from 2018-06-30 to 2020-11-05 to generate four surface displacement maps for the HLG Glacier snout. Since the area for image correlations for each pair was variable, we used different window sizes for the offset tracking (Table 6.3).

Table 6.3 Window sizes for each pair

Date	Window size for DIC-FFT (pixels)
2018-06-30 to 2018-10-28	**80**
2018-10-28 to 2019-10-03	**90**
2019-10-03 to 2020-09-05	**100**
2020-09-05 to 2020-11-05	**60**

The 2D offset magnitude and displacement vectors for each pair illustrate the spatial distribution of the surface velocity for the glacier snout (Figure 6.8). These four 2D offset magnitude maps reveal that the area with high offsets (i.e., dark red) are mainly distributed around the location of ice crevasses (e.g., Figure 6.8 a and c) or ice cliffs (e.g., Figure 6.8 b) with the maximum magnitude of about 10 m. Dashed polygons in Figure 6.8 (i.e., yellow in the second column, and black in third and fourth column) were used to indicate the areas in front of the glacier collapsed front. Relatively high surface offset magnitude was found around northern and western edges of theses polygons, which may be caused by crevassing and the developing of ice cliffs. There is a clear distinction in the flow dynamics between the area affected by calving and collapse and the area not affected by mechanical processes. There is a clear signal of flow being dominantly towards the collapsing region (right column in Figure 6.8), i.e., most of arrows point to the northwest and west side of these polygons (e.g., Figure 6.8 a and b), which also shows how ice collapsing events develop spatially. In other words, in the displacement vector maps, areas with consistent directions and densely distributed arrows pointing to the end of the glacier are often potential areas where ice collapsing events can occur. There is clear distinction between the displacement vectors in in Figure 6.8 a and b versus those in Figure 6.8 c and d; those in Figure 6.8 c and d do not closely concentrate on the northwest and east side of the polygons (i.e., the frontal collapsed margin), with some vectors even presenting the nearly ring-shaped pattern indicative of surface lowering caused by the roof collapsing of subglacial channel (Figure 6.8 d).

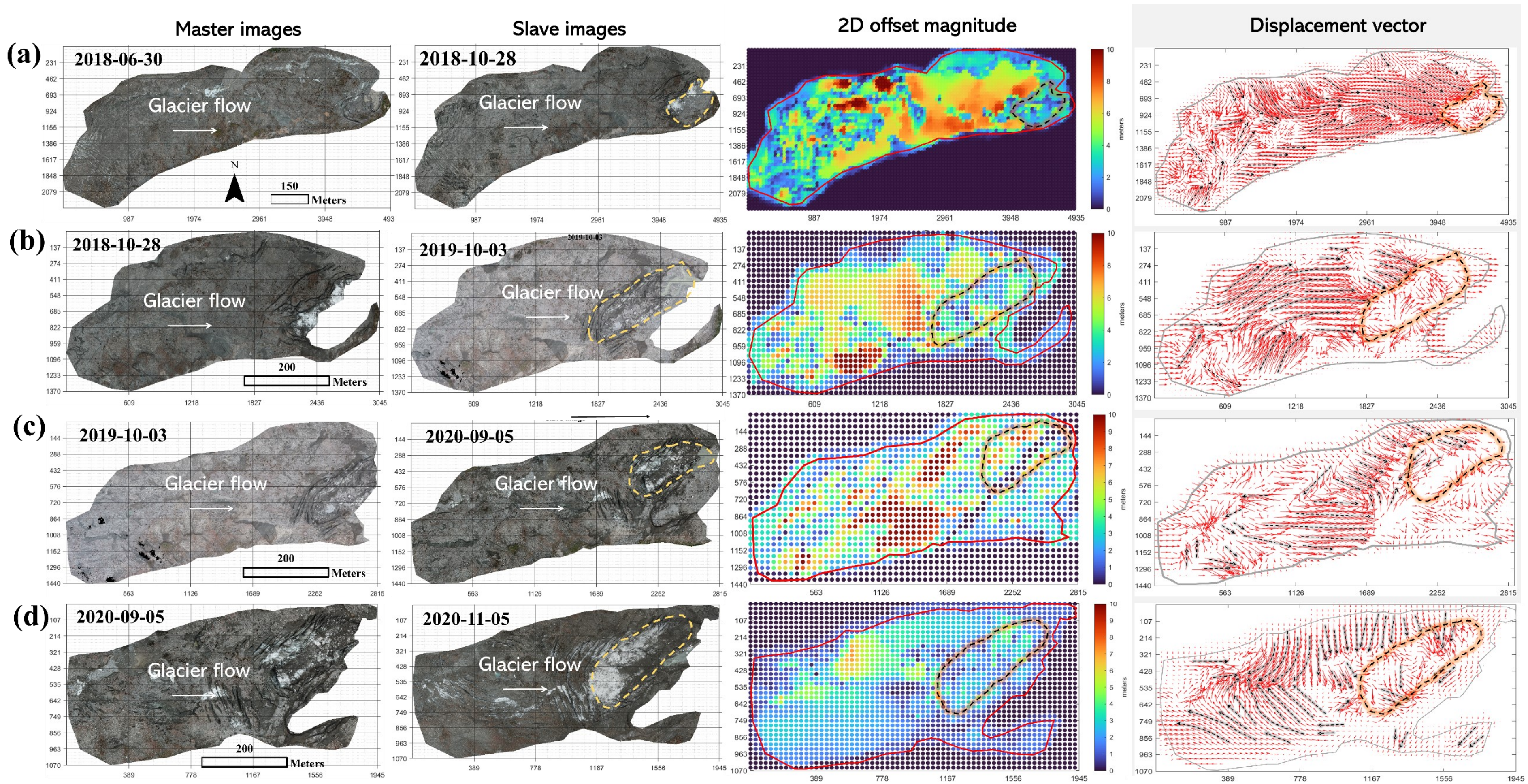

Figure 6.8 An illustration for the surface displacement of HLG Glacier generated by the method of DIC-FFT during the period from 2018-06-30 to 2020-11-05. The first to fourth column show the image pairs (i.e., master images and slave images), 2D offset magnitude maps and displacement vectors, respectively. Yellow dashed polygons represent areas in front of the glacier collapsed front, and the black dashed polygons also represent the same area.

6.6 Conclusion to this chapter

In this work, we estimated geomorphological changes of the HLG Glacier terminus area, southeastern Tibetan Plateau, from 2017 to 2020 by employing the SfM-MVS workflow with UAV images. The HLG Glacier is a rapidly receding temperate glacier in recent years and several ice collapsing events at the glacier terminus have been observed during the field trips. The variation of the glacier terminus is highly connected with the ice-water interactions within the glacier and these intensive ice-water interactions may induce the mechanical ablation (e.g., frontal ice collapsing events) at the subglacial channel outlet. The analysis shows that the ice collapsing at the glacier terminus partly dominated the glacier retreating. The volume and the area due to the ice mass loss induced by the frontal ice collapsing are significant. Also, the shallow proglacial waterbodies and the well-developed subglacial and englacial drainage system facilitate the ice-water interactions, thereby triggering the continuous thinning glacier to produce mechanical ablation events. Thus, mechanical ablation is important at this site and could become even more significant to the ice loss of HLG Glacier with the continuous warming. Moreover, the projection of the recession rate of the HLG Glacier may well be underestimated if based on surface mass balance alone, as the frontal ice collapsing might be more frequent and larger under the context of warming.

Chapter 7: Glacier mass balance changes (2002 to 2021) of HLG Glacier and the contribution of ice collapse

7.1 Introduction

Time sequenced fluctuations of the glacier have been acknowledged as the sensitive indicator for climate change (IPCC AR6, 2019). Global glacier mass balance has been reported in the recession in relation to the warming over recent decades (Bhattacharya et al., 2021; Zemp et al., 2013), which has greatly affected the local environment and regional runoff regime (Zhang et al., 2015), and has even contributed to sea level rise (Braithwaite and Raper, 2002). The core for accessing these impacts from the glacier recession is understanding the glacier mass balance. However there are only 12 continuous observations of glacier mass balance changes since 1906s globally (Wang et al., 2014; Zemp et al., 2013), and only about 33 glaciers across the world have been recorded for more than 40 years for their annual mass balance changes.

Time-series of glacier mass balance changes can be mainly derived from three methods, i.e., the glaciological measurements, the geodetical method, and the hydrometeorological approach (Wang et al., 2014). The main idea of hydrometeorological method to determine the mass balance of a glacier is based on the water balance of an entire glacierized basin. The hydrometeorological method was originally designed for catchment precipitation calculation, however, this was later shown to be used to calculate the changes of glacier mass balance and seasonal snowfall by using temperature and precipitation recorded by weather stations. Mass balance changes derived from the hydrometeorological approach is somewhat subject to the availability of data of hydrological and meteorological datasets, while using glaciological measurements and geodetic methods to calculate the glacier mass balance over a period has become commonly used methods. Glaciological measurements refer to conducting stake-surveying in-situ, but this method is only applied to a comparably small amount of glaciers in different parts of the world due to logistical and financial constraints (Rabatel et al., 2017). Monitoring of mass balance changes on a small number of glaciers limits the understanding of glacier dynamics associated with global climate change. The geodetic approach, therefore, is complementary to the in-suit measurements to quantify the glacier mass balance based on satellite datasets from single to regional, as so-called geodetic mass balance changes (Cogley, 2009; Dussaillant et al., 2018; Lv et al., 2020; Zhang et al., 2018).

In the past 40 years, the increased availability of satellites and their enhanced performance for Earth observation (i.e., spatial, temporal, and radiometric resolutions) has enabled glacier monitoring with more spatiotemporal details (Barella et al., 2020; Berthier et al., 2007). The 2D geometric characteristics of the glacier (e.g., length and area) can be derived from sparse or intermittent imagery easily, while the increased satellite-based stereo and the rapid development of space-borne stereophotogrammetry images further allow the glacier surface to be mapped repeatedly, to reconstruct the glacier elevation changes and consequently the geodetic mass balance to be inferred from converting volume change to mass change with predefined ice density (Cogley, 2009).

Specifically, middle/high-resolution imagery (e.g., SPOT-5/7 HRS images and ASTER) can be used to derive DEMs from stereo images (Berthier and Toutin, 2008; Gaddam et al., 2021; Hirano et al., 2003), and radar datasets (e.g., SRTM and TerraSAR) can also be used to generate DEMs by differential InSAR workflow (Krieger et al., 2007). However, the clouds on the images and the vertical accuracy of the derived DEMs of these optical and radar images limit the reconstruction of seasonal or even monthly mass balance changes (Rabatel et al., 2017). Nevertheless new very high-resolution imagery, including Worldview, Pléiades and Gaofen-2, can provide relatively reliable terrain information for the comparatively flat glacier tongue, but this method may not be conducted for a regional application as their relatively high financial costs and limited footprint (Berthier et al., 2016).

Deriving the ice volume change relies on sufficient contrast on the surface to complete the feature matching (i.e., tie points) and stereopair correlations. Therefore, we apply an automated, well-established, and free-sourced software, NASA Ames Stereo Pipeline (ASP; https://stereopipeline.readthedocs.io/en/latest/index.html) to generate multitemporal DEMs.

In this chapter, we focus on using all available ASTER L1A images, i.e., stereopairs images extracted from Band 3 of ASTER L1A (3N and 3B), for HLG Glacier, southeastern Tibetan Plateau, to reconstruct the glacier mass balance changes over 19 years (2002 to 2021). Differencing of DEMs is then applied to the generated ASP-DEMs to calculate the geodetic/volumetric changes and estimate mass balance changes based on the pre-defined conversion parameters of geodetic elevation changes to mass changes. The contribution of frontal ice collapse events that occurred at the glacier terminus that were identified from the satellite images is estimated subsequently based on the area-volume ratio (i.e., a linear relation between area and volume change derived from UAV datasets). Meteorological datasets acquired from weather stations near the HLG Glacier are also introduced to the discussion of the underlaying driver of the rapid glacier changes and its mass changes in recent 2 decades.

7.2 Time-sequenced DEMs derived from ASTER L1A stereo images based on NASA Ames Stereo Pipeline (ASP)

7.2.1 Functions used and parameters setting

As mentioned in ***Chapter 4.3.6.2***, two wavebands (i.e., 3N and 3B) extracted from ASTER L1A images were used to reconstruct the surface terrains by NASA Ames Stereo Pipeline (ASP). ASTER acquired stereoscopic images through a nadir-looking sensor of 14-band and a single band backward-looking sensor. These L1A data were raw datasets with a spatial resolution of 15 m and without geometric and radiometric rectifications. There are about 50 L1A datasets from February 2002 to September 2021 have been downloaded for the HLG Glacier region. For the sake of concision, the detailed list of the downloaded ASTER L1A data used for the ASP processing is not provided here but is listed in the Appendix Table S-table 3.

The environment for conducting NASA Ames Stereo Pipeline was built by Anaconda (https://www.anaconda.com) in the MacOS. Four functions were applied for processing ASTER L1A data, including *aster2asp*, *mapproject*, *parallel_stereo,* and *point2dem*. The details of each function and the workflow have been discussed before (see 4.3.6.2). Following are the parameters setting in the processing flow:

1) corr-seed mode =2
2) -t aster (rigorous ASTER sensor parameters)
3) mapproject --tr 0.0000898 (co-aligning images and then exporting with 10 m)
4) subpixel-mode = 2 (affine adaptive window, Bayes EM weighting)
5) corr-kernel = (7, 7)
6) –tr = 0.00027 (ground sampling = 30 m)

The core of generating ASTER-DEMs from AMES ASP is by matching a patch of pixels from 3N image and a similar patch of pixels in the 3B image. We firstly extracted stereoscopic pairs from all available ASTER L1A datasets in the approximate 20 year timespan. It should be noted that direct stereo correlation based on extracted image pairs might unreliable and unsuccessful if the differences between images in the pairs are too great, for example, the viewing angle of the sensors is too different, steep terrain (e.g., glacierized regions), massive cloud-covered portions and hill shadowed areas. These complexes in the image pairs may result in the wrong matching patches and subsequently too redundant searching ranges, which consumes too much computing time and produces DEMs with biases or even holes (Shean et al., 2016). To mitigate the uncertainties in the stereo correlations, we used the function of *mapproject* in NASA ASP to orthorectify extracted image pairs onto NASADEM (30 m spatial resolution). In this way, the pre-orthorectified 3N and 3B images were more spatially consistent as an initial spatial estimate and the consequent quality of the stereo correlation is higher. 7-pixel correlation kernel was used to generate the disparity maps and a subpixel refinement based on affined Bayes EM weighting was used to improve the pixel correlations. Rigorous postures and orientation of ASTER camera sensors were also involved in the correlation calculation. After the triangulation processing, point clouds were then converted to DEMs by using the function of *point2dem*.

7.2.2 DEMs derived from Ames Stereo Pipeline

7.2.2.1 DEM productions

We generated about **50** DEMs from the collected ASTER L1A data, of which **16** DEMs were produced from generally cloud-free images for the HLG Glacier region (**Error! Reference source not found.**; i.e., entire glacier with slightly/partly missing data or holes). The rest of the DEMs basically were produced from the images containing clouds, either the ice tongue is covered (mostly cases) or the upper reaches or entire glacier covered are covered. The manually delineated masks for cloud-covered regions are not created for the ASTER-derived DEMs as the low correlations across the cloudy regions are shown as the voids directly in the DEMs.

7.2.2.2 Outlier filtering and gaps/voids filling

The quality of photogrammetrically-derived DEMs may be influenced by the extensive clouds, which leads to some voids in the generated DEMs. Therefore, ***Mask Function*** and ***Elevation Void Fill Function*** were applied to remove unexpected outlier values and fill the holes in the DEMs by nearest neighboring interpolating methods, respectively.

We filled the data gaps or voids mainly over the upper part of the glacierized area. In other words, the lower part of the glacier is relatively slender, and the difference in height between the valley walls and the glacier surface on both sides is large, so it is not very meaningful to fill the gaps for this region as the error of interpolation is difficult to estimate. In contrast, the upstream area of the glacier is flatter and wider, so we mainly use this method to fill the gaps in this area.

With visual check, we divided the photogrammetrically ASTER-derived DEMs into two categories based on the locations of missing data and voids (Figure 7.1):

1) Missing lower patch of the glacier (e.g., terminus missing, lower tongue missing, and void of the lower ice fall);
2) Missing upper sections and the entire glacier tongue is clear.

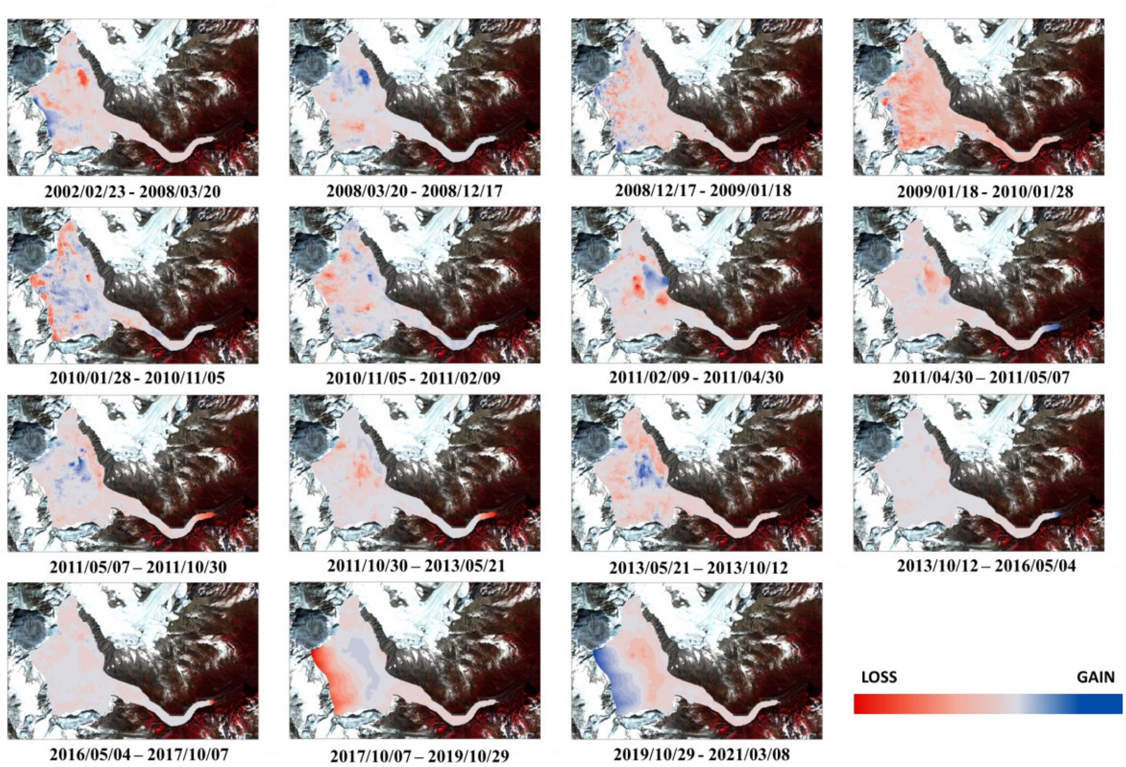

Figure 7.1 Time-sequenced changes of glacier surface elevation from 2002 to 2021

7.3 Time-sequenced Hailuogou Glacier extent from Planet

7.3.1 Delineation of time sequenced HLG Glacier outlines

The primary the dataset for extracting the HLG Glacier outlines is PlanetScope images (i.e., 3 to 5 m spatial resolution; Table 7.1). Due to the scope of the timespan of PlanetScope, we also used several Landsat TM images and ETM images to derive the outlines before 2009.

Basically, the area changes of HLG Glacier occurred around the region below the firn basin based on visual interpretation of the images (i.e., shrinks in the icefall and glacier tongue, and retreats of the glacier terminus). Therefore, we adopted the upper patch of the HLG Glacier outline from the Second Glacier Inventory of China as the steady accumulation zone.

Visual interpretation and manual digitization are the main approaches to delineating the glacier outlines. HLG Glacier, a debris-covered valley glacier, has a glacier tongue covered by a variable thickness of debris mantle (Zhang et al., 2011), and the thickness of debris gradually increases from the bottom of the icefall to the glacier terminus, making it difficult to distinguish the glacier terminus and the lateral margin from the preglacial zones and lateral valley walls, respectively. Although the PlanetScope images have a fine spatial resolution, i.e., 3 m, it is not reasonable to rely solely on the subjective interpretations of the mapper to determine the glacier outlines. Therefore, a plausible and clear delineation of the downstream outline of the HLG Glacier requires additional supporting evidence. There are five ways that can be used to assist visual identification of HLG Glacier outlines.

1) **Observations from field trips**: lateral boundaries or glacier terminus are difficult to confirm, but they might be mitigated based on the visual experience of multiple drone flights and glacier surface walking experience.
2) **UAV mapping results**: There are four UAV orthophoto mosaics covering the entire/or roughly glacier tongue (i.e., 2018, 2019, 2020, and 2021) that can be used for consulting the glacier extent identifications. Particularly, the ambiguous lateral boundaries of glacier margin (i.e., lateral margin covered with relative thick debris-mantle) can be roughly inferred from the 3D viewing model.

3) **False color composite (FCC)**: FCC images can provide distinguished texture and pattern of vegetation from other surface features. here, near infrared, red and green bands were used to generate the FCC images. In the middle section of the glacier tongue, some vegetation may rapidly colonize on lateral spots close to the glacier lateral margin. We can first identify the colonized vegetation and then roughly delineate the lateral boundaries. Secondly, there is a difference in brightness between the lateral wall (i.e., light) and the glacier lateral margin (i.e., dark) (Figure 7.2).
4) **Normalized Difference Water Index (NDWI)**: This is the most appropriate function for detecting water bodies. Due to the relatively thin debris mantle in the upper section of the glacier tongue, the NDWI can identify most of the glacier surface of that range. Moreover, the proglacial river (i.e., subglacial channel outlet) can also be detected and we can use this to roughly identify the glacier terminus (Figure 7.2).
5) **Ice crevasses**: along the glacier lateral margins, there are crevasses distributed on both sides. Their distribution also can be used to identify the glacier outlines (Figure 7.2).

Table 7.1 The collected PlanetScope images for HLG Glacier

2009-2014 (14 scenes)	2009-04-29	2018	2018-03-04	2021	2021-03-29
	2010-03-12		2018-03-15		2021-04-21
	2010-10-20		2018-04-04		2021-04-29
	2011-10-22		2018-04-20		2021-05-08
	2012-04-20		2018-05-15		2021-06-13
	2012-11-10		2018-06-29		2021-08-02
	2013-05-26		2018-07-21		2021-09-24
	2013-06-11		2018-11-30		2021-09-29
	2013-08-05	2019	2019-01-25		2021-10-02
	2013-09-28		2019-02-20	2022	2022-03-18
	2013-11-08		2019-03-29		2022-03-24
	2014-03-11		2019-04-13		2022-04-12
	2014-03-28		2019-06-03		2022-05-10
	2014-04-16		2019-07-28		2022-07-05
2015-2016 (5 scenes)	2015-04-03		2019-08-16		2022-07-14
	2016-07-20		2019-09-27	This table lists all available PlanetScope images that the HLG Glacier is visible or partly visible.	
	2016-08-17		2019-10-03		
	2016-10-24		2019-10-19		
	2016-11-17	2020	2020-04-16		
2017	2017-04-19		2020-05-04		
	2017-05-13		2020-06-24		
	2017-06-11		2020-07-03		
	2017-07-17		2020-08-20		
	2017-08-05		2020-08-23		
	2017-09-08		2020-08-26		
	2017-09-24		2020-10-29		
	2017-10-07				
	2017-10-27				
	2017-11-06				
	2017-11-16				
	2017-12-04				

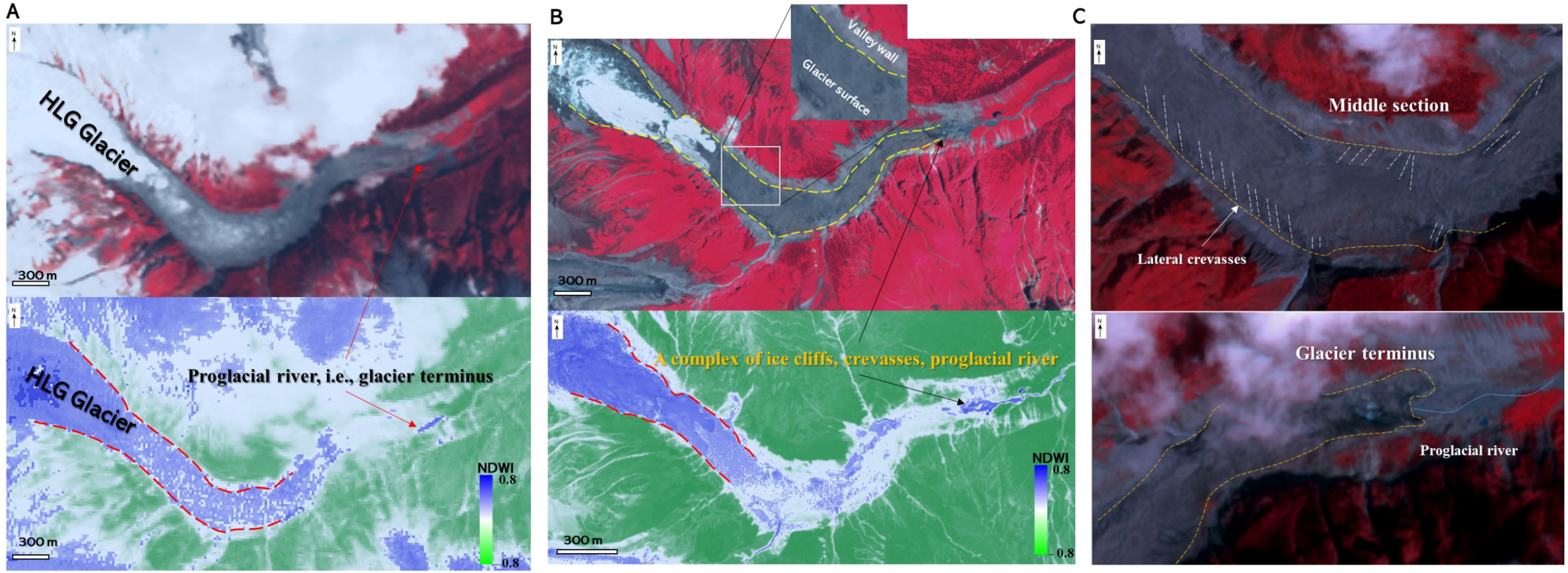

Figure 7.2 FCC maps and NDWI maps. (A) is Landsat TM of 2009-06-03. (B) is Sentinel-2 of 2021-08-04. (C) Middle section of the HLG Glacier and the glacier terminus

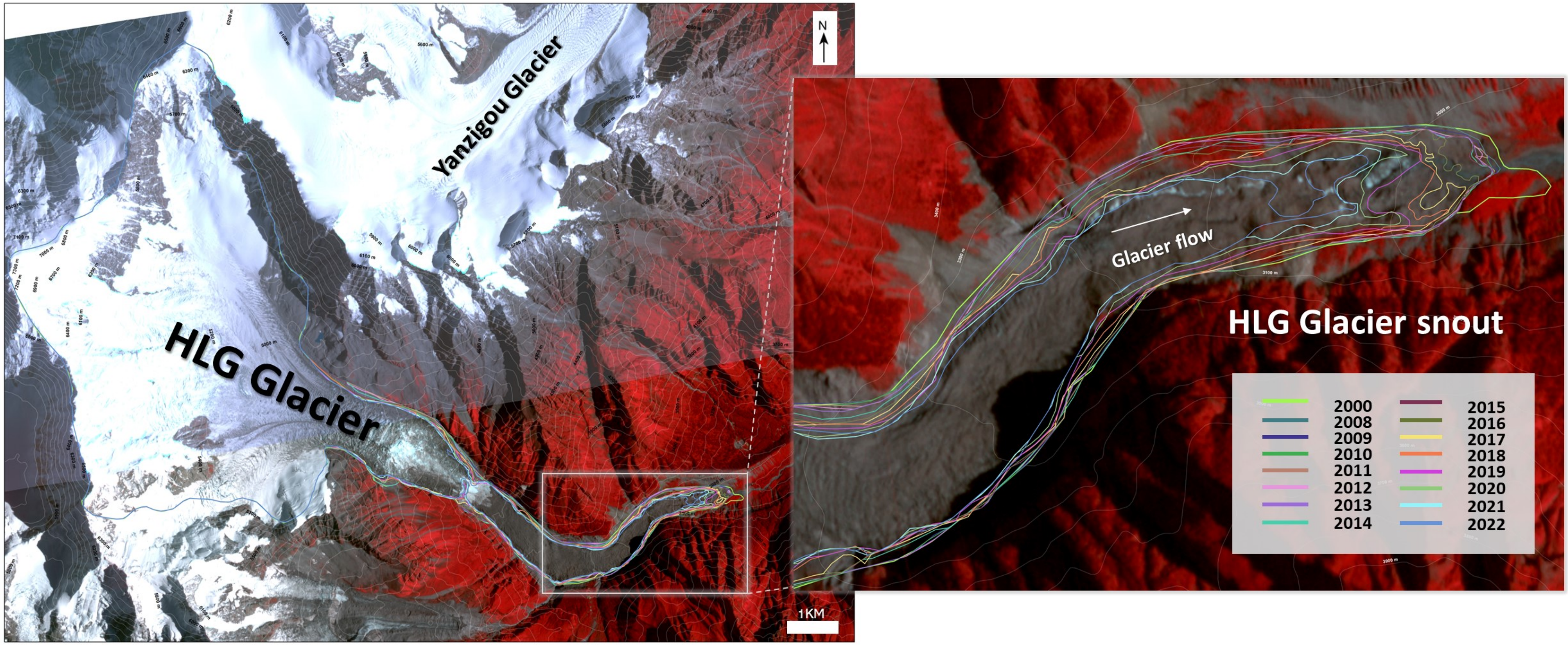

Figure 7.3 Glacier extent extractions from multi-sourced datasets (i.e., Landsat TM and PlanetScope images)

7.3.2 Glacier area changes of HLG Glacier from 2000 to 2022

Overall, the HLG Glacier shrunk about 1.17 km^2 from ~ 24.90 km^2 in 2000 to ~23.73 km^2 in 2022 (Figure 7.3). Basically, the ice surface loss can be divided into three phases from 2000 to 2022, that is, 2000 to 2008 (i.e., -0.63 * 10^4 km^2/year), 2008 to 2014 (-3.00 * 10^4 km^2/year), and 2014 to 2022 (i.e., -11.75 * 10^4 km^2/year). The majority of reduction of the surface areas occurred in the region below the firn basin. Specifically, the increased hole of icefall (exposed underlaying rocks), the narrowing glacier tongue, and the rapidly retreating glacier terminus.

A consistent and steady shrink of ice surface area in this period can be seen in Figure 7.4 and the recession continues with an accelerated tendency (i.e., from -0.0063 to -0.1175 km^2/year). For the periods of 2000 to 2008 and 2013 to 2022, both equally have a time interval of 8 years, the former only loses about 0.05 km^2, while the latter loses almost 1 km^2, which is equivalent to 4% of the total area in 2000, and more than 85% of the total area lost between 2000 and 2020. The area lost after 2008 accounts for 95% of the total loss. The total loss is approximately equivalent to 5% of the 2000 area but considering that the downstream area only accounts for about 15% of the total area, the total loss is therefore roughly equivalent to 33% of the downstream area in 2000. In terms of the rate of loss, the most recent eight years (2014 to 2022) were about 19 times greater than the first eight years (2000 to 2008) and about 4 times greater than from 2008 to 2014. Generally, the inflection point of change occurs around 2008.

Among the area changes of the HLG Glacier, the triggers that cause area changes can be classified into two categories roughly: ***1)*** area changes due to mechanical ablation, such as glacier terminus ice collapse and sustained ice avalanche of icefall; and ***2)*** area reduction due to general melting. Area changes of glacier terminus and glacier icefall approximately started to occur in 2017 and 2014, respectively. These areas change from mechanical ablation is about 0.06 km^2 totally (0.03 km^2 for both glacier terminus and glacier icefall), which accounts for about 12% of total glacier area lost.

Apart from the locations of areal reduction mentioned above, the upper part of the icefall (joint area of tributary glacier flow, 4500 to 5000 m a.s.l.) also shows an areal recession (Figure 7.3), which further illustrates the high intention of the glacier receding.

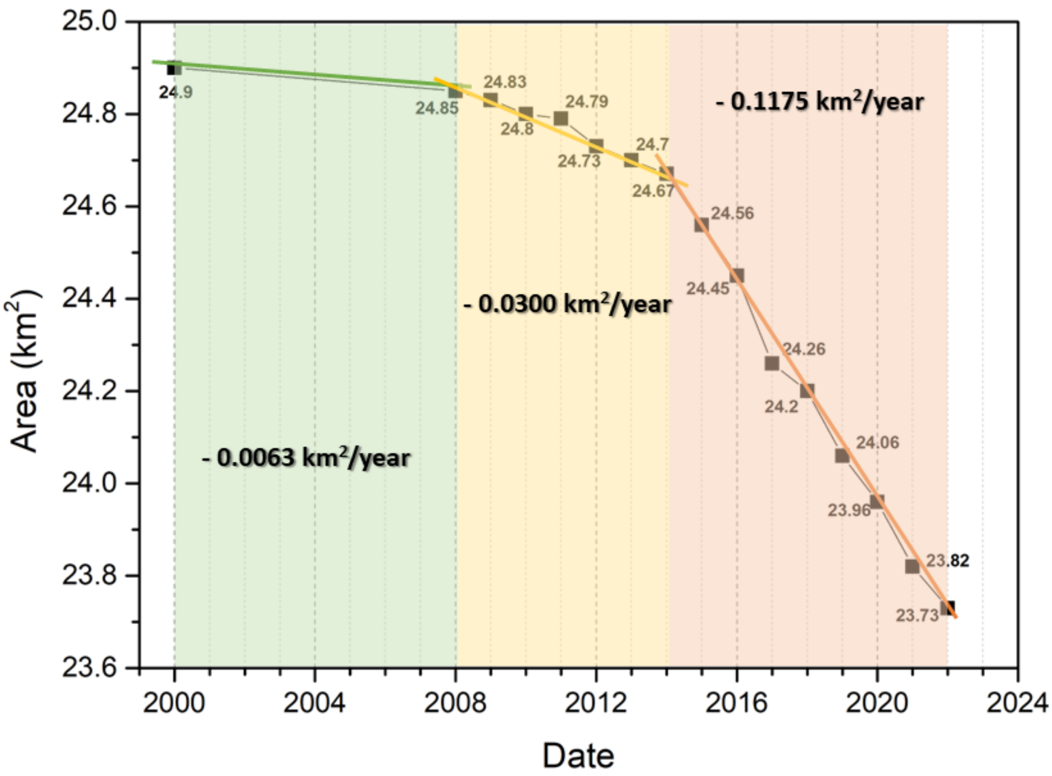

Figure 7.4 Glacier area changes from 2000 to 2020. Green, yellow and red indicate the three phases of the acceleration of glacier ice surface loss.

7.4 Ice mass changes derived from differencing of DEMs

7.4.1 Uncertainty analysis

The uncertainties of geodetic mass balance estimation are mainly from three sources, which are assumed mutual independent, that is, (1) errors in the rate of the elevation change, (2) errors in the area of glacierized area (i.e., glacier area), (3) assumed ice density (i.e., conversion from volume to mass). For the overall uncertainties of geodetic glacier mass balance changes, the methods of calculations were adopted from Brun et al (2017) and Taylor et al (2022).

1) **Estimated errors in the elevation changes ($\sigma_{\Delta h}$)**: the standard deviation of residuals of the non-glacier region (relative stable region) can be used to estimate the accuracy of glacier surface elevation changes. Therefore, we cast a ***Buffer Function*** to buffer glacier extent (i.e., glacier extent of 2000) outward about 250 m to calculate the standard deviation of pixels in this buffered region. Moreover, a large sampling area (e.g., HLG Glacier) may cause a relatively

strong correlation (i.e., spatial autocorrelation) in the elevation values between neighboring pixels. So we used an approximate 500 m decorrelation length (Brun et al., 2017; Taylor et al., 2022) to avoid overestimating the uncertainties of surface elevation changes as the spatial correlations can be negligible when less than 20 pixels (here, the pixel size is 30 m). Thus, the uncertainties of the rate of the glacier elevation change can be calculated by the following Equations (6) and (7):

$$\boldsymbol{A_{corr} = \pi \cdot L^2} \qquad (6)$$

$$\boldsymbol{\sigma_{\Delta h} = \sigma_{dh}\sqrt{\frac{A_{corr}}{nA}}} \qquad (7)$$

Where $\boldsymbol{A}$ is the area of the glacier, $\boldsymbol{L}$ is the decorrelation length (i.e., 500m), $\boldsymbol{\sigma_{dh}}$ is the standard deviation of the stable non-glacier area. $\boldsymbol{\sigma_{\Delta h}}$ is the uncertainty of glacier surface elevation changes and $\boldsymbol{n}$ is the factor for the errors of elevation change of un-surveyed area (here, 5 is used for $\boldsymbol{n}$) (Berthier et al., 2014).

2) **Estimated errors in the glacier area** ($\boldsymbol{\sigma_A}$) are calculated as the 10% of the total glacier area as we adopted the method based on Kääb et al. (2012) and Brun et al. (2017), hereby,

$$\boldsymbol{\sigma_A = 0.1A} \qquad (8)$$

3) **Errors in the assumed ice density**: we followed the assumed ice density from Huss (2013), using 850 kg m^{-3} as the ice density and 60 kg m^{-3} as the uncertainty.

So, the uncertainties of ice volume changes can be concluded as the following Equation (9):

$$\boldsymbol{\sigma_{\Delta V} = \sqrt{(\sigma_{\Delta h}(p_A + n(1 - p_A))A)^2 + (\sigma_A dh)^2}} \qquad (9)$$

Where, the $\boldsymbol{\sigma_{\Delta V}}$ is the uncertainty of the ice volume change, $\boldsymbol{dh}$ is the average rate of elevation change, $\boldsymbol{p_A}$ is the proportion of the area with the removal of the outlier.

Therefore, the overall uncertainty of glacier mass changes ($\boldsymbol{\sigma_{\Delta B}}$) was drawn as the following Equation (10):

$$\sigma_{\Delta B} = \sqrt{(\sigma_{\Delta V}\rho_i)^2 + (\sigma_{\rho_i}\Delta V)^2} \qquad (10)$$

Where, ρ_i is the ice density (850 kg m-3 ± 60 kg m^{-3}), σ_{ρ_i} is 60 kg m^{-3} and ΔV is the volume change (Brun et al., 2017).

The alternative factor is related to the characteristics of the terrain. Specifically, the elevation of HLG Glacier and the surrounding region ranges from less than 1000 m a.s.l. to more than 7000 m a.s.l., which leads to the massive shades in the layover of raw data and further results in the low matching accuracy of stereopairs. The poor texture and the oversaturated brightness on debris-free glacier surfaces (i.e., above the glacier icefall) also result in the wrong matching point pairs to some extent.

7.4.2 Ice volume changes and ice mass changes

7.4.2.1 Ice height changes and volume changes

We used the DoD workflow to calculate the ice surface height changes and their corresponding ice volume changes. In the DoD calculations, the level of detection (LOD) was set as 1 m as the debris that covered the glacier tongue was approximately less than 1 m, which can mitigate the impact from the debris mantle thickness. Some outlier values were masked out for the reliable estimations of glacier ice volume changes. The main outlier to be removed is the pixels that are more than 7000 m a.s.l. higher and those that are lower than 2000 m a.s.l.

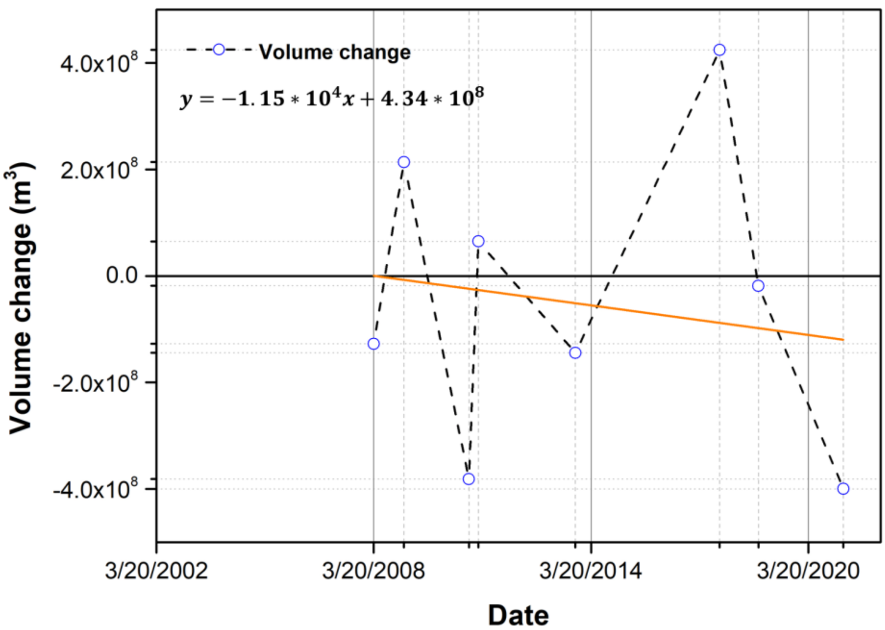

Figure 7.5 Ice volume changes from 2002 too 2021.

From combined calculations, the overall glacier ice volume changes reduced by about 0.37 ± 0.01 km^3 between 2002 to 2021 (Figure 7.5 and Table 7.2). HLG Glacier has experienced a massive ice volume recession within the recent two decades. In regards to the ice volume of HLG Glacier listed in the Second Glacier Inventory of China, this accounts for more than 14% of total glacier ice volume (~2.60 km^3) if the calculation is robust.

Table 7.2 Volume changes for each comparison pair

Date	**Interval days (years)**	**Volume changes for the entire glaciers (km^3)**
2002/02/20 - 2008/3/20	2220 (6-year)	-0.13 ± 0.01
2008/03/20 - 2009/01/18	304 (0.8-year)	0.21 ± 0.01
2009/01/18 - 2010/11/05	657 (1.8-year)	-0.38 ± 0.01
2010/11/05 - 2011/02/09	96 (0.3-year)	0.06 ± 0.01
2011/02/09 - 2013/10/12	976 (2.7-year)	-0.14 ± 0.01
2013/10/12 - 2017/10/07	1456 (4-year)	0.42 ± 0.01
2017/10/07 – 2018/11/02	391 (~1-year)	-0.02 ± 0.01
2018/11/02 - 2021/03/08	857 (2.3-year)	-0.40 ± 0.01
2002/02/20 - 2021/03/08	**6956 (19-year)**	**-0.37 ± 0.01**

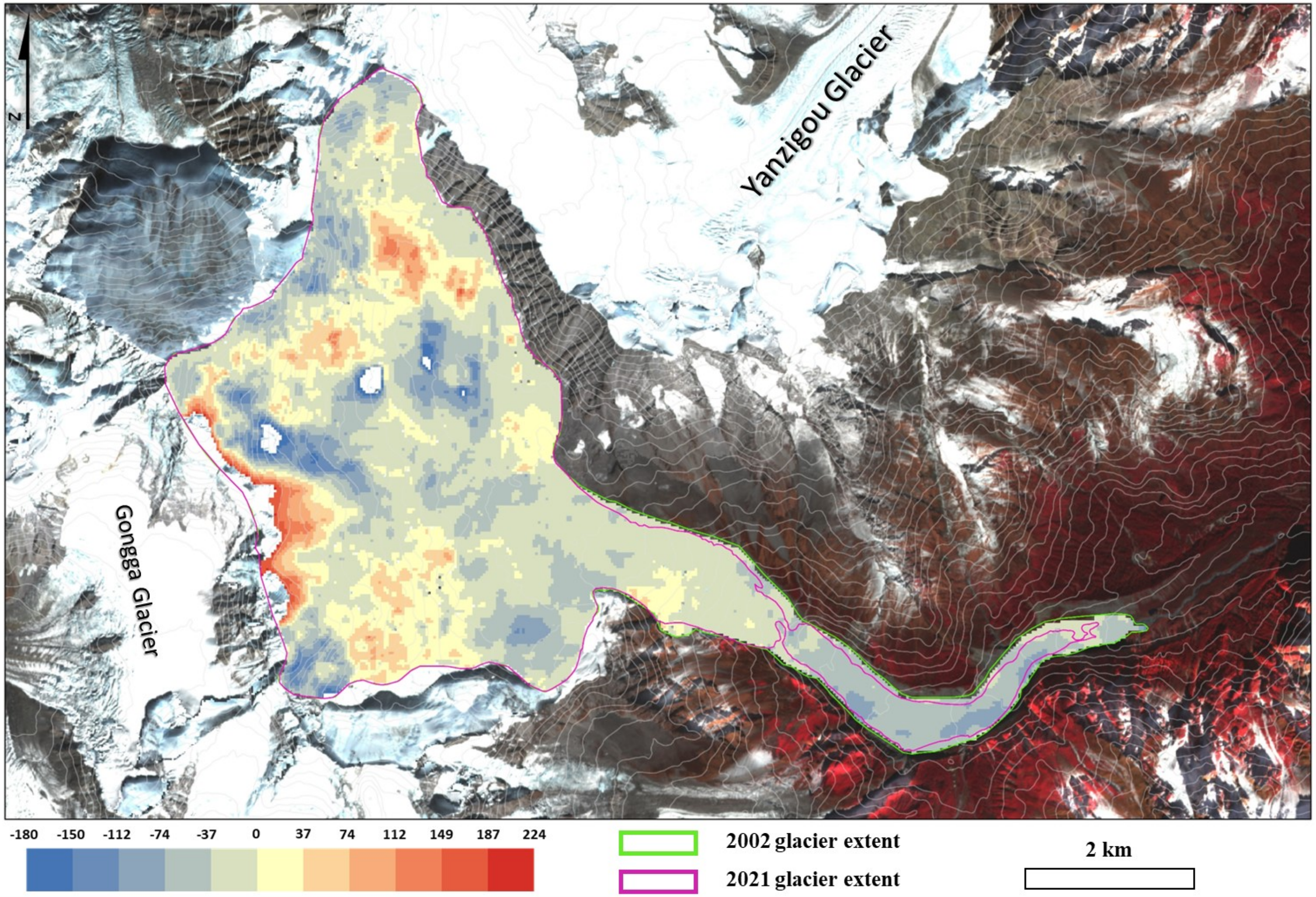

Figure 7.6 Surface elevation changes of the entire HLG Glacier from 2002 to 2021.

From the aspect of the spatial distribution of ice thickness changes (Figure 7.6), the entire glacier tongue and even a large part of the firn basin was in a significant recession. Specifically, the glacier terminus has completely vanished with surface height changes of about 30 to 113 m from 2002 to 2012. The south side of the glacier tongue shows a more severe surface height decline than the northern margin of the glacier tongue, for which some spots decreased more than 90 m in surface height (Figure 7.7). The icefall, as the connection between the glacier tongue and the upper patch, also recedes greatly with a surface reduction of about 90 m. The surface height recession also dominates the large part of the accumulation zone of HLG Glacier, i.e., the regions from 5600 m a.s.l to the top of the icefall. The area of positive changes in surface height was roughly distributed around the western margin of the glacier (i.e., regions near the summit).

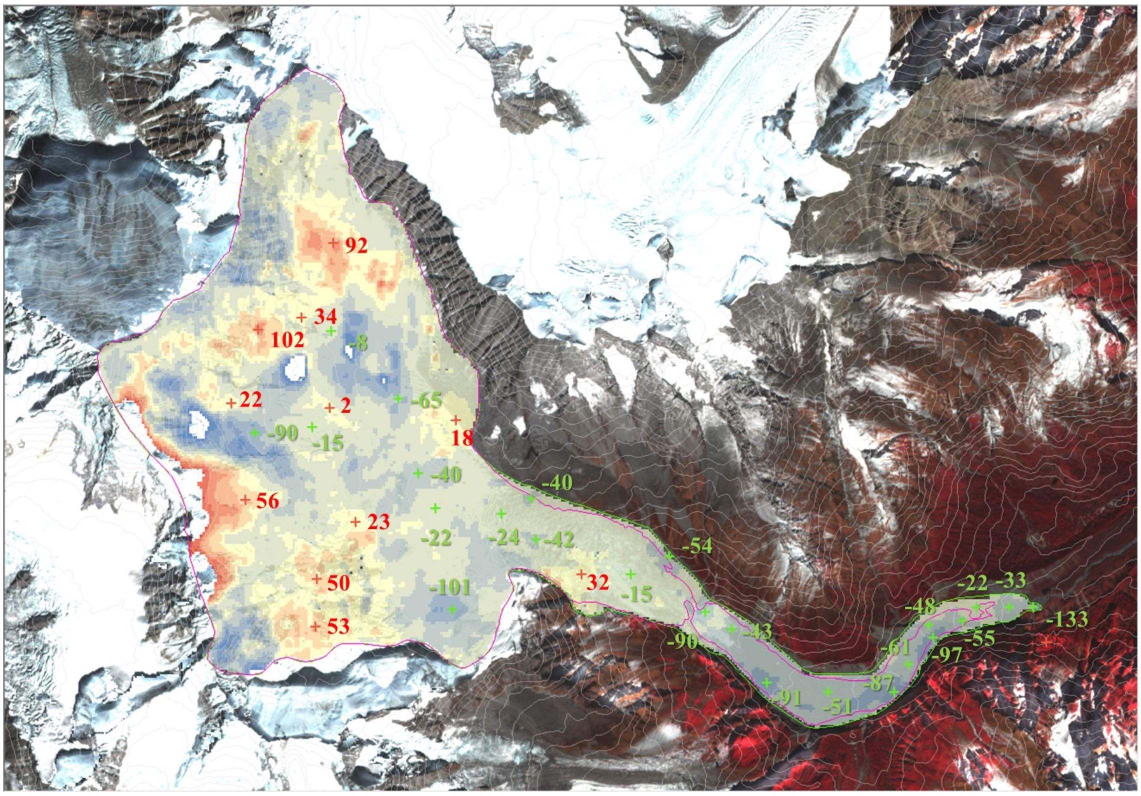

Figure 7.7 Ice thickness changes of selected points from 2002 to 2021. Green crosses indicate the negative changes and red crosses indicate positive changes.

The overall tendency of ice volume changes decreased from 2002 to 2021. The average change in thickness is -15.17 ±0.15 m from 2002 to 2021, and hereby the annual reduction in ice thickness is 0.80 ± 0.01 m (Table 7.3). Figure 7.8 illustrates the ice thickness change along the glacier centreline, more than 80% of the glacier was dominated by surface height reductions, which show a continuous and widely thinning from 2002 to 2021. The negative maximum value appears at the glacier terminus, which can be interpreted as the glacier terminus region of 2000 and following years having completely ablated.

The elevation change within the ice fall is still negative, but it shows a trend of progressively decreasing. In the ice fall, the most negative value exceeds 70 m, which mainly occurs in the lower part of the ice falls where the discussion occurred. At the upper end of the icefall (i.e., the part that meets the firn basin), there is a small elevation increase, but it does not exceed 10 m. This is probably due to the continuously equal accumulation and ablation, which makes this area close to the equilibrium line altitude (ELA). So, if the interpretation is plausible, then the ELA in 2021 might be near 5900 m a.s.l.

The overall firn basin was also dominated by the surface reduction, but the magnitude of the reduction is relatively smaller than the glacier tongue with an average value of –20 m. Only the high-altitude region close to the glacier peak is the area with positive changes in surface height while the magnitude is not significant with less than 10m in average.

Table 7.3 Ice surface change for each date intervals

Date intervals	Ice surface changes (m)
2002-2008	-5.22±0.05
2008-2013	-10.17±0.06
2013-2018	15.68±0.05
2018-2021	-16.64±0.05
2002-2021	**-15.17 ±0.15**

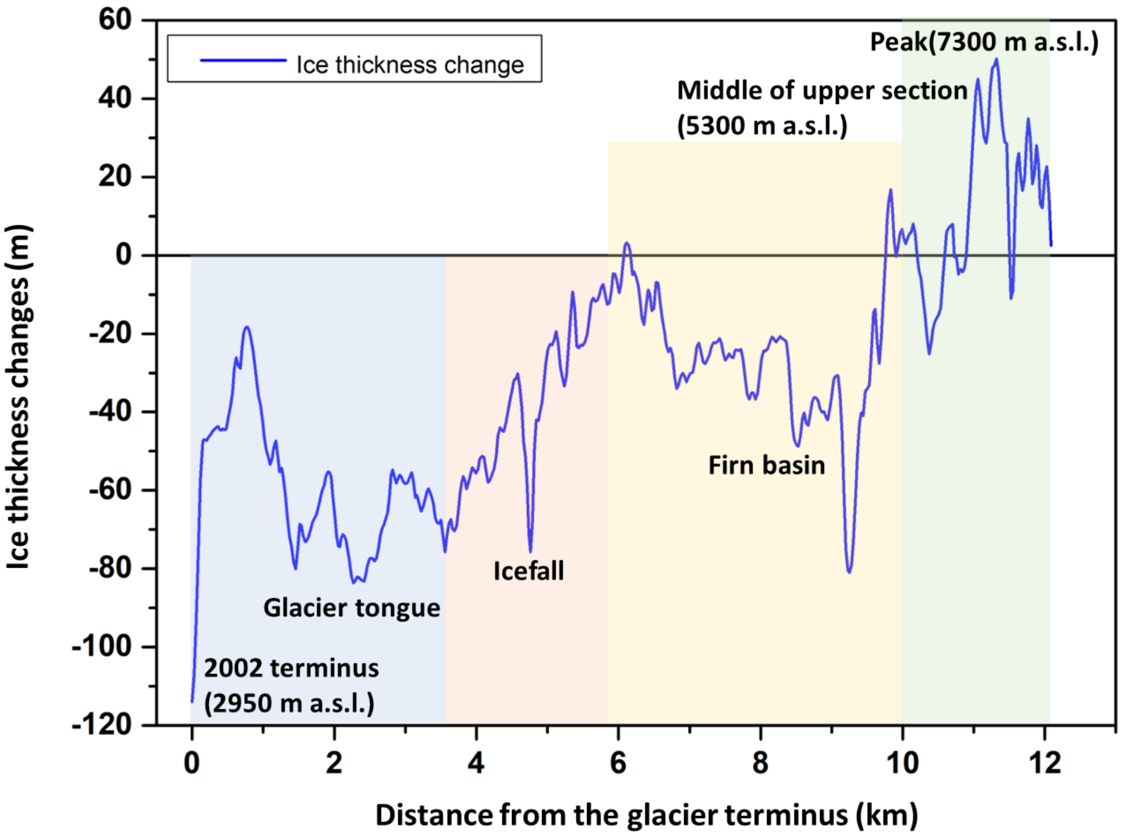

Figure 7.8 Ice thickness changes along the glacier centerline of HLG Glacier from 2002 to 2021

7.4.2.2 Ice mass changes

To calculate the change in mass balance from the change in glacier ice volume, all thickness change pixels within the polygon of the glacier extent were converted to the appropriate projection coordinate system (WGS84 UTM region 47N). The pixel value was next multiplied by their corresponding areas and summed. The resulting ice volume change was subsequently divided by the mean glacier area (here we use the average between 2002 and 2021) to obtain the glacier thickness change. Finally, the glacier thickness change was multiplied by the mean ice density and then divided by the density of water to calculate the glacier geodetic mass balance in a unit of m w.e. yr $^{-1}$.

The calculation of total ice mass changes from 2002 to 2021 is - 12.60 $\pm$ 0.89 m w.e., hereby the annual mean ice mass change is - 0.66 $\pm$ 0.05 m w.e.

7.4.3 Comparison with previous works

A surface energy-mass balance change model (Zhang et al., 2012) estimated a catchment scale of glacier mass balance change (i.e., 7 glaciers in the HLG Glacier catchment) from 1952 to 2009 (Figure 7.9). Previously it had been in a fluctuation period (slight negative balance) and went all the way down in about 2004 with an enhanced negative balance. Based on their estimation, the totally accumulative mass balance for the HLG Glacier catchment is -15.85 m w.e., and the annual mean is – 0.38 m w.e., within 40 years from 1968 to 2008. The mass balance change of HLG Glacier from 1968 to 2000 is about -14.19 ± 1.00 m w.e., and the annual mean mass balance is -0.43 ± 0.03 m w.e.

Results from Zhang et al. (2012) revealed that the ice mass balance of HLG Glacier was in a continuous negative balance from 1968 to 2000. Compared with this, the annual mean mass balance from 2002 to 2021 from this thesis is about - 0.66 ± 0.05 m w.e., which is roughly 1.5 times than the mass balance from 1968 to 2000. From the aspect of total mass balance, the cumulative ice loss from 2002 to 2021 (19 years) is 90% of the ice mass from 1968 to 2000 (i.e., 32 years). Thus, the comparison indicates that the glacier dynamics have been controlled by the glacier recession decades ago and the recession also has been enhanced in the recent decade.

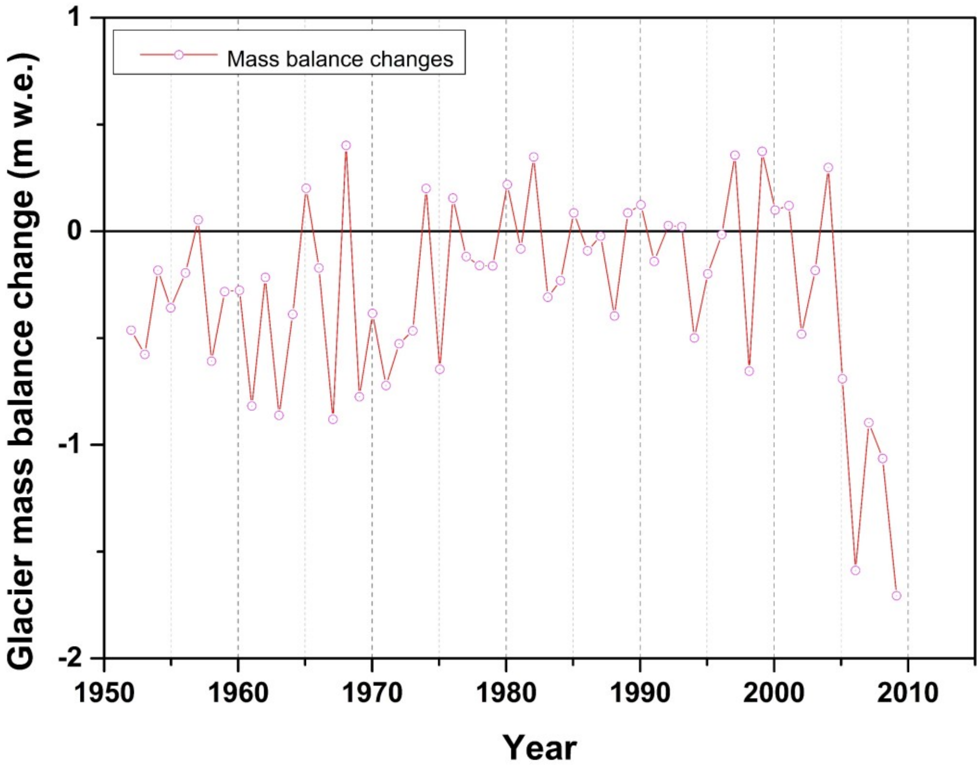

Figure 7.9 Mass balance of HLG Glacier basin from 1952 to 2009 (extracted from Zhang et al., 2012)

7.5 Frontal ice collapse events at Hailuogou Glacier terminus and their contributions to the mass balance of the entire glacier

7.5.1 Ice collapse events

About 27 collapsing events have been identified with varied sizes from collected optical satellite images (i.e., Planet scope) and 2 collapsing events (i.e., a large event and a small event; refer to Table 6.2) were captured during the field trips with UAV images. The interannual illustration of the ice collapse events (i.e., numbers of spots and area induced by collapse) is shown in Figure 7.10. Additionally, Figure 7.11 shows the areal magnitude and spatial distribution of ice collapse events collected from Planet scope images from 2017 to 2022. Details of the collapsing events are shown in Table 7.4. The results show that most of the identified ice collapse events occurred during the ablation season (or because it was difficult to identify ice collapses during the accumulation season), of which the highest number occurred in 2019 (i.e., 11), followed by 2021 and 2020 with 8 and 6 collapses, respectively. In 2020, there had the largest area of ice collapses, including two events with an intensity of more than 3000 m^2. There are two confirmed ice collapse events (2020/09/05-2020/09/10;

2020/09/10-2020/11/05) and we have collected aerial images before and afterward of the date that ice collapse events occurred.

We used FCC and NDWI to inter-consult the delineation of frontal ice collapse events. The frontal collapse events can show a relatively white-blue color (real color) that can be easily distinguished from the surrounding debris-covered glacier surface. As we cannot know the real area of the ice collapse event, we delineate the all white-blue pixels belonging to that collapse event. In other words, the delineated area might overestimate the area of a real ice collapse event. For example, compared with Figure 1.2 B and E, some small ice collapse events like Figure 1.2 B that occurred at the frontal cliffs are possibly overestimated as the ice debris from the collapse event will fall outward to the off-glacier area so that forming an expansion of an ice collapse event. While some ice collapse events like Figure 1.2 and the delineated area are basically the real collapsed area. Here, as we aim to estimate the rough contribution of the ice collapse events that occurred around the glacier terminus area, therefore all delineated areas are considered as the real area induced by collapse events for the subsequent estimation.

Table 7.4 A summary of ice collapse events at glacier terminus from 2017 to 2022

No.	Year	Date (YYYY/MM/DD)	Collapse spot	Collapsed area (m^2) (or ice debris caused by collapse)
1	2017 (5)	20170419	1	300.52
2		20170924	1	2869.39
3		20171007	1	1412.47
4		20171027	1	2610.99
5		20171106	1	921.19
6	2018 (3)	20180629	2	409.50 + 263.90 = 673.40
7		20180721	1	921.68
8	2019 (11)	20190329	1	738.91
9		20190603	1	111.01
10		20190728	2	283.77
11		20190816	2	908.53
12		20190927	3	505.66 + 578.45+ 1047.30 = 2131.41
13		20191003	1	308.79
14		20191019	1	307.00
15	2020 (6)	20200504	1	631.23
16		20200820	2	5770.15+1059.88 = 6,830.03
17		20200823	1	337.74
18		20200826	1	705.87
19		20201105 (UAV)	1	5927
20	2021 (8)	20210329	1	429.53
21		20210429	1	1429.96
22		20210802	1	798.51
23		20210924	3	1242.31+844.56+449.16 = 2,536.03
24		20210929	2	640.24+347.99 = 988.23
25	2022 (5)	20220318	1	527.24
26		20220324	1	596.00
27		20220324	1	890.18
28		20220705	2	482.19+896.84=1,379.03

Light orange = less than 1000 m^2; medium orange = 1000 m^2 – 3000 m^2; dark orange = more than 3000 m^2

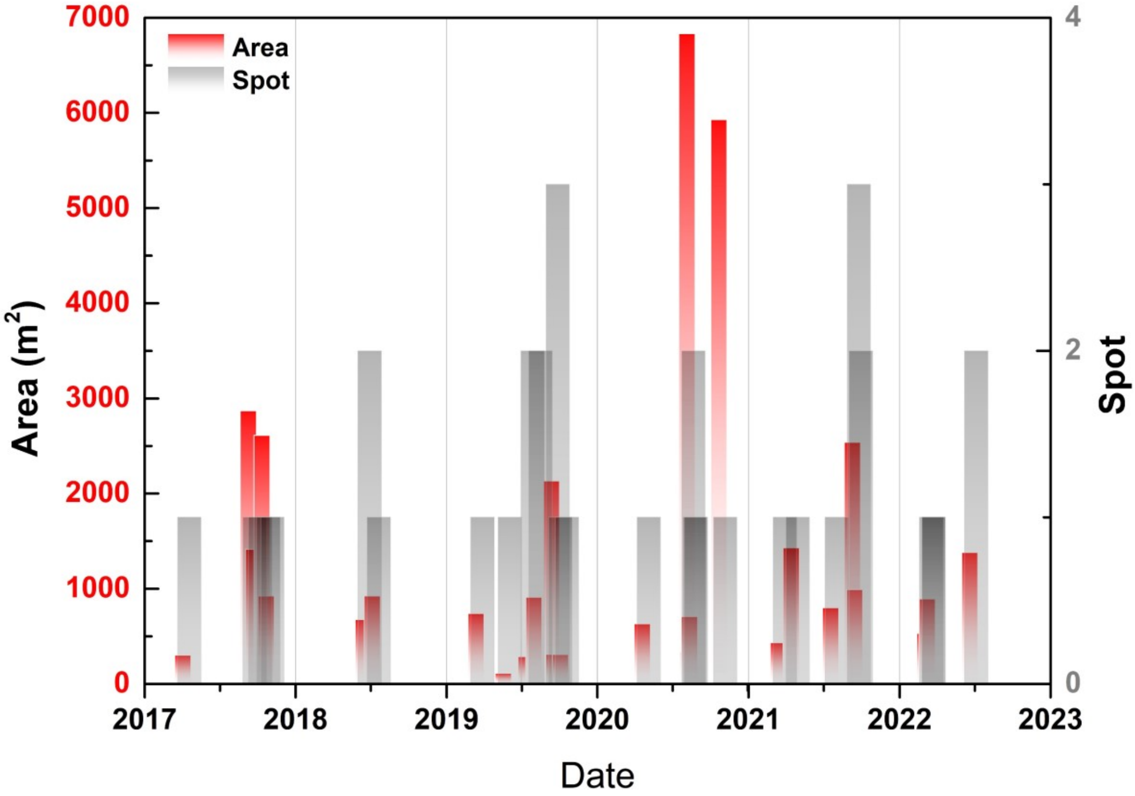

Figure 7.10 Areas and spots of ice collapse events that occurred at the HLG Glacier terminus from April 2017 to July 2022

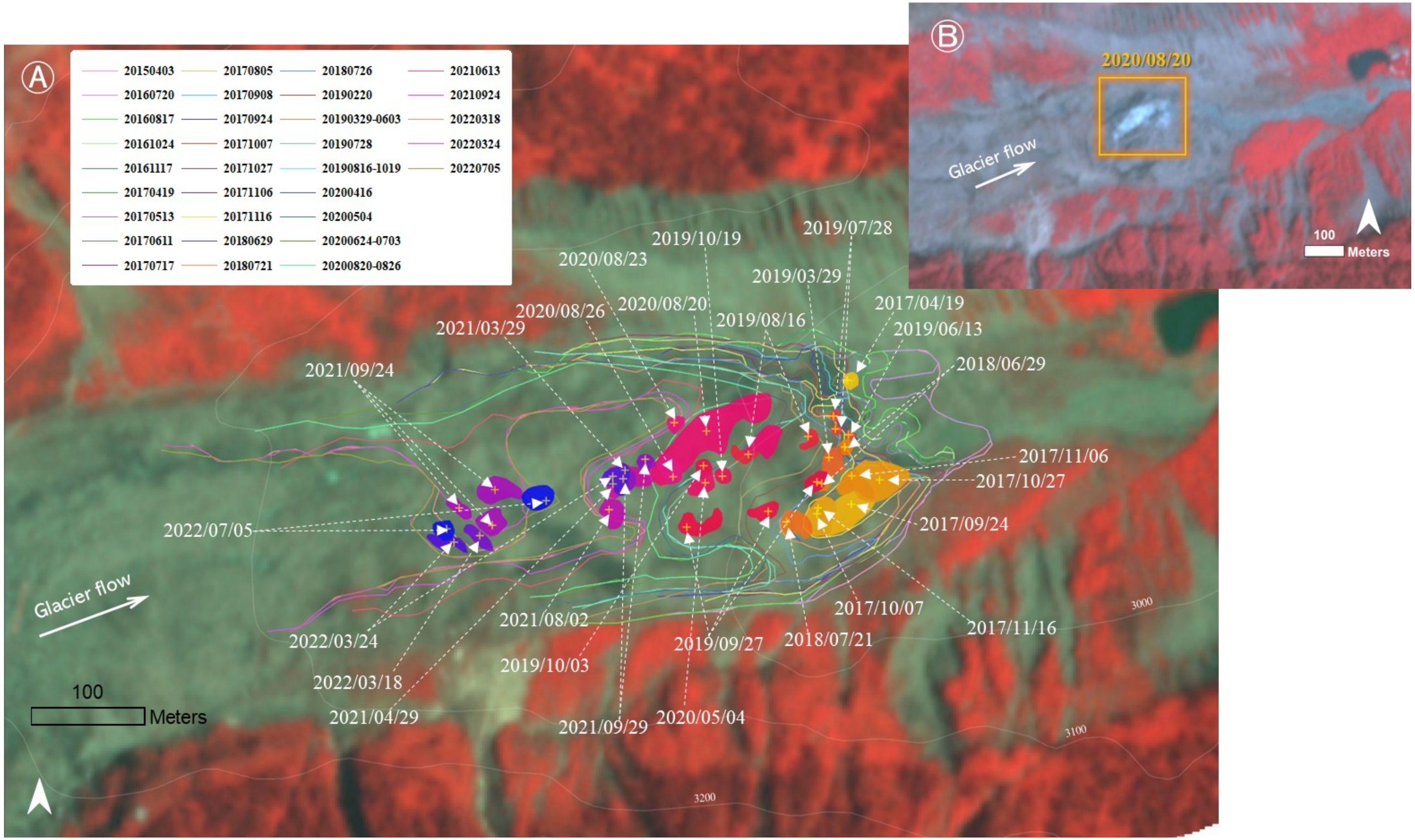

Figure 7.11 A: Identified collapse events at the HLG Glacier terminus and multiple years of HLG Glacier terminus extents (April 2015 to July 2022) delineated from the PlanetScope images. B: an example of a frontal ice collapse event (2020/08/20)

7.5.2 Contribution of frontal ice collapse to the mass balance change of the entire glacier

As mentioned in ***Section 7.5.1***, ice collapse events that occurred at the HLG Glacier terminus were visually identified and delineated from all available PlanetScope images. Based on the visual check, identifiable ice collapse events mainly occurred since the ablation season of 2017 (collapse events in Figure 7.11).

In ***Chapter 6***, large and small ice collapse events have been captured by UAV surveying (refer to Table 6.2). The area changes and the volume change induced by the collapse events were calculated using high-resolution orthophoto mosaics and DEMs. So, we can estimate the volume change based on areal changes from the perspective of magnitude level. Simply, for the glacier terminus area (i.e., here we use the statistics from Table 6.2 g), the correlation between the area changes (7,234 m^2) and the volume changes (495,100 m^3) can be interpreted as Equation (11):

$$\boldsymbol{1\,m^2(area\ change) \rightarrow 68\,m^3(volume\ change)} \quad (11)$$

Hereby, the formula between area changes and the volume changes can be written as:

$$\Delta\boldsymbol{A} * \mathbf{68} = \Delta\boldsymbol{V} \quad (12)$$

$$\frac{\Delta\boldsymbol{V}}{\boldsymbol{V_T}} = \boldsymbol{\rho_v} \times \mathbf{100}\% \quad (13)$$

where, in Equation (12), $\Delta\boldsymbol{A}$ is the areal changes attributed to the ice collapse events; $\Delta\boldsymbol{V}$ is the corresponding volume change; in Equation (13), $\boldsymbol{V_T}$ is the ice volume change of the entire glacier (i.e., here refer to Table 7.2; i.e., the volume change is **0.42 km^3** from 2017 to 2021); $\boldsymbol{\rho_v}$ is the portion of the contribution attributed to the ice collapse events.

Based on the interpretation of PlanetScope image from 2017 to 2021, the total area changes due to ice collapse events are about 30,000 m^2 (i.e., $\Delta\boldsymbol{A_p}$). Therefore, the volume changes ($\Delta\boldsymbol{V_p}$) due to the frontal ice collapse can be calculated by Equation (12) and rewritten as Equation (14):

$$\Delta\boldsymbol{A_p} * \mathbf{68} = \Delta\boldsymbol{V_p} \quad (14)$$

Therefore, the corresponding volume change (i.e., $\Delta \boldsymbol{V_p}$) due to frontal ice collapse events is **2,040,000 m³** (0.00204 km^3). Thus, the portion of the contribution attributed to the ice collapse events can be calculated by Equation (13), which is about **0.49%.**

Although we used as many satellite images as possible to identify the ice collapses, there are inevitably some ice collapses that are not identified and represented in Figure 7.11 due to cloud obscuration. Therefore, for a maximum case, if we attribute the area loss at the terminus of this glacier to ice collapse for all glaciers (i.e., excluding the area reduction on both sides, only the front margin of the glacier), then its approximate area loss is about **69,000 m²** (i.e., $\Delta \boldsymbol{A_m}$). Consequently, the estimated volume change for the maximum case is **4,692,000 m³** (i.e., $\Delta \boldsymbol{V_m}$), which leads to the portion of the contribution attributed to the ice collapse events under the maximum case – **1.12%**.

The contribution of that to the glacier tongue of the HLG Glacier was also calculated as additional information for the processes of glacier recession. The extent between the bottom of the icefall to the glacier terminus (2002) was delineated as the glacier tongue of the HLG Glacier. Figure 7.12 illustrates the ice volume changes in the glacier tongue of the HLG Glacier between 2017 to 2021 (Figure 7.12 A) and 2002 to 2021 (Figure 7.12 B). Based on the DoD estimation, the volume change between 2017 to 2021 is -72,312,591.15 ± 185,222.3 m^3. Therefore, the portion range of the contribution to the glacier tongue of HLG Glacier that is attributed to the ice collapse events can be calculated, which is about **2.82%** to **6.49%**.

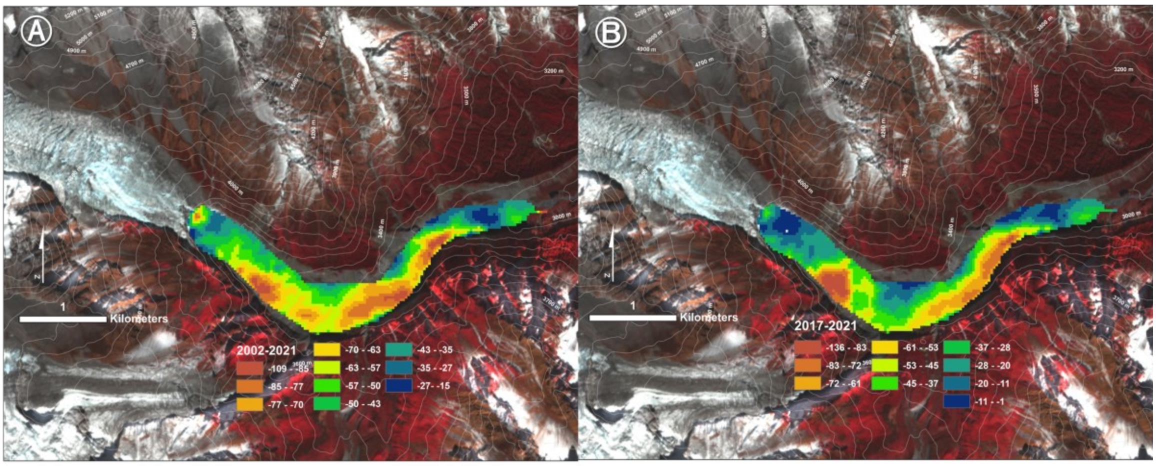

Figure 7.12 The ice surface elevation change (meter) for the glacier tongue of the HLG Glacier. A is ice volume changes from 2002to 2021. B is the ice volume changes from 2017 to 2021.

7.6 Response to climate change

The fluctuation of glacier mass balance is mainly influenced by two factors, the precipitation and the temperature, in which the former determines the accumulation, while the latter (especially the temperature of the ablation season) determines the ablation.

Given the meteorological data from Gongga station (~ 3000 m a.s.l.), the nearest meteorological station to the HLG Glacier, we extracted the annual average precipitation and the average temperature of the ablation season (May to October) from 1998 to 2018 (refer to ***Section 4.2.5***) and plotted them to illustrate their correlations with the ice volume changes of HLG Glacier (Figure 7.13).

As shown in Figure 4.4, the Gongga Station is located on the northeast side of the HLG Glacier with a distance of 1.5 km to the glacier terminus and the elevation is about 3000 m a.s.l. Therefore, considering the distance and the elevation of Gongga Station, the variation of temperature and the precipitation acquired by this station can reflect the regional climate change dominating the HLG Glacier valley to some extent, especially for the glacier tongue.

The changes in temperature and precipitation from 1998 to 2018 as shown in Figure 7.13 a and b, in which both of them are fluctuated over two decades, appearing with opposite tendencies. Specifically, the annual average temperature of the ablation season climbed undulatingly since 2004, despite the value of temperature reaching the lowest in 2017 (8.2 ℃) but it then climbed to the highest in the following year (11.5 ℃). A noticeable declining trend in precipitation can be interpreted from the plots, in which there are 14 years less than 160 mm a^{-1}. Levels of precipitation in the last decade have decreased considerably compared to the early years of 2000.

Within the context of climbed temperatures and reduced precipitation in the HLG valley, the HLG Glacier has responded with a clear signal as shown with the orange dashed line in Figure 7.13. The overall ice volume changes are a continuous reduction from 2002 to 2021. Combined with the established fact of nearly full disconnection between the glacier tongue and accumulation zone, the glacier tongue is basically in the process of becoming a block of dead ice in the near future.

Mt. Gongga region is the most glacierized area of the Hengduan Mountain region developed by maritime glaciers (Liu et al., 2018). The eastern slope of Mt. Gongga, where the HLG Glacier is mainly influenced by the southeast monsoon from the western Pacific. The majority of ice of HLG Glacier is close to the melting point and the glacier flow and the ablation is relatively rapid and intensive, respectively. Therefore, the HLG Glacier is highly sensitive to temperature fluctuation. The ablation rate might be enhanced greatly even if there is a slight change in temperature. Moreover, the precipitation is in continuous reduction since several decades ago. Thus, the negative dynamics of HLG Glacier are a reflection of regional climate changes.

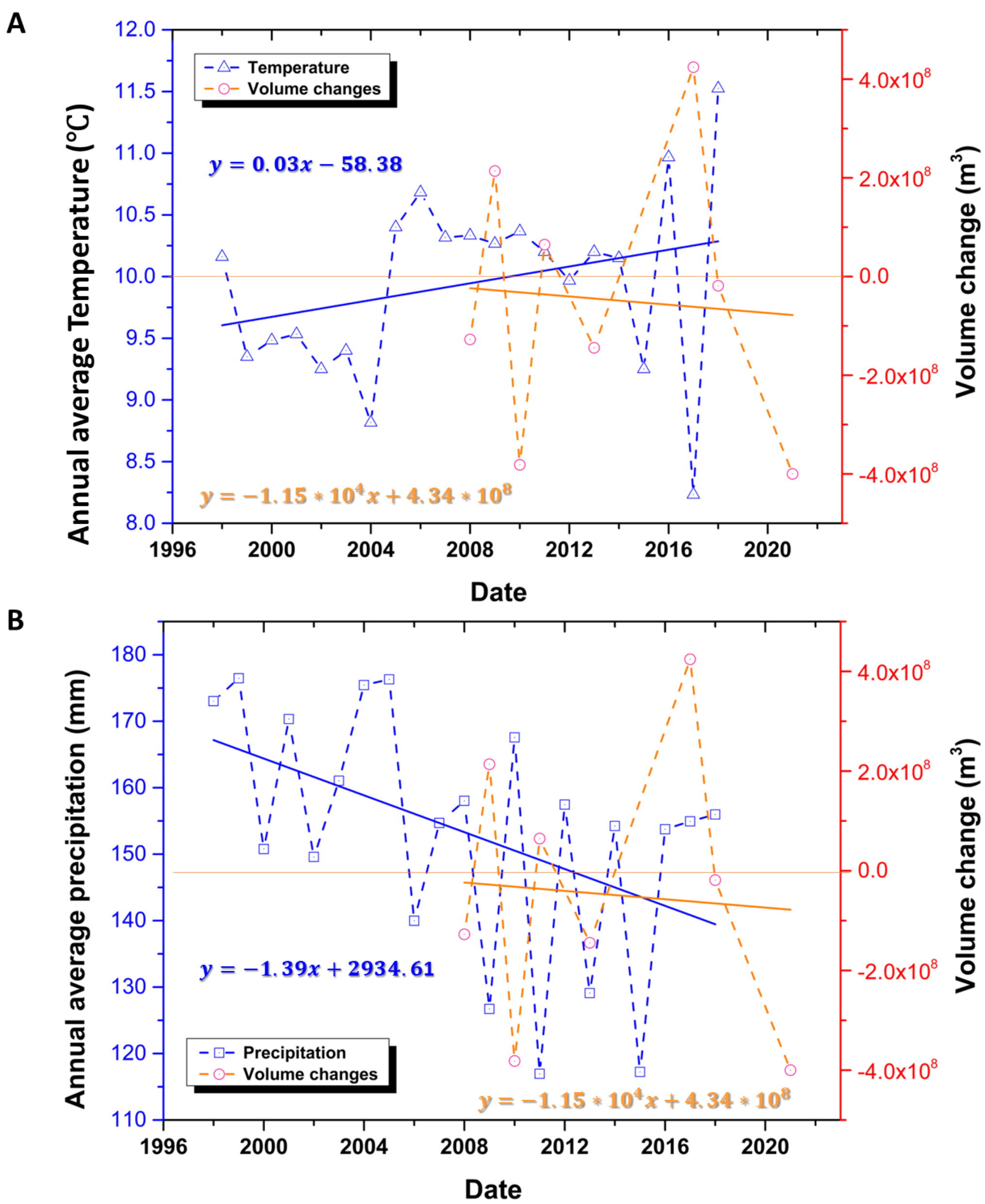

Figure 7.13 The changes in temperature and precipitation from 1998 to 2018 with the variation of Ice volume change from 2002 to 2021.

7.7 Conclusion to this Chapter

Photogrammetrical stereopsis was applied on ASTER stereo images to derive time sequenced DEMs for HLG Glacier from 2002 to 2021 by using NASA Ames Stereo Pipeline. The variation of glacier extent was also extracted from satellite images (e.g., PlanetScope). Results indicate that the overall mass balance change is negative and enhanced. The area of HLG Glacier was in a rapid reduction from ~ 24.90 km^2 in 2000 to ~23.73 km^2 in 2022. Our calculated mass balance is - 12.60 ± 0.89 m w.e. and the annual mean mass balance change is about- 0.66 ± 0.05 m w.e. The annual rate of mass loss is roughly 1.5 time than the mass balance from 1968 to 2000.

Since the ice collapse event was first identified on satellite images in 2017, about 27 ice collapse events have been identified with about 30,000m^2 in area loss. The estimated contribution to the mass balance change of the entire glacier that is attributed to frontal ice collapse is limited (i.e., 0.48% to 1.12%) and the contribution of that to the glacier tongue is about 2.82% to 6.49%. However, the mechanical ablation (e.g., frontal ice collapse and subglacial/englacial conduit’s roof collapse) has changed the glacier dynamics and the way of losing ice mass to some extent.

Chapter 8: Discussion

8.1 Introduction

This chapter presents discussions of the main findings and outlines the major contributions to the related research community.

8.2 Knowledge gap addressed and thesis novelty

Glaciers in the Tibetan Plateau are melting at an unprecedented rate in the context of global warming. HLG Glacier, a rapidly receding temperate land-terminating glacier in the southeastern Tibetan Plateau, has been observed to lose mass partly through ice frontal mechanical ablation (i.e., ice collapse). Mechanical ablation is no longer only observed in water-terminating, but also occurs in rapidly receding land-terminating glaciers. The mechanical ablation is an important element affecting glaciers in terms of ice recession patterns and mass balance changes, which has not been well documented and studied in previous studies.

To my knowledge, this thesis provides comprehensive analysis to-date of HLG Glacier, in terms of landscape mapping (***Chapter 5***), the quantification of the frontal ice collapse (***Chapter 6***) and recent mass balance change (***Chapter 7***), and the relationship between mechanical ablation and the glacier dynamics (***Chapter 8***). Previous analyses have been focused either on the frontal dynamics of lake-terminating glacier, or in the analysis of water-glacier interaction between the proglacial lake and the host glacier, or the glacier recession of southeastern Tibetan Plateau under the climate changes.

Chapter 5 and ***6*** present the recent changes of HLG Glacier and these analyses reveal that at the margins of the glacier terminus retreated 132.1 m over the period of analysis, and that in the area specifically affected by collapsing (i.e., the glacier collapsed terminus), it retreated 236.4 m. The volume changes due to observed collapsing events comprises approximately 28% of the total volume change for the observed areas. Ice volume changes at the terminus due to a single ice collapse event may exceed the interannual level of volume change. Therefore, results suggest that the evolution of the HLG Glacier terminus is dominantly controlled by the frontal ice collapse. Based on the reconstruction of mass balance change for HLG Glacier for recent 19 years (***Chapter 7***), the contribution to the mass balance change of the entire glacier that is attributed to frontal ice collapse is limited (i.e., ranges from 0.48% to 1.12% from 2017 to 2021). However, due to the rapid ablation of the glacier itself, and the fact that below the ice falls it has largely become a regenerated glacier, a transition of ablation patterns in the glacier tongue may have already undergone. In other words, in the context of climate warming, mechanical ablation will probably take up a greater portion of the overall ablation in the future. Thus, the projection of the recession rate of the HLG Glacier may well be underestimated if based on surface mass balance alone, as the frontal ice collapsing might be more frequent and larger.

A particular contribution is that the thesis improves the understanding of mechanical ablation of HLG Glacier terminus and also contribute the knowledge about how mechanical ablation (e.g., frontal ice collapse) affects the glacier mass balance changes and the glacier dynamics.

8.3 Change pattern and mechanism of glacier tongue from 2018 to 2021

8.3.1 Change pattern

The HLG Glacier was in rapid recession during the study period. The glacier surface elevation lowered consistently between 2018 and 2021, and the glacier terminus retreated more than 350 m (Figure 5.7 B). The overall area of the glacier tongue also reduced year on year (Figure 7C). Except for the lower part of the ice tongue, the spatial distribution of both crevasses and ice cliffs did not change significantly in Sectors 2, 3 and 4, with all three showing a slight decline in their key statistics (Figure 5.7 C and D). The main changes in crevasse and ice cliff characteristics are mainly observed near the end of the glacier terminus. The changes observed around the glacier terminus were mainly controlled by the combination of melting and ice collapsing (Xu et al., 2022). As evident by the statistical analysis of crevasses density (Figure 5.7 C), the glacier terminus (Sector 1) has become more crevassed. Due to intensified ablation and subsequent ice collapse events around the outlet of the subglacial river, the frontal ice margin is now arcuate, and ice debris and fresh ice were frequently found around the collapsed frontal cliffs at the glacier terminus.

8.3.2 Mechanism of variation of the glacier tongue

Interannual comparisons have revealed similar behavior through time relating to glacier dynamics and its rapid evolution. The most significant evidence for supporting that the glacier was in a heavy recession is the remarkable increase we record in crevasse density and cliff density for Sector 1, as well as the areal shrinkage and the systematic lowering of the ice surface profiles. Specifically, the increase in crevasse density for Sector 1 (i.e., 8.43 to 38.59 km/km^2) verified that the lower glacier tongue is in the process of progressive disintegration, with frequent frontal ice collapse particularly focusing on the subglacial portal (Xu et al., 2022).

By the end of 2021, the ice fall of HLG Glacier had become nearly disconnected with the accumulation area (Figure 8.1). Continuous thinning and narrowing of the ice fall reduce the mass flux transferred down-glacier, impacting heavily on the lower part of the glacier (Zhang et al., 2010; Zhong et al., 2022). Coincident with this reduction in mass from higher elevation is the onset of rapid terminus recession through ice collapse and its broader disintegration. The lower tongue is therefore being simultaneously starved of mass at its upper end, and eroded by hydrological processes at its lower end, a scenario which is not common for ablation of valley glaciers. The ring-shape cracks on the glacier surface have a strong relationship with the roof collapse of the englacial or subglacial conduits (Egli et al., 2021). Considerable areas of ice debris falling from the glacier terminus also indicate the unstable condition of the glacier snout. The number of glaciological features evident on the 2021 map is far fewer than in the earlier three years, suggesting that the glacier is becoming increasingly stagnant, and tending towards becoming dead ice due to its disconnection with the accumulation zone.

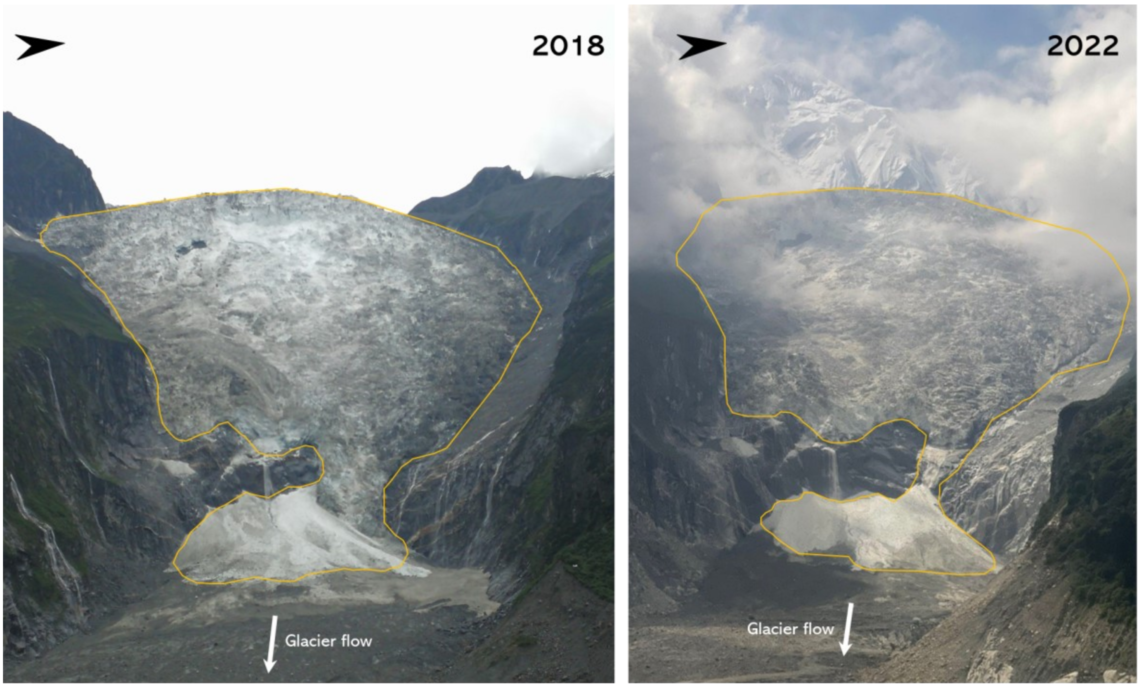

Figure 8.1 A comparison of the icefall of HLG Glacier between 2018 and 2022.

8.4 The significance of mechanical ablation to glacier mass loss

The measurements of daily area change (Table 6.2) revealed that the frontal ice collapsing events of the glacier snout may not affect the glacier area immediately but may exert lag and significant impacts on the areal shrinkage. For example, the area changes caused by an ice collapsing event (i.e., 2020/09/10 - 2020/11/05) account for more than 14% (i.e., 7,234 m^2) of the total area changes (i.e., 51,465 m^2) for the studied area. Owing to the isolated chunks of ice that might be melted and transferred by the glacier river easily, these effects were mainly induced by the ablation of massive dead ice stripped off from the glacier snout due to the ice collapsing events and enhanced subsequent melting of the exposed fresh ice. As for the ice volume changes, the total volumetric change for the observed area in the HLG Glacier snout was about $184.61 \pm 10.32 \times 10^4$ m^3 from 2017 to 2020. Based on the intercomparisons of ice volume changes for each pair, it is found that a large ice collapsing event in the glacier snout can contribute to huge ice mass losses in a short time, which could exceed the previous interannual ice volume changes. The daily volume changes obtained for the relatively longer observation periods range between 0.09 to 0.20×10^4 m^3. However, we observed that a single ice collapse event can routinely remove ice volumes of 0.50 ± 0.16 to $0.88 \pm 0.03 \times 10^4$ m^3 per day. These statistics about ice volume changes indicate the dominant impact of ice collapse as an ablation process, especially over the summer season. Consequently, and similar to lake-terminating glaciers (Carrivick and Tweed, 2013), its retreating may be controlled by the interactions of water and glacier near the glacier terminus. Furthermore, projections of the recession rate of the HLG Glacier that rely solely on surface mass balance probably underestimate its evolution, since the frontal ice collapsing might be more frequent and larger under the context of warming. Continuously collapsing events that occur at the glacier terminus may cause enhanced hydrological responses, leading to high magnitude debris flow or river blockage, as well as other glacial-hazards in this region (Liu et al., 2018; Lu and Gao, 1992).

The contribution of frontal ice collapse events in the glacier terminus is relatively small in the portion of mass balance changes (i.e., ranges from 0.48% to 1.12%) as stated in **Section 7.5**. The mechanical ablation that occurred at the glacier terminal areas (e.g., frontal ice collapse and subglacial/englacial conduit's roof collapse) has changed the morphology of the glacier terminus thoroughly and the way of ice losing.

8.5 Spatial pattern of mechanical ablation in the terminus

Our multi-temporal UAV imagery shows very clearly that the major ice collapse events occur around the position of the outlet of the subglacial channel. In common with marine- and lacustrine-terminating glaciers, ice crevasse patterns near the frontal margin appear to determine the size and frequency of subsequent calving events. Areas of ice loss detected in 2019 tie in almost perfectly with the presence of deep crevassing in the imagery acquired in 2018, for example, and similar patterns can be identified between September 2020 and November 2020 datasets. Our geomorphological mapping shows very clearly the evolution of these features through time, with crevasse traces likely emerging from the ice cliffs and being advected down-glacier beneath the surface debris, before being re-opened as lines of weakness by the change in stress around the terminus area. Although it is not possible to gauge crevasse depths from our data, the DoDs suggests that either these failures are able to propagate through the full ice thickness to the bed, or the subglacial channel associated with the outlet portal is large enough to induce a collapse event. Either way, the ice that is subsequently deposited in the outlet channel is quickly removed by meltwater, making this a highly efficient mechanism of ice ablation. Another study about the drainage system of the HLG Glacier indicated that the subglacial drainage network is a longitudinal-oriented steady system, which is also confirmed by the frequent collapsing subglacial conduit outlets (i.e., ice fracturing due to the expansion of the subglacial channels), where the hydraulic efficiency is high (Liu et al., 2018).

As discussed in **Section 6.4**, in the lower part of the center flowline (Figure 6.5b), a similar abnormal decline occurred at three surface profiles (i.e., 2020-09-05, 2020-09-10, and 2020-11-05). This decline may also correspond to the surface lowering or the roof collapsing of subglacial conduits (Figure 8.2 a), even for the upper section of the glacier terminus (Figure 8.2 f).

Additionally, ice height changes and their distributions also suggested that the large magnitude of an ice collapse event can facilitate the full-thickness ice fractures to remove massive ice chunks and accelerate the glacier retreating. Analysis of the spatial distribution of the ice crevasses and the collapsed zone between successive maps reveals that areas with dense ice crevasses were more likely to develop as areas of an ice collapse in the future. This can clearly be seen between Figure 6.8 c and d, with the area of fast flow in Figure 6.8 c (near 1689 along the x-axis) becoming the collapsed front in Figure 6.8 d. For the case in Figure 8.2 d, these fast flow arrows are not even concentrated at the glacier collapsed terminus, but form a ring-shaped pattern (or a cluster of arrows from northeast and southeast) at the upper section of the glacier terminus, which implies the destabilization and collapse of the roof of the subglacial/englacial channels (Egli et al., 2021). By comparing the image of 2021-07-28 and 2021-09-02 (Figure 8.2), this potential collapsing location is fully validated. It is possible given its timing that seasonally-enhanced precipitation and meltwater influx into the glacier led to increasing pressure on the hydrological system within the glacier, exceeding its capacity and resulting in mechanical instabilities (Mair et al., 2003). This ablation pattern seems a common feature for valley glaciers as evident by previous studies (Kavanaugh and Clarke, 2001; Mair et al., 2001, 2002), which is probably linked to the reorganization of the subglacial drainage system and significant ice motions on the glacier surface. Based on this interpretation, the potential trigger for this pattern is induced by the reduction of basal drag and the resultant increase in basal motion. Thus, for this reason, either the events are facilitating crevassing for the frontal ice and ice motions, or the subglacial drainage provides additional lubrication, hence enhancing the ice flow.

8.6 Control factors of mechanical ablation

8.6.1 Proglacial waterbodies

The persistence of proglacial waterbodies partly exacerbates the instability of the glacier frontal margin and facilitates the glacier retreat to some extent (King et al., 2019; Liu et al., 2020). Although the HLG Glacier is a non-lacustrine glacier (i.e., no proglacial lake), HLG Glacier has a well-developed drainage network connecting the supraglacial, englacial, and subglacial spaces (Liu et al., 2018; Liu and Liu, 2012). Melt streams from other small hanging or valley glaciers distributed in the HLG basin flow into the HLG Glacier via the drainage network (Liu et al., 2018). This drainage network can discharge runoff (including both melting water and overland flow from off-glacier) through the outlet in the glacier terminus, which has formed a shallow pool beneath the glacier terminus and these pools have been observed after collapsing of the ice above (Figure 8.2 c and d). These pools, which are fed by the drainage system of the glacier, play a similar role in water-glacier interactions compared with lake-terminating glaciers as it has been observed as stagnant water bodies. It is difficult to know how far these subglacial pools extend up-glacier, but it is likely that they at least facilitate an environment where the ice and water mutually interact continuously, which may weaken the stable structure of the glacier sole, even to form weakness lines for further potential ice fracturing.

During the major ablation season (i.e., May to October; also, the rainy season) of the HLG Glacier, the seasonally enhanced glacier runoff likely feeds more water into these pools, subsequently impacting the frequency of ice collapse events. The collapsed terminus of the HLG Glacier is roughly cave-shaped with an arch-shaped ice roof, which is often filled by ice debris (Figure 8.2 c and d). Collapsing occurs when ice crevasses continue to crack down through the arch-shaped ice roof and simultaneously the grounded ice sole becomes unstable due to water-glacier interaction. This leads to the exposure and deepening of further fractures as a consequence of the tensile stresses. Periodically, massive ice deposits can bury the outlet of the subglacial river, forcing the river to find another path and develop a new outlet and cave, and starting another cycle of undercutting, collapse, and fracture exposure. Previous studies on the drainage system of the lower part of the HLG Glacier tongue indicate that some small supraglacial lakes existing from April to May with a short life cycle may be drained completely by fully-connected englacial and subglacial conduits, thereby facilitating the mechanical ablation (Liu et al., 2018; Liu and Liu, 2012). Our mapping results also indicated the existence of supraglacial ponds between the elevation of 3000 to 3100 m a.s.l. (Figure 6.6)

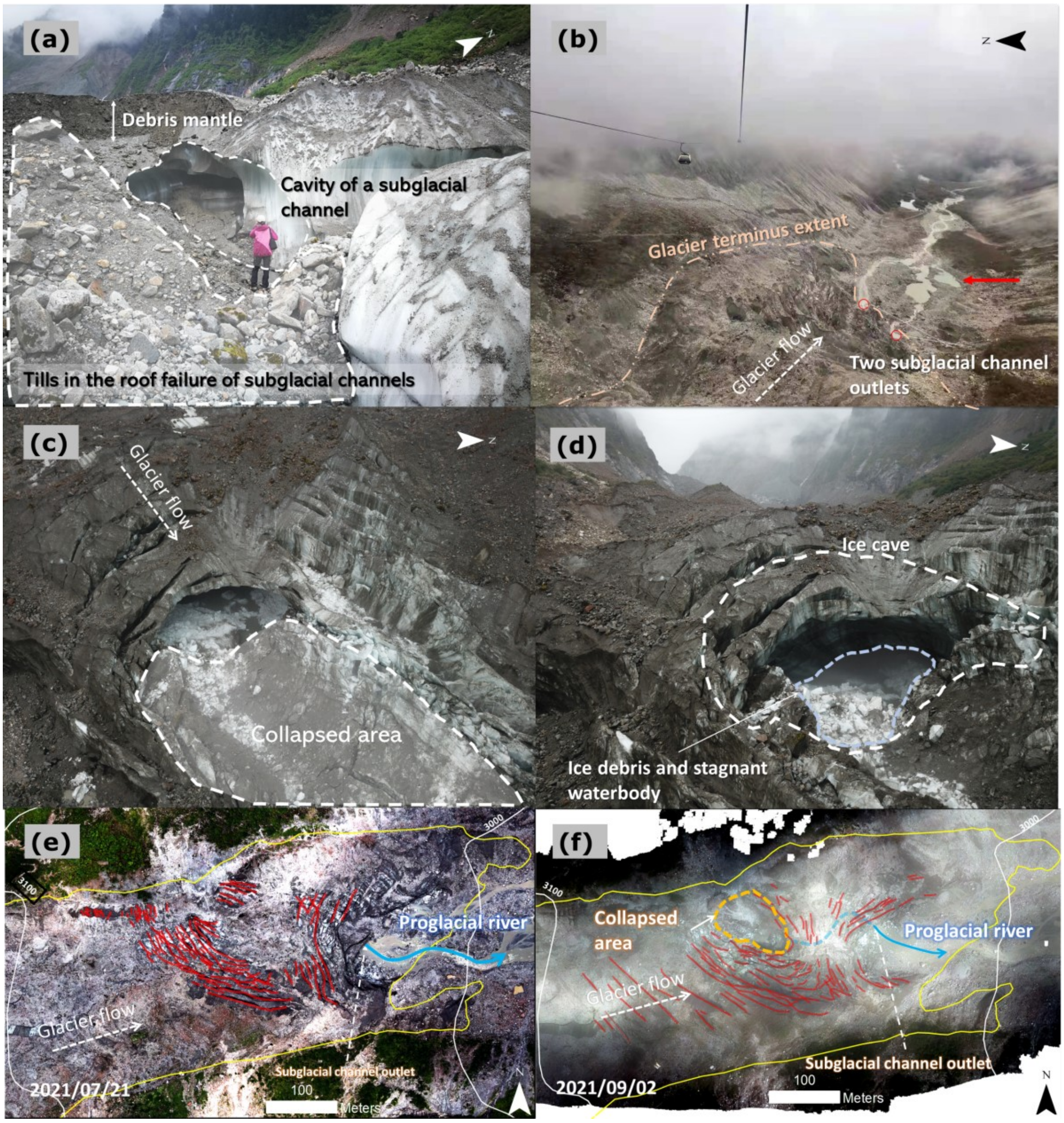

Figure 8.2 (a) The roof collapsing/failure of a subglacial channel in the upper part of the HLG Glacier terminus and the cavity of the subglacial channel was exposed due to the roof collapsing (Date of the photo taken 2018-06-23); (b) A observation of HLG Glacier snout from photographing in cable car by locals (2021-04-28). Two subglacial outlets were found and two ponds were connected and fed by a newly emerged proglacial river channel; (c) and (d) show the landscape of the glacier terminus on 2020-09-10. A collapsed area is located at the front of the glacier terminus (i.e., ice cave) and it blocked the runoff flow from the subglacial outlet and formed a stagnant water body beneath the glacier terminus; (e) and (f) were the ortho-mosaics of 2021-07-21 and 2021-09-02, and red polylines indicate the ice crevasses. The yellow dashed polygon in (f) shows the collapsed area and light blue dashed line indicates the potential subglacial channel.

The HLG Glacier, which is representative of many other land-terminating glaciers in the southeastern Tibetan Plateau, has intensive water-glacier interactions at the frontal ice margin (i.e., the outlet of the subglacial channels), which is evidently responsible for the ice collapse/calving events similar to lake-terminating glaciers. Although there is no proglacial lake at the HLG Glacier termini, several small ponds have formed in the periglacial land around October 2019, and have expanded to a string of connected ponds around November 2020. Furthermore, recent observations of the HLG Glacier snout by locals in April 2021 showed that these connected ponds continue to expand (Figure 8.2 b). The pond closest to the glacier is fed by a new stream emanating from the glacier terminus, despite the adjacent main glacier river remaining in a similar geomorphic pattern as before. These recent field observations combined with the previous UAV images suggest that a proglacial lake might be formed at the glacier terminus. Further, with the initiation and the development of the proglacial lake, the frontal ice-marginal collapse events could well be enhanced due to intensified water-glacier interactions (e.g., subaqueous melting or buoyancy-derived weak waterline), furthering forming a similar circumstance to the ice-marginal lake and facilitating the glacier receding.

8.6.2 Subglacial channel networks

HLG Glacier has a longitudinally steady subglacial channel network in the lower ablation region with a relatively high hydraulic efficiency (Liu et al., 2018). The subglacial drainage system of temperate glaciers transforms into a fast drainage system around the beginning of the ablation season and continues the high drainage capacity until the end of the ablation season (Fountain and Walder, 1998; Hooke, 1989; Liu and Liu, 2010; Walder, 2010). As for HLG Glacier, within the period from May to November, nearly all water from rain and melting enters the glacier via the crevasses and flows within the seasonal efficient drainage networks. In this situation, large amounts of water will flow through the englacial and subglacial drainage networks until it drains into the proglacial rivers (Liu and Liu, 2010). The increase in water volume and water pressure in the subglacial drainage system may result in intensified ice-water interactions, leading to more intense ablation. Under the constant impulse of such ablation, the slightly crevassed glacier terminus tends to be more triggered to produce ice collapsing events, even for the non-frontal terminus area (Figure 8.2 a), with the combined efforts of crevassing and thermal erosion within the subglacial drainage system, roof failures of subglacial channels can be clearly observed (Figure 8.2 e and f). Once the cavity has formed, it is easier to ablate due to the exposure to air, thus leading to more collapsing events (Egli et al., 2021)

With the thinning of the glacier ablation zone, ice creep may not compensate for the expansion of drainage channel walls due to the intensive ablation. The destabilizations of stress-strain balance in ice bodies were exacerbated due to the intensive englacial and subglacial ablations, thereby ice fracture (e.g. ice crevasses and ice collapse), and thus forming terminus ice cliffs (Mei et al., 2013; Nye, 1951; Thorsteinsson et al., 2003). Additionally, the dramatic retreating of the HLG Glacier over years may have forced the glacier terminus to retreat into a rugged and complex basal terrain, which is unsuitable for the thinned glacier terminus to maintain the stress balance, thus facilitating the ice fracturing. Successive observations have shown that the icefall, the link between the upstream firn basin and the downstream glacier tongue, is gradually becoming thinner and narrower. This situation suggests that the supply of mass from upstream is declining, which is probably one of the factors leading to the rapid thinning of the downstream glacier and thereby to stress destabilization and ice collapse.

8.7 Conceptual model of mechanical ablation process at Hailuogou Glacier terminus, 2017 to 2021

Based on the field observations of terminal areas of HLG Glacier, we concluded a schematic figure presenting the mechanical ablation processes of the HLG Glacier terminus area between 2017 to 2021 as shown in Figure 8.3. Generally speaking, this conceptual model illustrates the hierarchy of how these mechanical ablations drive the retreating of the glacier. Specifically, the limited ice flux controlled by the glacier flow (e.g., disconnecting icefall) leads to the ice stagnating and then rapid surface downwasting. Under the combined effect of crevasses at the terminus and the intense melting within the subglacial channels, structural instability at the glacier terminus appears with obvious signals of the chaotic highly crevassed surface. The cavity formed by the subglacial channel outlet become to fracture and leads to the collapse of the terminus ice body. Meanwhile, notching and over-steepening induced by crevassing are effect simultaneously to stripe some ice chunks from the frontal glacier terminus. The above is the process of stage No.1. With the continuous glacier surface thinning, some areas near the glacier terminus will form ring-shaped crevasses, which is a sign of surface depression. This feature is probably induced by the instability of the roof of the englacial conduit/subglacial channel. During the development of ring-shaped crevasses, a supraglacial pond will form subsequently in the center of that and disappears with the collapse of ring-shaped crevasses. Usually, this process might occur at the position near the glacier terminus instead of the most frontal glacier terminus. The above is stage No.2. After a severe collapse of the ring-shaped crevasses, the lower part of the glacier is often disintegrated into two sections (or only a small part is still connected) by this intense collapse. With several more collapses due to surface depression and continued thinning, the glacier terminus might be densely covered by long and chaotic crevasses and even intense inter-crevassed surfaces. Consequently, the glacier is on the course of becoming rapidly ablating dead ice.

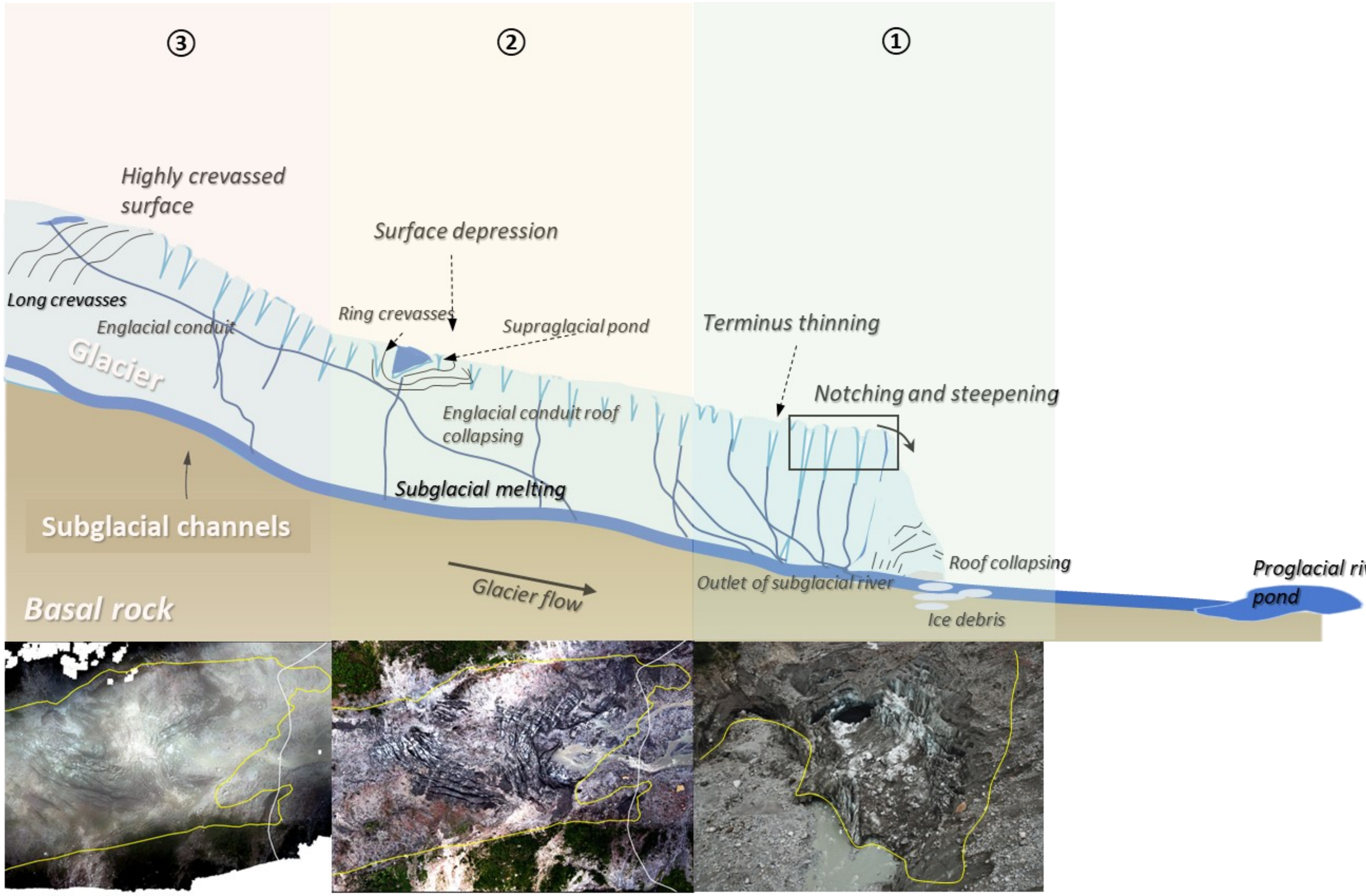

Figure 8.3 Conceptual diagram of the processes and potential mechanisms of the mechanical ablation at the HLG Glacier terminus area that has impacted the glacier retreating. Number 1 to 3 indicates the possible stages that the HLG Glacier terminus underwent from 2017 to 2021. Lower insets are the examples that could correspond to the three stages.

8.8 Potential effects of decoupling from climate changes

Lake-terminating glaciers have been influenced by the presence and behavior of ice-marginal water bodies, such as ice-marginal morphology, physical stability, and glacier dynamics (Carrivick and Tweed, 2013). A proglacial lake augments the ice mass loss and glacier velocity as the warm water transfers heat to glacier bodies and forms thermally induced melting and that then controls the calving by undercutting. In this base, the glacier might be partly decoupled with climate change under the impact of the ice-marginal lake (Carrivick and Tweed, 2013; Kirkbride, 1993; Kirkbride and Warren, 1999). For HLG Glacier, the glacier snout is also slightly immersed in its proglacial waterbodies and experiences high pressure in the seasonally efficient drainage networks (Liu and Liu, 2010), which forms a water-rich environment similar to the case of a lake-terminating glacier. Firstly, a stagnant pond beneath the glacier terminus was observed due to the exposure of the cavity of the frontal ice cave (Figure 8.2 c and d), and considerable water was discharged by the seasonal varied proglacial river even in the winter (Figure 6.4) (Liu et al., 2018). These water bodies (i.e., pond beneath the glacier terminus and proglacial river) may continually weaken the structure of the glacier base as discussed in ***Section 8.5.1***.

The subglacial channel of the lower part of the ablation zone was examined as a stable and highly efficient drainage system during the whole ablation season. This subglacial drainage system needs to handle considerable runoff from streams of external tributary, precipitation, and the melting runoff of the glacier itself as discussed in ***Section 8.5.2***. Therefore, the local ice flow and magnitude of the subglacial ablation might be strongly impacted due to the long-standing but seasonal enhanced subglacial drainage system, inducing ice collapsing in some cases (Figure 8.2 a, c, and d) (Liu et al., 2018). Furthermore, some supraglacial ponds with a short life span were found between the elevation of 3000 to 3100 m a.s.l. (Figure 6.4). These supraglacial ponds may be delivered to either internal conduits or ponded crevasses by supraglacial drainage networks, then discharged completely by fully-connected englacial and subglacial channels (Liu et al., 2018; Liu and Liu, 2012). Thus, there are extensive interactions between glacier and water in HLG that occur in the proglacial river, subglacial environment, and even in the supraglacial and englacial drainage system. In this scenario, heat can be transferred through mainly three ways in the terminus of HLG Glacier: a highly dynamic proglacial river and shallow pond beneath the glacier snout keeping the glacier snout in a state of continuous water-glacier interactions; a well-developed subglacial channel network and seasonally enhanced volume in conduits also allowing interactions of heat subglacially and englacially; and heat may be delivered by ponded water in the crevasses supplied from external precipitation or glacier surface runoff. Therefore, it is analogous that the mechanical ablation that occurred around the terminus of land-terminating by ice collapsing and frontal ice calving can be seen as an amplifier in its process of ice mass loss, which exacerbates the glacier retreating. To some extent, when the intensity of mechanical ablation is strong, it may have been possible to approximate the effect of the proglacial lake.

It is inarguable that the glacier-climate dynamics are complex. So far, the finite element-based approach of full Navier-Stokes considering the Glen Law is the mainstream for predicting mountain glacier evolution, e.g., ELMER, Icetool (Jarosch, 2008; Zwinger and Moore, 2009), but these models also do not fully (or reasonably) account for all impact factors, especially for ice collapse in the frontal ice margin for land-terminating glaciers. Hence, it is difficult to robustly characterize the relationship between glacier dynamics and mechanical ablation and to fully evaluate its causes. We acknowledge that these causes can span one or more full-thickness crevassing, points of structural weakness, highly dynamic hydraulic effects in the subglacial channels, undercutting, surface displacement, precipitation, and rapid thinning.

Chapter 9: Conclusion

9.1 Revisit of objectives

The primary aim of this study was to improve the understanding of mechanical ablation that occurred at the terminus of the HLG Glacier. This is for contributing the knowledge about how mechanical ablation (e.g., frontal ice collapse) affects the glacier mass balance changes and its impacts on the glacier dynamics. The following are objectives for revisiting:

1. to characterize the evolution of the surface features of the HLG Glacier tongue for indicating the changing ice dynamics as well as likely future patterns in ice loss.
2. to investigate the processes of mechanical ablation of the HLG Glacier terminus by using aerial images captured from uncrewed aerial vehicles (UAV) from 2017 to 2020.
3. to reconstruct the time-sequenced mass balance changes of HLG Glacier for showing the mass loss during recent decades and estimating the contributions of mechanical ablation that occurred in the HLG glacier terminus to the total ice mass balance.

In response to the above objectives, the main conclusions of this study were drawn as follows:

1. We have analyzed the geomorphological evolution of the terminus area of the HLG Glacier based on the collected UAV images. Multiple approaches were used to quantitively analyze the evolution of the terminus area of HLG Glacier, including SfM-MVS, geomorphic mapping, DoD, and DIC-FFT. The main finding is that the mechanical ablation induced by the intensive ice-water interactions in the glacier terminus, as well as the subglacial channel expansions might be the control factors that dominate the glacier shrinking. The collapsed frontal terminus (~236 m) retreated much more significantly than the common glacier terminus (~132 m). A single collapsing event may cause a large amount of ice loss, which can reach or exceed the order of magnitude of previous annual ice loss. The terminus evolution of the HLG Glacier was partly controlled by the frontal ice collapse.

2. Four comprehensive maps were attached to this thesis for providing the changes in landform features of the HLG Glacier tongue. Based on the mapping results and analyses, we assessed the evolution of the HLG Glacier tongue during 2018-2021, and we also interpret these features to illustrate the dynamics of the glacier. Mass perturbations of the glacier may be induced by the persistently accelerating glacier mass loss, and these mass perturbations cause the stress and strain within the glacier to be redistributed and then alter the glacier dynamics subsequently. Clearly, the dynamic has changed, and the glacier is in rapid recession and even possible disintegration. The disconnection between the glacier tongue and the accumulation zone has set the lower part of the glacier on a course to becoming stagnant, and ultimately existing only as a block of dead ice. Therefore, it can be hypothesized that the glacier will only recede more rapidly over the next decades, with the exact rate being determined largely by the magnitude-frequency of future terminus ice collapse events.
3. Photogrammetrically stereopsis was applied on ASTER stereo images to derive time-sequenced DEMs for HLG Glacier from 2002 to 2021 by using NASA Ames Stereo Pipeline. The variation of glacier extent was also extracted from satellite images (e.g., PlanetScope). Results indicate that the overall mass balance change is negative and enhanced. The area of HLG Glacier was in rapid reduction. Our calculated mass balance is - 12.60 ± 0.89 m w.e. and the annual mean mass balance change is about- 0.66 ± 0.05 m w.e. The annual rate of mass loss is roughly 1.5 time than the mass balance from 1968 to 2000.
4. The roughly estimated contribution to the mass balance change of the entire glacier that is attributed to frontal ice collapse is limited (i.e., 0.48% to 1.12%). The contribution to the glacier tongue ranges from 2.82 – 6.49%. However, the mechanical ablation (e.g., frontal ice collapse and subglacial/englacial conduit's roof collapse) has changed the glacier dynamics and the way of losing ice mass to some extent. A discussion about the changing pattern from the entire glacier tongue to the glacier terminus area has illustrated the significance of mechanical ablation in the HLG Glacier. A conceptual diagram of glacier evolution controlled by mechanical ablation was also provided to emphasize this.

9.2 Limitations

Although the initial aim was achieved by completing three objectives, some aspects were not fully accomplished in the study, as summarized below:

1. The mapping work needs further optimization. Although the various types of features within the HLG Glacier have been mapped in considerable detail and comprehensively in this study, some features need to be mapped in several dimensions to illustrate changes. For example, we only mapped the long axis of the ice crevasse as its length, but the fracture size of the ice crevasse, which is also significant evidence of glacier dynamics, was not mapped in our dataset.
2. Most of the mapping work relies on visual interpretation and manual mapping. The uncertainty of such mapping of glacier landscapes, which is done by subjective interpretation, is difficult to be well estimated.
3. The GCPs used are mainly concentrated in the ice-free area at the glacier terminus, while there are relatively large areas in the region without ground control point distribution. Although the UAV has a built-in positioning sensor, relying solely on the GCPs in the front area of the glacier cannot control the uncertainty of the results to a relatively good extent, especially in those areas far from the GCPs.
4. The errors in the estimation of glacier elevation changes based on ASTER-derived DEMs need to be considered. Using stereoscopic to generate DEMs requires ground matching points with sufficient contrast, and glaciated areas are often hardly found with enough matching points because of weak texture and high brightness. This makes the resulting DEM with noises or even errors.
5. The empirical equation for the area-volume conversion for the ice collapse event at the terminus of the HLG Glacier established in this study is very coarse (derived from data from only 2 field surveys), which requires more observations to optimize the equation.

9.3 Future work

Based on this study, there are several potential paths for future research on HLG Glacier and other collapsed-ablating margins have emerged:

1) Conducting continuous monitoring of HLG Glacier may improve a more comprehensive understanding of the pattern and key processes of mechanical ablating retreat, including high-resolution satellite imagery and fixed timelapse photography.
2) Investigations into the kinematics of the subglacial/englacial environment of the HLG Glacier tongue may provide more insights into the collapse induced by surface depression (i.e., conduits' roof collapses). As the HLG Glacier is on the course of becoming a block of dead ice, subglacial and englacial dynamics will be more involved in the evolution of the glacier.
3) Undertaking detailed surveying of the basal terrain of HLG Glacier tongue would allow estimating the long profile of the bedrock. This is important for the projection of glacier geometry and future volume changes.
4) Using other data to reconstruct the mass balance changes of HLG Glacier from semi-annual to seasonal or even monthly level, such as bistatic InSAR based on TerraSAR-X and TanDEM-X. SAR-derived datasets can also provide the displacement of glacier ice motions.
5) Focusing on the proglacial and paraglacial zones of the HLG Glacier tongue as the highly rapid evolution occurring around the glacier terminus and glacier tongue is bounded to induce the changes of surroundings around the HLG Glacier tongue. Although a paraglacial evolution has been investigated by others in 2021, it still needs more effort in the consideration of rapid thinning and retreating.
6) The HLG Glacier is not the only one that has evolved in collapsed ablating. Preconditions and boundary conditions for the collapse of the HLG Glacier need to be summarized to form an index and to search for analogous glaciers at a larger scale that will contribute to the knowledge of glacier ablation within the continuous climate changes.

9.4 Concluding remarks

This thesis has quantified and illustrated the processes of thinning-retreating with extensive mechanical ablation (i.e., frontal ice collapsing-ablation) in the HLG Glacier terminus. The time sequence of mass balance change from 2002 to 2021 has been reconstructed for describing the glacier dynamics and estimating the impacts of mechanical ablation. A set of comprehensive maps also has been presented to show geomorphological, hydrological, and glaciological feature changes of the HLG Glacier tongue (2018, 2019, 2020, and 2021). Hence, the thesis provides recent HLG Glacier dynamics, contributing to the understanding of ice loss of mechanical ablating margins and the insight into the projection of the HLG Glacier recession in the near future.

References

Aizen, V.B., Aizen, H.M., 1994. Regime and Mass-Energy Exchange of Subtropical Latitude Glaciers under Monsoon Climatic Conditions: Gongga Shan, Sichuan, China. Mountain Research and Development 14, 101–118. https://doi.org/10.2307/3673794

Altena, B., Kääb, A., 2017. Glacier ice loss monitored through the Planet cubesat constellation, in: 2017 9th International Workshop on the Analysis of Multitemporal Remote Sensing Images (MultiTemp)., pp. 1–4. https://doi.org/10.1109/Multi-Temp.2017.8035235

Andreassen, L.M., Huss, M., Melvold, K., Elvehøy, H., Winsvold, S.H., 2015. Ice thickness measurements and volume estimates for glaciers in Norway. Journal of Glaciology 61, 763–775. https://doi.org/10.3189/2015JoG14J161

Ashraf, A., Roohi, R., Naz, R., Mustafa, N., 2014. Monitoring cryosphere and associated flood hazards in high mountain ranges of Pakistan using remote sensing technique. Natural Hazards 73, 933–949. https://doi.org/10.1007/s11069-014-1126-3

Azzoni, R.S., Fugazza, D., Zennaro, M., Zucali, M., D'Agata, C., Maragno, D., Cernuschi, M., Smiraglia, C., Diolaiuti, G.A., 2017. Recent structural evolution of Forni Glacier tongue (Ortles-Cevedale Group, Central Italian Alps). Journal of Maps 13, 870–878. https://doi.org/10.1080/17445647.2017.1394227

Barella, R., Callegari, M., Marin, C., Notarnicola, C., Zebisch, M., Sailer, R., Klug, C., Galos, S., Dinale, R., Benetton, S., 2020. Automatic glacier outlines extraction from Sentinel-1 and Sentinel-2 time series, EGU General Assembly 2020, Online, 4–8 May 2020, EGU2020-13782, https://doi.org/10.5194/egusphere-egu2020-13782, 2020

Bash, E.A., Moorman, B.J., Gunther, A., 2018. Detecting Short-Term Surface Melt on an Arctic Glacier Using UAV Surveys. Remote Sensing 10, 1547. https://doi.org/10.3390/rs10101547

Beaney, C.L., Shaw, J., 2011. The subglacial geomorphology of southeast Alberta: evidence for subglacial meltwater erosion. Canadian Journal of Earth Sciences. https://doi.org/10.1139/e99-112

Benn, D.I., Åström, J.A., 2018. Calving glaciers and ice shelves. Advances in Physics: X 3, 1513819. https://doi.org/10.1080/23746149.2018.1513819

Benn, D.I., Bolch, T., Hands, K., Gulley, J., Luckman, A., Nicholson, L.I., Quincey, D., Thompson, S., Toumi, R., Wiseman, S., 2012. Response of debris-covered glaciers in the Mount Everest region to recent warming, and implications for outburst flood hazards. Earth-Science Reviews 114, 156–174. https://doi.org/10.1016/j.earscirev.2012.03.008

Benn, D.I., Evans, D.J.A., 2013. Glaciers & glaciation, 2.ed. ed. Routledge, London.

Benn, D.I., Lehmkuhl, F., 2000. Mass balance and equilibrium-line altitudes of glaciers in high-mountain environments. Quaternary International 65–66, 15–29. https://doi.org/10.1016/S1040-6182(99)00034-8

Benn, D.I., Thompson, S., Gulley, J., Mertes, J., Luckman, A., Nicholson, L., 2017. Structure and evolution of the drainage system of a Himalayan debris-covered glacier, and its relationship with patterns of mass loss. The Cryosphere 11, 2247–2264. https://doi.org/10.5194/tc-11-2247-2017

Benn, D.I., Warren, C.R., Mottram, R.H., 2007. Calving processes and the dynamics of calving glaciers. Earth-Science Reviews 82, 143–179. https://doi.org/10.1016/j.earscirev.2007.02.002

Berthier, E, Arnaud, Y., Kumar, R., Ahmad, S., Wagnon, P., Chevallier, P., 2007. Remote sensing estimates of glacier mass balances in the Himachal Pradesh (Western Himalaya, India). Remote Sensing of Environment 108, 327–338. https://doi.org/10.1016/j.rse.2006.11.017

Berthier, Etienne, Arnaud, Y., Kumar, R., Ahmad, S., Wagnon, P., Chevallier, P., 2007. Remote sensing estimates of glacier mass balances in the Himachal Pradesh (Western Himalaya, India). Remote Sensing of Environment 108, 327–338. https://doi.org/10.1016/j.rse.2006.11.017

Berthier, E., Cabot, V., Vincent, C., Six, D., 2016. Decadal Region-Wide and Glacier-Wide Mass Balances Derived from Multi-Temporal ASTER Satellite Digital Elevation Models. Validation over the Mont-Blanc Area. Front. Earth Sci. 4. https://doi.org/10.3389/feart.2016.00063

Berthier, E., Toutin, T., 2008. SPOT5-HRS digital elevation models and the monitoring of glacier elevation changes in North-West Canada and South-East Alaska. Remote Sensing of Environment 112, 2443–2454. https://doi.org/10.1016/j.rse.2007.11.004

Berthier, E., Vincent, C., Magnússon, E., Gunnlaugsson, Á. Þ., Pitte, P., Le Meur, E., Masiokas, M., Ruiz, L., Pálsson, F., Belart, J. M. C., and Wagnon, P., 2014. Glacier topography and elevation changes derived from Pléiades sub-meter stereo images, The Cryosphere, 8, 2275–2291, https://doi.org/10.5194/tc-8-2275-2014.

Beyer, R.A., Alexandrov, O., McMichael, S., 2018. The Ames Stereo Pipeline: NASA's Open Source Software for Deriving and Processing Terrain Data. Earth and Space Science 5, 537–548. https://doi.org/10.1029/2018EA000409

Bhardwaj, A., Sam, L., Akanksha, Martín-Torres, F.J., Kumar, R., 2016. UAVs as remote sensing platform in glaciology: Present applications and future prospects. Remote Sensing of Environment 175, 196–204. https://doi.org/10.1016/j.rse.2015.12.029

Bhattacharya, A., Bolch, T., Mukherjee, K., King, O., Menounos, B., Kapitsa, V., Neckel, N., Yang, W., Yao, T., 2021. High Mountain Asian glacier response to climate revealed by multi-temporal satellite observations since the 1960s. Nat Commun 12, 4133. https://doi.org/10.1038/s41467-021-24180-y

Bickel, V.T., Manconi, A., Amann, F., 2018. Quantitative Assessment of Digital Image Correlation Methods to Detect and Monitor Surface Displacements of Large Slope Instabilities. Remote Sensing 10, 865. https://doi.org/10.3390/rs10060865

Bishop, M. P., Shroder Jr, J. F., Haritashya, U. K., & Bulley, H. N. (2007). 25 Remote sensing and GIS for alpine glacier change detection in the Himalaya. Developments in Earth Surface Processes, 10, 209-234.

Bisset, R. R., Nienow, P. W., Goldberg, D. N., Wigmore, O., Loayza-Muro, R. A., Wadham, J. L., Macdonald, M. L. and Bingham, R. G. (2022) "Using thermal UAV imagery to model distributed debris thicknesses and sub-debris melt rates on debris-covered glaciers," Journal of Glaciology. Cambridge University Press, pp. 1–16. doi: 10.1017/jog.2022.116.

Bolch, T., Kamp, U., 2005. Glacier mapping in high mountains using DEMs, Landsat and ASTER data. In: 8th International Symposium on High Mountain Remote Sensing Cartography, La Paz (Bolivien), 20 March 2005 - 27 March 2005. Karl-Franzens-Universität Graz, 37-48. https://doi.org/10.5167/UZH-137251

Braithwaite, R.J., Raper, S.C.B., 2002. Glaciers and their contribution to sea level change. Physics and Chemistry of the Earth, Parts A/B/C 27, 1445–1454. https://doi.org/10.1016/S1474-7065(02)00089-X

Brun, F., Berthier, E., Wagnon, P., Kääb, A., Treichler, D., 2017. A spatially resolved estimate of High Mountain Asia glacier mass balances from 2000 to 2016. Nature Geosci 10, 668–673. https://doi.org/10.1038/ngeo2999

Brun, F., Buri, P., Miles, E.S., Wagnon, P., Steiner, J., Berthier, E., Ragettli, S., Kraaijenbrink, P., Immerzeel, W.W., Pellicciotti, F., 2016. Quantifying volume loss from ice cliffs on debris-covered glaciers using high-resolution terrestrial and aerial photogrammetry. Journal of Glaciology 62, 684–695. https://doi.org/10.1017/jog.2016.54

Brun, F., Wagnon, P., Berthier, E., Shea, J.M., Immerzeel, W.W., Kraaijenbrink, P.D.A., Vincent, C., Reverchon, C., Shrestha, D., Arnaud, Y., 2018. Ice cliff contribution to the tongue-wide ablation of Changri Nup Glacier, Nepal, central Himalaya. The Cryosphere 12, 3439–3457. https://doi.org/10.5194/tc-12-3439-2018

Cao, B., Pan, B., Wang, J., Shangguan, D., Wen, Z., Qi, W., Cui, H., Lu, Y., 2014. Changes in the glacier extent and surface elevation along the Ningchan and Shuiguan river source, eastern Qilian Mountains, China. Quaternary Research 81, 531–537. https://doi.org/10.1016/j.yqres.2014.01.011

Carrivick, J.L., Geilhausen, M., Warburton, J., Dickson, N.E., Carver, S.J., Evans, A.J., Brown, L.E., 2013. Contemporary geomorphological activity throughout the proglacial area of an alpine catchment. Geomorphology, Sediment sources, source-to-sink fluxes and sedimentary budgets 188, 83–95. https://doi.org/10.1016/j.geomorph.2012.03.029

Carrivick, J.L., Tweed, F.S., 2013. Proglacial lakes: character, behaviour and geological importance. Quaternary Science Reviews 78, 34–52. https://doi.org/10.1016/j.quascirev.2013.07.028

Chandler, B.M.P., Chandler, S.J.P., Evans, D.J.A., Ewertowski, M.W., Lovell, H., Roberts, D.H., Schaefer, M., Tomczyk, A.M., 2020. Sub-annual moraine formation at an active temperate Icelandic glacier. Earth Surface Processes and Landforms 45, 1622–1643. https://doi.org/10.1002/esp.4835

Chandler, B.M.P., Evans, D.J.A., Roberts, D.H., Ewertowski, M., Clayton, A.I., 2016. Glacial geomorphology of the Skálafellsjökull foreland, Iceland: A case study of ‘annual’ moraines. Journal of Maps 12, 904–916. https://doi.org/10.1080/17445647.2015.1096216

Chandler, B.M.P., Lovell, H., Boston, C.M., Lukas, S., Barr, I.D., Benediktsson, Í.Ö., Benn, D.I., Clark, C.D., Darvill, C.M., Evans, D.J.A., Ewertowski, M.W., Loibl, D., Margold, M., Otto, J.-C., Roberts, D.H., Stokes, C.R., Storrar, R.D., Stroeven, A.P., 2018. Glacial geomorphological mapping: A review of approaches and frameworks for best practice. Earth-Science Reviews 185, 806–846. https://doi.org/10.1016/j.earscirev.2018.07.015

Chauché, N., Hubbard, A., Gascard, J.-C., Box, J.E., Bates, R., Koppes, M., Sole, A., Christoffersen, P., Patton, H., 2014. Ice–ocean interaction and calving front morphology at two west Greenland tidewater outlet glaciers. The Cryosphere 8, 1457–1468. https://doi.org/10.5194/tc-8-1457-2014

Che, Y., Wang, S., Yi, S., Wei, Y., Cai, Y., 2020. Summer Mass Balance and Surface Velocity Derived by Unmanned Aerial Vehicle on Debris-Covered Region of Baishui River Glacier No. 1, Yulong Snow Mountain. Remote Sensing 12, 3280. https://doi.org/10.3390/rs12203280

Chen, J., Günther, F., Grosse, G., Liu, L., Lin, H., 2018. Sentinel-1 InSAR Measurements of Elevation Changes over Yedoma Uplands on Sobo-Sise Island, Lena Delta. Remote Sensing 10, 1152. https://doi.org/10.3390/rs10071152

Chen, S., Liu, Y., Axel, T., 2006. Climatic change on the Tibetan Plateau: Potential Evapotranspiration Trends from 1961–2000. Climatic Change 76, 291–319. https://doi.org/10.1007/s10584-006-9080-z

Chudley, T.R., Christoffersen, P., Doyle, S.H., Abellan, A., Snooke, N., 2019. High-accuracy UAV photogrammetry of ice sheet dynamics with no ground control. The Cryosphere 13, 955–968. https://doi.org/10.5194/tc-13-955-2019

Clark, M.K., 2011. Early Tibetan Plateau uplift history eludes. Geology 39, 991–992. https://doi.org/10.1130/focus102011.1

Clarke, G. (1987). A short history of scientific investigations on glaciers. Journal of Glaciology, 33(S1), 4-24. doi:10.3189/S0022143000215785

Cogley, J.G., 2009. Geodetic and direct mass-balance measurements: comparison and joint analysis. Annals of Glaciology 50, 96–100. https://doi.org/10.3189/172756409787769744

Cogley, J.G., Hock, R., Rasmussen, L.A., Arendt, A.A., Bauder, A., Braithwaite, R.J., Jansson, P., Kaser, G., Möller, M., Nicholson, L., Zemp, M., 2011. Glossary of glacier mass balance and related terms. IHP-VII Technical Documents in Hydrology 86. https://doi.org/10.5167/uzh-53475

Colgan, W., Rajaram, H., Abdalati, W., McCutchan, C., Mottram, R., Moussavi, M.S., Grigsby, S., 2016. Glacier crevasses: Observations, models, and mass balance implications. Reviews of Geophysics 54, 119–161. https://doi.org/10.1002/2015RG000504

Colonia, D., Torres, J., Haeberli, W., Schauwecker, S., Braendle, E., Giraldez, C., Cochachin, A., 2017. Compiling an Inventory of Glacier-Bed Overdeepenings and Potential New Lakes in De-Glaciating Areas of the Peruvian Andes:

Approach, First Results, and Perspectives for Adaptation to Climate Change. Water 9, 336. https://doi.org/10.3390/w9050336

Darnault, R., Rolland, Y., Braucher, R., Bourlès, D., Revel, M., Sanchez, G., Bouissou, S., 2012. Timing of the last deglaciation revealed by receding glaciers at the Alpine-scale: impact on mountain geomorphology. Quaternary Science Reviews 31, 127–142. https://doi.org/10.1016/j.quascirev.2011.10.019

Di Rita, M., Fugazza, D., Belloni, V., Diolaiuti, G., Scaioni, M., Crespi, M., 2020. GLACIER VOLUME CHANGE MONITORING FROM UAV OBSERVATIONS: ISSUES AND POTENTIALS OF STATE-OF-THE-ART TECHNIQUES. Int. Arch. Photogramm. Remote Sens. Spatial Inf. Sci. XLIII-B2-2020, 1041–1048. https://doi.org/10.5194/isprs-archives-XLIII-B2-2020-1041-2020

Ding, Y., Liu, S., Li, J., Shangguan, D., 2006. The retreat of glaciers in response to recent climate warming in western China. Annals of Glaciology 43, 97–105. https://doi.org/10.3189/172756406781812005

Diolaiuti, G., Smiraglia, C., Vassena, G., Motta, M., 2004. Dry calving processes at the ice cliff of Strandline Glacier northern Victoria Land, Antarctica. Annals of Glaciology 39, 201–208. https://doi.org/10.3189/172756404781813880

Dussaillant, I., Berthier, E., Brun, F., 2018. Geodetic Mass Balance of the Northern Patagonian Icefield from 2000 to 2012 Using Two Independent Methods. Frontiers in Earth Science 6.

Dykes, R.C., 2013. A multi-parameter study of iceberg calving and the retreat of Haupapa/Tasman Glacier, South Island, New Zealand. University of New Zealand.

Earth Resources Observation and Science Center/U.S. Geological Survey/U.S. Department of the Interior. 1997. USGS 30 ARC-second Global Elevation Data, GTOPO30. Research Data Archive at the National Center for Atmospheric Research, Computational and Information Systems Laboratory. https://doi.org/10.5065/A1Z4-EE71. Last accessed 14 Oct 2022.

Egli, P.E., Belotti, B., Ouvry, B., Irving, J., Lane, S.N., 2021. Subglacial Channels, Climate Warming, and Increasing Frequency of Alpine Glacier Snout Collapse. Geophysical Research Letters 48, e2021GL096031. https://doi.org/10.1029/2021GL096031

Evans, D.J.A., Ewertowski, M., Orton, C., 2016. Fláajökull (north lobe), Iceland: active temperate piedmont lobe glacial landsystem. Journal of Maps 12, 777–789. https://doi.org/10.1080/17445647.2015.1073185

Ewertowski, M.W., Evans, D.J.A., Roberts, D.H., Tomczyk, A.M., 2016. Glacial geomorphology of the terrestrial margins of the tidewater glacier, Nordenskiöldbreen, Svalbard. Journal of Maps 12, 476–487. https://doi.org/10.1080/17445647.2016.1192329

Ewertowski, M.W., Tomczyk, A.M., Evans, D.J.A., Roberts, D.H., Ewertowski, W., 2019. Operational Framework for Rapid, Very-high Resolution Mapping of Glacial Geomorphology Using Low-cost Unmanned Aerial Vehicles and Structure-from-Motion Approach. Remote Sensing 11, 65. https://doi.org/10.3390/rs11010065

Fahnestock, M., Scambos, T., Moon, T., Gardner, A., Haran, T., Klinger, M., 2016. Rapid large-area mapping of ice flow using Landsat 8. Remote Sensing of Environment, Landsat 8 Science Results 185, 84–94. https://doi.org/10.1016/j.rse.2015.11.023

Falatkova, K., Šobr, M., Neureiter, A., Schöner, W., Janský, B., Häusler, H., Engel, Z., Beneš, V., 2019. Development of proglacial lakes and evaluation of related outburst susceptibility at the Adygine ice-debris complex, northern Tien Shan. Earth Surface Dynamics 7, 301–320. https://doi.org/10.5194/esurf-7-301-2019

Farinotti, D., Huss, M., Bauder, A., Funk, M., Truffer, M., 2009. A method to estimate the ice volume and ice-thickness distribution of alpine glaciers. Journal of Glaciology 55, 422–430. https://doi.org/10.3189/002214309788816759

Fountain, A.G., Walder, J.S., 1998. Water flow through temperate glaciers. Reviews of Geophysics 36, 299–328. https://doi.org/10.1029/97RG03579

Forlani, G., Dall'Asta, E., Diotri, F., Cella, U.M. di, Roncella, R., Santise, M., 2018. Quality Assessment of DSMs Produced from UAV Flights Georeferenced with On-Board RTK Positioning. Remote Sensing 10, 311. https://doi.org/10.3390/rs10020311

Fu, B., Awata, Y., Du, J., He, W., 2005. Late Quaternary systematic stream offsets caused by repeated large seismic events along the Kunlun fault, northern Tibet. Geomorphology 71, 278–292. https://doi.org/10.1016/j.geomorph.2005.03.001

Fu, P., 2013. Paleoglaciology of Shaluli Shan, southeastern Tibetan Plateau (Physical Geography). Stockholm University, Stockholm.

Fu, P., Harbor, J.M., Stroeven, A.P., Hättestrand, C., Heyman, J., Zhou, L., 2013. Glacial geomorphology and paleoglaciation patterns in Shaluli Shan, the southeastern Tibetan Plateau — Evidence for polythermal ice cap glaciation. Geomorphology 182, 66–78. https://doi.org/10.1016/j.geomorph.2012.10.030

Fu, P., Heyman, J., Hättestrand, C., Stroeven, A.P., Harbor, J.M., 2012. Glacial geomorphology of the Shaluli Shan area, southeastern Tibetan Plateau. Journal of Maps 8, 48–55. https://doi.org/10.1080/17445647.2012.668762

Fu Y., Liu Q., Liu G., Zhang B., Zhang R., Cai J., Wang X., Xiang W., 2021. Seasonal ice dynamics in the lower ablation zone of Dagongba Glacier, southeastern Tibetan Plateau, from multitemporal UAV images. Journal of Glaciology 1–15. https://doi.org/10.1017/jog.2021.123

Fugazza, D., Scaioni, M., Corti, M., D'Agata, C., Azzoni, R.S., Cernuschi, M., Smiraglia, C., Diolaiuti, G.A., 2018. Combination of UAV and terrestrial photogrammetry to assess rapid glacier evolution and map glacier hazards. Natural Hazards and Earth System Sciences 18, 1055–1071. https://doi.org/10.5194/nhess-18-1055-2018

Fujita, K., Ageta, Y., Jianchen, P., Tandong, Y., 2000. Mass balance of Xiao Dongkemadi glacier on the central Tibetan Plateau from 1989 to 1995. Annals of Glaciology 31, 159–163. https://doi.org/10.3189/172756400781820075

Fujita, K., Suzuki, R., Nuimura, T., Sakai, A., 2008. Performance of ASTER and SRTM DEMs, and their potential for assessing glacial lakes in the Lunana region, Bhutan Himalaya. Journal of Glaciology 54, 220–228. https://doi.org/10.3189/002214308784886162

Gaddam, V.K., Kulkarni, A.V., Bjornsson, H., Gullapalli, S., Ballina, M., 2021. Applications of SPOT-7 tri-stereo imagery in deriving the surface topography and mass changes of glaciers in Indian Himalaya. Geocarto International 36, 1512–1532. https://doi.org/10.1080/10106049.2019.1648567

Gardelle, J., Berthier, E., Arnaud, Y., Kääb, A., 2013. Region-wide glacier mass balances over the Pamir-Karakoram-Himalaya during 1999–2011. The Cryosphere 7, 1263–1286. https://doi.org/10.5194/tc-7-1263-2013

Garg, P.K., Yadav, J.S., Rai, S.K., Shukla, A., 2022. Mass balance and morphological evolution of the Dokriani Glacier, central Himalaya, India during 1999–2014. Geoscience Frontiers 13, 101290. https://doi.org/10.1016/j.gsf.2021.101290

Ghuffar, S., 2018. DEM Generation from Multi Satellite PlanetScope Imagery. Remote Sensing 10, 1462. https://doi.org/10.3390/rs10091462

Gindraux, S., Boesch, R., Farinotti, D., 2017. Accuracy Assessment of Digital Surface Models from Unmanned Aerial Vehicles' Imagery on Glaciers. Remote Sensing 9, 186. https://doi.org/10.3390/rs9020186

Glasser, N.F., Etienne, J.L., Hambrey, M.J., Davies, J.R., Waters, R.A., Wilby, P.R., 2004. Glacial meltwater erosion and sedimentation as evidence for multiple glaciations in west Wales. Boreas 33, 224–237. https://doi.org/10.1111/j.1502-3885.2004.tb01143.x

Goodsell, B., Hambrey, M.J., Glasser, N.F., Nienow, P., Mair, D., 2005. The Structural Glaciology of a Temperate Valley Glacier: Haut Glacier d'Arolla, Valais, Switzerland. Arctic, Antarctic, and Alpine Research 37, 218–232. https://doi.org/10.1657/1523-0430(2005)037[0218:TSGOAT]2.0.CO;2

Guizar-Sicairos, M., Thurman, S.T., Fienup, J.R., 2008. Efficient subpixel image registration algorithms. Opt. Lett., OL 33, 156–158. https://doi.org/10.1364/OL.33.000156

Gulley, J., Benn, D.I., 2007. Structural control of englacial drainage systems in Himalayan debris-covered glaciers. Journal of Glaciology 53, 399–412. https://doi.org/10.3189/002214307783258378

Guo, W., Liu, S., Xu, J., Wu, L., Shangguan, D., Yao, X., Wei, J., Bao, W., Yu, P., Liu, Q., Jiang, Z., 2015. The second Chinese glacier inventory: data, methods and results. Journal of Glaciology 61, 357–372. https://doi.org/10.3189/2015JoG14J209

Haresign, E.C., 2004. Glacio-limnological interactions at lake-calving glaciers (Thesis). University of St Andrews.

Harrison, T.M., Copeland, P., Kidd, W.S.F., Yin, A., 1992. Raising Tibet. Science 255, 1663–1670. https://doi.org/10.1126/science.255.5052.1663

Heid, T., Kääb, A., 2012. Evaluation of existing image matching methods for deriving glacier surface displacements globally from optical satellite imagery. Remote Sensing of Environment 118, 339–355. https://doi.org/10.1016/j.rse.2011.11.024

Heim, A., 1936. The Glaciation and Solifluction of Minya Gongkar. The Geographical Journal 87, 444–450. https://doi.org/10.2307/1785645

Hendrickx, H., Vivero, S., Cock, L.D., Wit, B.D., Maeyer, P.D., Lambiel, C., Delaloye, R., Nyssen, J., Frankl, A., 2019. The reproducibility of SfM algorithms to produce detailed Digital Surface Models: the example of PhotoScan applied to a high-alpine rock glacier. Remote Sensing Letters 10, 11–20. https://doi.org/10.1080/2150704X.2018.1519641

Herreid, S., Pellicciotti, F., 2018. Automated detection of ice cliffs within supraglacial debris cover. The Cryosphere 12, 1811–1829. https://doi.org/10.5194/tc-12-1811-2018

Hill, A.C., Laugier, E.J., Casana, J., 2020. Archaeological Remote Sensing Using Multi-Temporal, Drone-Acquired Thermal and Near Infrared (NIR) Imagery: A Case Study at the Enfield Shaker Village, New Hampshire. Remote Sensing 12, 690. https://doi.org/10.3390/rs12040690

Hirano, A., Welch, R., Lang, H., 2003. Mapping from ASTER stereo image data: DEM validation and accuracy assessment. ISPRS Journal of Photogrammetry and Remote Sensing, Challenges in Geospatial Analysis and Visualization 57, 356–370. https://doi.org/10.1016/S0924-2716(02)00164-8

Hooke, R.LeB., 1989. Englacial and Subglacial Hydrology: A Qualitative Review. Arctic and Alpine Research 21, 221. https://doi.org/10.2307/1551561

Huang, M., Wang, M., Song, G., Li, G., Shen, Y., 1996. Hydraulic Effecrs in the Ablation Area of the Hailuogou Glacier. Journal of Glaciology and Geocryology 18, 46–50.

Hugonnet, R., McNabb, R., Berthier, E., Menounos, B., Nuth, C., Girod, L., Farinotti, D., Huss, M., Dussaillant, I., Brun, F., Kääb, A., 2021. Accelerated global glacier mass loss in the early twenty-first century. Nature 592, 726–731. https://doi.org/10.1038/s41586-021-03436-z

Huss, M., 2013. Density assumptions for converting geodetic glacier volume change to mass change, The Cryosphere, 7, 877–887, https://doi.org/10.5194/tc-7-877-2013.

Iken, A., 1981. The Effect of the Subglacial Water Pressure on the Sliding Velocity of a Glacier in an Idealized Numerical Model. Journal of Glaciology 27, 407–421. https://doi.org/10.3189/S0022143000011448

Iken, A., Röthlisberger, H., Flotron, A., Haeberli, W., 1983. The Uplift of Unteraargletscher at the Beginning of the Melt Season—A Consequence of Water Storage at the Bed? Journal of Glaciology 29, 28–47. https://doi.org/10.3189/S0022143000005128

Iken, A., Truffe, M., 1997. The relationship between subglacial water pressure and velocity of Findelengletscher, Switzerland, during its advance and retreat. Journal of Glaciology 43, 328–338. https://doi.org/10.3189/S0022143000003282

Immerzeel, W.W., Kraaijenbrink, P.D.A., Shea, J.M., Shrestha, A.B., Pellicciotti, F., Bierkens, M.F.P., de Jong, S.M., 2014. High-resolution monitoring of Himalayan glacier dynamics using unmanned aerial vehicles. Remote Sensing of Environment 150, 93–103. https://doi.org/10.1016/j.rse.2014.04.025

James, L.A., Hodgson, M.E., Ghoshal, S., Latiolais, M.M., 2012. Geomorphic change detection using historic maps and DEM differencing: The temporal dimension of geospatial analysis. Geomorphology 137, 181–198. https://doi.org/10.1016/j.geomorph.2010.10.039

Jarosch, A.H., 2008. Icetools: A full Stokes finite element model for glaciers. Computers & Geosciences 34, 1005–1014. https://doi.org/10.1016/j.cageo.2007.06.012

Jennings, S.J.A., Hambrey, M.J., 2021. Structures and Deformation in Glaciers and Ice Sheets. Reviews of Geophysics 59, e2021RG000743. https://doi.org/10.1029/2021RG000743

Jennings, S.J.A., Hambrey, M.J., Glasser, N.F., James, T.D., Hubbard, B., 2016. Structural glaciology of Austre Brøggerbreen, northwest Svalbard. Journal of Maps 12, 790–796. https://doi.org/10.1080/17445647.2015.1076744

Jones, C., Ryan, J., Holt, T., Hubbard, A., 2018. Structural glaciology of Isunguata Sermia, West Greenland. Journal of Maps 14, 517–527. https://doi.org/10.1080/17445647.2018.1507952

Jouberton, A., Shaw, T.E., Miles, E., McCarthy, M., Fugger, S., Ren, S., Dehecq, A., Yang, W., Pellicciotti, F., 2022. Warming-induced monsoon precipitation phase change intensifies glacier mass loss in the southeastern Tibetan Plateau. Proceedings of the National Academy of Sciences 119, e2109796119. https://doi.org/10.1073/pnas.2109796119

Kääb, A., 2008. Glacier Volume Changes Using ASTER Satellite Stereo and ICESat GLAS Laser Altimetry. A Test Study on EdgeØya, Eastern Svalbard. IEEE Transactions on Geoscience and Remote Sensing 46, 2823–2830. https://doi.org/10.1109/TGRS.2008.2000627

Kääb, A., 2007. Glacier volume changes using ASTER optical stereo. A test study in Eastern Svalbard. IEEE, pp. 3994–3996. https://doi.org/10.1109/IGARSS.2007.4423724

Kääb, A., Altena, B., Mascaro, J., 2019. River-ice and water velocities using the Planet optical cubesat constellation. Hydrology and Earth System Sciences 23, 4233–4247. https://doi.org/10.5194/hess-23-4233-2019

Kääb, A., Winsvold, S.H., Altena, B., Nuth, C., Nagler, T., Wuite, J., 2016. Glacier Remote Sensing Using Sentinel-2. Part I: Radiometric and Geometric Performance, and Application to Ice Velocity. Remote Sensing 8, 598. https://doi.org/10.3390/rs8070598

Karimi, N., Sheshangosht, S., Roozbahani, R., 2021. High-resolution monitoring of debris-covered glacier mass budget and flow velocity using repeated UAV photogrammetry in Iran. Geomorphology 389, 107855. https://doi.org/10.1016/j.geomorph.2021.107855

Kaushik, S., Joshi, P.K., Singh, T., 2019. Development of glacier mapping in Indian Himalaya: a review of approaches. International Journal of Remote Sensing 40, 6607–6634. https://doi.org/10.1080/01431161.2019.1582114

Kavanaugh, J.L., Clarke, G.K.C., 2001. Abrupt glacier motion and reorganization of basal shear stress following the establishment of a connected drainage system. Journal of Glaciology 47, 472–480. https://doi.org/10.3189/172756501781831972

King, O., Bhattacharya, A., Bhambri, R., Bolch, T., 2019. Glacial lakes exacerbate Himalayan glacier mass loss. Scientific Reports 9, 18145. https://doi.org/10.1038/s41598-019-53733-x

King, O., Dehecq, A., Quincey, D., Carrivick, J., 2018. Contrasting geometric and dynamic evolution of lake and land-terminating glaciers in the central Himalaya. Global and Planetary Change 167, 46–60. https://doi.org/10.1016/j.gloplacha.2018.05.006

Kirkbride, M.P., 1993. The temporal significance of transitions from melting to calving termini at glaciers in the central Southern Alps of New Zealand. The Holocene 3, 232–240. https://doi.org/10.1177/095968369300300305

Kirkbride, M.P., Warren, C.R., 1999. Tasman Glacier, New Zealand: 20th-century thinning and predicted calving retreat. Global and Planetary Change 22, 11–28. https://doi.org/10.1016/S0921-8181(99)00021-1

Krieger, G., Moreira, A., Fiedler, H., Hajnsek, I., Werner, M., Younis, M., Zink, M., 2007. TanDEM-X: A Satellite Formation for High-Resolution SAR Interferometry. IEEE Transactions on Geoscience and Remote Sensing 45, 3317–3341. https://doi.org/10.1109/TGRS.2007.900693

Kneib, M., Miles, E.S., Jola, S., Buri, P., Herreid, S., Bhattacharya, A., Watson, C.S., Bolch, T., Quincey, D., Pellicciotti, F., 2021. Mapping ice cliffs on debris-covered glaciers using multispectral satellite images. Remote Sensing of Environment 253, 112201. https://doi.org/10.1016/j.rse.2020.112201

Kumar, A., Negi, H.S., Kumar, K., Kanda, N., Singh, K.K., Pandit, A., Ramsankaran, R., 2020. Estimation of recent changes in thickness and mass balance of the Patsio glacier in the Great Himalayan region using geodetic technique and ancillary data. Geocarto International 35, 47–63. https://doi.org/10.1080/10106049.2018.1506506

Lardeux, P., Glasser, N., Holt, T., Hubbard, B., 2016. Glaciological and geomorphological map of Glacier Noir and Glacier Blanc, French Alps. Journal of Maps 12, 582–596. https://doi.org/10.1080/17445647.2015.1054905

Li, S., Benson, C., Gens, R., Lingle, C., 2008. Motion patterns of Nabesna Glacier (Alaska) revealed by interferometric SAR techniques. Remote Sensing of Environment 112, 3628–3638. https://doi.org/10.1016/j.rse.2008.05.015

Li, X., Cheng, G., Jin, H., Kang, E., Che, T., Jin, R., Wu, L., Nan, Z., Wang, J., Shen, Y., 2008. Cryospheric change in China. Global and Planetary Change 62, 210–218. https://doi.org/10.1016/j.gloplacha.2008.02.001

Li, Y., Fu, P., 2019. Mapping the Late-Holocene Glacial Geomorphology and Glacier Surface Types in the Mt. Harajoriha, Central Tian Shan. International Journal of Geosciences 10, 669. https://doi.org/10.4236/ijg.2019.106038

Li, Z., He, Y., Jia, W., Pang, H., He, X., Wang, S., Zhang, N., Zhang, W., Liu, Q., Xin, H., 2009. Changes in Hailuogou Glacier during the Recent 100 Years under Global Warming. Journal of Glaciology and Geocryology 31, 75–81. (in Chinese)

Li, Z., He, Y., Yang, X., Theakstone, W.H., Jia, W., Pu, T., Liu, Q., He, X., Song, B., Zhang, N., Wang, S., Du, J., 2010. Changes of the Hailuogou glacier, Mt. Gongga, China, against the background of climate change during the Holocene. Quaternary International 218, 166–175. https://doi.org/10.1016/j.quaint.2008.09.005

Li, Z., Sun, W., Zeng, Q., 1998. Measurements of Glacier Variation in the Tibetan Plateau Using Landsat Data. Remote Sensing of Environment 63, 258–264. https://doi.org/10.1016/S0034-4257(97)00140-5

Liao, H., Liu, Q., Zhong, Y., Lu, X., 2020. Landsat-Based Estimation of the Glacier Surface Temperature of Hailuogou Glacier, Southeastern Tibetan Plateau, Between 1990 and 2018. Remote Sensing 12, 2105. https://doi.org/10.3390/rs12132105

Lindholm, M.S., Heyman, J., 2016. Glacial geomorphology of the Maidika region, Tibetan Plateau. Journal of Maps 12, 797–803. https://doi.org/10.1080/17445647.2015.1078182

Liu, Q., Guo, W., Nie, Y., Liu, S., Xu, J., 2016. Recent glacier and glacial lake changes and their interactions in the Bugyai Kangri, southeast Tibet. Annals of Glaciology 57, 61–69. https://doi.org/10.3189/2016AoG71A415

Liu, Q., Liu, S., 2012. Tracer Test of Englacial and Subglacial Drainage System Evolution and a Case Study at Hailuogou Glacier. Journal of Glaciology and Geocryology 34, 1207–1219. (in Chinese)

Liu, Q., Liu, S., 2010. Seasonal evolution of the englacial and subglacial drainage systems of a temperate glacier revealed by hydrological analysis. Sciences in Cold and Arid Regions 2, 51–58. (in Chinese)

Liu, Q., Liu, S., Cao, W., 2018. Seasonal Variation of Drainage System in the Lower Ablation Area of a Monsoonal Temperate Debris-Covered Glacier in Mt. Gongga, South-Eastern Tibet. Water 10, 1050. https://doi.org/10.3390/w10081050

Liu, Q., Liu, S., Zhang, Yong, Wang, X., Zhang, Yingsong, Guo, W., Xu, J., 2010. Recent shrinkage and hydrological response of Hailuogou glacier, a monsoon temperate glacier on the east slope of Mount Gongga, China. Journal of Glaciology 56, 215–224. https://doi.org/10.3189/002214310791968520

Liu, Q., Mayer, C., Wang, X., Nie, Y., Wu, K., Wei, J., Liu, S., 2020. Interannual flow dynamics driven by frontal retreat of a lake-terminating glacier in the Chinese Central Himalaya. Earth and Planetary Science Letters 546, 116450. https://doi.org/10.1016/j.epsl.2020.116450

Liu, Q., Zhang, Y., 2017. Studies on the Dynamics of Monsoonal Temperate Glacier in Mt. Gongga: a Review. Mountain Research 35, 717–726. http://dx.doi.org/10.16089/j.cnki.1008-2786.000271(in Chinese)

Liu, S., Guo, W., Xu, J., ShangGuan, D., Wu, L., Yao, X., Zhao, J., Liu, Q., Jiang, Z., Li, P., Wei, J., Bao, W., Yu, P., Ding, L., Li, G., Ge, C., Wang, Y., 2014. The Second Glacier Invertory Dataset of China (Version 1.0). Cold and Arid Regions Science Data Center. https://doi.org/10.3972/glacier.001.2013.db

Liu, S., Yao, X., Guo, W., Xu, J., ShangGuan, D., Wei, J., Bao, W., Wu, L., 2015. The contemporary glaciers in China based on the Second Chinese Glacier Inventory. Acta Geographica Sinica 70, 4–16.

Liu, X., Chen, B., 2000. Climatic warming in the Tibetan Plateau during recent decades. International Journal of Climatology 20, 1729–1742. https://doi.org/10.1002/1097-0088(20001130)20:14<1729::AID-JOC556>3.0.CO;2-Y

Liu, X., Xu, Z., Yang, H., Vaghefi, S.A., 2021. Responses of the Glacier Mass Balance to Climate Change in the Tibetan Plateau During 1975–2013. Journal of Geophysical Research: Atmospheres 126, e2019JD032132. https://doi.org/10.1029/2019JD032132

Lowe, D.G., 2004. Distinctive Image Features from Scale-Invariant Keypoints. International Journal of Computer Vision 60, 91–110. https://doi.org/10.1023/B:VISI.0000029664.99615.94

Lu, R., Gao, S., 1992. Debris Flow in the Ice Tongue Area of Hailuogou Glacier on the Eastern Slope of Mt.Gongga. Journal of Glaciology and Geocryology 73–80. (in Chinese)

Lu, R., Zhong, X., 1996. Block and Burst of the Water channels inside Hailuogou Glacier. Journal of Glaciology and Geocryology 18, 257–263. (in Chinese)

Lv M., Quincey D.J., Guo H., King O., Liu G., Yan S., Lu X., Ruan Z., 2020. Examining geodetic glacier mass balance in the eastern Pamir transition zone. Journal of Glaciology 66, 927–937. https://doi.org/10.1017/jog.2020.54

Ma, L., Tian, L., Pu, J., Wang, P., 2010. Recent area and ice volume change of Kangwure Glacier in the middle of Himalayas. Chinese Science Bulletin 55, 2088–2096. https://doi.org/10.1007/s11434-010-3211-7

Magnússon, E., Muñoz-Cobo Belart, J., Pálsson, F., Ágústsson, H., Crochet, P., 2016. Geodetic mass balance record with rigorous uncertainty estimates deduced from aerial photographs and lidar data – Case study from Drangajökull ice cap, NW Iceland. The Cryosphere 10, 159–177. https://doi.org/10.5194/tc-10-159-2016

Mair, D., Nienow, P., Sharp, M., Wohlleben, T., Willis, I., 2002. Influence of subglacial drainage system evolution on glacier surface motion: Haut Glacier d’Arolla, Switzerland. Journal of Geophysical Research: Solid Earth 107, EPM 8-1-EPM 8-13. https://doi.org/10.1029/2001JB000514

Mair, D., Nienow, P., Willis, I., Sharp, M., 2001. Spatial patterns of glacier motion during a high-velocity event: Haut Glacier d’Arolla, Switzerland. Journal of Glaciology 47, 9–20. https://doi.org/10.3189/172756501781832412

Mair D., Willis I., Fischer U.H., Hubbard B., Nienow P., Hubbard A., 2003. Hydrological controls on patterns of surface, internal and basal motion during three “spring events”: Haut Glacier d’Arolla, Switzerland. Journal of Glaciology 49, 555–567. https://doi.org/10.3189/172756503781830467

Mair, D.W.F., Sharp, M.J., Willis, I.C., 2002. Evidence for basal cavity opening from analysis of surface uplift during a high-velocity event: Haut Glacier d’Arolla, Switzerland. Journal of Glaciology 48, 208–216. https://doi.org/10.3189/172756502781831502

Mallalieu, J., Carrivick, J.L., Quincey, D.J., Smith, M.W., James, W.H.M., 2017. An integrated Structure-from-Motion and time-lapse technique for quantifying ice-margin dynamics. Journal of Glaciology 63, 937–949. https://doi.org/10.1017/jog.2017.48

Maurer, J.M., Schaefer, J.M., Rupper, S., Corley, A., 2019. Acceleration of ice loss across the Himalayas over the past 40 years. Science Advances 5, eaav7266. https://doi.org/10.1126/sciadv.aav7266

Maussion, F., Butenko, A., Champollion, N., Dusch, M., Eis, J., Fourteau, K., Gregor, P., Jarosch, A.H., Landmann, J., Oesterle, F., Recinos, B., Rothenpieler, T., Vlug, A., Wild, C.T., Marzeion, B., 2019. The Open Global Glacier Model (OGGM) v1.1. Geoscientific Model Development 12, 909–931. https://doi.org/10.5194/gmd-12-909-2019

Mei, Z., Zhi-jiu, C., Geng-nian, L., Yi-xin, C., Zhen-yu, N., Hai-rong, F., 2013. Formation and deformation of subglacier deposits of Hailuogou Glacier in Mt. Gongga, Southeastern Tibetan Plateau. Journal of Glaciology and Geocryology 35, 1143–1155. (in Chinese)

Miles, E.S., Steiner, J., Willis, I., Buri, P., Immerzeel, W.W., Chesnokova, A., Pellicciotti, F., 2017. Pond Dynamics and Supraglacial-Englacial Connectivity on Debris-Covered Lirung Glacier, Nepal. Front. Earth Sci. 5. https://doi.org/10.3389/feart.2017.00069

Miles, K.E., Hubbard, B., Irvine-Fynn, T.D.L., Miles, E.S., Quincey, D.J., Rowan, A.V., 2020. Hydrology of debris-covered glaciers in High Mountain Asia. Earth-Science Reviews 207, 103212. https://doi.org/10.1016/j.earscirev.2020.103212

Motyka, R.J., Hunter, L., Echelmeyer, K.A., Connor, C., 2003. Submarine melting at the terminus of a temperate tidewater glacier, LeConte Glacier, Alaska, U.S.A. Annals of Glaciology 36, 57–65. https://doi.org/10.3189/172756403781816374

Nakawo, M., Young, G.J., 1982. Estimate of Glacier Ablation under a Debris Layer from Surface Temperature and Meteorological Variables. Journal of Glaciology 28, 29–34. https://doi.org/10.3189/S002214300001176X

Nie, Y., Pritchard, H.D., Liu, Q., Hennig, T., Wang, W., Wang, X., Liu, S., Nepal, S., Samyn, D., Hewitt, K., Chen, X., 2021. Glacial change and hydrological implications in the Himalaya and Karakoram. Nat Rev Earth Environ 2, 91–106. https://doi.org/10.1038/s43017-020-00124-w

Nie, Y., Sheng, Y., Liu, Q., Liu, L., Liu, S., Zhang, Y., Song, C., 2017. A regional-scale assessment of Himalayan glacial lake changes using satellite observations from 1990 to 2015. Remote Sensing of Environment 189, 1–13. https://doi.org/10.1016/j.rse.2016.11.008

Nye, J.F., 1951. The Flow of Glaciers and Ice-Sheets as a Problem in Plasticity. Proceedings of the Royal Society A: Mathematical, Physical and Engineering Sciences 207, 554–572. https://doi.org/10.1098/rspa.1951.0140

Oerlemans, J., Giesen, R.H., Broeke, M.R.V.D., 2009. Retreating alpine glaciers: increased melt rates due to accumulation of dust (Vadret da Morteratsch, Switzerland). Journal of Glaciology 55, 729–736. https://doi.org/10.3189/002214309789470969

Östrem, G., 1959. Ice Melting under a Thin Layer of Moraine, and the Existence of Ice Cores in Moraine Ridges. Geografiska Annaler 41, 228–230, , DOI: 10.1080/20014422.1959.11907953

Owen, L.A., Finkel, R.C., Barnard, P.L., Haizhou, M., Asahi, K., Caffee, M.W., Derbyshire, E., 2005. Climatic and topographic controls on the style and timing of Late Quaternary glaciation throughout Tibet and the Himalaya defined by 10Be cosmogenic radionuclide surface exposure dating. Quaternary Science Reviews 24, 1391–1411. https://doi.org/10.1016/j.quascirev.2004.10.014

Owen, L.A., Caffee, M.W., Finkel, R.C., Seong, Y.B., 2008. Quaternary glaciation of the Himalayan–Tibetan orogen. Journal of Quaternary Science 23, 513–531. https://doi.org/10.1002/jqs.1203

Pajares, G., 2015. Overview and Current Status of Remote Sensing Applications Based on Unmanned Aerial Vehicles (UAVs). Photogrammetric Engineering & Remote Sensing 81, 281–330. https://doi.org/10.14358/PERS.81.4.281

Pan, B.T., Zhang, G.L., Wang, J., Cao, B., Geng, H.P., Wang, J., Zhang, C., Ji, Y.P., 2012. Glacier changes from 1966–2009 in the Gongga Mountains, on the south-eastern margin of the Qinghai-Tibetan Plateau and their climatic forcing. The Cryosphere 6, 1087–1101. https://doi.org/10.5194/tc-6-1087-2012

Patel, A., Prajapati, R., Dharpure, J.K., Mani, S., Chauhan, D., 2019. Mapping and monitoring of glacier areal changes using multispectral and elevation data: A case study over Chhota-Shigri glacier. Earth Sci Inform 12, 489–499. https://doi.org/10.1007/s12145-019-00388-x

Paul, F., 2000. Evaluation of different methods for glacier mapping using Landsat TM. EARSeL eProceedings, 1(1), 239-245.

Paul, F., Winsvold, S., Kääb, A., Nagler, T., Schwaizer, G., 2016. Glacier Remote Sensing Using Sentinel-2. Part II: Mapping Glacier Extents and Surface Facies, and Comparison to Landsat 8. Remote Sensing 8, 575. https://doi.org/10.3390/rs8070575

Paterson, W. S. B. 1977. Secondary and tertiary creep of glacier ice as measured by borehole closure rates, Rev. Geophys., 15 (1), 47– 55, doi:10.1029/RG015i001p00047.

Phan, V.H., Lindenbergh, R., Menenti, M., 2012. ICESat derived elevation changes of Tibetan lakes between 2003 and 2009. International Journal of Applied Earth Observation and Geoinformation, Retrieval of Key Eco-hydrological Parameters for Cold and Arid Regions 17, 12–22. https://doi.org/10.1016/j.jag.2011.09.015

Pralong, A., Funk, M., 2005. Dynamic damage model of crevasse opening and application to glacier calving. Journal of Geophysical Research: Solid Earth 110. https://doi.org/10.1029/2004JB003104

Pu, J., 1994. Glacier Inventory of China (the Chanjing River Drainage Basin). Gansu Culture Press, Lanzhou (in Chinese).

Pu, J., Yao, T., Wang, N., Su, Z., Shen, Y., 2004. Fluctuations of the Glaciers on the Qinghai-Tibetan Plateau during the Past Century. Journal of Glaciology and Geocryology 5. (in Chinese)

Quincey, D.J., Lucas, R.M., Richardson, S.D., Glasser, N.F., Hambrey, M.J., Reynolds, J.M., 2005. Optical remote sensing techniques in high-mountain environments: application to glacial hazards. Progress in Physical Geography 29, 475–505.

Quincey, D.J., Richardson, S.D., Luckman, A., Lucas, R.M., Reynolds, J.M., Hambrey, M.J., Glasser, N.F., 2007. Early recognition of glacial lake hazards in the Himalaya using remote sensing datasets. Global and Planetary Change, Climate Change Impacts on Mountain Glaciers and Permafrost 56, 137–152. https://doi.org/10.1016/j.gloplacha.2006.07.013

Rabatel, A., Sirguey, P., Drolon, V., Maisongrande, P., Arnaud, Y., Berthier, E., Davaze, L., Dedieu, J.-P., Dumont, M., 2017. Annual and Seasonal Glacier-Wide Surface Mass Balance Quantified from Changes in Glacier Surface State: A Review on Existing Methods Using Optical Satellite Imagery. Remote Sensing 9, 507. https://doi.org/10.3390/rs9050507

Racoviteanu, A.E., Williams, M.W., Barry, R.G., 2008. Optical Remote Sensing of Glacier Characteristics: A Review with Focus on the Himalaya. Sensors 8, 3355–3383. https://doi.org/10.3390/s8053355

Rea, B.R., Evans, D.J.A., 2007. Quantifying climate and glacier mass balance in north Norway during the Younger Dryas. Palaeogeography, Palaeoclimatology, Palaeoecology 246, 307–330. https://doi.org/10.1016/j.palaeo.2006.10.010

Reynolds, J.M., 2000. On the formation of supraglacial lakes on debris- covered glaciers. Seattle: IAHS-AISH Publication, 153–161.

Rignot, E., 2006. Changes in the Velocity Structure of the Greenland Ice Sheet. Science 311, 986–990. https://doi.org/10.1126/science.1121381

Rivera, A., & Bown, F. (2013). Recent glacier variations on active ice capped volcanoes in the Southern Volcanic Zone (37–46 S), Chilean Andes. Journal of South American Earth Sciences, 45, 345-356.

Rossini, M., Di Mauro, B., Garzonio, R., Baccolo, G., Cavallini, G., Mattavelli, M., De Amicis, M., Colombo, R., 2018. Rapid melting dynamics of an alpine glacier with repeated UAV photogrammetry. Geomorphology 304, 159–172. https://doi.org/10.1016/j.geomorph.2017.12.039

Rusnák, M., Sládek, J., Kidová, A., Lehotský, M., 2018. Template for high-resolution river landscape mapping using UAV technology. Measurement 115, 139–151. https://doi.org/10.1016/j.measurement.2017.10.023

Ryan, J.C., Hubbard, A.L., Box, J.E., Todd, J., Christoffersen, P., Carr, J.R., Holt, T.O., Snooke, N., 2015. UAV photogrammetry and structure from motion to assess calving dynamics at Store Glacier, a large outlet draining the Greenland ice sheet. The Cryosphere 9, 1–11. https://doi.org/10.5194/tc-9-1-2015

Sakai, A., 2012. Glacial Lakes in the Himalayas: A Review on Formation and Expansion Processes 8.

Sakai, A., Fujita, K., 2010. Formation conditions of supraglacial lakes on debris-covered glaciers in the Himalaya. Journal of Glaciology 56, 177–181. https://doi.org/10.3189/002214310791190785

Sakai, A., Nakawo, M., Fujita, K., 2002. Distribution Characteristics and Energy Balance of Ice Cliffs on Debris-covered Glaciers, Nepal Himalaya. Arctic, Antarctic, and Alpine Research 34, 12–19. https://doi.org/10.1080/15230430.2002.12003463

Sakai, A., Nishimura, K., Kadota, T., Takeuchi, N., 2009. Onset of calving at supraglacial lakes on debris-covered glaciers of the Nepal Himalaya. Journal of Glaciology 55, 909–917. https://doi.org/10.3189/002214309790152555

Sato, Y., Fujita, K., Inoue, H., Sunako, S., Sakai, A., Tsushima, A., Podolskiy, E.A., Kayastha, R., Kayastha, R.B., 2021. Ice Cliff Dynamics of Debris-Covered Trakarding Glacier in the Rolwaling Region, Nepal Himalaya. Frontiers in Earth Science 9, 398. https://doi.org/10.3389/feart.2021.623623

Schneider, R.A.A., Blomdin, R., Fu, P., Xu, X.K., Stroeven, A.P., 2021. Paleoglacial footprint and fluvial terraces of the Shaluli Shan, SE Tibetan Plateau. Journal of Maps 0, 1–14. https://doi.org/10.1080/17445647.2021.1946443

Scott Watson, C., Quincey, D.J., Carrivick, J.L., Smith, M.W., 2017. Ice cliff dynamics in the Everest region of the Central Himalaya. Geomorphology 278, 238–251. https://doi.org/10.1016/j.geomorph.2016.11.017

Shean, D.E., Alexandrov, O., Moratto, Z.M., Smith, B.E., Joughin, I.R., Porter, C., Morin, P., 2016. An automated, open-source pipeline for mass production of digital elevation models (DEMs) from very-high-resolution commercial stereo satellite imagery. ISPRS Journal of Photogrammetry and Remote Sensing 116, 101–117. https://doi.org/10.1016/j.isprsjprs.2016.03.012

Shi, Y., Zheng, B., Yao, T., 1999. Glaciers and Environments during the Last Glacial Maximun (LGM) on the Tibetan Plateau. Journal of Glaciology and Geocryology 19, 97–113. (in Chinese)

Shiramizu, K., Doi, K., Aoyama, Y., 2017. Generation of a high-accuracy regional DEM based on ALOS/PRISM imagery of East Antarctica. Polar Science 14, 30–38. https://doi.org/10.1016/j.polar.2017.10.002

Shreve, R.L., 1985. Esker characteristics in terms of glacier physics, Katahdin esker system, Maine. GSA Bulletin 96, 639–646. https://doi.org/10.1130/0016-7606(1985)96<639:ECITOG>2.0.CO;2

Śledź, S., Ewertowski, M.W., Piekarczyk, J., 2021. Applications of unmanned aerial vehicle (UAV) surveys and Structure from Motion photogrammetry in glacial and periglacial geomorphology. Geomorphology 378, 107620. https://doi.org/10.1016/j.geomorph.2021.107620

Smith, M.W., Carrivick, J.L., Quincey, D.J., 2016. Structure from motion photogrammetry in physical geography. Progress in Physical Geography 40, 247–275. https://doi.org/10.1177/0309133315615805

Soncini, A., Bocchiola, D., Confortola, G., Minora, U., Vuillermoz, E., Salerno, F., Viviano, G., Shrestha, D., Senese, A., Smiraglia, C., Diolaiuti, G., 2016. Future hydrological regimes and glacier cover in the Everest region: The case study of the upper Dudh Koshi basin. Science of The Total Environment 565, 1084–1101. https://doi.org/10.1016/j.scitotenv.2016.05.138

Strozzi, T., Luckman, A., Murray, T., Wegmuller, U., Werner, C.L., 2002. Glacier motion estimation using SAR offset-tracking procedures. IEEE Transactions on Geoscience and Remote Sensing 40, 2384–2391. https://doi.org/10.1109/TGRS.2002.805079

Stucky de Quay, G., Roberts, G.G., Rood, D.H., Fernandes, V.M., 2019. Holocene uplift and rapid fluvial erosion of Iceland: A record of post-glacial landscape evolution. Earth and Planetary Science Letters 505, 118–130. https://doi.org/10.1016/j.epsl.2018.10.026

Su, Z., Shi, Y., 2000. Response of Monsoonal Temperature Glacier in China to Global Warming Since the Little Ice Age. Journal of Glaciology and Geocryology 22, 223–229. (in Chinese)

Sun, J., Zhou, T., Liu, M., Chen, Y., Shang, H., Zhu, L., Shedayi, A.A., Yu, H., Cheng, G., Liu, G., Xu, M., Deng, W., Fan, J., Lu, X., Sha, Y., 2018. Linkages of the dynamics of glaciers and lakes with the climate elements over the Tibetan Plateau. Earth-Science Reviews 185, 308–324. https://doi.org/10.1016/j.earscirev.2018.06.012

Sun, Y, Jiang, L., Liu, L., Sun, Y, Wang, H., 2017. Spatial-Temporal Characteristics of Glacier Velocity in the Central Karakoram Revealed with 1999–2003 Landsat-7 ETM+ Pan Images. Remote Sensing 9, 1064. https://doi.org/10.3390/rs9101064

Sutherland, J.L., Carrivick, J.L., Gandy, N., Shulmeister, J., Quincey, D.J., Cornford, S.L., 2020. Proglacial Lakes Control Glacier Geometry and Behavior During Recession. Geophysical Research Letters 47, e2020GL088865. https://doi.org/10.1029/2020GL088865

Suzuki, R., Fujita, K., Ageta, Y., 2007. Spatial distribution of thermal properties on debris-covered glaciers in the Himalayas derived from ASTER data. Bulletin of Glaciological Research 11.

Tadono, T., Nagai, H., Ishida, H., Oda, F., Naito, S., Minakawa, K., Iwamoto, H., 2016. Generation of the 30 M-Mesh Global Digital Surface Model by Alos Prism. ISPRS - International Archives of the Photogrammetry, Remote Sensing and Spatial Information Sciences 41B4, 157–162. https://doi.org/10.5194/isprs-archives-XLI-B4-157-2016

Tămaș, D.M., Kis, B.M., Tămaș, A., Szalay, R., 2022. Identifying CO2 Seeps in a Long-Dormant Volcanic Area Using Uncrewed Aerial Vehicle-Based Infrared Thermometry: A Qualitative Study. Sensors 22, 2719. https://doi.org/10.3390/s22072719

Taylor, L.S., Quincey, D.J., Smith, M.W., Baumhoer, C.A., McMillan, M., Mansell, D.T., 2021. Remote sensing of the mountain cryosphere: Current capabilities and future opportunities for research. Progress in Physical Geography: Earth and Environment 03091333211023690. https://doi.org/10.1177/03091333211023690

Taylor, L. S., Quincey, D. J., Smith, M. W., Potter, E. R., Castro, J., & Fyffe, C. L. (2022). Multi-decadal glacier area and mass balance change in the Southern Peruvian Andes. Frontiers in Earth Science, 468.

Thorsteinsson, T., Raymond, C.F., Gudmundsson, G.H., Bindschadler, R.A., Vornberger, P., Joughin, I., 2003. Bed topography and lubrication inferred from surface measurements on fast-flowing ice streams. Journal of Glaciology 49, 481–490. https://doi.org/10.3189/172756503781830502

Urbanski, J.A., 2018. A GIS tool for two-dimensional glacier-terminus change tracking. Computers & Geosciences 111, 97–104. https://doi.org/10.1016/j.cageo.2017.11.004

USGS 30 ARC-second Global Elevation Data, GTOPO30, Research Data Archive at the National Center for Atmospheric Research, Computational and Information Systems Laboratory, 1997. https://doi.org/10.5065/A1Z4-EE71

Van der Veen, C.J., 2002. Calving glaciers. Progress in Physical Geography: Earth and Environment 26, 96–122. https://doi.org/10.1191/0309133302pp327ra

Vasuki, Y., Holden, E.-J., Kovesi, P., Micklethwaite, S., 2014. Semi-automatic mapping of geological Structures using UAV-based photogrammetric data: An image analysis approach. Computers & Geosciences 69, 22–32. https://doi.org/10.1016/j.cageo.2014.04.012

Vaughan, D.G., 1993. Relating the occurrence of crevasses to surface strain rates. Journal of Glaciology 39, 255–266. https://doi.org/10.3189/S0022143000015926

Verhoeven, G., 2011. Taking computer vision aloft – archaeological three-dimensional reconstructions from aerial photographs with photoscan. Archaeological Prospection 18, 67–73. https://doi.org/10.1002/arp.399

Vieli, A., Funk, M., Blatter, H., 2001. Flow dynamics of tidewater glaciers: a numerical modelling approach. Journal of Glaciology 47, 595–606. https://doi.org/10.3189/172756501781831747

Villanueva, J.K.S., Blanco, A.C., 2019. Optimization of Ground Control Point (GCP) Configuration for Unmanned Aerial Vehicle (UAV) Survey using Structure from Motion (SFM). Int. Arch. Photogramm. Remote Sens. Spatial Inf. Sci. XLII-4/W12, 167–174. https://doi.org/10.5194/isprs-archives-XLII-4-W12-167-2019

Walder, J.S., 2010. Röthlisberger channel theory: its origins and consequences. Journal of Glaciology 56, 1079–1086. https://doi.org/10.3189/002214311796406031

Wang, J., Pan, B., Zhang, G., Cui, H., Cao, B., Geng, H., 2013. Late Quaternary glacial chronology on the eastern slope of Gongga Mountain, eastern Tibetan Plateau, China. Sci. China Earth Sci. 56, 354–365. https://doi.org/10.1007/s11430-012-4514-0

Wang, S., Che, Y., Wei, Y., 2021. Spatiotemporal dynamic characteristics of typical temperate glaciers in China. Sci Rep 11, 657. https://doi.org/10.1038/s41598-020-80418-7

Wang, P., Li, Z., Jin, S., Zhou, P., Yao, H., Wang, W., 2014. Ice thickness, volume and subglacial topography of Urumqi Glacier No. 1, Tianshan mountains, central Asia, by ground penetrating radar survey. Journal of Earth System Science 123, 581–591. https://doi.org/10.1007/s12040-014-0421-4

Wang, P., Li, Z., Li, H., Wang, W., Yao, H., 2014. Comparison of glaciological and geodetic mass balance at Urumqi Glacier No. 1, Tian Shan, Central Asia. Global and Planetary Change 114, 14–22. https://doi.org/10.1016/j.gloplacha.2014.01.001

Watson, C.S., Quincey, D.J., Smith, M.W., Carrivick, J.L., Rowan, A.V., James, M.R., 2017. Quantifying ice cliff evolution with multi-temporal point clouds on the debris-covered Khumbu Glacier, Nepal. Journal of Glaciology 63, 823–837. https://doi.org/10.1017/jog.2017.47

Wei, J., Liu, S., Guo, W., Yao, X., Xu, J., Bao, W., Jiang, Z., 2014. Surface-area changes of glaciers in the Tibetan Plateau interior area since the 1970s using recent Landsat images and historical maps. Ann. Glaciol. 55, 213–222. https://doi.org/10.3189/2014AoG66A038

Westoby, M.J., Brasington, J., Glasser, N.F., Hambrey, M.J., Reynolds, J.M., 2012. 'Structure-from-Motion' photogrammetry: A low-cost, effective tool for geoscience applications. Geomorphology 179, 300–314. https://doi.org/10.1016/j.geomorph.2012.08.021

Wheaton, J.M., Brasington, J., Darby, S.E., Sear, D.A., 2009. Accounting for uncertainty in DEMs from repeat topographic surveys: improved sediment budgets. Earth Surf. Process. Landforms, 35: 136-156.. https://doi.org/10.1002/esp.1886

Winsvold, S. H., Kääb, A., Nuth, C., Andreassen, L. M., van Pelt, W. J. J., and Schellenberger, T.: Using SAR satellite data time series for regional glacier mapping, The Cryosphere, 12, 867–890, https://doi.org/10.5194/tc-12-867-2018, 2018.

Winsvold, S.H., Kääb, A., Nuth, C., 2016. Regional Glacier Mapping Using Optical Satellite Data Time Series. IEEE Journal of Selected Topics in Applied Earth Observations and Remote Sensing 9, 3698–3711. https://doi.org/10.1109/JSTARS.2016.2527063

Wu, K., Liu, S., Jiang, Z., Xu, J., Wei, J., Guo, W., 2018. Recent glacier mass balance and area changes in the Kangri Karpo Mountains from DEMs and glacier inventories. The Cryosphere 12, 103–121. https://doi.org/10.5194/tc-12-103-2018

Wu, K., Liu, S., Zhu, Y., Liu, Q., Jiang, Z., 2020. Dynamics of glacier surface velocity and ice thickness for maritime glaciers in the southeastern Tibetan Plateau. Journal of Hydrology 590, 125527. https://doi.org/10.1016/j.jhydrol.2020.125527

Wu, Y., Li, W., Zhou, J., Cao, Y., 2013. Temperature and precipitation variations at two meteorological stations on eastern slope of Gongga Mountain, SW China in the past two decades. J. Mt. Sci. 10, 370–377. https://doi.org/10.1007/s11629-013-2328-y

Xie, Z., Su, Z., Shen, Y., Feng, Q., 2001. Mass Balance and Water Exchange of Hailuoguo Glacier in Mount Gongga and Their Influence on Glacial Melt Runoff. Journal of Glaciology and Geocryology 7–15. (in Chinese)

Xu, J., Liu, S., Zhang, S., Guo, W., Wang, J., 2013. Recent Changes in Glacial Area and Volume on Tuanjiefeng Peak Region of Qilian Mountains, China. PLoS ONE 8, e70574. https://doi.org/10.1371/journal.pone.0070574

Xu, S., Fu, P., Quincey, D., Feng, M., Marsh, S., Liu, Q., 2022. UAV-based geomorphological evolution of the Terminus Area of the Hailuogou Glacier, Southeastern Tibetan Plateau between 2017 and 2020. Geomorphology 108293. https://doi.org/10.1016/j.geomorph.2022.108293

Xu, X., Yi, C., 2017. Timing and configuration of the Gongga II glaciation in the Hailuogou valley, eastern Tibetan Plateau: A glacier-climate modeling method. Quaternary International 444, 151–156. https://doi.org/10.1016/j.quaint.2017.01.011

Yang, K., Liu, Q., 2016. Supraglacial drainage system: a review. Journal of Glaciology and Geocryology 38, 1666–1678. (in Chinese)

Yang, W., Guo, X., Yao, T., Zhu, M., Wang, Y., 2016. Recent accelerating mass loss of southeast Tibetan glaciers and the relationship with changes in macroscale atmospheric circulations. Clim Dyn 47, 805–815. https://doi.org/10.1007/s00382-015-2872-y

Yang, W., Yao, T., Guo, X., Zhu, M., Li, S., Kattel, D.B., 2013. Mass balance of a maritime glacier on the southeast Tibetan Plateau and its climatic sensitivity: MASS BALANCE OF A TIBETAN GLACIER. Journal of Geophysical Research: Atmospheres 118, 9579–9594. https://doi.org/10.1002/jgrd.50760

Yang, W., Zhao, C., Westoby, M., Yao, T., Wang, Y., Pellicciotti, F., Zhou, J., He, Z., Miles, E., 2020. Seasonal Dynamics of a Temperate Tibetan Glacier Revealed by High-Resolution UAV Photogrammetry and In Situ Measurements. Remote Sensing 12, 2389. https://doi.org/10.3390/rs12152389

Yao, T., Greenwood, G., 2009. A New “Polar” Program: Third Pole Environment (TPE) Workshop; Beijing, China, 14–16 August 2009. Eos, Transactions American Geophysical Union 90, 515–515. https://doi.org/10.1029/2009EO520003

Yao, T., Pu, J., Lu, A., Wang, Y., Yu, W., 2007. Recent Glacial Retreat and Its Impact on Hydrological Processes on the Tibetan Plateau, China, and Surrounding Regions. Arctic, Antarctic, and Alpine Research 39, 642–650. https://doi.org/10.1657/1523-0430(07-510)[YAO]2.0.CO;2

Yao, T., Thompson, L., Yang, W., Yu, W., Gao, Y., Guo, X., Yang, X., Duan, K., Zhao, H., Xu, B., Pu, J., Lu, A., Xiang, Y., Kattel, D.B., Joswiak, D., 2012. Different glacier status with atmospheric circulations in Tibetan Plateau and surroundings. Nature Climate Change 2, 663–667. https://doi.org/10.1038/nclimate1580

Yu, B., 2018. Timing and Climate Drivers of Quaternary Glaciations in the Gongga Shan, Eastern Tibetan Plateau (Quaternary Geology). Lanzhou University, Lanzhou. (in Chinese)

Zemp, M., Thibert, E., Huss, M., Stumm, D., Rolstad Denby, C., Nuth, C., Nussbaumer, S.U., Moholdt, G., Mercer, A., Mayer, C., Joerg, P.C., Jansson, P., Hynek, B., Fischer, A., Escher-Vetter, H., Elvehoy, H., Andreassen, L.M., 2013. Reanalysing glacier mass balance measurement series. The Cryosphere 7, 1227–1245. https://doi.org/10.5194/tc-7-1227-2013

Zhang, B., Zhang, E., Liu, L., Khan, S.A., van Dam, T., Yao, Y., Bevis, M., Helm, V., 2018. Geodetic measurements reveal short-term changes of glacial mass near Jakobshavn Isbræ (Greenland) from 2007 to 2017. Earth and Planetary Science Letters 503, 216–226. https://doi.org/10.1016/j.epsl.2018.09.029

Zhang, G., 2012. The Study of Glacier Changes in the Gongga Mountains. Lanzhou University, Lanzhou. (in Chinese)

Zhang, G., Pan, B., Cao, B., Wang, J., Cui, H., Cao, X., 2015. Elevation changes measured during 1966–2010 on the monsoonal temperate glaciers' ablation region, Gongga Mountains, China. Quaternary International, Updated Quaternary Climatic Research in parts of the Third Pole Selected papers from the HOPE-2013 conference, Nainital, India 371, 49–57. https://doi.org/10.1016/j.quaint.2015.03.055

Zhang, Y., Liu, S., Liu, Q., Wang, X., Jiang, Z., Wei, J., 2019. The Role of Debris Cover in Catchment Runoff: A Case Study of the Hailuogou Catchment, South-Eastern Tibetan Plateau. Water 11, 2601. https://doi.org/10.3390/w11122601

Zhang, Y., Fujita, K., Liu, S., Liu, Q., Nuimura, T., 2011. Distribution of debris thickness and its effect on ice melt at Hailuogou glacier, southeastern Tibetan Plateau, using in situ surveys and ASTER imagery. Journal of Glaciology 57, 1147–1157. https://doi.org/10.3189/002214311798843331

Zhang, Y., Fujita, K., Liu, S., Liu, Q., Wang, X., 2010. Multi-decadal ice-velocity and elevation changes of a monsoonal maritime glacier: Hailuogou glacier, China. Journal of Glaciology 56, 65–74. https://doi.org/10.3189/002214310791190884

Zhang, Y., Gao, T., Kang, S., Shangguan, D., Luo, X., 2021. Albedo reduction as an important driver for glacier melting in Tibetan Plateau and its surrounding areas. Earth-Science Reviews 220, 103735. https://doi.org/10.1016/j.earscirev.2021.103735

Zhang, Y., Hirabayashi, Y., Fujita, K., Liu, S., Liu, Q., 2016. Heterogeneity in supraglacial debris thickness and its role in glacier mass changes of the Mount Gongga. Sci. China Earth Sci. 59, 170–184. https://doi.org/10.1007/s11430-015-5118-2

Zhang, Y., Hirabayashi, Y., Liu, Q., Liu, S., 2015. Glacier runoff and its impact in a highly glacierized catchment in the southeastern Tibetan Plateau: past and future trends. Journal of Glaciology 61, 713–730. https://doi.org/10.3189/2015JoG14J188

Zhang, Y., Hirabayashi, Y., Liu, S., 2012. Catchment-scale reconstruction of glacier mass balance using observations and global climate data: Case study of the Hailuogou catchment, south-eastern Tibetan Plateau. Journal of Hydrology 444–445, 146–160. https://doi.org/10.1016/j.jhydrol.2012.04.014

Zhang, Y., Liu, S., Wang, X., 2018. A dataset of spatial distribution of debris cover on Hailuogou Glacier of Mount Gongga in 2009. Science Data Bank.

Zhang, Y., Wu, H., Jin, S., Wang, H., 2013. MONITORING OF GLACIER VOLUME VARIATION FROM MULTI-SOURCE DATA OVER GELADANDONG AREA. ISPRS - International Archives of the Photogrammetry, Remote Sensing and Spatial Information Sciences XL-7/W1, 199–203. https://doi.org/10.5194/isprsarchives-XL-7-W1-199-2013

Zhang, Z., Wang, J., Xu, X., Bai, S., Chang, Z., 2015. Cosmogenic ^{10}Be and ^{26}Al Chronology of the Last Glaciation of the Palaeo-Daocheng Ice Cap, Southeastern Qinghai-Tibetan Plateau. Acta Geologica Sinica - English Edition 89, 575–584. https://doi.org/10.1111/1755-6724.12448

Zhang, Z., Liu, S., Zhang, Y., Wei, J., Jiang, Z., Wu, K., 2018. Glacier variations at Aru Co in western Tibet from 1971 to 2016 derived from remote-sensing data. Journal of Glaciology 1–10. https://doi.org/10.1017/jog.2018.34

Zhao, L., Tian, L., Zwinger, T., Ding, R., Zong, J., Ye, Q., Moore, J.C., 2014. Numerical simulations of Gurenhekou glacier on the Tibetan Plateau. Journal of Glaciology 60, 71–82. https://doi.org/10.3189/2014JoG13J126

Zheng, B., Ma, Q., 1994. THE GLACIER VARIATION, CLIMATIC CHANGE AND THE RIVER VALLEY DEVELOPMENT IN THE HOLOCENE ON THE GONGGA MOUNTAINS. Acta Geographica Sinica 6, 500–508. doi: 10.11821/xb199406003

Zhong, Y., Liu, Q., Westoby, M., Nie, Y., Pellicciotti, F., Zhang, B., Cai, J., Liu, G., Liao, H., Lu, X., 2022. Intensified paraglacial slope failures due to accelerating downwasting of a temperate glacier in Mt. Gongga, southeastern Tibetan Plateau. Earth Surface Dynamics 10, 23–42. https://doi.org/10.5194/esurf-10-23-2022

Zhu, H., Xu, P., Shao, X., Luo, H., 2013. Little Ice Age glacier fluctuations reconstructed for the southeastern Tibetan Plateau using tree rings. Quaternary International, Dendrochronology in Asia 283, 134–138. https://doi.org/10.1016/j.quaint.2012.04.011

Zhu, Q., Ke, C., Li, H., 2021. Monitoring glacier surges in the Kongur Tagh area of the Tibetan Plateau using Sentinel-1 SAR data. Geomorphology 390, 107869. https://doi.org/10.1016/j.geomorph.2021.107869

Zwinger, T., Moore, J.C., 2009. Diagnostic and prognostic simulations with a full Stokes model accounting for superimposed ice of Midtre Lovénbreen, Svalbard. The Cryosphere 3, 217–229. https://doi.org/10.5194/tc-3-217-2009

Appendix

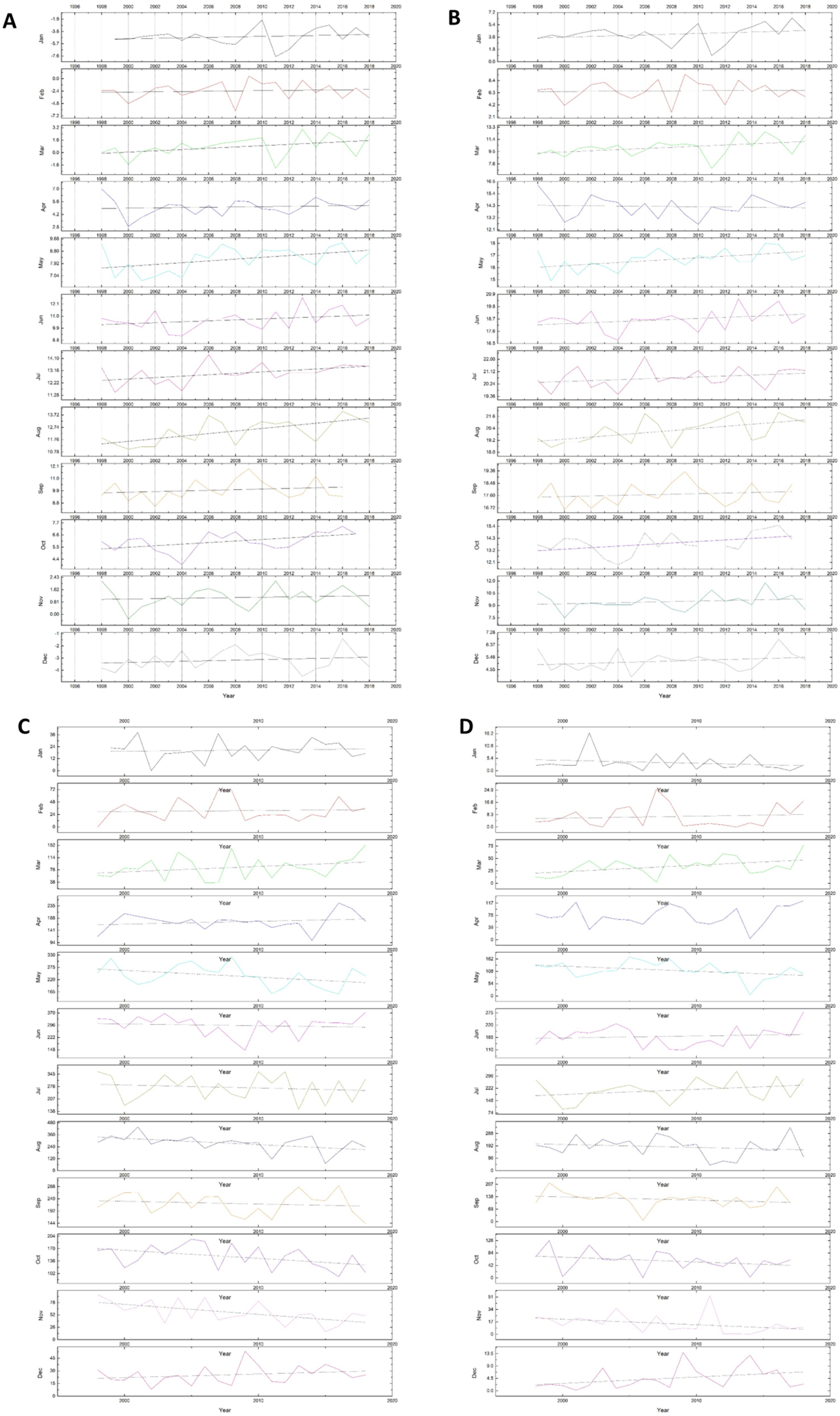

S 1 Monthly temperature data collected by meteorological Gongga station and Moxi station

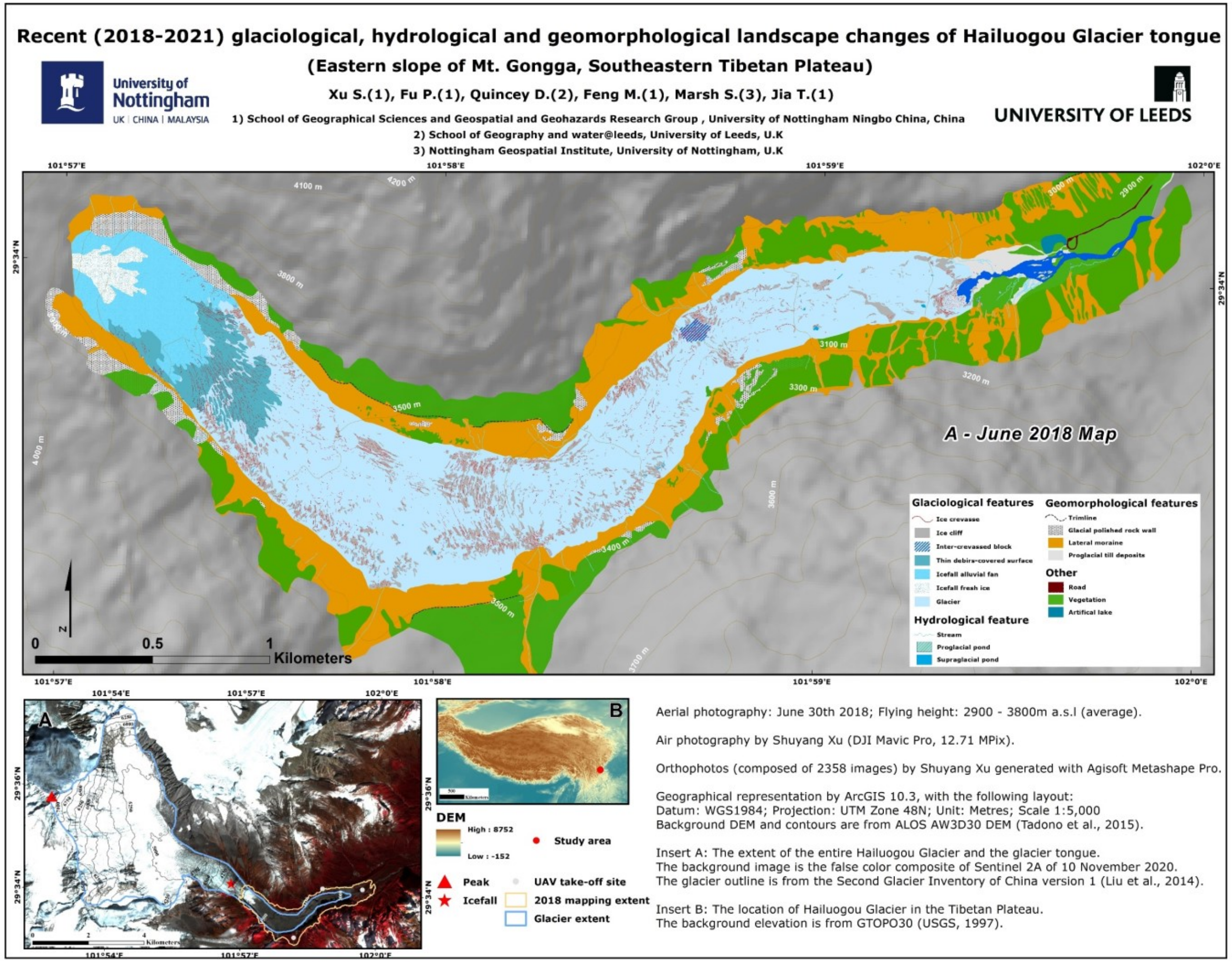

Appendix Map 1: 2018

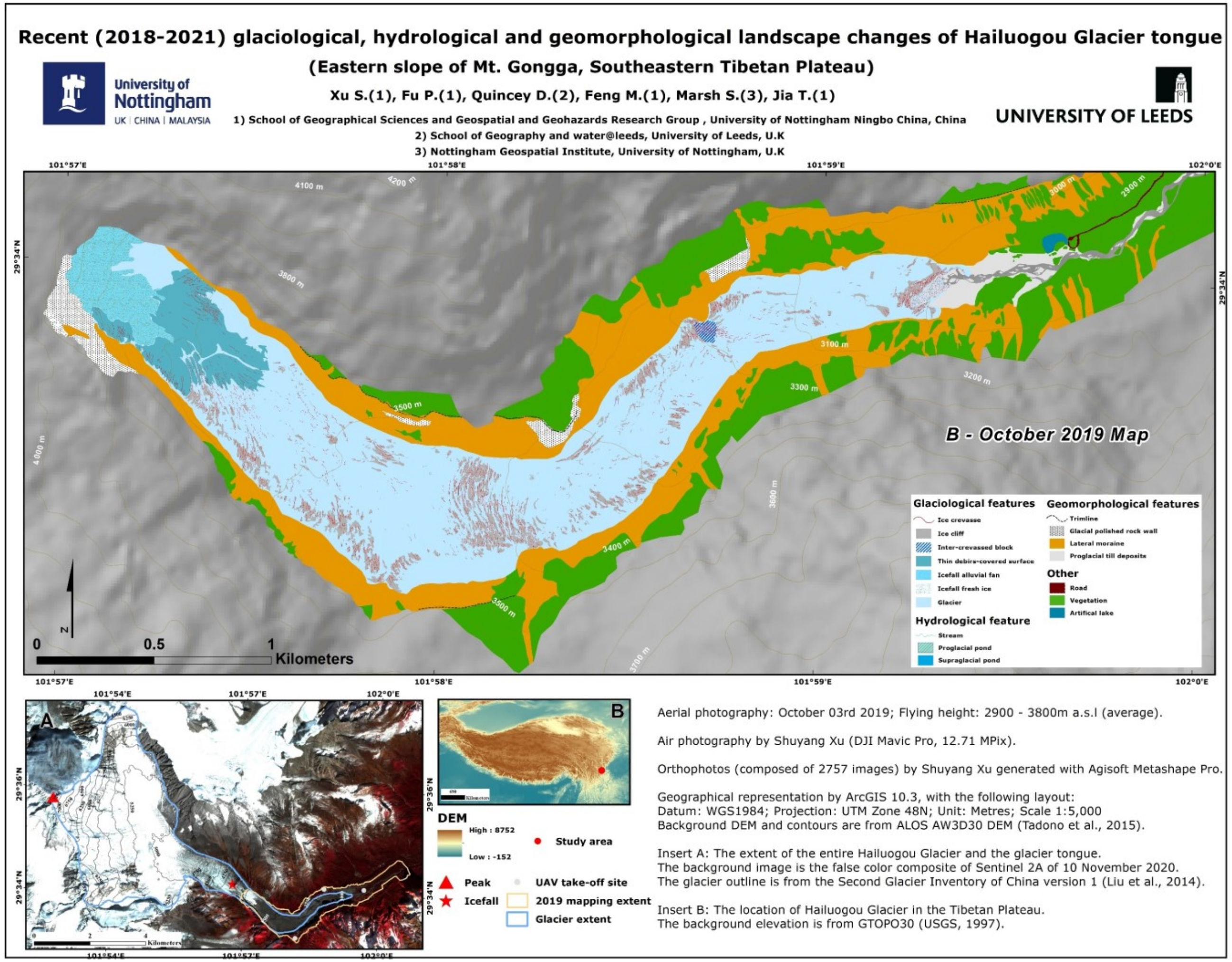

Appendix Map 2: 2019

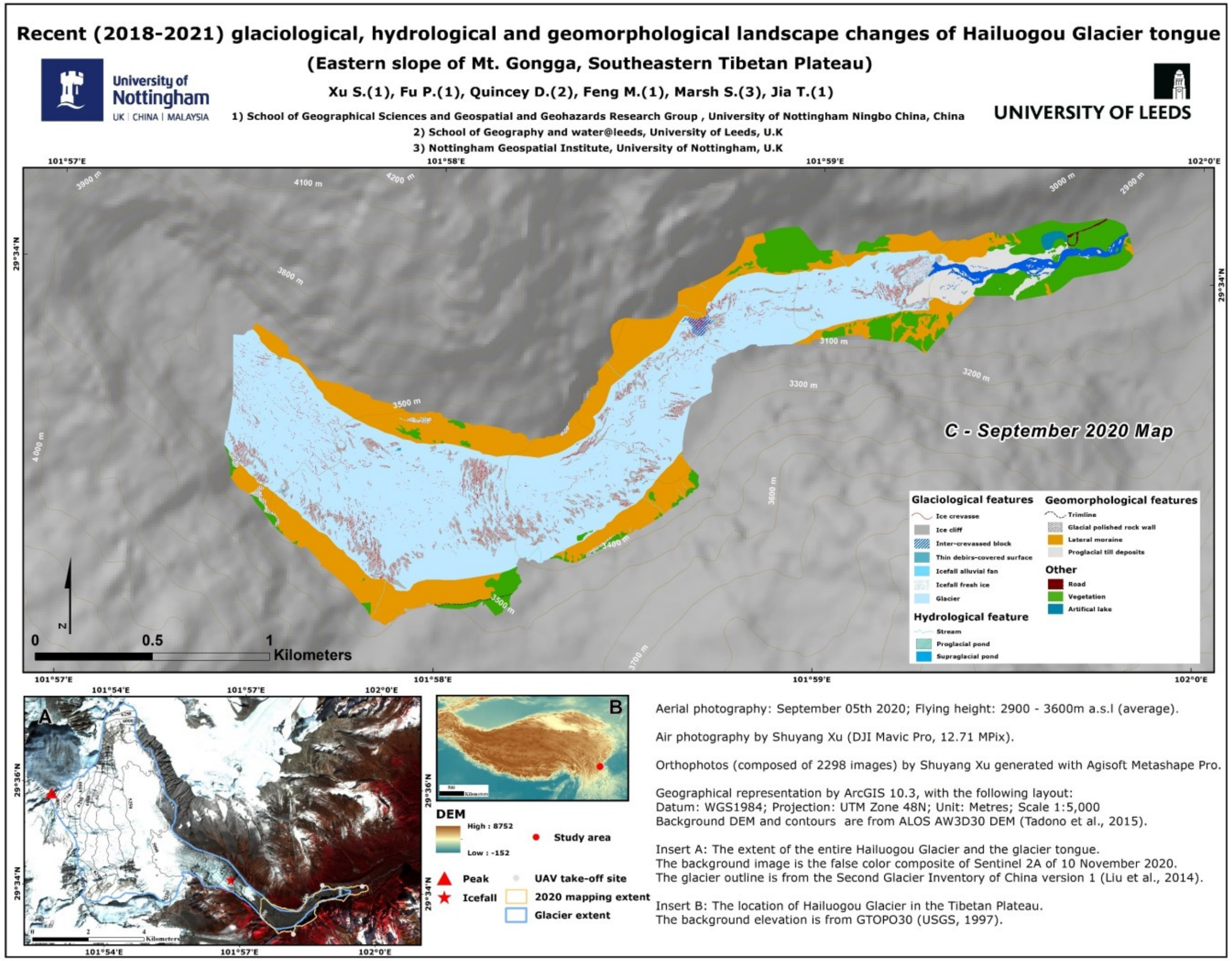

Appendix Map 3: 2020

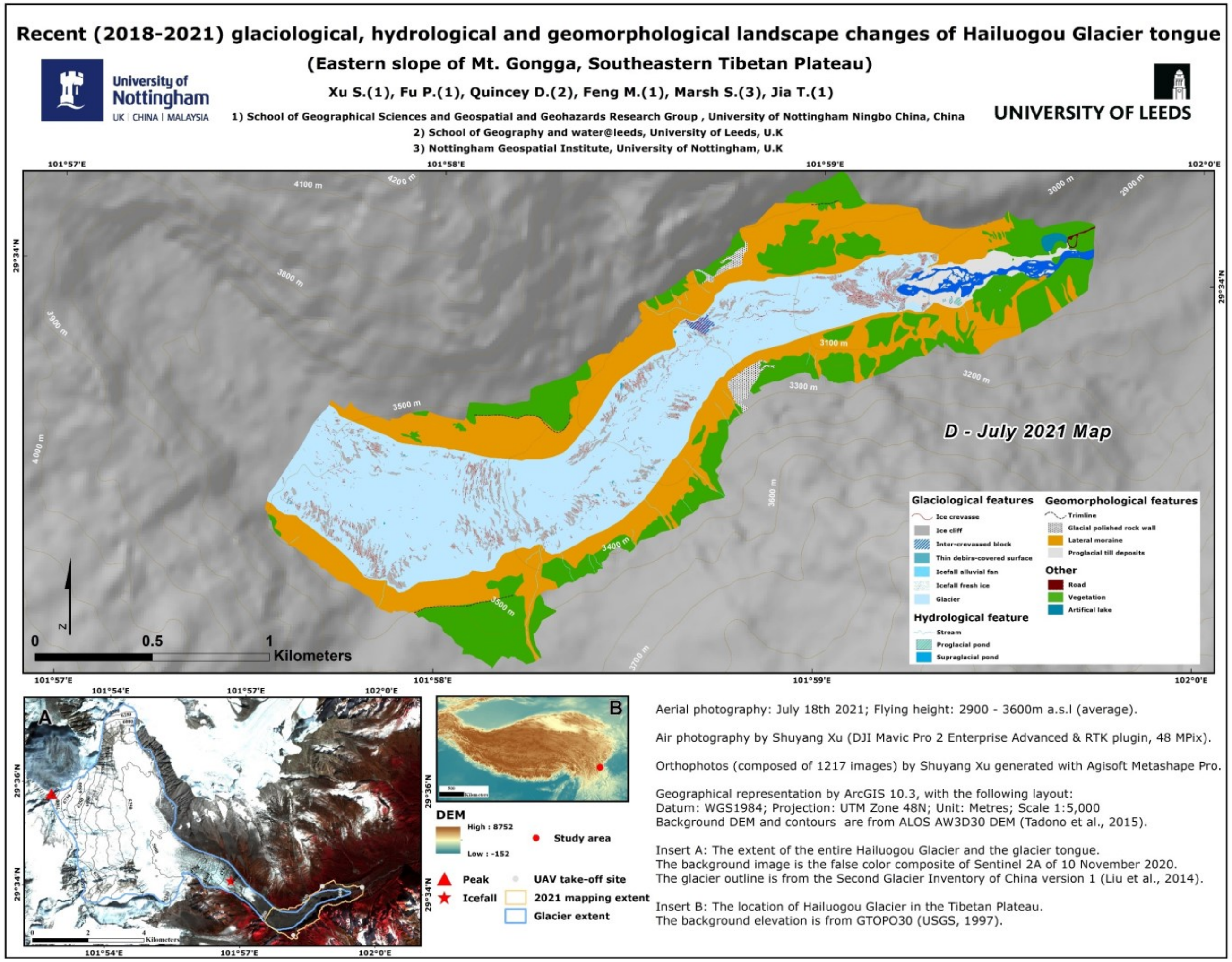

Appendix Map 4: 2021

S 2 The aspects of ice cliffs

	N		NW		W		SW		S		SE		E		NE		Total
2018	**Cell Num**	**Ratio**	**Cell Num**	**Ratio**	**Cell Num**	**Ratio**	**Cell Num**	**Ratio**	**Cell Num**	**Ratio**	**Cell Num**	**Ratio**	**Cell Num**	**Ratio**	**Cell Num**	**Ratio**	**Cell Num**
1	28553	15.99%	66015	36.96%	29415	16.47%	30869	17.28%	8778	4.92%	4073	2.28%	3083	1.73%	7805	4.37%	178591
2	85699	27.21%	81094	25.75%	48588	15.43%	24129	7.66%	11373	3.61%	6629	2.10%	13270	4.21%	44172	14.02%	314955
3	95075	10.14%	185918	19.83%	223588	23.85%	121756	12.99%	89356	9.53%	92876	9.91%	73493	7.84%	55467	5.92%	937529.9
4	16191	6.82%	31376	13.23%	35674	15.04%	59338	25.01%	38106	16.06%	24707	10.41%	21416	9.03%	10429	4.40%	237238
Total	225518	13.52%	364403	21.84%	337265	20.22%	236092	14.15%	147613	8.85%	128285	7.69%	111262	6.67%	117873	7.07%	1668314
2019	**Cell Num**	**Ratio**	**Cell Num**	**Ratio**	**Cell Num**	**Ratio**	**Cell Num**	**Ratio**	**Cell Num**	**Ratio**	**Cell Num**	**Ratio**	**Cell Num**	**Ratio**	**Cell Num**	**Ratio**	
1	24893	16.04%	38970	25.11%	23725	15.28%	33872	21.82%	8079	5.20%	4944	3.19%	5220	3.36%	15517	10.00%	155220
2	73907	23.29%	77949	24.56%	45997	14.49%	24152	7.61%	15333	4.83%	13778	4.34%	20950	6.60%	45334	14.28%	317400
3	183944	11.40%	306607	19.01%	325924	20.21%	220365	13.66%	143801	8.92%	171713	10.65%	134475	8.34%	126093	7.82%	1612922
4	6891	3.12%	17375	7.86%	35440	16.03%	38340	17.34%	38291	17.32%	57256	25.90%	20452	9.25%	7060	3.19%	221105
Total	289635	12.56%	440901	19.11%	431086	18.69%	316729	13.73%	205504	8.91%	247691	10.74%	181097	7.85%	194004	8.41%	2306647
2020	**Cell Num**	**Ratio**	**Cell Num**	**Ratio**	**Cell Num**	**Ratio**	**Cell Num**	**Ratio**	**Cell Num**	**Ratio**	**Cell Num**	**Ratio**	**Cell Num**	**Ratio**	**Cell Num**	**Ratio**	
1	84357	16.34%	65582	12.71%	94076	18.23%	116504	22.57%	43488	8.43%	29580	5.73%	25350	4.91%	57218	11.09%	516155
2	169559	22.61%	150506	20.07%	114713	15.30%	67886	9.05%	55892	7.45%	34543	4.61%	45826	6.11%	111037	14.81%	749962
3	225332	9.40%	429804	17.93%	563278	23.50%	309806	12.93%	214608	8.95%	254583	10.62%	242765	10.13%	156444	6.53%	2396620
4	12957	4.21%	31429	10.21%	47782	15.52%	38417	12.48%	43784	14.22%	89626	29.12%	29733	9.66%	14104	4.58%	307832
Total	492205	12.40%	677321	17.06%	819849	20.65%	532613	13.41%	357772	9.01%	408332	10.28%	343674	8.66%	338803	8.53%	3970569
2021	**Cell Num**	**Ratio**	**Cell Num**	**Ratio**	**Cell Num**	**Ratio**	**Cell Num**	**Ratio**	**Cell Num**	**Ratio**	**Cell Num**	**Ratio**	**Cell Num**	**Ratio**	**Cell Num**	**Ratio**	
1	151799	18.82%	178079	22.08%	91399	11.33%	135541	16.81%	109911	13.63%	65826	8.16%	34916	4.33%	38978	4.83%	806449
2	223209	25.36%	199438	22.66%	123321	14.01%	72175	8.20%	42698	4.85%	26873	3.05%	58468	6.64%	134065	15.23%	880247
3	218835	9.01%	487936	20.08%	557003	22.93%	290149	11.94%	203678	8.38%	238292	9.81%	251358	10.35%	182215	7.50%	2429466
Total	593843	14.43%	865453	21.03%	771723	18.75%	497865	12.10%	356287	8.66%	330991	8.04%	344742	8.38%	355258	8.63%	4116162

Note: 1, 2, 3 and 4 refer to the elevation range of terminus-3100, 3100-3300, 3300-3500 and 3500-3600 m a.s.l., respectively. Yellow, red and green refer to the maximum, the second maximum and the minimum value.

S 3 ASTER L1A data

Date	Hailuogou Glacier	Dagongba/Xiaogongba Glacier and Yanzigou Glacier
2002-02-23	Overall visible; lower patch- no cloud; upper patch -little cloud	Dagongga/Xiaogongga Glaciers: visible Yanzigou Glacier: visible
2002-11-06	Mostly cloud covered	Dagongga/Xiaogongga Glaciers: visible Yanzigou Glacier: visible
2005-11-07	Overall visible; missing lower tongue	Dagongga/Xiaogongga Glaciers: visible Yanzigou Glacier: no
2006-05-18	Mostly cloud covered	Dagongga/Xiaogongga Glaciers: no Yanzigou Glacier: no
2007-12-15	Upper patch- no cloud; lower patch: cloud	Dagongga/Xiaogongga Glaciers: visible Yanzigou Glacier: visible
2008-03-20	Overall visible	Dagongga/Xiaogongga Glaciers: mostly visible Yanzigou Glacier: visible
2008-04-05	Mostly cloud-covered; terminus is clear	All invisible
2008-11-15	Lower patch invisible	Dagongga/Xiaogongga Glaciers: visible Yanzigou Glacier: visible
2008-12-08	Overall visible; no glacier terminus	Dagongga/Xiaogongga Glaciers: visible Yanzigou Glacier: visible
2008-12-17	Overall visible	Dagongga/Xiaogongga Glaciers: visible Yanzigou Glacier: visible
2008-12-24	Overall visible; no terminus	Dagongga/Xiaogongga Glaciers: visible Yanzigou Glacier: visible
2009-01-18	Overall visible	Dagongga/Xiaogongga Glaciers: visible Yanzigou Glacier: visible
2009-02-03	Mostly cloud covered	Dagongga/Xiaogongga Glaciers: upper visible Yanzigou Glacier: visible
2009-04-08	Cloud-covered	Dagongga/Xiaogongga Glaciers: lower visible Yanzigou Glacier: visible
2009-06-11	Mostly cloud-covered	Dagongga/Xiaogongga Glaciers: terminus invisible Yanzigou Glacier: visible
2009-09-06	Lower patch cloud covered	Dagongga/Xiaogongga Glaciers: visible Yanzigou Glacier: visible
2009-10-17	Lower patch cloud covered	Dagongga/Xiaogongga Glaciers: visible Yanzigou Glacier: visible
2009-11-09	Overall visible; but missing terminus	Dagongga/Xiaogongga Glaciers: visible Yanzigou Glacier: visible
2009-11-25	Overall visible	Dagongga/Xiaogongga Glaciers: visible Yanzigou Glacier: visible
2009-12-04	Overall visible	Dagongga/Xiaogongga Glaciers: visible Yanzigou Glacier: visible
2009-12-11	Overall visible	Dagongga/Xiaogongga Glaciers: visible Yanzigou Glacier: visible
2010-01-28	Overall visible	Dagongga/Xiaogongga Glaciers: visible Yanzigou Glacier: visible
2010-11-05	Overall visible	Dagongga/Xiaogongga Glaciers: visible Yanzigou Glacier: visible
2011-02-09	Overall visible	Dagongga/Xiaogongga Glaciers: visible Yanzigou Glacier: visible
2011-04-30	Overall visible	Dagongga/Xiaogongga Glaciers: visible Yanzigou Glacier: visible
2011-05-07	Overall visible	Dagongga/Xiaogongga Glaciers: visible Yanzigou Glacier: visible
2011-10-07	Icefall cloudy	Dagongga/Xiaogongga Glaciers: terminus invisible Yanzigou Glacier: visible
2011-10-30	Overall visible; no terminus）	Dagongga/Xiaogongga Glaciers: visible Yanzigou Glacier: visible
2012-03-15	Upper cloud-covere	Dagongga/Xiaogongga Glaciers: visible Yanzigou Glacier: visible
2013-05-21	Overall visible	Dagongga/Xiaogongga Glaciers: visible Yanzigou Glacier: visible
2013-10-12	Overall visible	Dagongga/Xiaogongga Glaciers: visible Yanzigou Glacier: visible
2014-09-20	Overall visible	Dagongga/Xiaogongga Glaciers: visible Yanzigou Glacier: visible
2014-10-15	Lower invisible	Dagongga/Xiaogongga Glaciers: visible Yanzigou Glacier: visible
2014-10-31	Lower invisibl	Dagongga/Xiaogongga Glaciers: visible Yanzigou Glacier: visible

2016-02-14	Lower invisible	Dagongga/Xiaogongga Glaciers: visible Yanzigou Glacier: visible
2016-05-04	Overall visible	Dagongga/Xiaogongga Glaciers: visible Yanzigou Glacier: cloudy
2016-10-27	Overall visible	Dagongga/Xiaogongga Glaciers: visible Yanzigou Glacier: visible
2017-03-20	Lower invisible	Dagongga/Xiaogongga Glaciers: visible Yanzigou Glacier: upper visible
2017-10-07	Overall visible	Dagongga/Xiaogongga Glaciers: visible Yanzigou Glacier: visible
2018-11-02	Overall visible	Dagongga/Xiaogongga Glaciers: mostly visible; terminus cloudy Yanzigou Glacier: visible
2019-09-18	Lower invisible	Dagongga/Xiaogongga Glaciers: mostly visible; terminus cloudy Yanzigou Glacier: visible
2019-10-13	Lower invisible	Dagongga/Xiaogongga Glaciers: mostly visible; terminus cloudy Yanzigou Glacier: mostly visible; terminus cloudy
2019-10-20	Lower invisible	Dagongga/Xiaogongga Glaciers: visible but cloudy Yanzigou Glacier: visible
2019-10-29	Upper cloudy	Dagongga/Xiaogongga Glaciers: mostly visible; terminus cloudy Yanzigou Glacier: cloudy
2020-03-28	Mostly cloud-covered	Dagongga/Xiaogongga Glaciers: visible Yanzigou Glacier: visible
2020-09-20	Lower invisible	Dagongga/Xiaogongga Glaciers: joint is cloud Yanzigou Glacier: visible
2020-10-15	Lower invisible	Dagongga/Xiaogongga Glaciers: visible Yanzigou Glacier: visible
2021-03-08	Overall visible	Dagongga/Xiaogongga Glaciers: visible Yanzigou Glacier: visible
2021-04-16	Overall visible	Dagongga/Xiaogongga Glaciers: joint is cloud Yanzigou Glacier: visible
2021-09-23	Lower invisible	Dagongga/Xiaogongga Glaciers: upper invisible Yanzigou Glacier: visible